UNIVERSITY OF
LIVERPOOL

Automotive Driveline Control by Nonparametric QFT Methods

Thesis submitted in accordance with the requirements of the
University *of* Liverpool for the
Degree of Doctor in Philosophy

by

Ahmed Abass

May 2011

Statement of Originality

This thesis is submitted for the degree of Doctor in Philosophy in the Faculty of Engineering at the University of Liverpool. The research project reported herein was carried out, unless otherwise stated, by the author in the Department of Engineering at the University of Liverpool between 5/7/2007 and 5/5/2011.

No part of this thesis has been submitted in support of an application for a degree or qualification of this or any other University or educational establishment. However, some parts of this thesis have been published, or submitted for publication, in the following papers:

- S. Zhao, A. Abass, and A. T. Shenton, "Nonparametric Design Of Robust Linear Controllers and their Experimental Application to Idle Control," IASTED, pp. 651–061, International Conference on Control and Applications, 2009.
- A. Abass, S. Zhao and A. T. Shenton, "Nonparametric Driveline Identification and Control," ISMS, pp. 238–243, International Conference on Intelligent Systems, Modelling and Simulation, 2010.
- A. Abass and A. T. Shenton, "Automotive Driveline Modelling, Inverse-Simulation and Compensation," ISMS, pp. 244–249, International Conference on Intelligent Systems, Modelling and Simulation, 2010.
- A. Abass, Paul B. Dickinson and A. Thomas Shenton, "Electronic Throttle Control by a Nonparametric QFT Method", AVEC, 10th International Symposium on Advanced Vehicle Control,2010.
- A. Abass and A. T. Shenton, "Automotive Driveline Control by a Nonlinear Nonparametric QFT Method", pp. 1316–1321, ICARCV, International Conference on Control, Automation, Robotics and Vision, 2010.

Ahmed Abass
5th May 2011

Abstract

This thesis develops and applies novel identification and control methods for automotive vehicle driveline control. The driveline system has internal backlash combined with resonances which make its control a difficult nonlinear problem. The automotive industry has become very competitive during the last few years and in addition to style and fuel economy, the vehicle performance is a very important issue for the customer. The driveline response to driver demand is a key factor in the customer perception of vehicle quality. A major challenge in its control is that individual driving skills differ greatly among drivers, which leads to a large uncertainty in uncontrolled vehicle response. Current industrial methodologies for the driveline control problem are heuristic and trial and error and require considerable time and resources including extensive on-road vehicle testing. The presented work in thesis in contrast, presents a rapid and systematic methodology which allows the control engineer to achieve pre-determined quantified tracking bounds on the driveline response despite significant system nonlinearity and uncertainty.

Firstly a novel mathematical model of the driveline is presented which is subsequently used as one means to evaluate the proposed control methods. Both clutch and backlash nonlinearities are included in the model, and unlike in other published models, backlash is more realistically sandwiched between the compliant clutch and compliant drive shafts. The thesis integrates a Nonparametric (NP) identification approach with Quantitative Feedback Theory (QFT) control methods to result in a novel NP QFT method for nonlinear systems. A NP frequency response identification method is proposed for obtaining a Linear Time Invariant Equivalent (LTIE) sets for the nonlinear system using a frequency weighted windowing method to allow the use of experimentally obtained finite Input/Output (I/O) data records. The NP model is obtained by a local frequency smoothing estimation method in which a frequency set is selected to cover the system bandwidth. This novel NP QFT method has the usual benefits of NP identification such as avoiding concentrating the system information in a limited number of parameters and also permits the acknowledged benefits of QFT control such as the effective linear controller design for nonlinear systems which cannot otherwise be applied without parametric models. A novel technique, based on the discrete Hilbert transform is presented for obtaining an equivalent Minimum Phase (MP) plant for a None Minimum Phase (NMP) nominal plant and determining their phase shift difference which

allows the QFT design of such systems based on NP data for the first time.

Another application of the NP identification method which is presented is to parameter space control and develops a novel NP parameter space method which has the advantage over QFT of simplicity of controller design and structure at the expense of reduced performance. This method is validated experimentally on the vehicle Internal Combustion (IC) engine idle speed problem. The presented NP QFT method is used to design a controller for a gasoline electronic throttle valve which is a key component of all driveline control systems. Although nonlinear compensation could significantly enhance the outcomes of the process further, it is shown that an effective linear controller can be designed by the NP QFT method without any nonlinear compensation and with an acceptable time response in a quick and systematic method from readily obtained test-data.

All used experimental validation approaches use an entirely black box approach in which the controllers are developed directly from experimental testing. The experimental results show that both the new NP parameter space and new NP QFT methods are able to robustly achieve good engine idle speed control and good driveline wheel speed control respectively. In driveline control, the wheel speed response was experimentally found to be always inside the pre-designed boundaries and the controlled system was found able to reject the external disturbances within the desired boundary. The presented techniques can be applied to any similar systems where only experimental test data is available without any need to change the methodology or to use any trial and error sequences. The presented methods provide considerable reduction in the design and testing effort for driveline, electronic throttle valve and idle speed control problems.

Acknowledgments

I am very grateful to my supervisor Dr Tom Shenton. His guidance and support were appreciated in the completion of this work. I would like also to thank Mr. Derek Neary for his technical assistance with the experimental setup.

I would like also to thank many friends I have made during my PhD. Paul Dickinson, Christian Matthews, Chris Ward, Nick Rivara, Shiyu Zhao, Zongyan Li, Ke Fang, Jack Mullett and Ming-Yen Chen for their project arguments during the different stages of this work.

I would like to thank the Egyptian government for its financial support and my wife Randa Ayad for her patience and support.

Contents

List of Figures

Acronyms

A/D Analog to Digital

ABS Anti-lock Braking System

ABV Air Bleed Valve

AFR Air to Fuel Ratio

ARMAX Autoregressive Moving Average with eXogenous Input Model Structure

ARX Auto Regressive with eXogenous Input Model Structure

BJ Box Jenkins

CAD Computer Aided Design

CFM Cubic Feet per Minute

CPU Central Processing Unit

D/A Digital to Analog

DC Direct Current

DFT Discrete Fourier Transform

ECU Electronic Control Unit

EM Electromagnetic

FFT Fast Fourier Transformation

FRF Frequency Response Function

I/O Input/Output

IC Internal Combustion

LAN Local Area Network

LQ Linear Quadratic

LQSF Linear Quadratic State Feedback

LTI Linear Time Invariant

LTIE Linear Time Invariant Equivalent

MIMO Multi Input Multi Output

MISO Multi Input Single Output

MP Minimum Phase

NARX Nonlinear AutoRegressive with eXogenous Input Model Structure

NMP None Minimum Phase

NP Nonparametric

PAU Power Absorption Unit

PC Personal Computer

PP Perturbation Period

PPS Pulse Per Second

PRBS Pseudo Random Binary Sequence

PWM Pulse Width Modulated

QFT Quantitative Feedback Theory

RAM Random Access Memory

RF Radio Frequency

RPM Revolution Per Minute

RQ Regler Quer

RQV Regler Quer Verstellung

RTI Real-Time Interface

SISO Single Input Single Output

TDC Top Dead Center

VM Vector Margin

Chapter 1

Introduction

Automotive performance, fuel economy and exhaust emissions are considerable requirements in the automotive industry [1] which became very competitive during the last few decades. Each producer should be able to persuade customers to purchase his car. It is correct that the vehicle structural superiority is an important factor but the producer should market the vehicle dynamic performance also [2]. To do that, he should be able to show the good driveability of his vehicle. The term driveability in the vehicle industry is used to describe the vehicle performance and how pleasing it is to the driver. Vehicle driveability is a key factor for marketability and competitiveness of passenger automobiles, since the decision of customers to buy a certain car is usually taken after testing [3]. Moving from low speed to high speed soon after launch is one of the specific driveability issues that car manufacturers face in order to ensure their vehicles are regarded as quality products. Of course, one of the first impressions the costumer may feel is how easy and comfortable it is to launch the vehicle then to achieve the speed he likes without shuffling (driveline torsional vibrations which causing an oscillating vehicle speed) and without stalling (sudden stopping) the engine at the same time.

Modern fuel efficient engines are increasingly using turbo-charging and direct injection technologies which introduce time lags and difficult dynamics. These new engines may make the avoidance of shuffle more difficult particularly in launch and more advanced control is necessary to make them acceptable to the customer.

Strictly speaking, the work which has been done in this thesis took place while the first gear is fully engaged, however the term "vehicle launch" in automotive industry means to depress the clutch pedal to the end, then to engage the first gear, to release the clutch pedal and then finally increase the vehicle speed. As the automobile wheels start to move when the driver releases the clutch pedal, the control system presented in this thesis deals with this situation as a disturbance.

In general, there are two essential elements of any launch event relevant to the vehicle driving. The driver interaction with the vehicle and the vehicle response. It is difficult to predict the interaction of different drivers accurately enough to avoid certain undesirable conditions such as stall or shuffle. Also, classification of drivers skills is not very useful in the driveline speed control problem because the application here is developed to be applicable to conventional vehicles and ordinary drivers. Customers with low driving skills may never admit that their driving skills are low. Instead, they may start to blame the car producer when shuffle and stall take place. This represents a challenge to the designers because the customer is always right or he should be considered right.

Of course, the smooth controlled speeding up as the car pulls away from the traffic lights, for example, gives a positive impression to the driver. The driver demand when he pushes the accelerator pedal is not necessarily ideal for smooth pull away. Engine flare or engine stall are possible results when the driver demand is too much or too little, this could be considered as poor, or lower than expected, performance by the customer.

The solution of the driveline speed control problem could be separated into two main tasks; system identification and plant control. System identification is the process for constructing models of dynamic systems from experimental time series test data [4]. Once a good model is obtained, control design techniques can be applied and tested. An overview of the strategy of control is displayed in Figure 1.1.

This chapter provides a general introduction for the work achieved in this thesis. Section 1.1 shows the objectives of the thesis and section 1.2 presents an overview of the thesis. The elements of novelty in this thesis are listed in section 1.3. Finally, the chapter conclusions are presented in section 1.4.

1.1 Objectives of the Thesis

The objectives of this work was to develop a black-box modelling and controller design technique which can rapidly and accurately capture the system dynamics and achieve the require controller performance. The method should reduce the modelling difficulties associated with parameter model such as structure and model order selection. The method should be able to successfully handle nonlinear system and generate robust controllers which meet the specified requirements. The resulting methodology was demonstrated on a variety of practical nonlinear powertrain systems.

To achieve this objective the following sub-tasks were established:

- Develop a mathematical model for the driveline in which both clutch nonlinearity and

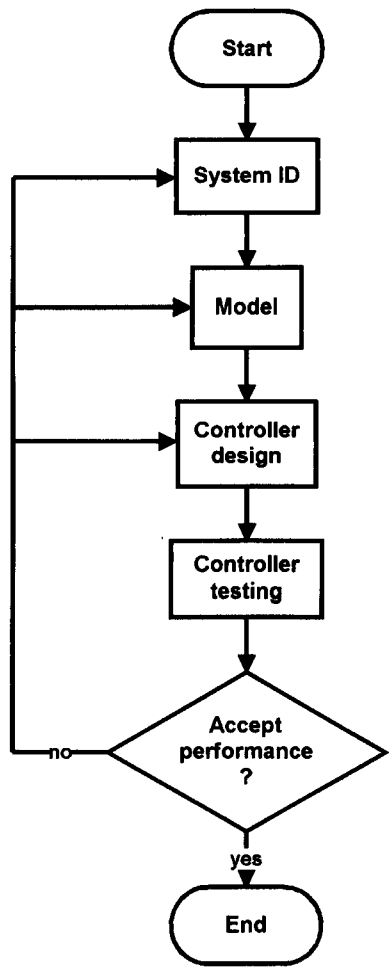

Figure 1.1: The strategy of control problem solution

backlash nonlinearity are considered in their realistic position. The model should be such that is useful for subsequent control systems development.

- Extend the low order parameter space control method to handle NP data and apply it experimentally validate the technique on the IC engine idle speed problem.
- Combine NP identification approaches with the QFT control methods to the take advantage of both techniques. The resulting methodology was demonstrated on the driveline model and validated using a physical tested.
- Validate the NP system identification and controller design methodology using other powertrain examples, such as the electronic throttle.

1.2 Overview of the Thesis

In this thesis, a novel mathematical model of the vehicle driveline driveline is presented. A novel NP parameter space method for the vehicle IC engine idle speed problem is presented. A novel NP QFT design methodology for automotive driveline control system is presented. In addition to the use of NP model in the QFT method including applying the presented methods experimentally on the IC engine, the driveline, and the electronic throttle valve are also novel applications. A summary of the next chapters can be described as the following:

Chapter 2: Background

This chapter gives important background concepts and information. It discusses system modelling, robust systems identification, control of dynamic systems and driveline speed control problem.

Chapter 3: NP Identification Analysis

In this chapter, the basics of NP techniques are discussed. This includes transfer function estimation by impulse response analysis, frequency response analysis by Fourier transform, errors in digital frequency response estimation and NP system identification.

Chapter 4: Driveline Modelling

A novel mathematical model for the driveline is presented in this chapter. Driveline constitutive equations are constructed. The modelling process starts with the engine and ends with

the wheels through the clutch, transmission and couplings. Both, clutch and backlash nonlinearities are included in this model. In contrast with other published models, the backlash in the presented model is sandwiched between the compliant clutch and compliant drive shafts. This allows testing of the control methodology with an arbitrary driveline nonlinearity. At the end of this chapter, a linear model is obtained and the effect of nonlinearity is thereby displayed by comparison.

Chapter 5: Quantitative Feedback Design

This chapter provides a background of the work done in this thesis. The benefits of using the feedback control techniques are discussed in this chapter. The used plant uncertainty templates and basic frequency domain characteristics are then explained. QFT time domain requirements and translating time domain requirements to frequency domain boundaries are then discussed. The logic of selecting the frequency domain specification and the QFT boundaries representation in Nichols chart is then discussed. As NMP plants need special arrangements in the QFT method, the background to this issue is described and a novel methodology is for this problem case by using a Hilbert transform approach is presented. Finally, the QFT prefilter design technique is explained.

Chapter 6: Parameter Space Engine Control Based on NP Modelling

In this chapter, the idle speed feedback control system is discussed. Then, the NP identification technique and the identification data are displayed. Parameter space control technique is covered and the obtained controller performance is displayed.

Chapter 7: Simulation Driveline Speed Control by NP QFT

The developed NP QFT method is applied to the model obtained in Chapter 4. This includes the I/O data collection, NP identification of the LTIE set, setting of stability, tracking and disturbance bounds, and the determination of the stable NMP nominal system required for the QFT design. An approach for setting of stability, tracking and disturbance bounds, open loop shaping and prefilter design are presented.

Chapter 8: Experimental Setup

An overview of the tools and equipments which are used for achieving the experimental work for this thesis can be found in this chapter. Prototyping system, software, driveline specification, interfacing hardware, angular encoders and solenoid air valve are described and

discussed in details. The driveline experimental setup, the chassis dynamometer and the throttle valve experimental setup are also detailed out in this chapter.

Chapter 9: Experimental Driveline Speed Control by NP QFT

In this chapter, the developed NP QFT method is applied in a real world problem. The driveline experimental setup described in Chapter 8 is used for collection of the driveline I/O data which is then processed to obtain a NP model. Selection of the excitation signals is discussed before the method of constructing the LTIE I/O data set. Setting of stability, tracking and disturbance bounds for the driveline speed control is then discussed.

Chapter 10: Electronic Throttle Control by a NP QFT Method

Due to technical reasons discussed in Chapter 8, throttle valve duty was not used as an input signal in the experimental setup. Chapter 10 focuses on the electronic throttle in particular as an important subsystem of the complete driveline control system. This was to investigate the developed NP QFT technique on an essential and very nonlinear component of the driveline. The NP QFT design technique is applied successfully on the electronic throttle valve in this chapter. The chapter starts with defining the electronic throttle then explains how the NP Nonlinear QFT method is applied on it. Finally, the results and conclusions for the designed electronic throttle controller based on the NP QFT method are presented.

Chapter 11: Conclusions and Future Work

This chapter presents the conclusions of the thesis and discusses the suggested future work.

1.3 Contribution of the Thesis

The elements of novelty in this thesis are:

- A novel mathematical model of the driveline is presented in Chapter 4. In this model, a realistic representation of the driveline clutch and the backlash nonlinearities are developed. Unlike the published models, backlash is sandwiched between the compliant clutch and compliant drive shafts. The developed model has been used for testing the control techniques presented in this thesis. Also, and at the same time, it can be used for a novel inverse technique applications.
- A novel NP parameter space controller design method is presented and used for the IC engine idle speed control problem in Chapter 6. NP model is obtained by local frequency

smoothing estimation method. An identification frequency set has been selected to cover the system bandwidth. An experimental implementation of the NP parameter space technique is applied to the idle speed problem for the IC engine of the University of Liverpool and the attached low inertia dynamometer. The experimental validation showed the advantages of using closed loop control for the problem in terms of accurate tracking and efficient disturbance rejection.

- A novel NP QFT controller design approach is presented. It has the advantages of nonparametric identification including that the information in the model is not constrained into a small set of parameters and unlike in parametric modelling, there is no need for a series of user decisions such as selecting the model order. At the same time the method exploits the main advantage of the conventional QFT method, which is the effective linear controller design for a nonlinear system, which can not otherwise be applied without a parametric model. The technique is tested in Chapter 7 on the model of Chapter 4 and validated experimentally on Chapters 9 and 10.

- A novel technique, based on discrete Hilbert transform, for obtaining an equivalent MP plant for NMP nominal plant and determining the phase shift between them is developed. This technique is used in Chapters 7 and 9. As the plant in NP identification techniques is represented by a frequency response locus rather than the mathematical equations used in parametric identification techniques.

- Novel implementation of the NP QFT method to the driveline speed (Chapters 7 and 9) control problem are presented. Applying the developed method on the electronic throttle valve control problem is novel (Chapter 10).

1.4 Conclusions

The Conclusions of this chapter are:

- In this thesis, a new mathematical model of the driveline is presented. The model is shown to give realistic results and may be useful for driveline control system design.

- A novel NP parameter space controller design method is presented and verified experimentally on the IC engine idle speed control problem. The method works directly from input-output test data obtained from the system.

- A novel NP QFT design methodology for automotive driveline control system is presented. This worked directly with the set of frequency responses obtained by NP identification.

- A novel technique, based on discrete Hilbert transform, for obtaining an equivalent MP plant for NMP nominal plant and determining the phase shift between them is presented. This allows a fully NP approach to the QFT method to be employed for the first time.
- New applications of the NP parameter space and NP QFT control are applied to the IC engine idle speed problem, to the driveline speed control problem and to the electronic throttle valve control problem.

Chapter 2

Background

2.1 Introduction

The driveline is the mechanical components that transmits the engine power to the vehicle wheels. As a dynamic system, some of its components can be treated as linear components, however, some other components and responses should be represented nonlinearly to reflect the physical components behavour.

In this chapter, driveline modelling as a dynamic system is discussed in section 2.2. This includes description of white-box, grey-box, and black-box models. The main procedure of parametric identification are displayed before discussing the robust systems identification techniques in section 2.3. Two main phases are used to obtain theoretical results that are closely related to the experimental aspects of the controlled system. These phase are the simulation phase and the experimentation phase which are explained in last mentioned section. Also, a definition of uncertainty is given just before moving to discuss the control of dynamic systems in section 2.4. Section 2.5 focusing on the driveline control problem and section 2.6 discussing the limitations of it. It answers the question why and when rotational velocities/torques can be used in driveline speed/torque control problems.

2.2 Driveline Modelling as a Dynamic System

In automatic control field, a model of a dynamic system is a description for some or all of its characteristics according to the application. Because the model is just a representation so it should be clear that this model is always obtained to serve a certain purpose and to operate within a certain bandwidth and at certain conditions. To be beneficial for control purposes, the obtained models should be able to describe the systems dynamics over the desired dynamic range. Of course, the accuracy of the model has a significant effect on

the performance of the controller eventually applied on the physical system. Also, noisy measurements and the influence of unmodelled dynamics are always exist [5].

Modelling strategies can be classified in three main categories according to the approaches used to the obtain them; white-box modelling, grey-box modelling and black-box modelling. The model should be suitable for the purpose to which it will be used. In some applications like Riccati $\mathcal{H}_\infty$, the controller order is determined by the model order [6]. In such a situation, a low order model is recommended. As the driveline studied in this project is a nonlinear system and linear controller may often be preferred, so the system nonlinear model can be linearised. Alternatively, a linear model can be obtained directly by selecting an appropriate linear identified process.

2.2.1 White-Box Models

A white-box model, also known as phenomenological or physical model, is a physical process that describes a dynamic system by assembling the low level mathematical representation of its components. For white-box model to be accurate, the process needs to be well understood and not too complected. This approach uses basic scientific principles like Newton's laws, Kirchhov's laws, thermodynamic laws and reaction kinetics to drive an analytical model [7]. A good phenomenological model should be easily adapted to similar systems [8], such as different capacity drivelines. These phenomenological models assume that all the system dynamics are fully understood and its physical parameters are known with a degree of certainty. It also assumes that all system dynamics can be represented mathematically in significant patterns. Because white-box models do not contain many approximations, they are often expected to be complex models. White-box models are difficult to set up and to implement. The associated complexity also causes slow running performance when digital software is used to implement them. Of course, the elaboration of white-box models requires fast computers with powerful Central Processing Units (CPU) and large amounts of Random Access Memory (RAM) in addition to sufficient digital storage space.

A white-box model is only necessary where a high level of details in the physical processes is required. For example, when monitoring the driveline speeds and torques of different shafts during running the model is necessary for control, white-box model is a good choice for modelling process. A grey-box model can be used for many application instead of a white-box model, however white-box model provides more detailed mathematical representation of the physical component.

2.2.2 Grey-Box Models

A grey-box model provides a physical mathematical representation of a dynamic system. It is ideal for describing a system whose way of working is partially understood. In grey-box models, some of the system physics are approximated. As it can be considered as an intermediate methodology between white-box and black-box models, one can say that the the greater number of simulation models are grey-box models. The reason for that is the difficulty of describing some nonlinearities in an accurate equation as required in white-box models. Grey-box model provides more flexibility than white-box models as it enable the designer to use modelling to optimise a design, rather than giving answers based on fixed model structure. In brief, grey-box approach attempt to bridge the gap between purely theory based modelling in white-box modelling and purely data based modelling in black-box modelling. As a systematic approach, it combines physical modelling with experimental data from industrial processes, so the physical meaning of the model parameters may be retained, which is beneficial during identification because the designer can judge if the obtained parameters are sensible or not.

2.2.3 Black-Box Models

The black-box modelling approach assumes no prior physical understanding of the system. That is the reason why the system is referred as a black-box. This approach is wholly dependent on the use of I/O data collected from the physical system in real time experiments. System identification, in this case, is a behavioural approach for developing a model without requirement of physical understanding of of the process [9]. The outcome of a system identification process is a model representing the original dynamic system. For those models, the structure must me defined first before calculating the model parameter. Black-box identified models can be classified as parametric models and NP models. Parametric methods estimate parameters in a user specified model such as transfer functions and state-space matrices. However, NP methods techniques try to estimate a generic model such as impulse responses and frequency responses. The main procedure to parametric identification are displayed in the flow chart in Figure 2.1 [4]. It starts by designing the experimental setup, then collecting the I/O data and pre-processing it. After that, a model structure is defined according to the designer selection. The selected model structure parameters are then estimated and the model is validated. The designer is required to go back to modify the methods and techniques during the identification until an acceptable model is obtained. The following is an overview of the parametric system identification procedure.

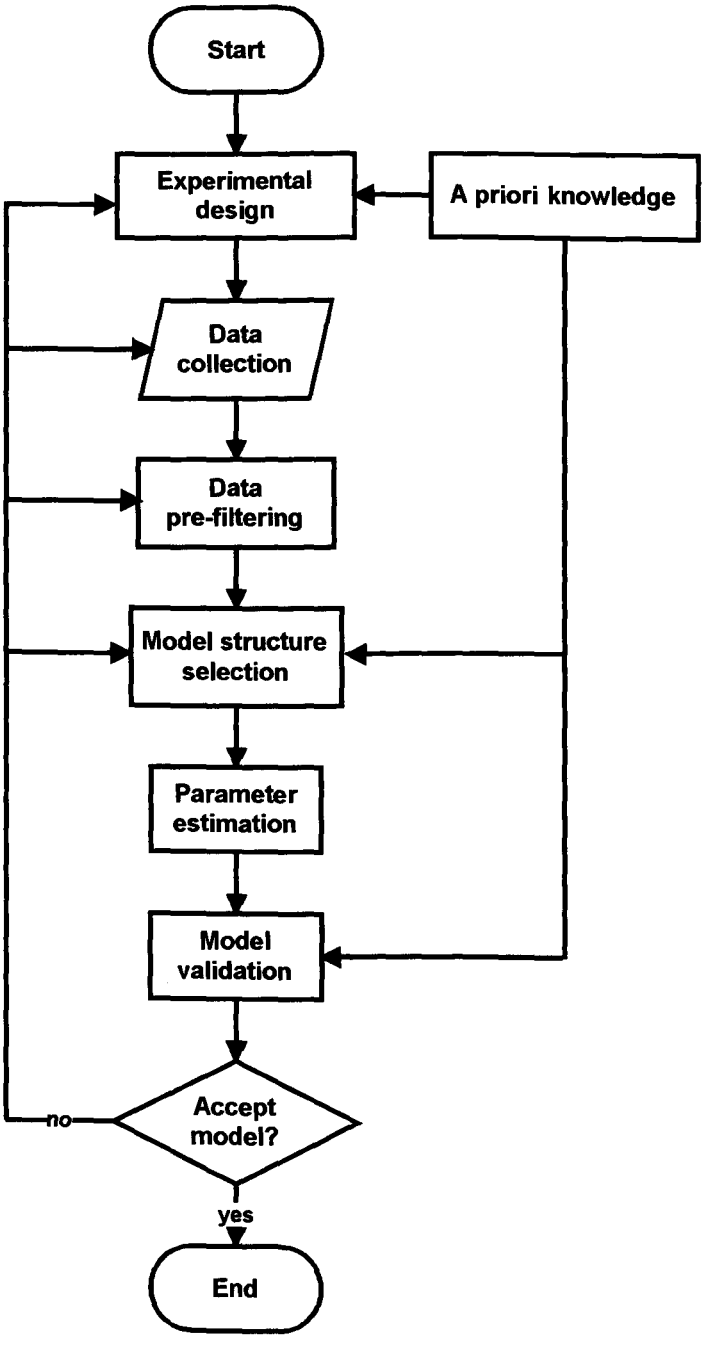

Figure 2.1: Flow chart illustrating the system identification process [9, 10, 4]

Design of Experiment

The first element in the design of the experimental setup is the selection of the input and output signals according to the purpose of the identification and control processes. The setup should allow the designer to repeat a certain perturbation signal if necessary and to record the I/O data with a sensible time rate. A priori knowledge of the investigated system is an advantage but this knowledge is not always available. The selection of the excitation signal is one of the things that needs previous experience if possible. The reason for that is the difficulty of the direct measurement of some parameters such as the driveline driving torque which is a preferred input signal in driveline identification problem. Another example is the use of the Air Bleed Valve (ABV) duty instead of the throttle valve duty as an input signal to the drive line.

1. Frequency Content of Perturbation Signals

   For identifying dynamic systems correctly, the perturbation signal should be rich enough to excite the system across its bandwidth. Of course, step type input signals are usually preferred because they contain infinite superpositions of sinusoidal components. The difficulty in using such that steps appears when the constraint on the investigated system do not allow the designer to use a large step input because of possible damage. White noise is one of the preferred input signals because it contain a very wide range of frequency content as it is a random signal with a flat power spectral density. This means that it has approximately an equal power within a fixed bandwidth at any frequency. The Pseudo Random Binary Sequence (PRBS) signal which is a digital version of white noise with the same autocorrelation is usually favoured in linear identification. Another important parameter in forming the excitation signal is the perturbation time. If a perturbation time does not cover the possible delays in the system, the resulting model con not be considered as a good representation of the system dynamics [11, 12].

2. Excitation Signal Amplitude

   The amplitude of the input signal can be limited to a small range in linear system identification applications. When the system is considered as a linear system, no significant effect is expected when the input amplitude is changed. In this case, the two distinct levels to the PRBS signal can provide sufficient information for characterising the system since the output response is directly proportional to the input. However, a random walk signal is considered as a good choice when the system is considered as nonlinear.

   If the identified system is believed to be nonlinear and a set of linear models are to be identified to represent the system over a range of operating conditions, the input

signal amplitude must be varied to cover this range. This variation of the input signal amplitude is necessary in order to capture the uncertainty due to the nonlinearity of the investigated system.

3. Decimation (Sampling Rate)

   The sampling rate is the rate at which the input and output data is captured from the system. Of course, the quality of the experimental setup is a sensitive issue in this point as the used instruments should be selected to be able to achieve the required sampling rate. The guide lines given in [4] suggest a sampling rate 10 times the approximate system bandwidth. Usually, the highest possible sampling rate is used to record the data experimentally to allow the user to decide later what degree of down sampling is needed to achieve a successful model. If a digital anti-aliasing filter is needed, it must be applied prior to down sampling [13]. Logically, the input signal should be designed to match the sampling rate as it is not possible to capture any change in the input signal which takes place at a rate faster that the sampling rate.

Data Processing

For many reasons, the raw data collected from the system identification process may not be suitable for use in system identification algorithms. These reasons include the associated sensors noise, the switch on and off electronic noise, and the oversampling of the recorded data.

1. Removal of Offsets & De-trending the Data

   In linear system identification analysis, removing the offset or bias caused by physical units of measurements such as absolute pressure or temperature from steady state data improves the quality of the identification process using this data [14]. In such case, the I/O data can be processed by subtracting the mean value of the data from each sample. Alternatively, a constant offset terms can be taken into account in the identification procedure. These offset terms can be included as unknown parameters to be estimated. Offsets not only can be found in the collected data but also in general trends like linear drifts or seasonal trends which can be detected. One way of removing such trends is subtracting the best fitted trend through the I/O data [13].

2. Remove of Outlier Points

   There is no doubt that a clean data set leads to a good identified model. Outlier points are nonsense pieces of data caused by measurement errors or anomalous events like misfire in an IC engine. Such a piece of data can cause severe difficulties in the

identification process. If it is not possible to avoid outliers points, the I/O data is pre-processed and outliers points are removed and considered as missing points.

3. Prefiltering

Distortion in the identification data can often be separated from the identified system frequency band of interest by filtering the data. The frequency content of the collected I/O data could include unwanted frequency components. The reason for that could be the the structure of the experimental setup which sets important parameters such as natural frequency. This natural frequency could appear when the system is excited around it. It can affect the system identification negatively. Another important source of unwanted frequencies is the external noise and disturbances. The fact that the cross interference of signals due to the electronic field set up by the different experimental equipments are affecting each other is another source of electronic noise generation. Also, the measurement equipment is sometimes sensitive to magnetic power fields generated by motor rotors. The maximum expected frequency content of a signal should be the signal Nyquist frequency F_N which is half of the sampling frequency $F_s = 1/T_s$, where T_s is the sampling interval. Obviously, any frequency content greater than the Nyquist frequency is likely to be an external noise.

The filtering methodology should be chosen according to the expected unwanted frequency components. Both input and output data should be treated similarly to avoid the drawbacks of filtering on the identified dynamics. It has been reported in [4] that filtering the I/O data through the same filter did not effect the I/O relationship assuming that the identified system is linear. The main kinds of filters which can be used to overcome the unwelcome frequencies content problem are low-pass filters, high-pass filters, band pass filters and band stop filters.

(a) Low-pass Filters

Low-pass filters allow low frequency components to pass through it and prevent high frequency components from passing. A low-pass filter is defined by its cut-off frequency F_{pass} and stop band attenuation F_{stop} as in the Bode magnitude plot displayed in Figure 2.2 (a). Low-pass filters are routinely applied to data to eliminate the high frequency noise coming from Radio Frequency (RF) radiation and Electromagnetic (EM) radiation. RF and EM radiations consist of waves of electric and magnetic energy moving together through space at the speed of light. It is common to both electric fields and magnetic fields associated with the use of electronic equipment to affect the quality of the measurements during the experiments.

(b) High-pass Filters

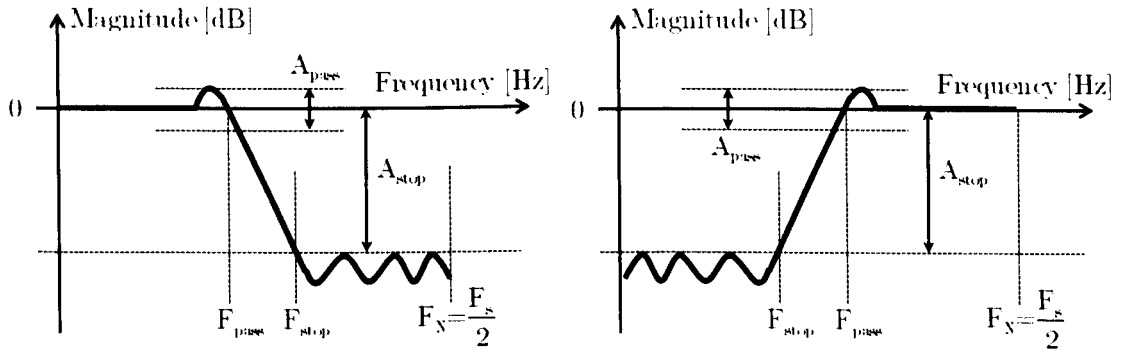

(a) low-pass (b) high-pass

Figure 2.2: Pass filters

In contrast to low-pass filters, high-pass filters only pass signals above the selected cut-off frequency. They are defined by their cut-off frequency F_{pass} and stop band attenuation F_{stop} as in Figure 2.2 (b). These filters can remove the frequency components due to interference acting in the high frequency range.

(c) Band-pass Filters

This type of filter allows a certain band of frequency components to pass. It is really useful when a specific range of frequencies are investigated. Figure 2.3 (a) describes this type of filters.

(d) Band-stop Filters

Some situations take place during recording the I/O data showing that an additional frequency component is coming from exciting the experimental setup structure around its natural frequency. If the structural natural frequency is inside the range of interest, low or high pass filters can not remove it without distorting the surrounding frequencies components. When the band stop is made very narrow to stop a certain frequency, the filter is termed as a notch filter. Band-stop filters takes the form in the magnitude versus frequency plot as in Figure 2.3 (b).

In many filtering techniques, it is very difficult to avoid additional phase lag distortion to the filtered data [15]. This drawback of such a filtering process has a significant affect on the identification process because longer time delays could appear to be detected than are actually present. Non-causal filtering techniques can be applied during off-line data processing. To avoid phase lag distortion, the methodology is to pass the data through the filter then reverse the resulting data which can be called as 1^{st} stage filtered data. Of course, phase delay is expected between the raw data and the 1^{st} stage filtered data. To eliminate this additional phase, the 1^{st} stage filtered data is reversed in time then passed again through the same filter. As it is reversed, the additive phase to the

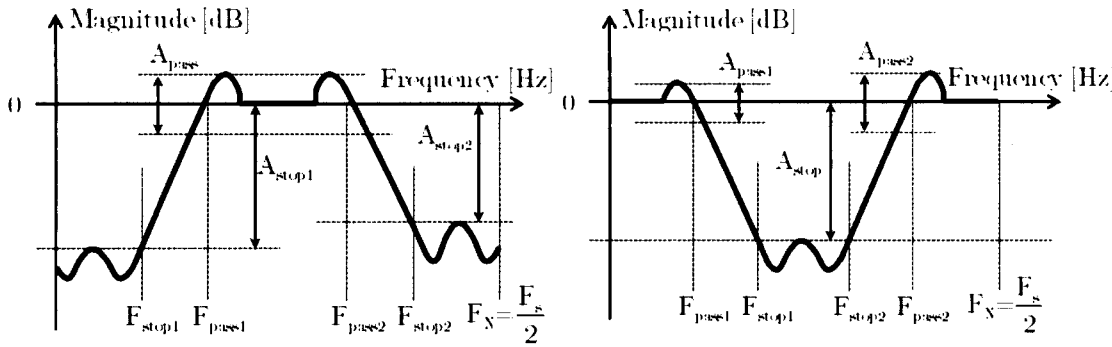

(a) band-pass (b) band-stop

Figure 2.3: Band filters

2^{nd} stage filtered data is actually canceling the phase added to the 1^{st} stage filtered one. Finally, the 2^{nd} stage filtered data is reversed to obtain the filtered data which has no phase delay from the raw data. An overview of the process is presented in Figure 2.4.

Model Structure Selection

Selecting a model structure in parametric modelling is a hard task and should be taken by the designer. The challenge is big because previous knowledge and experience is needed at this point, which could be initially unavailable. If this is the case, a range of statistical based structure selection techniques can be applied to the problem [16, 17, 18]. In linear identification, model structures like Output Error (OE), Box Jenkins (BJ) , Auto Regressive eXogenous (ARX), Auto Regressive Moving Average eXogenous (ARMAX) and so on are usually used [4]. In nonlinear identification, model structures like Nonlinear Output Error (NOE), Nonlinear Auto Regressive eXogenous (NARX), Nonlinear Auto Regressive Moving Average eXogenous (NARMAX), Nonlinear Box-Jenkins (NBJ), Neural Networks (NN) are used [14]. The expression autoregressive in describing a model means that the output of the model is based on a combination of previous inputs and outputs. The following are the most used parametric identification model structures.

1. Polynomial Model Structure

   Polynomial structures which are describing discrete systems are among the most popular linear model structures are used in dynamic system identification.

$$A(q^{-1})y(t) = \sum_{i=1}^{n_u} \left(\frac{B_i(q^{-1})}{F_i(q^{-1})} u_i(t - n_{k_i}) \right) + \frac{C(q^{-1})}{D(q^{-1})} e(t) \tag{2.1}$$

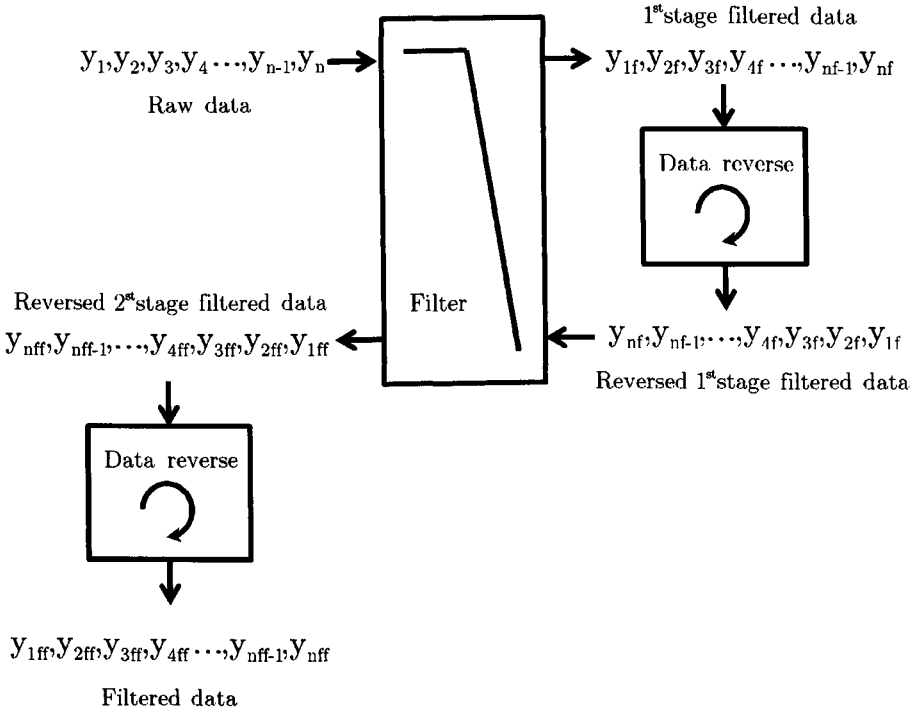

Figure 2.4: Non-causal filtering

The polynomials A, B_i, C, D, and F_i are functions of the time-shift operator q where

$$u(t-1) = q^{-1}u(t) \tag{2.2}$$

and u_i is the i^{th} input, n_u is the total number of inputs, and n_{k_i} is the i^{th} input delay that characterises the delay response time.

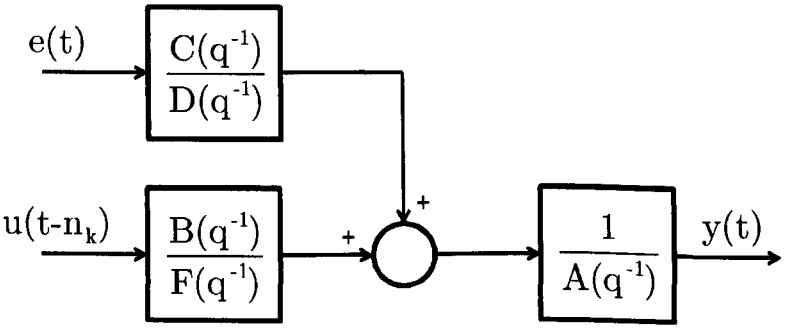

Figure 2.5: Polynomial model [4, 19]

2. Box-Jenkins Model Structure

When $A(q^{-1})$ in Eqn. (2.1) is set to unity, the resulting model is termed Box-Jenkins model. The model structure as can be seen in Figure 2.6 can be expressed as

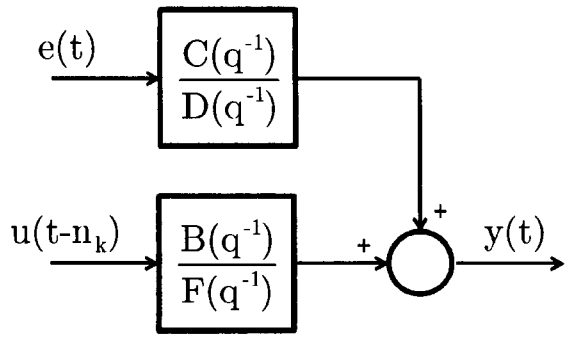

Figure 2.6: Box Jenkins model [4, 19]

$$y(t) = \frac{B(q^{-1})}{F(q^{-1})}u(t - n_k) + \frac{C(q^{-1})}{D(q^{-1})}e(t) \tag{2.3}$$

where,

$$B(q^{-1}) = \quad b_1 q^{-1} + \ldots + b_{n_b} q^{-n_b+1} \tag{2.4}$$

$$C(q^{-1}) = \quad 1 + c_1 q^{-1} + \ldots + c_{n_c} q^{-n_c} \tag{2.5}$$

$$D(q^{-1}) = \quad 1 + d_1 q^{-1} + \ldots + d_{n_d} q^{-n_d} \tag{2.6}$$

$$F(q^{-1}) = \quad 1 + f_1 q^{-1} + \ldots + f_{n_f} q^{-n_f} \tag{2.7}$$

and b_i, c_j, d_k and f_l are polynomial parameters, $i = 1, \ldots, n_b$, $j = 1, \ldots, n_c$, $k = 1, \ldots, n_d$ and $l = 1, \ldots, n_f$. The order of these polynomials are n_b, n_c, n_d and n_f with n_k process delays in number of time samples.

3. Autoregressive Moving Average with eXogenous Input(ARMAX) Model Structure

In an ARMAX model structure, the denominators $F(q^{-1})$ and $D(q^{-1})$ in the Box-Jenkins model are set to unity, leaving the single common denominator $A(q^{-1})$. The ARMAX model structure can be expressed as in Figure 2.7 as

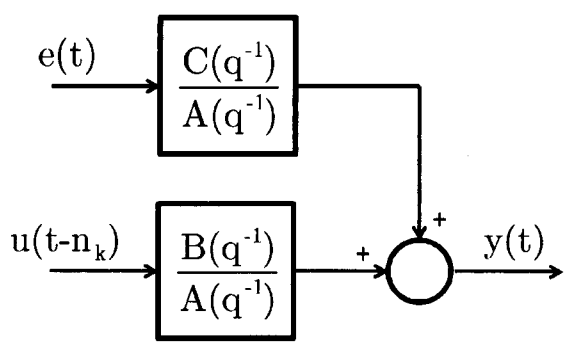

Figure 2.7: ARMAX model [4, 19]

$$A(q^{-1})y(t) = B(q^{-1})u(t-n_k) + C(q^{-1})e(t) \quad (2.8)$$

$$y(t) = \frac{B(q^{-1})}{A(q^{-1})}u(t-n_k) + \frac{C(q^{-1})}{A(q^{-1})}e(t) \quad (2.9)$$

$$A(q^{-1}) = 1 + a_1 q^{-1} + \ldots + a_{n_a} q^{-n_a} \quad (2.10)$$

$$B(q^{-1}) = b_1 q^{-1} + \ldots + b_{n_b} q^{-n_b+1} \quad (2.11)$$

$$C(q^{-1}) = 1 + c_1 q^{-1} + \ldots + c_{n_c} q^{-n_c} \quad (2.12)$$

where i, j and k are the parameters of the polynomial, $i = 1, \ldots, a_n$, $j = 1, \ldots, n_b$. The order of these polynomial are n_a, n_b and n_c.

4. Auto Regressive with eXogenous (ARX) Input Model Structure

More simplification in polynomial model structure can be found in the ARX model structure. In this structure, $C(q^{-1})$ is a unity.

$$A(q^{-1})y(t) = B(q^{-1}u(t-n_k)) + e(t) \quad (2.13)$$

$$y(t) = \frac{B(q^{-1})}{A(q^{-1})}u(t-n_k) + \frac{1}{A(q^{-1})}e(t) \quad (2.14)$$

The polynomial parameters i, j in Eqn. (2.14) have the same definition as in Eqn. (2.12).

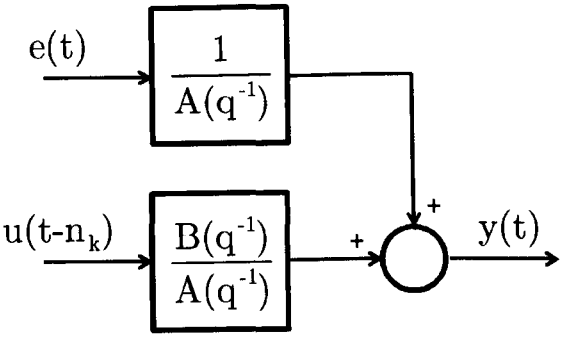

Figure 2.8: ARX model structure [4, 19]

5. Nonlinear AutoRegressive with eXogenous (NARX) Input Model Structure

A NARX model is a nonlinear structure. It uses a parallel combination of nonlinear and linear blocks as can be seen in Figure 2.9. Nonlinear and linear functions are expressed in terms of regressors which are functions of measured I/O data. The predicted output can expressed as

$$F(x(t)) = F(y(t-1), \ldots, y(t-n_a), \ldots, u(t-n_k-n_b+1)) = \sum_{k=1}^{d} \alpha_k \kappa(\beta_k(x-\gamma_k)) \quad (2.15)$$

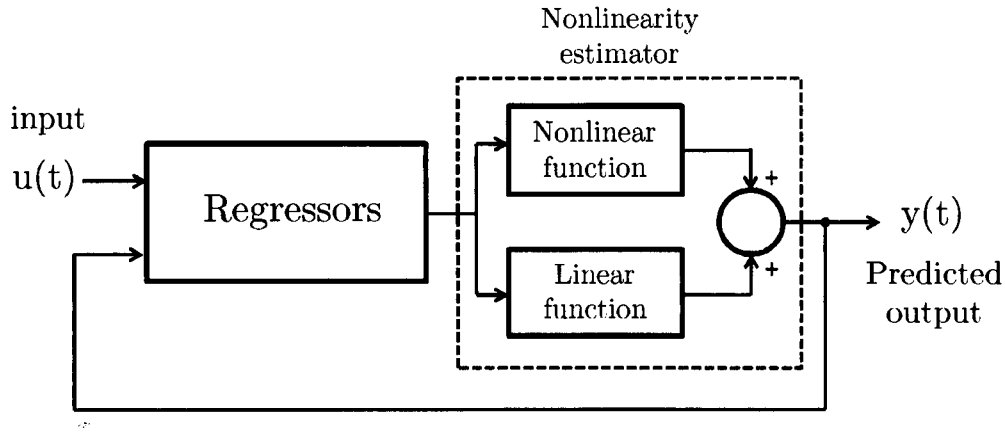

Figure 2.9: NARX model structure [14]

where F is a nonlinear regression function, which is approximated by a nonlinearity estimators like neural network, wavelets. α_k, β_k, and γ_k are the parameters of the nonlinearity estimator. κ is the unit nonlinear function and d is the number of nonlinearity units. n_a is the number of past output terms used to predict the current output. n_b is the number of past input terms used to predict the current output. n_k is the delay from input to the output in terms of the number of samples. This value defines the least delayed input regressor.

All previous structures are for parametric models based on regressors which are functions of the corresponding coefficients or parameters. Another important type of model is the NP model which will be discussed in details in Chapter 3. Parametric models require a series of user decisions such as selection of the model order. They employ a finite dimensional parameter vector, so the information is condensed into a small set of parameters [20].

Model Acceptance

The user decision of accepting the identified model is taken within the context of a validation process. In this process, an unseen data set is used and compared against the predicted output obtained by the identified model. Visual inspection of the validation data can immediately demonstrate whether the model fit is unacceptable. Model residuals are defined as the difference between the recorded output and the model output. If a good fit is visually observed, the analysis of the residuals can be used to highlight the fitness of the obtained model.

2.3 Robust Systems Identification

The main goal of robust identification and control theory is to obtain theoretical results that are closely related to the experimental aspects of the controlled system. Two main phases are used in this purpose; simulation and experimentation.

2.3.1 Simulation

Simulation in control means the calculation of the expected behavior of a plant through a mathematical model. Modern technology and powerful modern computers enable the control designers to have computational models of the plants which are under investigation for control purposes. Some of the reasons justifying simulation of the controlled plants are listed below.

1. Sometimes, any direct experiment with the hardware is difficult, as in the case of satellites, airplanes and vehicles. It is clear that many difficult situations can be tested in simulation much more easily than in the real world due to safety reasons or possible permanent damage of equipments. In such situations, it is sensible to start with simulation models. These models include the system dynamics and all other necessary elements to represent the actual system.

2. The cost of experimentation could be very high. No doubt that this is a strong reason to simulate a plant, like the case of many nuclear power applications and expensive materials in some chemical processes. Testing over a computer model provides a very fast and inexpensive method of validating a controller design or control technique.

3. When human lives are involved, as in the case of aircraft and vehicles, computer simulation always gives a safe means of testing in which high risk maneuvers can be applied without concern of causing real harm to people.

2.3.2 Experimentation

The experimental phase of robust systems identification involves engineering disciplines because it is basically technological. It also involves knowledge on the sensors, actuators, and technical aspects of microprocessors and their I/O equipment for digital control. The interaction of any physical plant with its environment is performed by real world signals provided by the sensors and physical stimulations to the plant through the actuators which modify its behaviour. In some cases, I/O signals provide the only known information of the physical plant. In many cases there are no known physical laws that explain the plant behaviour or they are extremely complex. It goes without saying that trial and error techniques are

unrealistic. Furthermore, in many cases they would not even be practical because of the cost or simply to prevent accidents.

The information of a system through I/O signals and physical laws is never complete. The reason for that is that the physical laws which may applied to the sensors and actuators describe only certain aspects of the behaviour but not all. For example, Ohm's law could be used to describe the output voltage of a given resistance through which a known current is circulating. Nevertheless, the temperature, and magnetic field could also effect the measured data as well as the physical properties of the voltage sensors and current power supply.

2.3.3 Uncertainty

Due to assumptions which are usually associated with systems modelling, a fair amount of uncertainty between the mathematical model and the experimental results will usually appear. In the simulation phase, the simplifying hypotheses are made due to computational restrictions such as time and money. Instead, in the theoretical calculations, the assumptions that generate the uncertainty are depending on the mathematical techniques that the designer has decided to use [21, 22]. The regions in which the identified system parameters are located are called uncertainty templates. More about this issue will be discussed in section 5.3 of Chapter 5. When a nonlinear system is represented by a set of linear models, the nonlinear nature of the plant can be seen as a form of uncertainty.

2.4 Control of Dynamic Systems

An automatically controlled system is a collection of components working with each other in such a manner that the whole system acts in a previously desired way [23]. The goal of control engineering design is to make a system meet an actual need by putting it into a certain configuration and determine the key parameters and specifications of this configuration [24]. In the following subsections, classical control and robust control will be discussed in sections 2.4.1 and 2.4.3 respectively.

2.4.1 Classical Control

The earliest application in control field is acknowledged to be Watts flyball governor which introduced feedback control to industrial steam engines in the milling industry (see Figure 2.10 [25]). The centrifugal governor controls the speed of an engine by regulating the amount of steam passing through an inlet valve [26]. The continuously improvements to Watts invention led to the first analysis of the problem of closed loop stability and ultimately the work

of Routh and Hurwitz. Later, the invention of the feedback amplifier provided accelerated development of important practical theories by Nyquist, Black and Bode [27, 28, 29]. This momentum was increased with the onset of the Second World War between 1939 and 1945, specifically with application to the field of Radar. After the war had ended, some of the

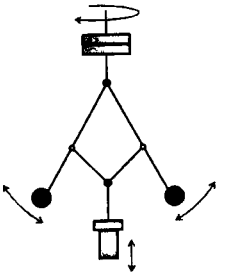

Figure 2.10: Flyball governor

previously classified work which had been closely guarded during hostilities was released, and a proliferation of new work was generated. The root locus technique developed by Evans [30] was one of the earliest formalised design methods and is still being taught and used until today. Classical control techniques can be separated into frequency domain techniques and time domain techniques. Frequency domain techniques are a suite of analysis and design tools that include root locus, state space, Bode and Nyquist plots. State-space model based control methods are the portion of classical control that is done in the time domain environment.

The Closed Loop System

In closed loop systems such as the one in Figure 2.11 which consists of a plant $G(s)$ controlled by a feedback controller $K(s)$, the input reference r is compared with the controlled output y to produce the error signal e. As the purpose of the control process is to make the output track the reference input in a satisfactory way, the magnitude of the error signal is increasing as much as feasible to achieve balance stably when a difference between y and r is detected. Such a system is generally also subjected to an external disturbance d governed by the transfer function $G_d(s)$ and to sensor noise n each of which have a significant effect on the error signal e. The plant input u can be expressed as

$$u = eK(s), \quad \text{or} \quad u = (r - y - n)K(s) \tag{2.16}$$

The system output signal y can be described by

$$y = uG(s) + dG_d(s) \tag{2.17}$$

Substituting from Eqn.(2.16) in Eqn.(2.17) leads to

$$y\,[1 + K(s)G(s)] = (r - n)K(s)G(s) + dG_d(s) \tag{2.18}$$

(2.19)

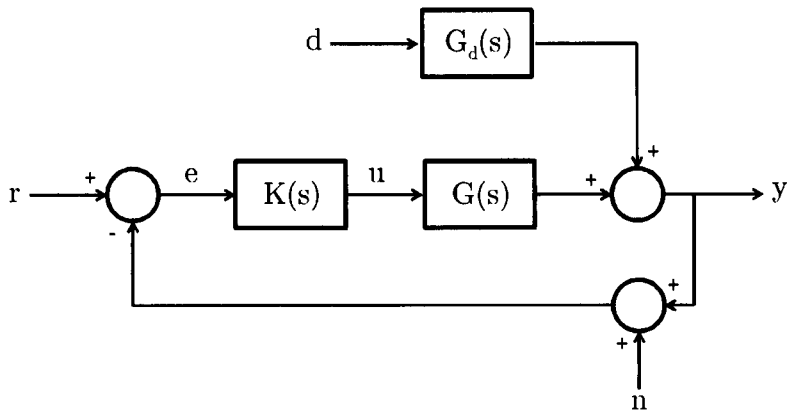

Figure 2.11: Closed loop system with disturbance and sensor noise

or, in another form

$$y = \frac{K(s)G(s)}{1+K(s)G(s)}r - \frac{K(s)G(s)}{1+K(s)G(s)}n + \frac{G_d(s)}{1+K(s)G(s)}d \tag{2.20}$$

Eqn. 2.20 shows that the closed loop system output y can be expressed by the summation of the effects of the excitations r, d and n on the output sensitivity functions.

Sensitivity Functions

A sensitivity function is normally expressed as a frequency domain transfer function which describes how the closed loop system responds to a certain input. In other words, how much the system is responsive to change in excitation signals such as disturbances and noises.

Primary sensitivity function describes how the system output y will respond to a disturbance d, which usually occur at low frequencies range. The primary sensitivity function can be obtained in terms of the open loop transfer function $L(j\omega)$ from the third term of Eqn. (2.20) by setting $G_d = 1$ to unity. In terms of the open loop transfer function, $L(j\omega)$

$$S(j\omega) = \frac{Y(j\omega)}{D(j\omega)} = \frac{1}{1+L(j\omega)}, \quad \text{where } L(j\omega) = K(j\omega)G(j\omega) \tag{2.21}$$

The idea is to reduce the sensitivity of the system to disturbances, by ensuring that the magnitude of $S(j\omega)$ is bounded at low frequencies. This reduction of $|S(j\omega)|$ improves the disturbance rejection performance. It is clear from Eqn.(2.21) that increasing the controller gain in $K(j\omega)$ reduces the primary sensitivity. So, increasing $|L(j\omega)|$ at low frequencies reduces $|S(j\omega)|$ at low frequencies.

The complementary sensitivity describes the sensitivity of the system output y to sensor noise n, which typically takes place at higher frequencies Thus, limiting the sensitivity of the

system to noise by ensuring that the magnitude $T(j\omega)$ is bounded at the higher frequencies as necessary to reduce the effect of sensor noise. Looking back to the second term of Eqn. (2.20), complementary sensitivity $T(j\omega)$ is expressed as

$$T(j\omega) = \frac{Y(j\omega)}{R(j\omega)} = \frac{L(j\omega)}{1 + L(j\omega)} \tag{2.22}$$

and similarly, the controller action sensitivity $S_u(j\omega)$ can be expressed as

$$S_u(j\omega) = \frac{Y(j\omega)}{U(j\omega)} = \frac{K(j\omega)}{1 + L(j\omega)} \tag{2.23}$$

The relations between these sensitivity functions can be described by the following equations:

$$S(j\omega) + T(j\omega) = 1.0 \tag{2.24}$$

$$S(j\omega)K(j\omega) = S_u(j\omega) \tag{2.25}$$

It can be concluded from Eqn.(2.22) that, unlike primary sensitivity function, increasing the gain of $K(j\omega)$ increases the magnitude of the complementary sensitivity function, and therefore the closed loop sensitivity, to noise at high frequencies. In classical control, the loop function $L(j\omega)$ is shaped using bounds on the sensitivity functions $S(j\omega)$ and $T(j\omega)$) as a way of achieving the design specifications.

2.4.2 Internal Model Control

The internal model control is a control strategy depending on the philosophy that the control can be achieved if the controller includes a representation of the controlled process [31]. Figure 2.12 displays the classical feedback structure where $P(s)$ is the plant and $K(s)$ is the system controller. When the internal model strategy is considered, the controller $K(s)$ is expanded to include the plant model $\bar{P}(s)$ as in Figure 2.13. The plant model $\bar{P}(s)$ is added in parallel to the actual plant $P(s)$ and the error signal is determined by comparing the reference input $R(s)$ with the signal $\bar{D}(s)$ which compares the controlled process output with the model output. The internal model controller $K(s)$ can be expressed as

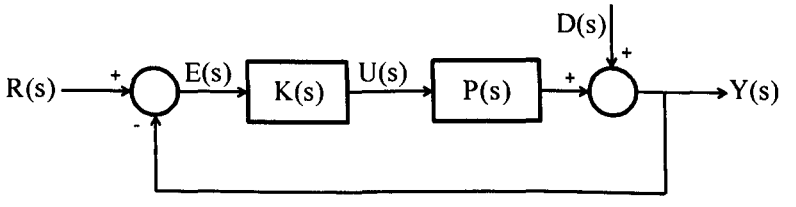

Figure 2.12: Internal model control structure

$$K(s) = \frac{Q(s)}{1 - \bar{P}(s)Q(s)} \tag{2.26}$$

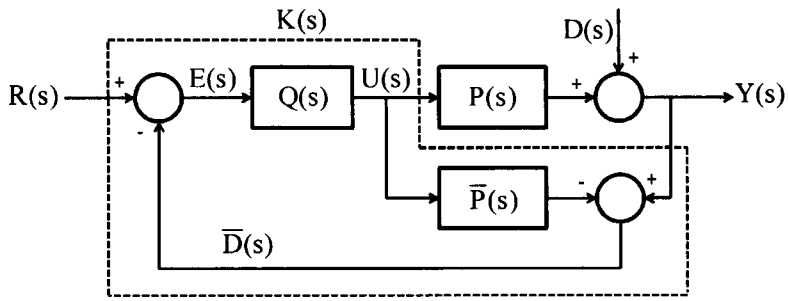

Figure 2.13: Evaluation of the internal model control structure

and the result of comparing the plant response and the model output is

$$\bar{D}(s) = [P(s) - \bar{P}(s)]U(s) + D(s) \tag{2.27}$$

However, the control action $U(s)$ which is the input to both the plant and the model can be expressed as

$$U(s) = E(s)Q(s) = [R(s) - \bar{D}(s)]Q(s) \tag{2.28}$$

substituting Eqn. 2.27 in Eqn. 2.28 gives

$$U(s) = \left[R(s) - (P(s) - \bar{P}(s))U(s) + D(s))Q(s)\right] \tag{2.29}$$

or

$$U(s) = \frac{[R(s) - D(s)]Q(s)}{1 + [P(s) - \bar{P}(s)]Q(s)} \tag{2.30}$$

Since

$$Y(s) = P(s)U(s) + D(s) \tag{2.31}$$

and from Eqn. 2.30

$$Y(s) = \frac{[R(s) - D(s)]P(s)Q(s)}{1 + [P(s) - \bar{P}(s)]Q(s)} + D(s) \tag{2.32}$$

the closed loop response of the internal model controlled process is

$$Y(s) = \frac{Q(s)P(s)}{1 + [P(s) - \bar{P}(s)]Q(s)}R(s) + \frac{1 - Q(s)\bar{P}(s)}{1 + [P(s) - \bar{P}(s)]Q(s)}D(s) \tag{2.33}$$

As can be seen from Eqn. 2.33, the perfect reference input tracking is achieved when $Q(s) = \bar{P}(s)^{-1}$ and the perfect disturbance rejection is achieved when $P(s) = \bar{P}(s)$.

2.4.3 Robust Control

The earliest application of robust control problem can be pointed to Black in 1927 [32] when he proposed feedback and large loop gains for the design of the vacuum tube amplifier given significant plant uncertainties, however the concepts of robust control design was developed by Bode [33] in 1945. The Bode approach to the design of robust systems was extended later to finite plant variation by Horowitz [34] in 1963. A number of key state variable concepts like the optimal Linear Quadratic State Feedback (LQSF) are introduced by Kalman in 1960. In 1973, Cruz [35] summarized the major results in sensitivity theory developed between 1960 and 1972. Further sensitivity results were reported in a special issue on sensitivity of the Journal of the Franklin Institute in March/April 1981.

The term "robust control" appeared for the first time in a Davison's article [35] in 1972. After that much work has done to extend the classical problems and emerge them with robust design philosophy. IEEE came out with a special issue on Linear Multivariable Control Systems in which a number of papers in robust control applications were presented. The optimal $\mathcal{H}_\infty$ sensitivity problem is posed for Single Input Single Output (SISO) systems by Francis [36] in 1984 and since then, many attempts has been made to modify the classical control methodologies to make them robustly stable and preform a well controlled way even if the system parameters are changing between their uncertainty limits. The methods that use a geometrical approximation of the uncertainty templates such as $\mathcal{H}_\infty$ methods are more conservative. For mathematical reasons in the $\mathcal{H}_\infty$ methodology the uncertainty templates are approximated to circles in the complex plane. This means that each template could include additional area because of collecting the frequency response points in a circular shape. As a result, the obtained controller is expected to be conservative. Some other robust control techniques such as QFT can be applied on the uncertainty templates as they are without any geometrical approximation. This means the an unconservative controller can be obtained with the required robust stability and performance.

Robust Stability

When an uncertain linear controlled plant is represented in a Nyquist plot as in Figure 2.14, each point of the open loop locus $L(j\omega)$ expands to an area or multi areas due to the plant uncertainty. If a minimum radius circle containing all possible frequency domain responses of $L(j\omega)$ is drawn at each frequency ω, basic requirement is necessary to achieve closed loop system stability is to avoid enclosing the point -1.0 in the uncertainty circles. This ensures that any arbitrary chosen nominal plant representation of the closed loop system is always stable. According to the Nyquist stability criterion, the critical point -1.0 should not be included by the loop locus of a system in the complex plane to achieve closed loop stability of

this system [37]. When a nominal loop locus $L_o(j\omega)$ is chosen as the centre of the uncertainty disc, the stability condition can achieved by insuring that the distance between the critical point -1.0 and the point $L_o(j\omega)$ exceed the radius of the uncertainty disk $\Delta L_o(j\omega)$, otherwise the system can not be considered as robustly stable [38].

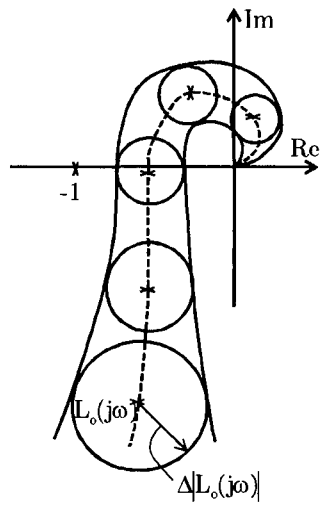

Figure 2.14: Nyquist plot of a controlled system with unstructured uncertainty

Robust Performance

It is a fundamental fact that robust stability of a system is not a sufficient condition for a reliable performance. Closed loop stability margins are necessary to ensure that the controlled system is preforming well. This can be reached by defining primary and complementary sensitivity weighted functions. A weighting function $W_S(\omega)$ may be applied to the primary sensitivity according to the the inequality

$$|S(j\omega)| = \left|\frac{1}{1+L(j\omega)}\right| \leq \frac{1}{W_S(\omega)} \tag{2.34}$$

The aim of the primary sensitivity inverse weighting function $W_S^{-1}(\omega)$ of the system is to bounded its sensitivity to disturbance $S(j\omega)$ by low gain at low frequencies in order to ensure reduced sensitivity to low frequency disturbances. Thus Eqn.(2.34) can be formulated as

$$|W_S(\omega)S(j\omega)| \leq 1, \forall\omega \in \Omega \tag{2.35}$$

Similarly, a weighted complementary inverse sensitivity weighting function $|T(j\omega)W_T(\omega)|$ is constructed from

$$|T(j\omega)| = \left|\frac{L(j\omega)}{1+L(j\omega)}\right| \leq \frac{1}{W_T(\omega)} \tag{2.36}$$

Complementary sensitivity of the system should be bounded at all frequencies such that it is less than or equal to the inverse of the weighting function W_T^{-1}. The shape of W_T^{-1} should therefore be selected such that it enforces low gain at high frequencies in order to ensure the reduction of sensitivity to sensor noise at high frequencies. So, Eqn.(2.36) can be formulated as

$$|W_T(\omega)T(j\omega)| \leq 1, \forall\omega \in \Omega \tag{2.37}$$

The robust performance problem is solved with a controller $K(j\omega)$, which simultaneously satisfies the boundaries defined by inequalities in Eqn.(2.35) and Eqn.(2.37).

2.5 Driveline Control

Driveline control techniques have been made considerably more efficient in the last decade through adoption of design of experiment methodologies and modern hardware technologies.

The most important modes that a driveline controller should avoid are shunt and shuffle. These are predominantly due to the backlash in the driveline as well as the elasticity of various driveline components. For the purpose of increasing the drivability by controlling the backlash effects, two major approaches can be used. The first strategy is to actively control the driveline when it passes through the backlash gab. This means that two control modes are required; one for when the driveline is inside the backlash gab and anther one when the driveline is outside the backlash region. This strategy uses a nonlinear backlash model that represents the driveline dynamics when passing through the backlash gap. The second strategy is to apply a linear approach which does not include backlash model in the controller design process and consider the backlash effect as disturbance. In this approach the controller should be robust enough to handle the disturbance.

Legerberg [39] proposed three strategies to control the driveline; a linear passive controller, a nonlinear passive controller and a nonlinear active controller. A robust linear controller was designed to handle the backlash nonlinearity in the linear passive approach and no backlash model was included in the controller. The nonlinear passive strategy included a backlash model; it adopted a specific approach when the driveline moved inside the backlash region. In the third strategy which is the nonlinear active approach that including backlash, the adopted philosophy was to get out of backlash region as quick as possible. These strategies were identified but they were not commonly used in simulations.

Lagerberg and Egardt [40] investigated a set of controllers for the driveline control problem; standard PID controller, a PID controller with a torque compensator, a simple active switching controller and modified switching controller. Loading rate was used as controlled output in the standard PID controller, however, a first order shaft torque estimate combined

with the load acceleration were used as controlled output in the PID controller with a torque compensator. The simple active switching controller was switching between two control signals; the first one when the driveline was crossing the backlash region and the other one when it was not. The modified switching controller had a similar strategy to that of the simple switching controller but included the engine dynamics in the backlash mode. Lagerberg and Egardt concluded that the switching controllers become unstable if the backlash angle is overestimated. Therefore, switching controllers are not robust enough to be implemented in an actual vehicle; however, they give a better performance in simulation when the backlash angel is accurately estimated, which is not easy in real world problems. To allow switching controllers to turn from mode to mode, backlash estimators were developed for this propose [41] where nonlinear backlash models and Kalman filtering techniques were used to estimate the backlash size and position. Lagerberg and Egardt validated these backlash estimators experimentally in [42].

There are two important parameters that have been given a special interest in driveline control problem. These parameters are rotational velocities and torques [43]. In the case of the disel engine fuel-injection strategy can be used for torque or speed control purposes. For diesel engines, speed control is often referred to as Regler Quer Verstellung (RQV), since much of this work has been developed by German engineers, and torque control is refered as Regler Quer (QR) control. In the RQ control, the accelerator pedal displacement is accounted for as a desired engine torque, and with RQV control the accelerator pedal position is interpreted as a desired engine speed. RQV control is a proportional controller controlling the fueling according to the error between the desired speed demanded by the vehicle driver and the actual speed. In the case of a gasoline engine the amount of air entering the engine is used

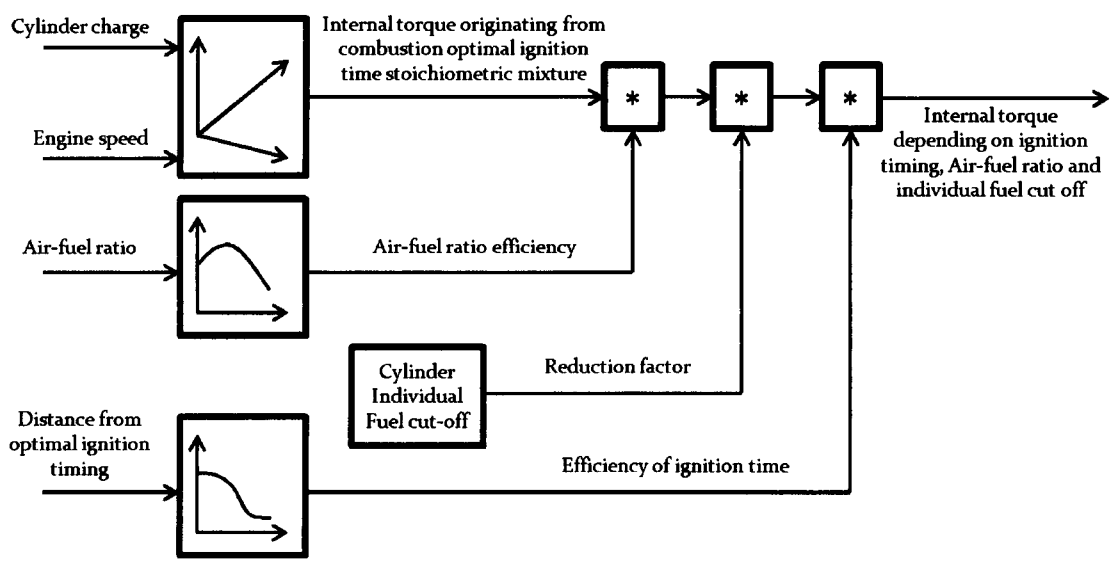

Figure 2.15: Simplified torque model [44]

for regulation of engine speed and torque. Under idling condition the air is regulated by closed loop controllers, typically PID. The air is regulated by either an ABV or electric throttle valve. Torque controller is an open loop strategy where the drivers pedal position is interpreted as a torque demand and the EMS regulated the engine engine actuators including the throttle and spark advance to achieve this. Under the situations the fuel mass is calculated by the EMS and corrected by a PID controller to achieve a stoichiometric Air-to-Fuel ratio (AFR) which is required for good tailpipe out emissions on vehicles equipped with a three way catalytic converter.

2.6 Limitations in Driveline Control

The main goal of driveline control problem presented in this thesis is the enhancement of dynamical behaviour and driving comfort. Fast engine torque changes during tip-in and tip-out operations improve the dynamical behaviour but induce unintentional driveline jerk (fast increase in driveline acceleration) at the same time. Because of the fact that the passenger comfort is often contradictory to vehicle dynamics, a robust control strategy is required, which can achieve a good engineer compromise of both targets simultaneously. Challenges in vehicles driveline torque control can be summarised in the following points:

1. The output torque of the engine or the wheels is not measurable for reasons of cost. Accordingly, the torque is usually estimated from other variables. Figure 2.15 displays a simplified engine torque model in which the engine torque is estimated by using look up tables of air charge passing to the cylinder, engine speed, AFR and ignition timing [44].

2. The engine torque is not smooth because of the combustion inside the engine cylinder. Of course, the flywheel exists to reduce this torque variation but is limited in size to preserve driveability.

3. The engine output torque is limited in different modes of operation. The maximum engine torque is restricted as a function of engine speed. Torque level is also restricted at low turbo pressures. Any controller should work within these restrictions and give the expected performance.

4. The driveline dynamic behaviour is influenced by friction which must be modelled in a satisfactory way to controller design methodology.

2.7 Conclusions

This chapter conclusions are:

- A model of a dynamic system is a description for some or all of its characteristics according to the application. Models can be classified according to approaches used to obtain them to three main categories; white-box modelling, grey-box modelling and black-box modelling. The model should be suitable for the purpose for which it will be used.
- Selection of the input signal is a very sensitive issue in system identification. Frequency content of perturbation signals, excitation signal amplitude and sampling rate are the most important parameters in the input signal used for identification.
- Usually, and due to technical reasons, the raw data collected from the system identification process may not be suitable for system identification algorithms without pre-processing. Removal of offsets and outlier points is usually the first pre-processing stage. Frequency domain filtering techniques provide a tool for eliminating the unwanted frequency content from the system identification data. Non-causal filters are used in off-line data processing to prevent adding phase lag.
- More experience is necessary of the practitioner when parametric identification is used as parametric models require a series of user decisions such as selection of the model order and model structure. Parametric models employ finite dimensional parameter vectors, so the modelling information is condensed into a small set of parameters.
- Two main phases are used in the control applications; simulation and experimentation. It is often suggested for the designer to start with simulation. Difficulty in hardware availability, cost of experimentation and safety are typical reasons for the use of simulation. However, the experimental phase is usually essential for validating control designs.
- Due to assumptions associated with systems modelling, a degree of uncertainty between the mathematical model and the experimental results is often found.
- The science which aims to control the dynamic systems in a certain way without human influence is so called automatic control.
- There are two important parameters that have been given a special interest in the driveline control problem. These parameters are the rotational speeds and the torques. In the driveline torque control, the accelerator pedal displacement is accounted for as a desired driveline torque. The output torque of the engine or the wheels is not

measurable for reasons of cost. Therefore, the torque is usually estimated from other variables.

Chapter 3

NP Identification Analysis

3.1 Introduction

Fundamentally, NP methods of linear system identification are based on impulse response analysis. Of course, characterising dynamical systems by their impulse responses started with the early engineering applications. The impulse response technique has been used in other fields and applications rather than system identification, such as Prony in 1795 [45], many years before using it as a tool for identifying dynamical systems. The early use of impulse response methods in control engineering was by Lee [46] in 1966 [47]. He used impulse response methods for developing his statistical theory of communication. In 1965, Peterson [48] developed the PRBS and used it as an error correcting code. The theoretical appeal of the PRBS based methods gave a great progress to the NP frequency response estimations in 1965 [49]. The methodology of PRBS impulse response estimation was developed by Godfrey [50] in 1969. The main feature of PRBS testing signal, which is considered as digital version of white noise, relates to its auto correlation properties which are periodic.

Patrick Guillaume [51] developed NP Frequency Response Function (FRF) estimators based on nonlinear estimator averaging techniques in 1992. Guillaume concluded that the estimator should be an analytic function of the measured Fourier coefficients in order to reduce the bias.

In 1997, Schoukens developed NP noise models estimated from a small number of data sets to identify systems in the frequency domain by periodic excitation [52]. In the same year, Pintelon [53] shows that by simultaneously estimating some initial conditions and system model parameters, non-periodic signals can be used in frequency domain system identification. Pintelon's method is validated by simulation only.

Ljung and Glover presented a comprehensive comparison between frequency domain and time domain methods in system identification in 1981 [54]. Ljung and Glover concluded that

spectral analysis is a good initial step in the procedure of building a more accurate parametric model.

In 1999, Minesh [55] presented a frequency based controller design methodology for a class of nonlinear systems that can be characterized by a class of Hammerstein models. Classical loop shaping was used in the controller design which has been tested in the idle speed problem of a fuel injected engine. Minesh's methodology applies to limited class of nonlinear models that are not affine in the controlled input. Glass and Matthew presented a frequency based nonlinear controller design methodology of regulating systems subject to time domain constraints in 2000 [56]. A describing function approach was used to design a nonlinear controller for idle speed control of a fuel injected engine.

In 2001, Tamer presented a framework based on interpolation theory which allows the combination of parametric and NP models and the use of both time and frequency domain data for robust identification. A lightly damped flexible structure was identified by this mixed parametric/NP approach [57]. Two years later, Balogh presented a generalization algorithm of the total least squares problem in frequency domain system identification [58].

In 2004, Ljung presented his integrated frequency and time domain tools for system identification in the system identification MATLAB tool box [59] in which, many useful system identification tools are programmed. A year after, Miao used cross correlation methods in [60]. Miao built his modified cross correlation method on the averaging of cross correlations calculated from multiple period of PRBS input signals to get the system impulse response. The obtained impulse response is then used to compute the system frequency response.

Luk [61] used discrete wavelet transforms to identify a filter in a NP model in 2006. A special input signal should be used in this method because the input signal works as analyzing function for the discrete wavelet transforms. The approach worked well in simulation but there was no experimental validation.

In this chapter, estimation of transfer function by impulse response analysis is discussed in section 3.2, then calculation of the system frequency response by Fourier transform is reported in section 3.3. The chapter then explains in section 3.4 the main three sources of errors in digital frequency response estimation. Finally, the most effective NP identification methods are presented in section 3.5.

3.2 Transfer Function Estimation by Impulse Response Analysis

A system as in Figure 3.1 is called time invariant system if its response $y(t)$ to a certain input signal $u(t)$ does not depend on absolute time. This system is considered as linear if its response to a linear combination excitation is the same as the combination of its response to the excitations individually (super position). The system is called causal if its output at a certain time depends on its input up to that time only i.e. the output at any time depends only on past and present values of input [4]. The output signal $y(t)$, which appears as a

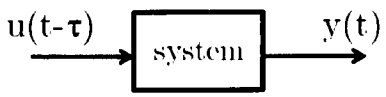

Figure 3.1: The system

result of applying an input $u(t)$ on a LTI causal system, can be described by the integration of the product of the system impulse response $g(\tau)$ and the delayed pulse input $u(t-\tau)$ for different values of delays τ as:

$$y(t) = \int_{\tau=0}^{\infty} g(\tau)u(t-\tau)d\tau \tag{3.1}$$

When dealing with observations in a discrete time digital environment, t_k enumerates the sampling instants and n_k is the time delay in unit samples. Also, and to be more realistic, an

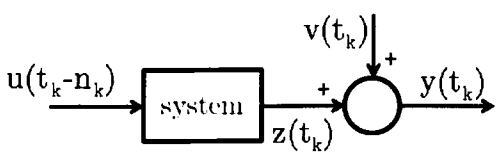

Figure 3.2: The system with disturbance

additional term $v(t_k)$ is often added to represent undesired signals affecting the system as in Figure 3.2, which is usually termed the output noise. So, the output signal can be expressed in the form

$$y(t_k) = \sum_{n_k=1}^{\infty} g(t_k)u(t_k - n_k) + v(t_k), \quad t_k = 1, 2, \ldots \tag{3.2}$$

By defining a unit sample backward shift operator q^{-1} so that, $u(t_k - 1) = q^{-1}u(t_k)$ or in general form $u(t_k - n_k) = q^{-n_k}u(t_k)$ and substituting, we obtain

$$y(t_k) = \sum_{t_k=1}^{\infty} g(t_k)u(t_k - n_k) = \sum_{t_k=1}^{\infty} g(t_k)(q^{-n_k}u(t_k)) \tag{3.3}$$

$$= \left[\sum_{t_k=1}^{\infty} g(t_k)q^{-n_k}\right] u(t_k) = G(q)u(t_k) \tag{3.4}$$

Then, substituting Eqn. (3.4) in Eqn. (3.2) yields

$$y(t_k) = G(q)u(t_k) + v(t_k) \tag{3.5}$$

where G(q) is the transfer function from the input signal $u(t_k)$ to $y(t_k)$ and given by

$$G(q) = \sum_{n_k=1}^{\infty} g(n_k)q^{-n_k} \tag{3.6}$$

3.3 Frequency Response Analysis by Fourier Transform

The primary observations from a dynamical system may take the form

$$y(t_k) = \{y(t_1), y(t_2), \ldots, y(t_N)\}, \quad u(t_k) = \{u(t_1), u(t_2), \ldots, u(t_N)\} \tag{3.7}$$

The relationship between the time domain data recorded with a constant sample time $T_s = t_k - t_{k-1}$ and its frequency domain representation can be found by the Discrete Fourier Transform (DFT) of the data signals defined by

$$Y(k) = \sum_{n=1}^{N} y(n)e^{-\omega_k nj}, \quad \text{and} \quad U(k) = \sum_{n=1}^{N} u(n)e^{-\omega_k nj} \tag{3.8}$$

where the relevant DFT frequency grid is given by

$$\omega_k = \frac{2\pi(k-1)}{N}, \quad k = 1, 2, ..., N \tag{3.9}$$

and the relevant frequency vector is given by

$$\omega_f = \omega_k F_s \quad \& \quad F_s = \frac{1}{T_s} \tag{3.10}$$

Thus, Eqn. (3.5) can be described in the frequency domain by

$$Y(\omega_f) = G(\omega_f)U(\omega_f) + V(\omega_f) \tag{3.11}$$

3.4 Errors in Digital Frequency Response Estimation

The resolution quality of the FRF obtained from the digital spectral estimations is generally affected by statistical and systematic errors. Understanding these errors is essential in processing the system identification data to eliminate or reduce the errors associated with the digital estimation of the system frequency response. The most common errors in spectral estimation of frequency response are aliasing, leakage and data windowing errors.

3.4.1 Aliasing Error

The phenomenon of aliasing is the spectral distortion that occurs when a continuous time signal has frequencies higher than half of the sampling rate. In this case, frequency components

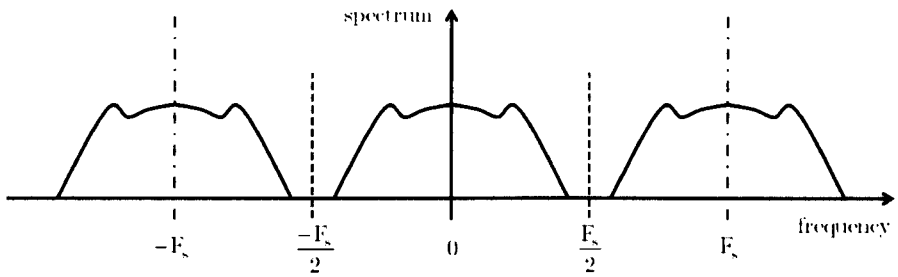

Figure 3.3: Aliasing free.

which are higher than half of the sampling frequency F_s (known as Nyquist frequency) overlap with the lower frequency components causing aliasing distortion of the signal spectrum .

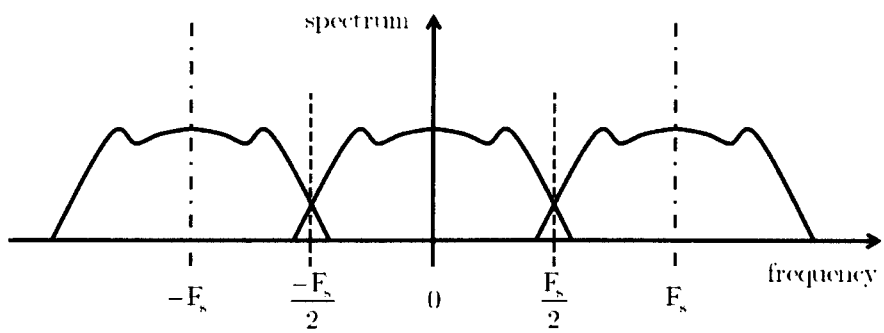

Figure 3.4: Aliasing.

A common solution for the aliasing problem is to ensure that the sampling rate is higher than the band of the signal to avoid any spectral overlap, or to use an anti-aliasing filter. Of course, the first solution will not eliminate aliasing if the time domain data is not band

limited. In this case, the solution is to reduce aliasing by choosing a sampling frequency higher than the frequency range which the designers are interested in. At the same time an anti-aliasing filter is recommended to be applied on the time domain data. An anti-aliasing filter can be described as a low-pass filter with sharp cutoff at the signal Nyquist frequency.

3.4.2 Leakage Error

When a continuous signal is sampled at a uniform sample time T_s with a sampling frequency $F_s = 1/T_s$, its frequency representation can be described as a uniform grid spaced by integer multiplies of $\frac{1}{N}F_s$ (Hz), where N is the number of the frequencies in the frequency grid. When the continuous signal contains frequencies that are not integer multiples of $\frac{1}{N}F_s$, the energy of those frequencies will leak to the spectrum of the nearest frequencies on the sampled frequencies grid.

Suppose we have a signal $y(t_k) = 2sin(2\pi 0.5t_k) + sin(2\pi 2t_k)$ sampled at a rate of $F_s =$ 5Hz by $N = 50$ frequency samples. Thus, both frequencies 0.5Hz and 2Hz lay on the frequency grid because $0.5 = \frac{5}{50}5$ and $2 = \frac{20}{50}5$, so their spectrum can be estimated without leakage as in Figure 3.5.

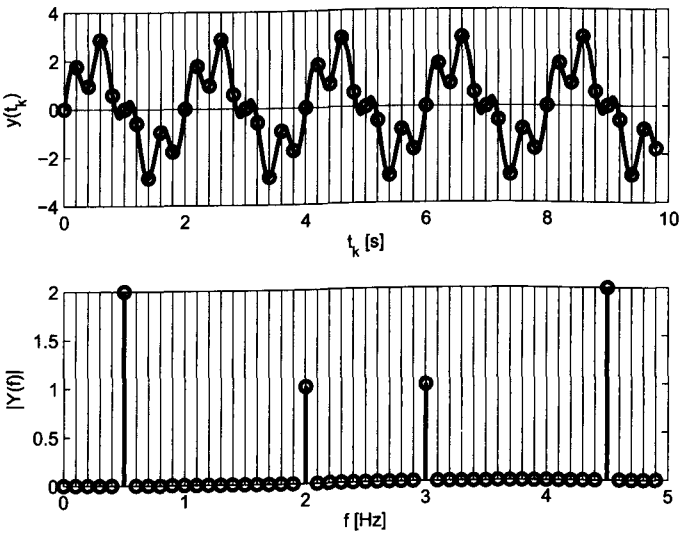

Figure 3.5: No leakage when $N = 50$.

If the number of frequencies has been changed to $N = 45$, the frequency 2Hz will still be on the frequency grid as $2 = \frac{18}{45}5$, however 0.5Hz will lay between $\frac{4}{45}5 = 0.44$Hz and $\frac{5}{45}5 = 0.56$Hz. As a result, the spectrum of the continuous signal at 0.5Hz leaks to the nearest frequencies on the frequency grid as in Figure 3.6.

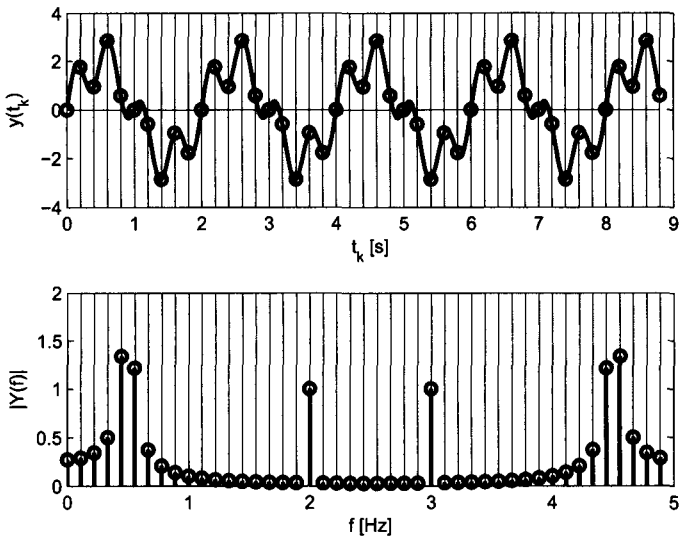

Figure 3.6: Leakage takes place when $N = 45$.

In real world problems, signals can contain an infinite number of frequencies and adjusting the number of frequencies on the grid to make all these frequencies lay on the grid could be impossible. Obviously, increasing the number of grid frequencies reduces the spectral leakage, but does not eliminate the problem because the number of frequencies on the grid is always a finite number.

3.4.3 Data Windowing Error

The continuous time Fourier transform is defined analytically for signals of infinite duration as

$$Y(\omega) = \int_{-\infty}^{\infty} y(t)e^{j\omega t}dt \tag{3.12}$$

however, only finite data records can be obtained in real world problems. Thus a finite segment of data is treated in DFT as a periodic signal with period equal to the duration of the data segment. This means that a discontinuity coming from the differences between the starting and ending values of the data will make the Fourier transform detect false high frequency components. As a result, the spectral estimates are systematically in error. This can be avoided by scaling down the start and the end of the time segment magnitude by multiplying the time domain signal by a window function $w(t_k)$. One of the common window functions is Hann window given by

$$w(t_k) = 0.5\left(1 - cos\left(\frac{2\pi t_k}{N}\right)\right), \quad t_k = 1, 2, \ldots, N \tag{3.13}$$

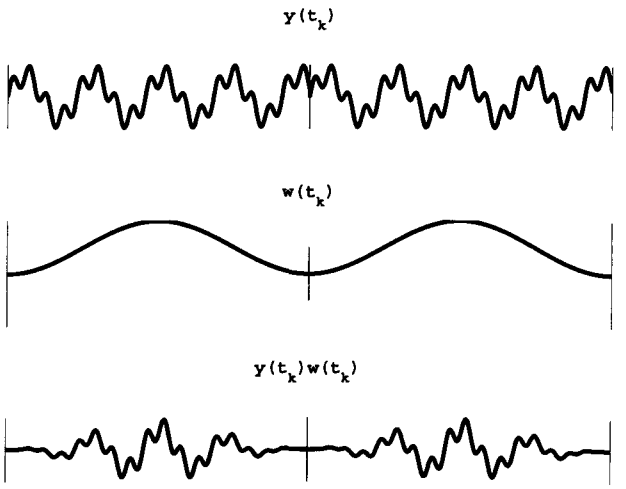

Figure 3.7: Reducing data discontinuity by windowing

3.5 NP System Identification

Parametric identification techniques requires a series of user decisions such as selection of the model order and they employ a finite dimensional parameter vector [62], so the gained information is condensed into a small set of parameters.

NP techniques take this name as the information given by them is not constrained into a small set of finite dimensional parameters to describe the identified system model. The most dependable NP techniques in system identification are direct spectral estimation, Blackman-Tukey spectral estimation, and local frequency smoothing estimation.

3.5.1 Direct Spectral Estimation

The direct spectral estimation method can be described by the following consequences [47, 62]:

I/O data pairs are digitised at a uniform frequency F_s and stored in frames of M sample pairs each as in Figure 3.8. DFT is then used to get a set of discrete Fourier coefficient for the input and output data as in Eqn. (3.8). After that, Fourier coefficients are used to calculate the periodogram and the cross-periodgram of the Fourier coefficients in each of ith frame as

$$P_{uy}(j\omega_k)_i = Y_i(k)U_i^*(k) \tag{3.14}$$

$$P_{uu}(\omega_k)_i = U_i(k)U_i^*(k) \tag{3.15}$$

Then, by using Bartlett's direct estimation procedure, auto-spectrum and cross spectrum are

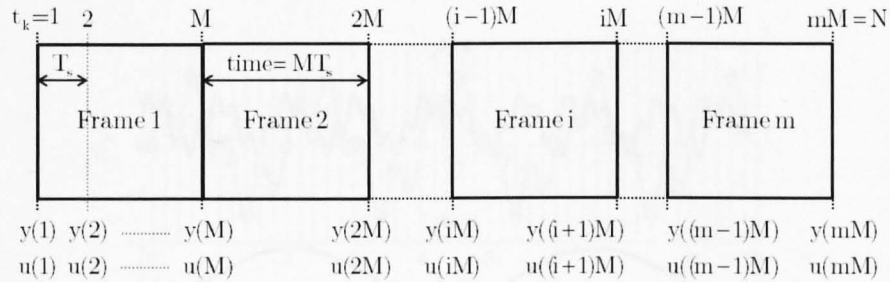

Figure 3.8: Data frames for direct spectral estimation

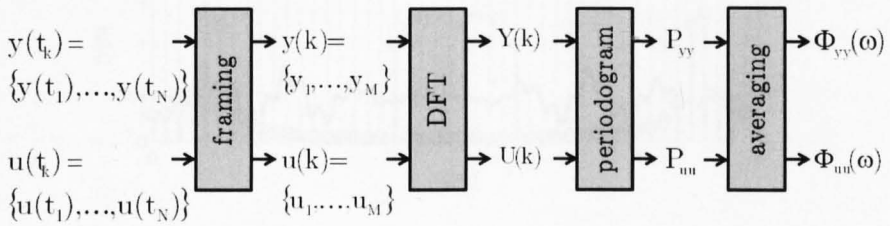

Figure 3.9: Computational steps for direct spectral estimation

estimated by averaging the periodogram for all frames, thus

$$\Phi_{uy}(j\omega_k) = \frac{1}{m}\sum_{i=1}^{m} P_{uy}(j\omega_k)_i \tag{3.16}$$

$$\Phi_{uu}(\omega_k) = \frac{1}{m}\sum_{i=1}^{m} P_{uu}(\omega_k)_i \tag{3.17}$$

Finally, the FRF is estimated by the ratio

$$G(j\omega_k) = \frac{\Phi_{uy}(j\omega_k)}{\Phi_{uu}(\omega_k)} \tag{3.18}$$

In addition to windowing error due to using rectangular frames in this method, a variance error is expected too. The direct auto-spectral estimate has a variance of

$$\frac{Var\{|G(j\omega_k)|\}}{|G(j\omega_k)|^2} = \frac{1}{2m}\left(\frac{1}{\gamma^2_{uy}(\omega_k) - 1}\right) \tag{3.19}$$

which is depends on the coherency which is a frequency domain representation of noise to signal ratio of a system as in Figure 3.2 and is given by

$$\gamma^2_{uy}(\omega_k) = \left[\frac{|\Phi_{uy}(j\omega_k)|^2}{\Phi_{uu}(\omega_k)\Phi_{yy}(\omega_k)}\right]^{-1} \tag{3.20}$$

Egn. 3.19 shows that the variability of cross-spectral and frequency response estimates is reduced by increasing the number of data frames m. This means that with a fixed data length record there will be a trade off between variability and bias [47].

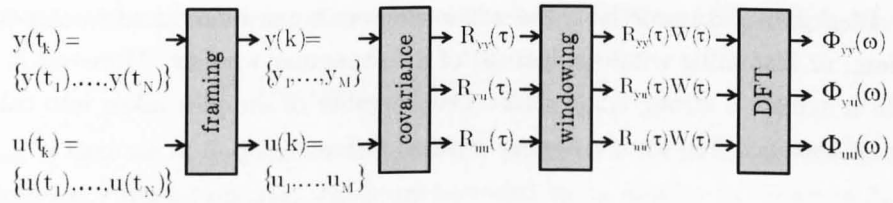

Figure 3.10: Computational steps for Blackman-Tukey spectral estimation.

3.5.2 Blackman-Tukey spectral estimation

In the Blackman-Tukey approach [4], cross and auto covariance functions are estimated as

$$R_{yu}(\tau) = \frac{1}{N}\sum_{t_k=1}^{N} y(t_k+\tau)u(t_k)\ , \quad \tau = 1,2,\ldots,M \tag{3.21}$$

$$R_{uu}(\tau) = \frac{1}{N}\sum_{t_k=1}^{N} u(t_k+\tau)u(t_k) \tag{3.22}$$

The alternative way suggested by Ljung [19] for SISO system with equally spaced frequency points , of expressing these covariance estimations is by using the Fourier coefficients of the periodograms $P_{yu}(\omega), P_{uu}(\omega)$ as

$$R_{yu}(\tau) = \frac{1}{2\pi}\int_{-\pi}^{\pi} P_{yu}(\omega)e^{i\tau\omega}d\omega \tag{3.23}$$

$$R_{uu}(\tau) = \frac{1}{2\pi}\int_{-\pi}^{\pi} P_{uu}(\omega)e^{i\tau\omega}d\omega \tag{3.24}$$

Then, a lag window is constricted with width M, for example as in a Hamming window with the form

$$w(\tau) = 0.54 - 0.46cos\left(\frac{2\pi\tau}{M}\right)\ , \quad \tau = 1,2,\ldots,M \tag{3.25}$$

After that, the spectral functions of the windowed covariances is estimated as

$$\Phi_{yu}(\omega_k) = \sum_{\tau=1}^{M} R_{yu}(\tau)w(\tau)e^{-j\omega_k\tau} \tag{3.26}$$

$$\Phi_{uu}(\omega_k) = \sum_{\tau=1}^{M} R_{uu}(\tau)w(\tau)e^{-j\omega_k\tau} \tag{3.27}$$

where M is the window size and the maximum delay minus one for which the covariance function is estimated. Finally, the transfer function estimate is found as the ratio of two spectral estimates as

$$G(\omega_k) = \frac{\Phi_{yu}(\omega_k)}{\Phi_{uu}(\omega_k)} \tag{3.28}$$

In the Blackman-Tukey method, the windowing error can be reduced to a good extent by using Hann or Hamming windows instead of a rectangular window. Moreover it still has features which exhibit a strong trade off between number of samples taken into calculation and quality of obtained frequency response representation.

3.5.3 Local Frequency Smoothing Estimation

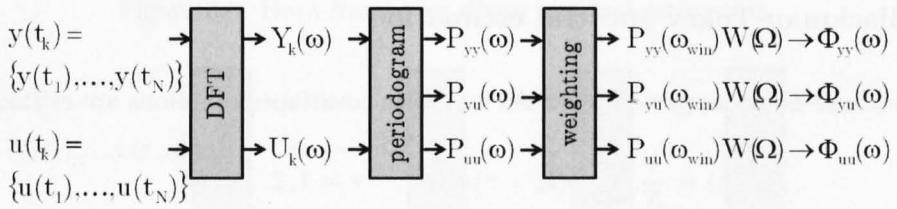

Figure 3.11: Computational steps for local frequency smoothing estimation.

When the system time domain I/O data is represented by Fourier coefficients through the DFT, it may takes the form

$$Y(\omega_k) = [Y_1, Y_2, \ldots, Y_N], \quad U(\omega_k) = [U_1, U_2, \ldots, U_N] \tag{3.29}$$

which corresponds to a frequency vector

$$\omega_k = [\omega_1, \omega_2, \ldots, \omega_N] \tag{3.30}$$

The local smoothing technique is based on choosing a frequency vector containing the important frequencies according to the system under investigation [63]. Then smoothing is done by designing a weighting function to strengthen the spectrum of the selected frequencies and reduce the leakage errors from surrounding frequencies. The main difference between the local smoothing technique and the Blackman-Tukey approach is in the use of weighting function with the Fourier coefficients, however in the Blackman-Tukey approach a lag window is used with covariance and cross covariance of the time domain data to smooth the signal spectrum.

Smoothing starts by defining a frequency vector Ω_i as

$$\Omega_i = [\Omega_1, \Omega_2, \ldots, \Omega_m], \quad i = 1, 2, \ldots, m \tag{3.31}$$

To facilitate the technique, the selected frequency vector Ω_i should have a length m less than the length of the original frequency vector N. The frequency resolution of the selected frequency vector is determined by measuring the frequency distances between each sequential frequencies as

$$\Delta\Omega_i = [2(\Omega_2 - \Omega_1), 2(\Omega_2 - \Omega_1), 2(\Omega_3 - \Omega_2), \ldots, 2(\Omega_x - \Omega_{x-1}), \ldots, 2(\Omega_m - \Omega_{m-1})] \tag{3.32}$$

A weighting function is constructed around each selected frequency $\Omega_x \in \Omega_i$ in the form

$$W(\Omega_x, \omega_{win}) = cos\left(\frac{\Omega_x - \omega_{win}}{\Delta\Omega_x}\pi\right) \tag{3.33}$$

where ω_{win} is that set of frequencies on the DFT grid which lay inside the resolution of the selected frequency resolution $\Delta\Omega_x$ which are bounded by k_L and k_U as shown in Figure 3.12. Then, the cross periodogram P_{yu} and auto periodograms P_{yy}, P_{uu} are calculated around each

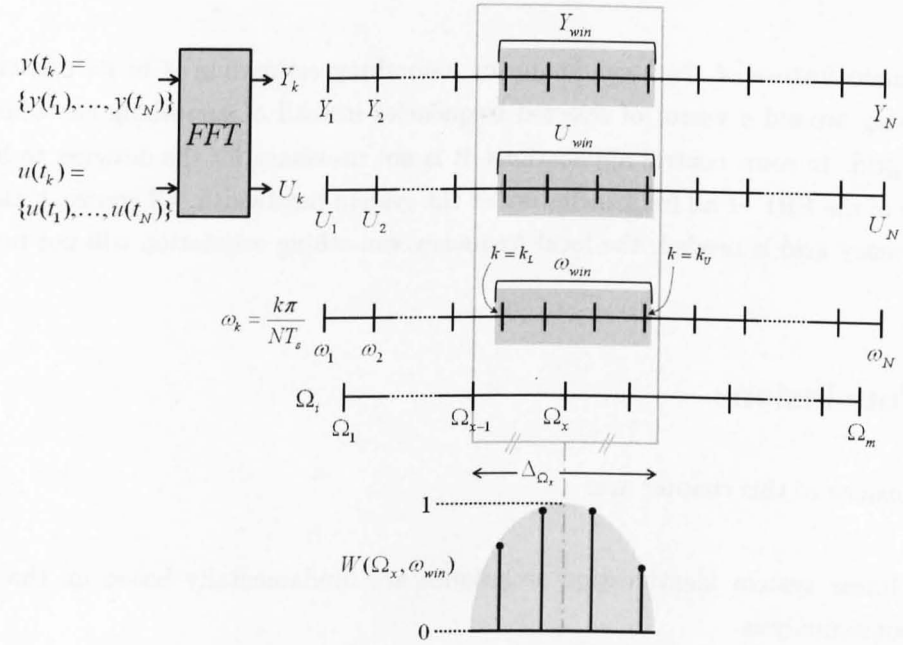

Figure 3.12: Weighting function.

selected frequency Ω_x as

$$P_{yu}(\omega_{win}) = Y_{win}U^*_{win}\ , \quad P_{uu}(\omega_{win}) = U_{win}U^*_{win}\ \&\quad P_{yy}(\omega_{win}) = Y_{win}Y^*_{win} \tag{3.34}$$

where Y_{win} and U_{win} are the frequency domain representation of the I/O data on the DFT grid corresponding to ω_{win}.

Then, weighted cross spectrum Φ_{yu} and weighted auto spectra Φ_{yy} & Φ_{uu} at Ω_x are obtained by multiplying the relevant periodograms by the weighting function $W(\Omega_x, \omega_{win})$ as

$$\Phi_{yu}(\Omega_x) = P_{yu}(\omega_{win})W(\Omega_x, \omega_{win}) \tag{3.35}$$

$$\Phi_{uu}(\Omega_x) = P_{uu}(\omega_{win})W(\Omega_x, \omega_{win})\ \&\quad \Phi_{yy}(\Omega_x) = P_{yy}(\omega_{win})W(\Omega_x, \omega_{win}) \tag{3.36}$$

Then, the locally smoothed frequency response at the selected frequency Ω_x is represented by

$$G(\Omega_x) = \frac{\Phi_{yu}(\Omega_x)}{\Phi_{uu}(\Omega_x)} \tag{3.37}$$

with a noise spectrum given by

$$\Phi_v(\Omega_x) = \Phi_{yy}(\Omega_x) - \Phi_{yu}(\Omega_x)G(\Omega_x) \tag{3.38}$$

By applying the same sequence on all selected frequencies Ω_i, a smoothed version of 3.11 can be obtained as

$$Y(\Omega_i) = G(\Omega_i)U(\Omega_i) + V(\Omega_i), \quad i = 1, 2, \ldots, m \tag{3.39}$$

The main feature of the local frequency smoothing estimation is in its concentration on smoothing around a vector of selected frequencies instead of smoothing the whole DFT frequency grid. In some control applications, it is not necessary for the designer to have the knowledge of the FRF at all frequencies under the system bandwidth. Of course, if the whole DFT frequency grid is needed, the local frequency smoothing estimation will not be a good choice.

3.6 Conclusions

The conclusions of this chapter are:

- NP linear system identification techniques are fundamentally based on the impulse response analysis.
- LTI systems can be described by their FRFs.
- Transfer functions can be represented by their impulse response analysis.
- Frequency response analysis can be carried out by using DFT.
- The main errors usually associated with spectral estimations are aliasing, leakage and data windowing errors.
- Unlike parametric identification, NP identification techniques do not condense the model knowledge in a finite vector of parameters, hence are termed NP.
- Different NP techniques have been investigated by researchers. The direct spectral estimation and Blackman-Tukey spectral estimation are the most common techniques in NP identification. The local frequency smoothing estimation is suitable for use with control methods in which only selected frequency responses are needed at certain frequency points such as in the applications presented in Chapters 7, 9 and 10 of this thesis.

Chapter 4

Driveline Modelling

4.1 Introduction

Vehicle driveline oscillations and shuffle modes must be carefully controlled to avoid excessive vehicle jerk (rapid change in vehicle acceleration) and consequent bad driveability, especially in the most difficult low speed, high requested-torque region. The calibration (design and tuning) of actively controlled electronic-throttle based driveline controllers currently incurs considerable expense and effort. Acceptable driveability is essential to allow customer acceptance of the new fuel-efficient emission-reducing technologies. A thorough quantitative account of vehicle driveability measures is presented in [3], and modeling of the driveline is surveyed in [64] in which parameter identification is used. Time delays in the responses in current engine technologies are also present and represent a severe constraint on achievable levels of control. The driveline system also contains significant nonlinearities due to clutch behaviour, tyre characteristics, and backlash in gear-box, couplings and engine mounts [40]. In addition the driveline is a structural system with highly uncertain damping and hysteresis characteristics and nonlinear stiffnesses. The backlash accentuates oscillitary behaviour in tip-in and tip-out manoeuvres and presents a particularly severe control problem [65]. Due to the difficulty of identifying such backlash systems, model-based control techniques are not extensively applied to the driveline control problem, and industrial practice in driveline calibration remains largely heuristic and involves extensive trial-and-error experimental track based testing and parameter tuning.

Mo et.al. [66] present a partially NP driveline control approach consisting of the spectral identification of a third order linear discrete model from a nonlinear driveline model excited by a PRBS test signal. The associated speed-torque feedback controller is designed using a pole-placement observer scheme. The control design accordingly does not directly address the significant time delay, nonlinearity or explicitly the controller robustness.

In [67] a model-based scheme is described and experimentally tested. Different parameters, like inertia and damping, were estimated at each engine speed range. A parametric continuous time linear phenomenological model is used and its parameters are identified from experimental data. The parameters were found to be highly dependent on engine speed, and this dependency was attributed mainly to the system backlash. An observer scheme was used in conjunction with a Smith predictor. The continuous observer model and controller were discretized and their parameters were scheduled in a look-up table. Robustness of the controller for the model was addressed by a Root Locus synthesis, however it was found necessary at the end of the design process to tune the controller on the vehicle, which thereby compromised the actual controller robustness and made the final key design step unsystematic.

A parametric approach to driveline control in an injection controlled Diesel driveline is described in [68]. This study is based on an experimentally validated driveline model. Discrete linear control models were obtained. Gain scheduling is introduced to address the likely significant system parameter variations. Pole assignment is used as the control design technique. The use of gain scheduling and tuning suggest that the process is not fully systematic. The results in-vehicle are nevertheless qualitively reported as promising.

Both system identification and controller design for systems with backlash are difficult. The most common approach to backlash control is based on the use of limit-cycle analysis using describing functions [69, 70]. The analytic or experimental determination of the overall system describing function however, may not be feasible, unless the problem is of special structure, or the system can be subject experimentally to a full range of sinusoidal test inputs. In the driveline problem test signals at the electronic throttle must be similar to those produced by driver input both to be representative and to prevent vehicle stall.

In this chapter, driveline constitutive equations are presented in section 4.2. The model includes the driveline IC engine in subsection 4.2.1, the clutch in subsection 4.2.2, the transmission in subsection 4.2.3, the couplings in subsection 4.2.4 and the wheels in subsection 4.2.5. A linearised version of the driveline model is presented in section 4.3 before investigating the effect of the driveline nonlinearities in section 4.4.

4.2 Driveline Constitutive Equations

For validating the proposed methodology, a four inertia model for a typical European mid-range passenger vehicle is developed.The model contains a clutch nonlinearity which is represented by a discontinuity of the elastic coefficients as described in 4.1. The backlash nonlinearity is represented as a dead zone of width $2\alpha_{bl}$ as shown in figure 4.2.

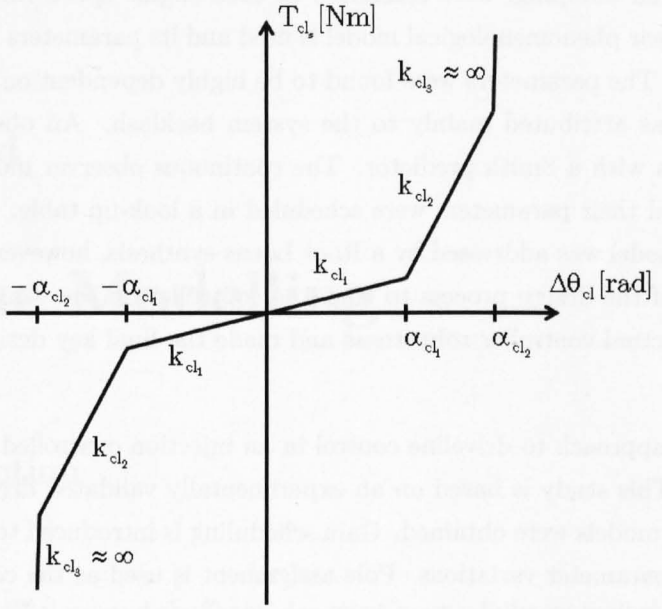

Figure 4.1: Nonlinear clutch elastic torque characteristics

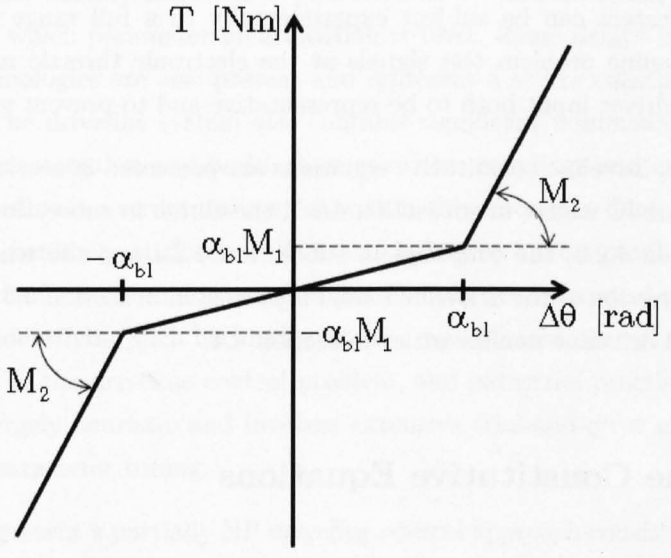

Figure 4.2: Backlash torque characteristics

Crucially, for both realism and also to allow testing of our methodology with an arbitrary driveline nonlinearity, the backlash in the proposed model is sandwiched between the compliant clutch and compliant drive shafts. The model contains four inertias which are engine, transmission, coupling, and an equivalent inertia representing the vehicle chassis and wheels. A physical representation of the vehicle driveline is shown in Figure 4.3.

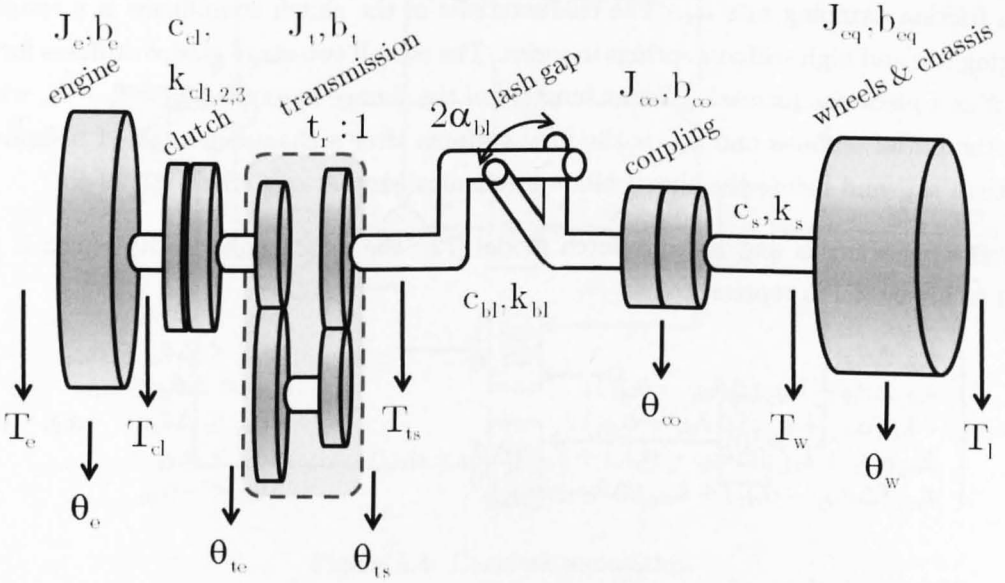

Figure 4.3: Driveline mathematical model

4.2.1 Engine

The engine is a machine in which a combustible mixture of air and fuel is taken in and burnt to convert the released energy of the burnt fuel into mechanical energy. This mechanical energy rotates a crankshaft which drives the other moving components of the driveline [71]. The output torque of the engine T_{cl}, the driving torque T_e, the engine inertia J_e and the engine damping b_e are related by

$$T_e - T_{cl} = J_e \frac{d^2\theta_e}{dt^2} + b_e \frac{d\theta_e}{dt} \tag{4.1}$$

4.2.2 Clutch

The clutch is a device which is designed to work as a mechanical connection between the flywheel of the engine and the transmission's input shaft. The clutch mechanism enables the vehicle to be brought to standstill without stalling the engine. Smoothing the engagement of the engine and the wheels through different gearing ratios is another important function of

the clutch. Only the fully engaged clutch is considered in the model presented in this thesis. The clutch torque T_{cl} is the sum of friction torque T_{cl_f} and the clutch spring torque T_{cl_s} are which related by

$$T_{cl} = T_{cl_f} + T_{cl_s} \quad ; \quad T_{cl_f} = c_{cl}\frac{d\Delta\theta_{cl}}{dt} \tag{4.2}$$

with a friction damping rate c_{cl}. The characteristic of the clutch compliance is a result of arranging low and high stiffness springs in series. The overall two-stage graded stiffness for T_{cl} is given as a piecewise increasing linear function of the change in angle $\Delta\theta_{cl} = \theta_e - \theta_{te}$ where k_{cl_1} is the initial stiffness and k_{cl_2} is the final stiffness after a change in angle of magnitude more than α_{cl_1} and before the clutch hits a mechanical stop at α_{cl_2} where $k_{cl_3} \approx \infty$.

Following Kiencke and Nelson clutch model [72], the clutch nonlinearity which is displayed in Figure 4.1 is represented as

$$T_{cl_s} = \begin{cases} k_{cl_1}\Delta\theta_{cl}; & -\alpha_{cl_1} \leq \Delta\theta_{cl} \leq \alpha_{cl_1} \\ k_{cl_2}\Delta\theta_{cl} + k_{cl_2}\left(\Delta\theta_{cl_1} - \alpha_{cl_1}\right); & \alpha_{cl_1} < \Delta\theta_{cl} \leq \alpha_{cl_2} \\ -k_{cl_1}\alpha_{cl_1} + k_{cl_2}\left(\Delta\theta_{cl_1} + \alpha_{cl_1}\right); & -\alpha_{cl_2} \leq \Delta\theta_{cl} < -\alpha_{cl_1} \\ k_{cl_1}\alpha_{cl_1} + k_{cl_2}\left(\Delta\theta_{cl_2} - \alpha_{cl_1}\right) + k_{cl_3}\left(\Delta\theta_{cl} - \alpha_{cl_2}\right); & \Delta\theta_{cl} > \alpha_{cl_2} \\ k_{cl_2}\left(\Delta\theta_{cl_2} - \alpha_{cl_1}\right) + k_{cl_3}\left(\Delta\theta_{cl} + \alpha_{cl_2}\right); & \Delta\theta_{cl} < -\alpha_{cl_2} \end{cases} \tag{4.3}$$

4.2.3 Transmission

A number of different gear ratios are selected by the vehicle designer to cover the speed range and accelerating conditions expected from the vehicle. The largest torque is required when the largest reduction gearing ratio is used to maximise the delivered torque. Taking the combined gear ratio of the gearbox and final drive as t_r, the difference of torque on the engine side T_{te} and on the shaft side T_{ts} is determined from

$$T_{cl} - T_{te} = J_t\frac{d^2\theta_{te}}{dt^2} + b_t\frac{d\theta_{te}}{dt} \tag{4.4}$$

where J_t is the transmission inertia and b_t the transmission damping. The transmission torque on the shaft side T_{ts} and the transmission angle of rotation θ_{ts} are obtained from

$$T_{ts} = T_{te}t_r \quad ; \quad \theta_{ts}t_r = \theta_{te} \tag{4.5}$$

4.2.4 Coupling

Couplings are necessary components for delivering the power to the vehicle wheels and to allow those wheels to have the required degrees of freedom during steering operation. Assuming

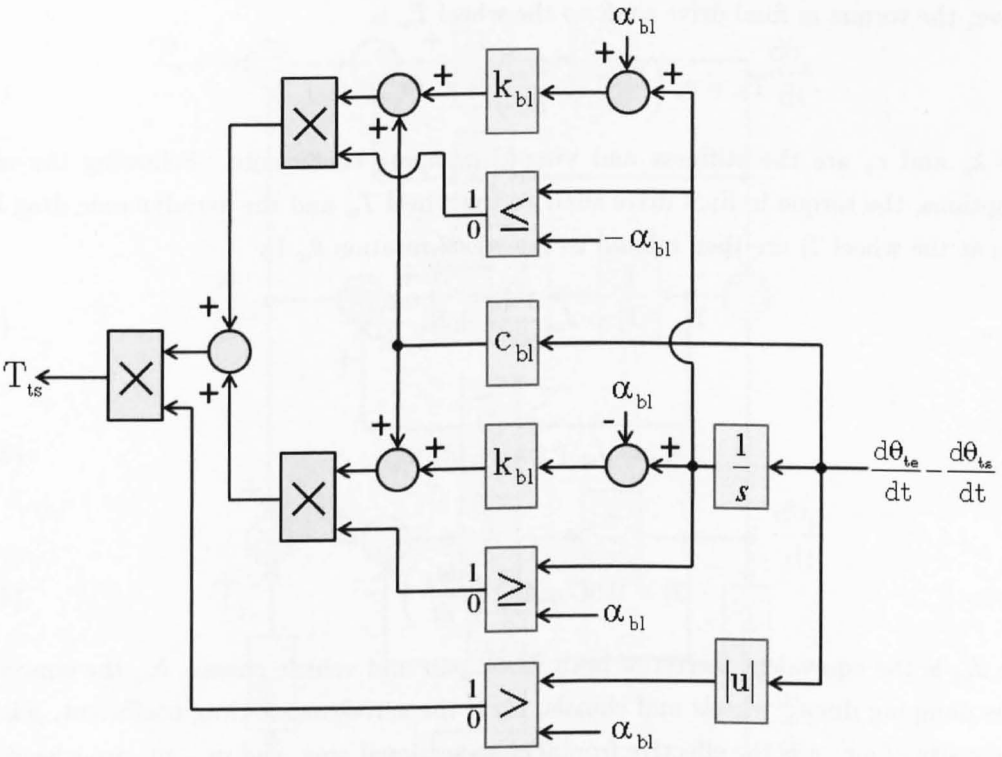

Figure 4.4: Backlash simulation

frictionless couplings the difference between the transmission torque T_{ts} and the driveshaft torque T_w is

$$T_{ts} - T_w = J_{co}\frac{d^2\theta_{co}}{dt^2} + b_{co}\frac{d\theta_{co}}{dt} \tag{4.6}$$

where inertia and damping constant of the coupling are J_{co}, b_{co} and the coupling rotation is θ_{co}.

4.2.5 Wheels

The wheels are assumed compliantly coupled to the transmission through the backlash element of the coupling with backlash gap $2\alpha_{bl}$. Taking $\Delta\theta_{bl}$ as the angular difference in the coupling shaft ends, $\Delta\theta_{bl} = \theta_{ts} - \theta_{co}$ the transmission torque at the shaft end is then

$$T_{ts} = \begin{cases} 0; & -\alpha_{bl} \leq \Delta\theta_{bl} \leq \alpha_{bl} \\ k_{bl}\left(\Delta\theta_{bl} - \alpha_{bl}\right) + c_{bl}\frac{d\Delta\theta_{bl}}{dt}; & \Delta\theta_{bl} > \alpha_{bl} \\ k_{bl}\left(\Delta\theta_{bl} + \alpha_{bl}\right) + c_{bl}\frac{d\Delta\theta_{bl}}{dt}; & \Delta\theta_{bl} < -\alpha_{bl} \end{cases} \tag{4.7}$$

where k_{bl} is the lash contact mode stiffness and c_{bl} is the lash contact mode damping after a change in angle of magnitude of more than α_{bl}. Equation 4.7 is simulated as in Figure 4.4

however, the torque in final drive shaft to the wheel T_w is

$$T_w = c_s \left(\frac{d\theta_{co}}{dt} - \frac{d\theta_w}{dt} \right) + k_s \left(\theta_{co} - \theta_w \right) \tag{4.8}$$

where k_s and c_s are the stiffness and viscous damping coefficients. Following the usual assumptions, the torque in final drive shaft to the wheel T_w and the aerodynamic drag load torque at the wheel T_l are then related to the wheel rotation θ_w by

$$T_w - T_l = J_{eq} \frac{d^2\theta_w}{dt^2} + b_{eq} \frac{d\theta_w}{dt} \tag{4.9}$$

where

$$J_{eq} = J_w + (m_v + m_w) r_w^2 \tag{4.10}$$

and

$$T_l = 0.5 C_d \rho A r_w^3 \left(\frac{d\theta_w}{dt} \right)^2 \tag{4.11}$$

where J_{eq} is the equivalent inertia of both wheel pair and vehicle chassis, b_{eq} the equivalent viscous damping due to wheels and chassis, C_d is the aerodynamic drag coefficient, ρ is the mass density of air, A is the effective frontal cross sectional area, and m_w, m_v are wheels and vehicle masses respectively.

4.2.6 Engine Demand Torque Restrictions

The maximum negative torque that can be provided by the engine for control processes is the engine internal friction and damping torque which can be expressed as:

$$T_f = T_{cl} + b_e \omega_e \tag{4.12}$$

The strategy which is used to model this behaviour in the developed model is described in the flow chart in Figure 4.6. A time delay also exists the the real control problem so a delay time of 0.15 s obtained from experimental work experience in the University of Liverpool IC engine lab is added to the torque demand path in the model as in Figure 4.6 which shows also how the negative torque restriction is modeled.

4.3 Linearised Model

For the purpose of comparing the nonlinear model with its linearised equivalent, equations (4.2), (4.3), and (4.7) can be combined and presented in linear form as

$$T_{cl} = c_{cl} \left(\frac{d\theta_e}{dt} - \frac{d\theta_{te}}{dt} \right) + k_{cl} \left(\theta_e - \theta_{te} \right) \tag{4.13}$$

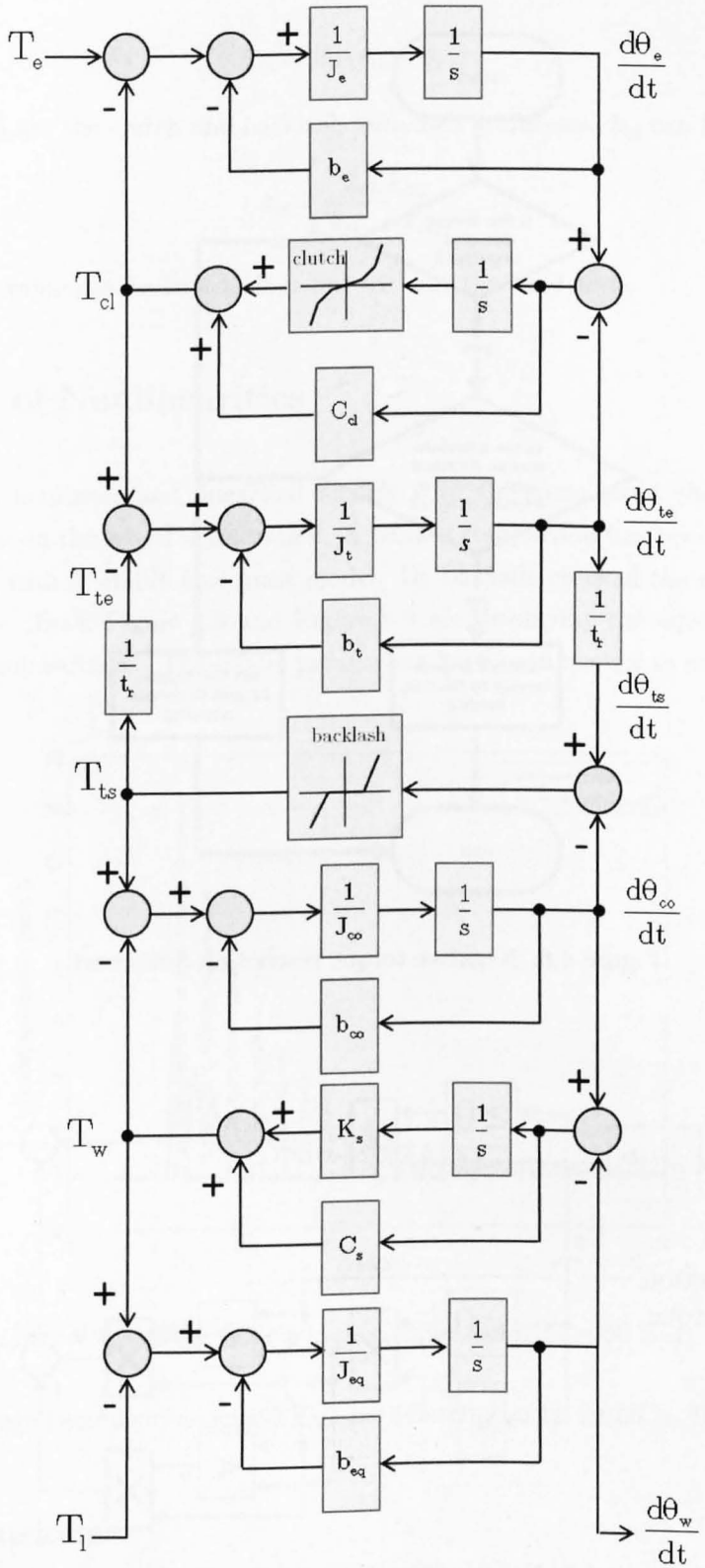

Figure 4.5: Driveline model block digram

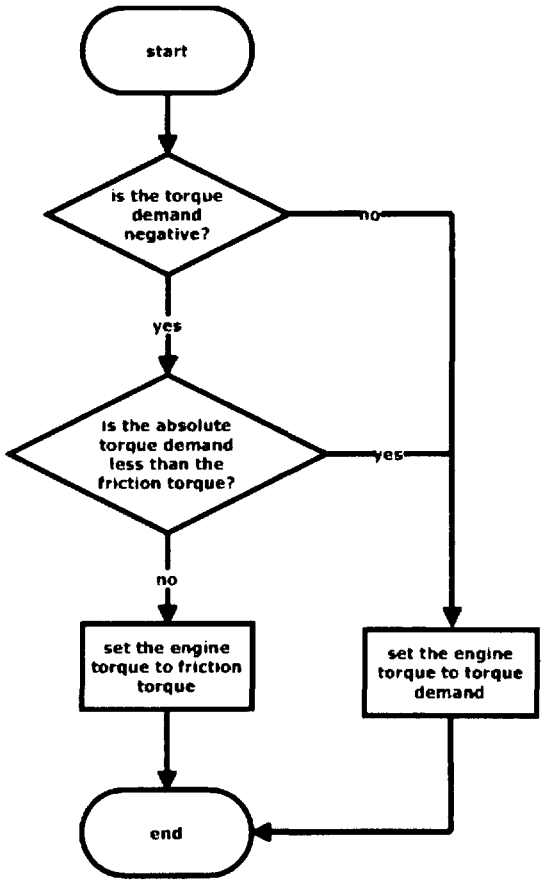

Figure 4.6: Negative torque restriction flow chart

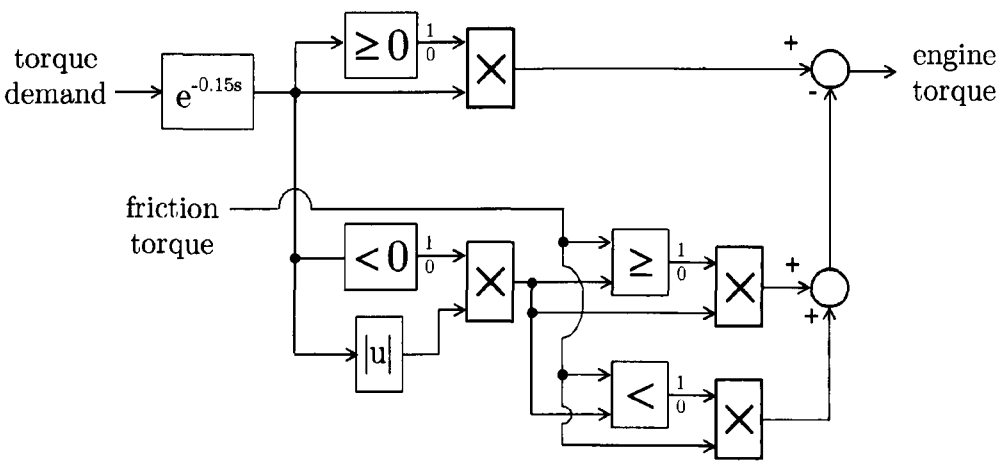

Figure 4.7: Negative torque restriction block diagram

and

$$T_{ts} = k_{bl} \left(\theta_{ts} - \theta_{co} \right) \tag{4.14}$$

where k_{cl} and k_{bl} are the clutch and backlash linearised stiffnesses. k_{cl} can be determined as

$$k_{cl} = \frac{k_{cl_1} k_{cl_2}}{k_{cl_1} + k_{cl_2}} \tag{4.15}$$

however, the k_{bl} value can be kept as it is but without the dead zone.

4.4 Effect of Nonlinearities

Simulating both nonlinear and linearised models with the same input shows the effect of the nonlinearities on the wheel acceleration. A similar comparison has been made by De La Salle in [65] but with a simple four mass model. De La Salle checked the effect of backlash nonlinearity only. Both Figure 4.8 and Figure 4.9 are displaying the effect of both clutch and backlash nonlinearities. The model parameters have been chosen to represent a typical

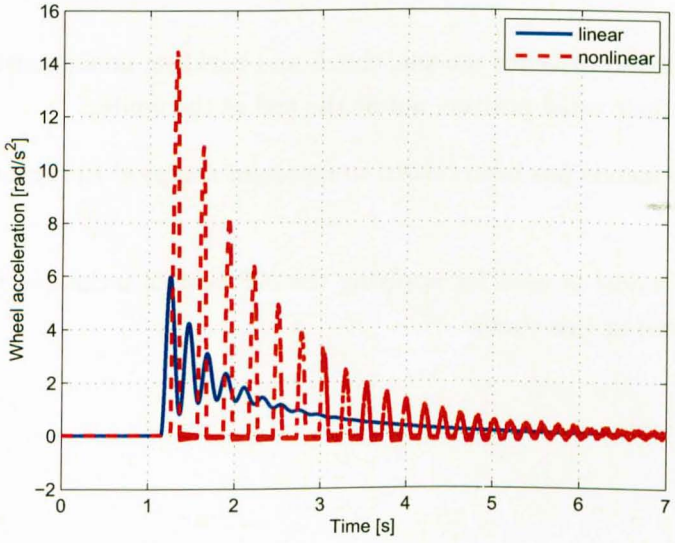

Figure 4.8: Slow vehicle launch (light tipin, $T_e = 50$ Nm)

European midrange passenger vehicle. These parameters can be found in Table 7.1.

4.5 Conclusions

The conclusions of this chapter are:

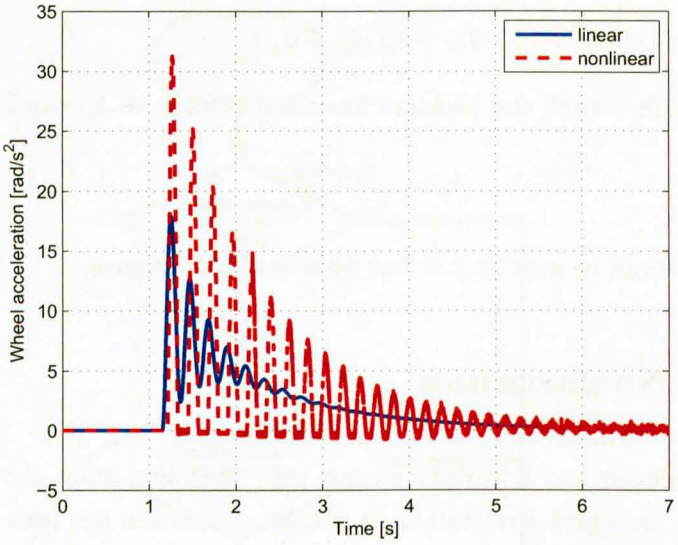

Figure 4.9: Slow vehicle launch (heavy tipin, $T_e = 150$ Nm)

- A novel mathematical model representing the driveline as a dynamic system is presented.
- Unlike the published driveline models, clutch and backlash nonlinearities are included, and located in their usual position not at the end of the model.
- The model parameters has been chosen to represent a typical European midrange passenger vehicle.
- The presented model is used for applying the NP control technique which is a novel method presented in this thesis.

Chapter 5

Quantitative Feedback Design

5.1 Introduction

One of the fundamental problems in robust control is the optimum design of a controller for a system with large uncertainty in its model representation parameters. Usually, the expected time domain response of such that system lies within definite tolerances. One among several reasons for using feedback techniques in control design is to reduce the effect of the parameters variation of the system during operation. When a quantitative description of the plant uncertainty in the frequency domain in the form of templates exists, design techniques which allow the designer to move those templates to the acceptable loop frequency response region can be obtained. One of the techniques for achieving that purpose is the QFT method developed by Horowitz.

Horowitz and Sidi [73] initiated to the first step of developing the QFT method by synthesise of feedback systems with large plant ignorance for prescribed time domain tolerance in 1972. Krishnan [74] used the idea in 1977 to present a frequency domain design of feedback systems for specified insensitivity of time domain response to parameter variation. In 1978, Horowitz and Sidi developed their technique to make the designer able to synthesis a linear time varying NMP systems with plant uncertainty [75] and they suggested an optimisation technique for doing that [76]. Horowitz [77] justified the representation of a nonlinear uncertain system by a Linear Time Invariant (LTI) set by using Schauder's fixed point theorem. He suggested also a cancellation technique to reduce the uncertainty templates size [78]. In 1982, Horowitz extended the technique and applied it on uncertain Multi Input Multi Output (MIMO) systems with internal variable feedback [79] and presented a comprehensive description of the QFT theory and methodology [80].

Since then, many researchers developed methods and techniques to improve the QFT controller design method. For example, East developed the "dominant chord" approach to

determine the uncertain plant variation bounds [81]. Bailey [82] summarised the steps in loop gain-phase shaping design and described a family of Computer Aided Design (CAD) tools that implement the design procedure. Several useful guidelines and a QFT CAD package was presented by Houpis in 1994 [83] but, unfortunately, the package cannot be used with NP identification method presented in this thesis. Bryant [84] presented an optimal loop-shaping technique for system with large parameter uncertainty via linear programming in 1995. By 2003, Horowitz [85] concluded that most QFT problems had been solved but he did not considered how the designer could use the QFT method with a NP plant model.

In this chapter, the benefits of using the QFT technique are discussed in section 5.2. The basics of constructing plant uncertainty templates are presented in section 5.3. In section 5.4, basic frequency domain characteristics are listed. Then, QFT time domain requirements are discussed in section 5.5. This is including tracking boundary design in subsection 5.5.1 and disturbance rejection boundary design in subsection 5.5.2. Converting time domain requirements to frequency domain boundaries is an important issue in the QFT methodology as can be seen in section 5.6. An overview of frequency domain specification can be read in section 5.7 before discussing the QFT boundaries in Nichols chart in section 5.8 which includes tracking boundaries in the Nicholas chart in subsection 5.8.1, disturbance rejection boundaries in the Nicholas chart and stability boundaries in the Nicholas chart in subsection 5.8.2. Then, dealing with NMP plants is covered in section 5.9. Section 5.10 presents an introduction to the Hilbert transform. This includes discrete Hilbert transform numerical calculations in subsection 5.10.1 and the use of discrete Hilbert transform for Estimating Equivalent MP Plant from a NMP Plant in subsection 5.10.2. After that, the QFT prefilter design methodology is covered in section 5.11. Finally, the limitations of the NP QFT methodology is discussed in section 5.12 before the chapter conclusions are given in section 5.13.

5.2 The Benefits of Using the QFT Technique

QFT offers a number of benefits such as the facility to take phase information into account in the design process and the capability to assess quantitatively the cost of feedback. The first question one should answer here in this chapter is why it is necessary to use QFT type technique is needed to achieve performance and stability goals. Consider an open loop system compensated by controller G which contains an uncertain plant $\mathcal{P}$ as in Figure 5.1 with a reference input R, a disturbance D, and an output Y. So,

$$Y_R = GP_oR \;\; ; \;\; Y_D = D \tag{5.1}$$

where P_o is the "nominal plant" which is arbitarily chosen as any $P_o \in \mathcal{P}$. Bode [33] called the ratio $\frac{\delta Y}{\delta P_o}/\frac{Y}{P_o}$ the sensitivity function S of the output Y with respect to a plant P_o [37, 86].

Thus, the output sensitivity functions in Eqn. (5.1) to change in P_o is 100% and can be expressed as:

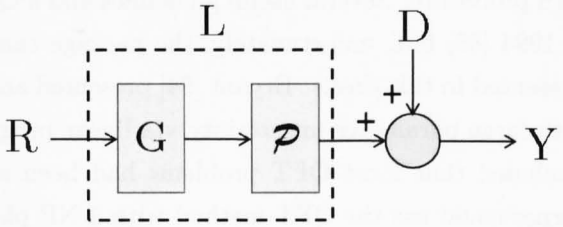

Figure 5.1: Open loop compensated system

$$S_{P_o}^{Y_R} = S_{P_o}^{Y_D} = 1 \tag{5.2}$$

However, the sensitivity functions of the closed loop compensated system, as in Figure 5.2, to P_o can be calculated from the outputs

$$Y_R = \frac{GP_oR}{1+GP_o}\,, \quad Y_D = \frac{D}{1+GP_o} \tag{5.3}$$

as

$$S_{P_o}^{Y_R} = \frac{1}{1+GP_o}\,, \quad S_{P_o}^{Y_D} = \frac{-GP_o}{1+GP_o} \tag{5.4}$$

By comparing Eqn. 5.4 with Eq. 5.2, it is clear that the effect of uncertainty in the plant $\mathcal{P}$

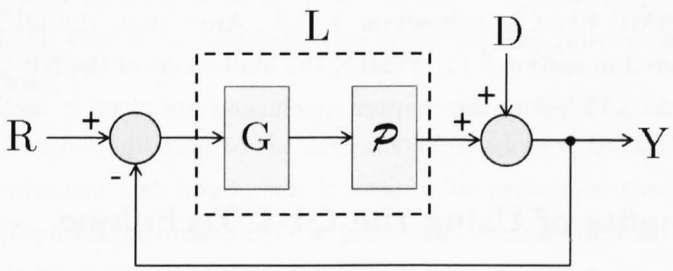

Figure 5.2: Closed loop compensated system

upon the outputs related to R and D of the closed loop compensated system is reduced by factors of $\frac{1}{1+GP_o}$ and $\frac{-GP_o}{1+GP_o}$ respectively. This reduction of the sensitivity to the uncertainty is the main reason why feedback systems are used.

5.3 Plant Uncertainty Templates

System structured uncertainty representing the model errors result from assuming that the actual system is LTI. When these errors are approximated to bubble shapes like circles, they

termed as unstructured uncertainties as can be seen in the example in Figure 5.3. A simple example of structured uncertainty can be seen through an uncertain plant P represented by a set $\mathcal{P}$ due to uncertain parameters in its transfer function coefficients.

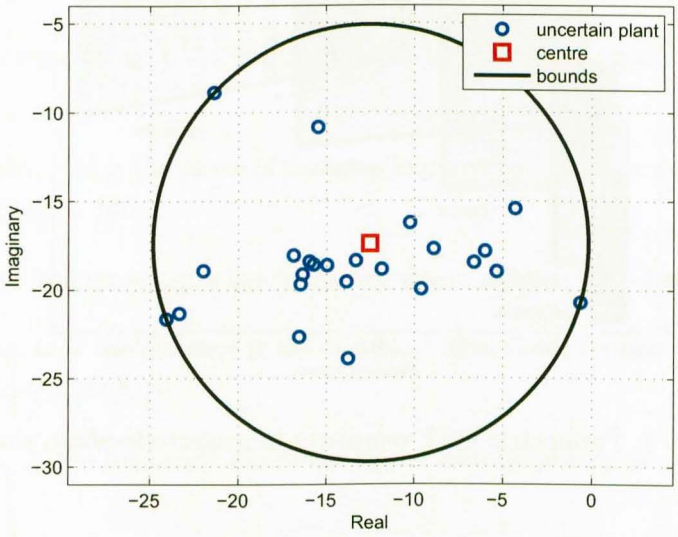

Figure 5.3: Unstructured uncertainty

$$\mathcal{P} = \left\{ P = \frac{k}{s+a};\ k \in [1, 10],\ a \in [1, 4] \right\} \tag{5.5}$$

The plant $\mathcal{P}$ with uncertain coefficients given in Eqn. (5.5) is illustrated in Figure 5.4 over several discrete frequencies in the range of interest. As the templates follow the plant boundaries at each frequency, this representation of uncertainty is commonly known as structured uncertainty. These templates are also described as parametric templates as they are generated through substitution in a parametric model of the plant which is given by Eqn. (5.5). An alternative way of representing the structured uncertainty of a physical plant is to obtain several models of the plant by a using system identification approach over a range of operating points. Drawing the FRF at each chosen discrete frequency can then be used for constructing the plant template at this frequency. One particular benefit of QFT is the ability to work directly with both structured and unstructured uncertainties. However, in the $\mathcal{H}_\infty$ approach, only unstructured uncertainties are applicable. The extension to μ-synthesis [87, 88], however, allows structured uncertainty to be considered. Converting the structured uncertainty to unstructured can be done by representing a typical set of a plant models $P_i(j\omega) \in \mathcal{P}$ at a particular frequency in the complex plane, the nominal plant $P_o(j\omega)$ can be taken as the center of the minimum radius circle which containing all elements of the set $P_i(j\omega)$ at this particular frequency ω. Moreover, $\mathcal{H}_\infty$ can be excessively conservative. An approach for boundary calculation and circular approximation was presented by East [89, 81].

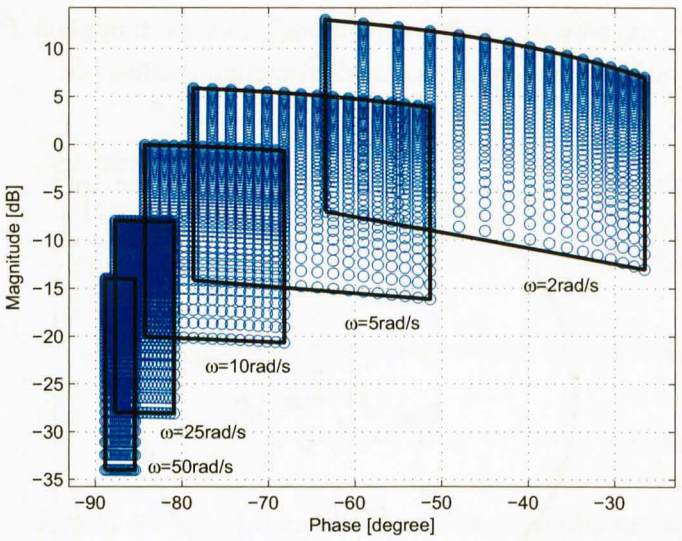

Figure 5.4: Parametric QFT templates in magnitude-phase plane

It calculates the boundary shape according to the format of the transfer function. However East's paper presents a method for dealing with poles and zeros position uncertainties, it cannot be used when NP identification is considered. Two algorithms were proposed firstly by Bailey and Gu [90]. The main idea is to assume that the plant transfer function can be represented by numerator polynomial divided by a denominator polynomial. The method becomes very conservative when varying parameters appear in more than one polynomial. Also, it is not applicable when NP modelling is considered. However, Bailey [91] technique allows the parameters of the numerator and denominator to be affine functions of the underlying parameters, further his method is still conservative if a real parameter appears in the numerator and denominator at the same time. Bartlett [92, 93] and Fu [94] provide farther simplifications for the technique presented in [91]. Bartlett [93] modifications made the technique non-conservative for linear in parameters polynomial coefficients system models. Kharitonov polynomial also has been used in some publications to develop approaches to determine the outer bounds of uncertainty templates, for example in Chapellat [95], Keel [96], and Pande [97]. As these methods are not suitable for NP models where there are no transfer functions or parameter models, the Quickhull algorithm [98] for convex hulls is used in this thesis for determining the outer boundaries of the uncertainty templates. The algorithm is already implemented in the MATLAB function "convhull" which used in Figures 7.3, 7.6, 9.6, 9.7 and 10.5 in this thesis. The Quickhull algorithm does not need any parametric representation of the frequency response template areas, so it is considered to be suitable for NP identification applications.

5.4 Basic Frequency Domain Characteristics

Frequency domain characteristics referred to inside this chapter and the following chapters will first be defined here and illustrated in Figure 5.5 as:

- Cross over frequency, ω_c is the frequency where the open loop magnitude is 1.0, $|L(j\omega_c)| =$ 0 dB
- Phase margin, PM is the phase of the open loop at the cross over frequency over -180^o, $PM = \angle L(j\omega_g) + 180$
- Gain margin frequency, ω_g is the frequency where $\angle L(j\omega_g) = -180^o$
- Gain margin, GM the distance in dB of $L(j\omega_g)$ from the -1.0 point on the Nyquist plot, $GM = -20\log_{10}|L(j\omega_g)|$
- Bandwidth, ω_b the frequency where the closed loop amplitude is -3 dB

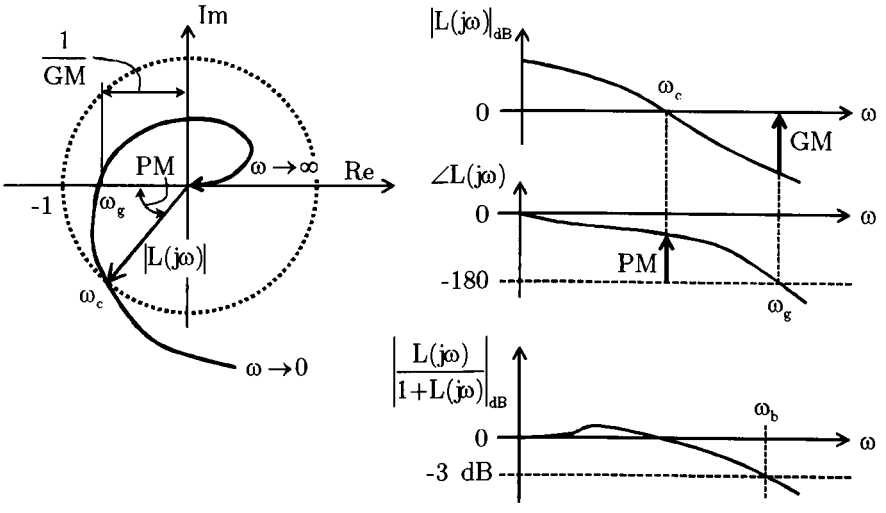

Figure 5.5: Frequency domain characteristics

5.5 QFT Time Domain Requirements

To conduct a quantitative controller design, The closed loop specifications of a system, such as the one in Figure 5.2, are required in terms of plant expected input and output signals. Upper and lower bounds are chosen for each plant according to the nature of the plant and the required performance. In nonlinear uncertain mechanical systems, the controlled plant

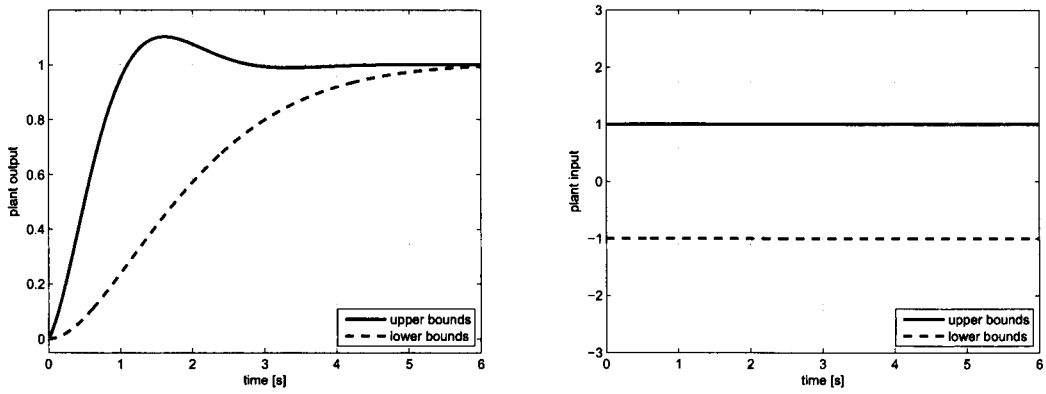

(a) Output constrains (b) Input constrains

Figure 5.6: Plant input and output time specifications for a given initial condition

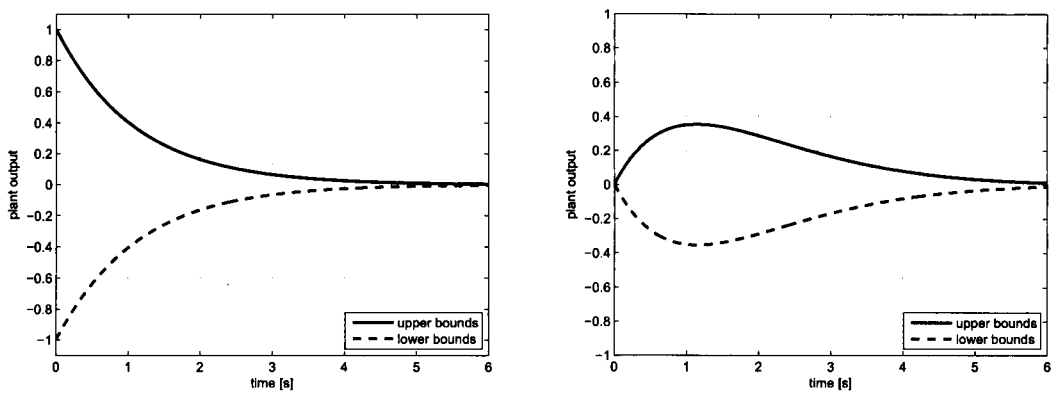

(a) Wide space (b) Narrow space

Figure 5.7: Plant output for a given initial condition

output is often required to follow a certain desired bounded trajectory within a pre-selected upper and lower time functions. An example of boundaries suitable for such a system is shown in Figure 5.6a.The plant input is needed to be constrained also to avoid saturation or overloading. The tracking command or disturbance signal could also be bounded with in a certain region as in Figure 5.6b. However, in some other systems like regulation systems, the controlled output time domain requirements in design could be chosen to damp a given disturbance within a certain time and remain inside upper and lower bounds which can be described as time functions as in Figure 5.7. The classical time domain specifications like delay time t_d, rise time t_r, peak time t_p, maximum overshoot OS, and settling time t_s are chosen and represented by time functions. Those time domain functions are used then for calculating the design boundaries in the frequency domain.

5.5.1 Tracking Boundary Design

The required system tracking performance limits for $Y(s)/R(s)$ are chosen to satisfy a certain requirement. The upper bound T_U is chosen to give a certain peak overshoot OS on a time t_p, and a certain settling time t_s. Similarly the lower bound T_L is chosen to satisfy an OS of 0, a rise time of t_r, by choosing a non-oscillatory second order system with $\zeta \geq 0.707$ and an acceptable steady state error e_{ss}. We then obtain $\omega_n = 2\zeta/e_{ss}$. This approach converts the time domain requirements to the frequency domain by assuming the requirements initially are for an equivalent second order linear system excited by a unit step input, so that its output takes the form

$$y_R = 1 - e^{-\zeta\omega_n t}[\cos(\omega_d t) + \frac{\zeta\omega_n}{\omega_d}\sin(\omega_d t)] \quad \text{,where} \quad \omega_d = \omega_n\sqrt{1-\zeta^2} \tag{5.6}$$

for which

$$OS = e^{\frac{-\zeta\pi}{\sqrt{1-\zeta^2}}} \tag{5.7}$$

and

$$t_s = \frac{4}{\zeta\omega_n} \quad \text{for 2\% error criterion} \tag{5.8}$$

For example, when a response with $OS = 0.1$, and $ts = 3$ s is required, ζ can be calculated from Eqn. (5.7) as $\zeta = \sqrt{\frac{\log_e(OS)}{\pi^2+\log_e^2(OS)}} = 0.5912$, and $\omega_n = \frac{4}{\zeta t_s} = 2.2555$ rad/s. The resulting second order transfer function could be used as an upper limit of time domain specification as can be seen in Figure 5.6a. Lower bounds can be achieved by choosing $\zeta = 0.9 > 0.707$ and $e_{ss} = 2\%$, so $\omega_n = \frac{2\zeta}{e_{ss}} = 0.9$ rad/s for the resulting bounds shown in Figure 5.6a as a dashed line. The resulting second order transfer functions can be used as initial choice for time domain performance. Additional poles and zeros can be added later to widen or tighten the gap between the upper and lower boundaries in the frequency domain at certain frequencies without much effect on the time domain performance.

5.5.2 Disturbance Rejection Boundary Design

Design of the disturbance rejection boundary starts with assuming that the controlled system response to a disturbance in the plant output will take the form of a time function consisting of a negative power exponential term (see Figure 5.8a) multiplied by a cosine term (see Figure 5.8b) to construct a shape as in Figure 5.8c. This time function takes the form [99]

$$y_D(t) = e^{-at}\cos(bt) \tag{5.9}$$

in the time domain and is represented for different parameters in Figure 5.9. Parameters a and b are adjusted to achieve the required decay rate during the specified period in the design.

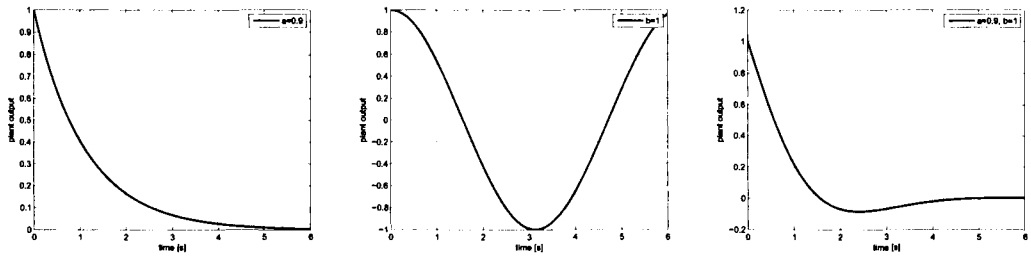

(a) e^{-at} (b) $\cos(bt)$ (c) $e^{-at}\cos(bt)$

Figure 5.8: Constructing disturbance rejection boundary

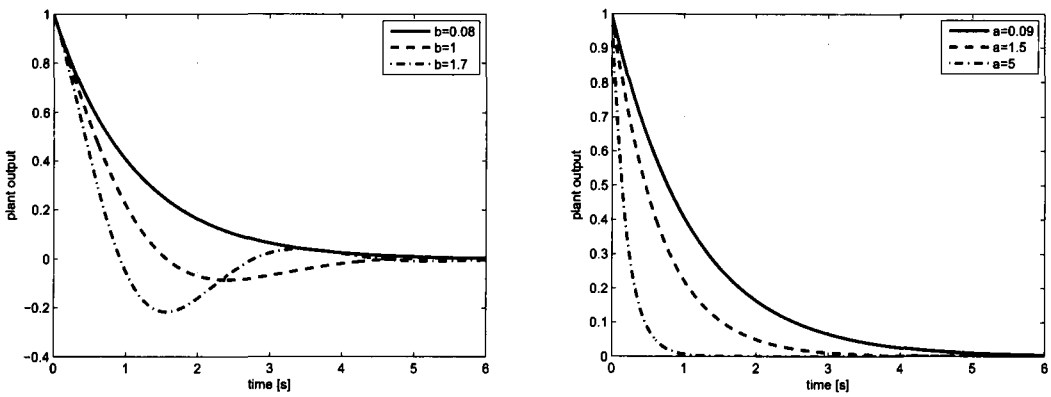

(a) $a = 0.9$ (b) $b = 0.08$

Figure 5.9: Adjusting disturbance rejection boundary

5.6 Converting Time Domain Requirements to Frequency Domain Boundaries

There are many frequency domain equivalent representations for the same time domain performance. The frequency domain representation of the second order model can be expressed as

$$\frac{Y_R(s)}{R(s)} = \frac{\omega_n^2}{s^2 + 2\zeta\omega s + \omega_n^2} \tag{5.10}$$

in the frequency domain. When the numerical values in subsection 5.5.1 are used, an initial representation of upper and lower boundaries in the frequency domain can be represented as in Figure 5.10. Sometimes, synthesizing the tracking model in the frequency domain needs the multiplication of additional poles or zeros by the upper or the lower boundaries tracking models to tighten or widen the design magnitude area between them. Of course, the choice of the set of those additional poles or zeros requires adjustment of the design area in the frequency domain without violating the desired time domain performance and characteristics. There is no one to one translation from t-domain to ω-domain but there is always a translation which can be used effectively in design [100]. Multiplying a zero term in the form $(1 + \frac{1}{\omega_x}s)$ by the upper boundary will widen the magnitude of the design area at this frequency ω_x, however, a pole in the same form can perform the widening effect when multiplied by the lower boundary tracking model. The purpose of increasing the magnitude

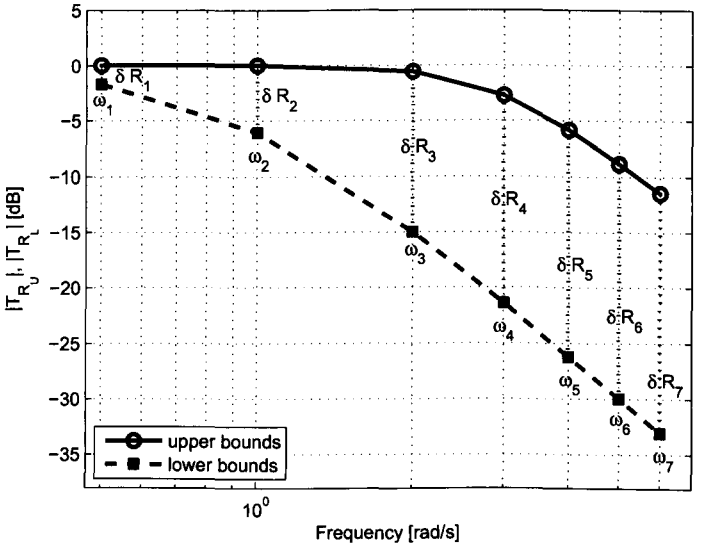

Figure 5.10: Bode plot of frequency domain tracking boundaries

difference δ_R between the upper boundary T_{R_U} and lower boundary T_{R_L} in tracking models in high frequencies (close to the system bandwidth) is to respond to the fact that both initial choices of upper and lower boundaries are second order models. This means that both of

them have the same slope (40 dB/decade) after their natural frequency ω_n, however, the uncertainty of plants is generally increasing with frequency. To be able to design a robust controller with the QFT technique, the frequency domain boundaries should be wide enough to allow the designer to set the uncertainty templates inside the design boundaries.

When applying the Laplace transform, Eqn. (5.9) can be expressed in the frequency domain as

$$Y_D(s) = \frac{s+a}{(s+a)^2+b^2} \tag{5.11}$$

Because $Y_D(s)$ may be interpreted as a frequency response for a unit step disturbance $D(s) = \frac{1}{s}$, the model of the disturbance rejection ratio will take the form

$$\frac{Y_D(s)}{D(s)} = \frac{s^2+as}{(s+a)^2+b^2} \tag{5.12}$$

5.7 Frequency Domain Specifications

The closed loop specifications of the desired system are essential in the QFT design process. The closed loop specifications of the system in Figure 5.11 may be represented as inequalities in the form

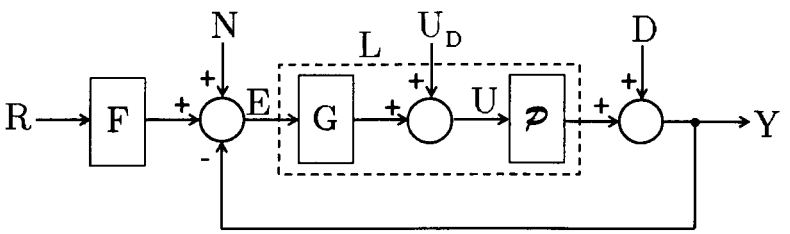

Figure 5.11: QFT structure

- Robust stability margin: for any $P_o \in \mathcal{P}$, the loop transfer function is bounded by

$$\left|\frac{L_o(j\omega)}{1+L_o(j\omega)}\right| < \gamma \tag{5.13}$$

- Plant output disturbance rejection: for any $P_o \in \mathcal{P}$, the transfer function from output disturbance to the plant output is bounded by

$$\left|\frac{Y}{D}\right| = \left|\frac{1}{1+L_o(j\omega)}\right| < |T_D(j\omega)| \tag{5.14}$$

- Tracking: for any $P_o \in \mathcal{P}$, the amplitude of the transfer function from R to Y is bounded by

$$|T_{R_L}(j\omega)| \leq \left|\frac{L_o(j\omega)F(j\omega)}{1+L_o(j\omega)}\right| \leq |T_{R_U}(j\omega)| \tag{5.15}$$

- Plant input disturbance rejection: for any $P_o \in \mathcal{P}$, the transfer function from input disturbance to the plant output is bounded by

$$\left|\frac{Y}{U_D}\right| = \left|\frac{P_o(j\omega)}{1 + L_o(j\omega)}\right| < \delta_U(\omega) \tag{5.16}$$

- Control effort: for any $P_o \in \mathcal{P}$, the transfer function from the sensor output to the plant input is bounded by

$$\left|\frac{U}{N}\right| = \left|\frac{G(j\omega)}{1 + L_o(j\omega)}\right| < \delta_C(\omega) \tag{5.17}$$

5.8 QFT Boundaries in Nichols Chart

The Nichols chart is a graphical representation of gain versus phase of the closed loop systems [101]. The magnitude M of the control ratio for a unity feedback controlled system can be expressed as

$$M(\omega) = \frac{|L(j\omega)|}{|1 + L(j\omega)|} \tag{5.18}$$

Because the open loop gain $L(j\omega)$ can be expressed as a complex number $x + jy$ at each ω, and by substituting in Eqn. (5.18) gives

$$M = \frac{|x + jy|}{|1 + x + jy|} = \sqrt{\frac{x^2 + y^2}{(1 + x)^2 + y^2}} \tag{5.19}$$

$$\text{or} \quad M^2 = \frac{x^2 + y^2}{(1 + x)^2 + y^2} \tag{5.20}$$

At each ω, rearranging the terms in Eqn. (5.20) yields

$$\left(x + \frac{M^2}{M^2 - 1}\right)^2 + y^2 = \frac{M^2}{(M^2 - 1)^2} \tag{5.21}$$

which is the equation of a circle with its centre at the point (x_o, y_o) with a radius r where

$$(x - x_o)^2 + (y - y_o)^2 = r^2 \tag{5.22}$$

This can be compared with Eqn. (5.21) to give a centre point at

$$x_o = -\frac{M^2}{M^2 - 1} \quad , \quad y_o = 0 \tag{5.23}$$

and a radius

$$r = \left|\frac{M}{M^2 - 1}\right| \tag{5.24}$$

By using the centre points from Eqn. (5.23) and the relevant radii from Eqn. (5.24), circles for different closed loop magnitudes can be drawn in the complex plane as in Figure 5.12 Those constant M contours can then be mapped to phase magnitude charts by calculating the relevant amplitude in decibels and phase in degrees for each point on each M circle. The resulting chart is known as the Nichols chart.

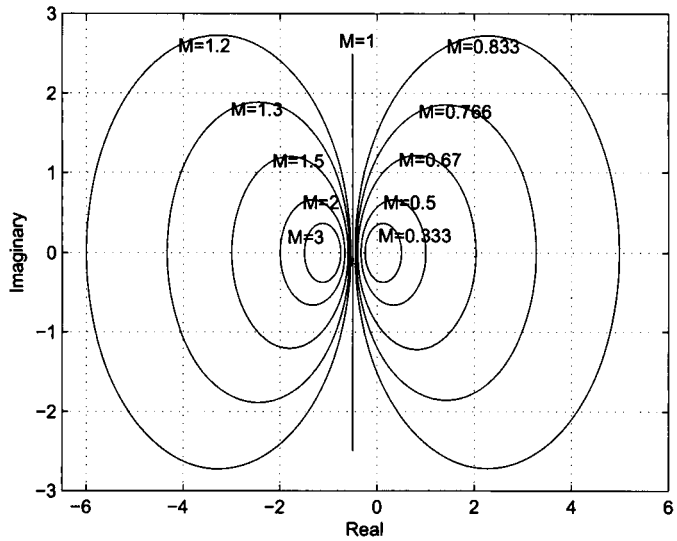

Figure 5.12: Constant M contours

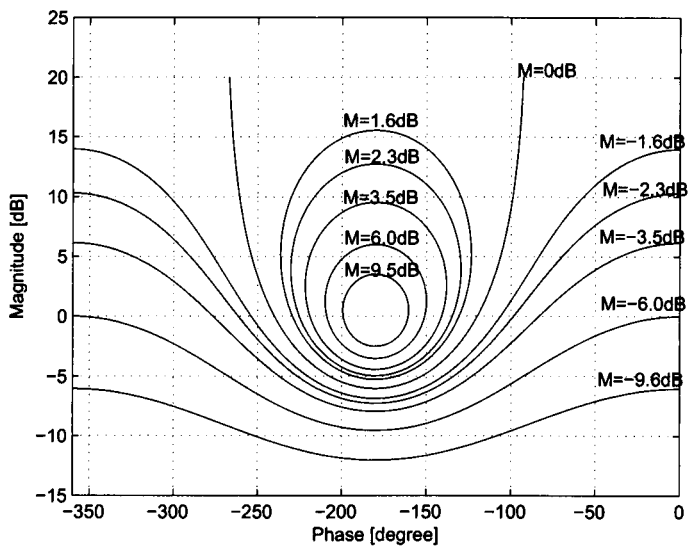

Figure 5.13: Nichols chart

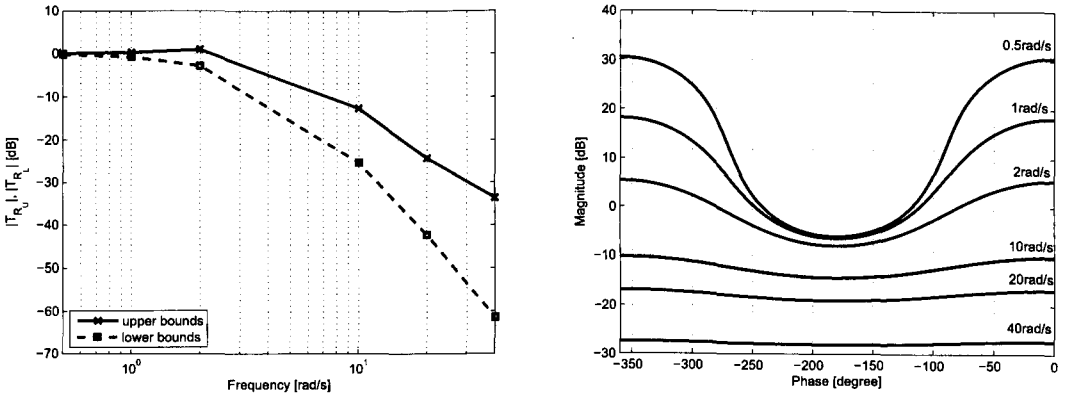

(a) boundaries in Bode plot

(b) boundaries in Nichols chart

Figure 5.14: Constructing tracking boundaries

5.8.1 Tracking Boundaries in Nichols Chart

In the QFT design approach, once the upper and lower limits boundaries obtained, they should be then translated to Nichols chart plane. The values of $\delta_R(j\omega)$ at the selected frequency range is mapped to the Nichols chart as in Figure 5.14. For example [99], if the upper and lower limits are in the form

$$T_{R_U}(s) = \frac{0.6584s + 19.75}{s^2 + 4s + 19.75} \quad , \quad T_{R_L}(s) = \frac{3520}{s^4 + 62.4s^3 + 671.2s^2 + 2630s + 3520} \tag{5.25}$$

then, the upper and lower tracking boundaries can be represented in logarithmic magnitude against frequency form as in Figure 5.14a. The magnitude difference in decibels between the upper and lower limits at each frequency δ_{R_i} is then translated to the Nichols chart plane as in Fig 5.14b. To achieve the desired performance, the plant templates at each design frequency should then be positioned above the relevant boundary in Nichols chart.

5.8.2 Disturbance Rejection Boundaries in Nichols Chart

Moving the disturbance rejection boundaries from the Bode plot, as in Figure 5.15a, to the Nichols chart, as in Figure 5.15c, can be done by modifying the mathematical representation of the disturbance rejection model to be suitable for the Nichols chart plane. The disturbance control ratio T_D for a two degrees of freedom system like the system in Figure 5.11 is

$$T_D(j\omega) = \frac{Y_D(j\omega)}{D(j\omega)} = \frac{1}{1 + L_D(j\omega)} \tag{5.26}$$

however, the mathematical format required for use in the Nichols chart is different as can be seen in Eqn. (5.18). To adjust the mathematical representation in Eqn. (5.26), the

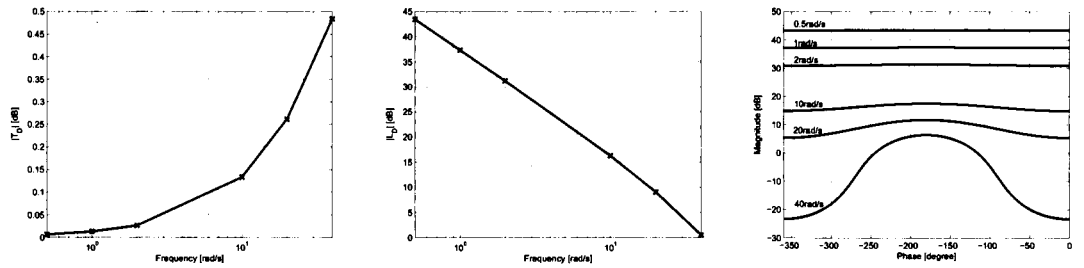

(a) Bode plot of $|T_D(j\omega)|$ (b) Bode plot of $|L_D(j\omega)|$ (c) Nichols chart of $l_D(j\omega)$

Figure 5.15: Constructing disturbance boundaries in Bode plot and Nichols chart

substitution $L_D(j\omega) = 1/l_D(j\omega)$ can be used. This substitution yields the form

$$T_D(j\omega) = \frac{l_D(j\omega)}{1 + l_D(j\omega)} \tag{5.27}$$

which can be translated to the Nichols chart plane. As the target of disturbance rejection is to reduce the effect of the disturbance signal $D(j\omega)$ over the specified bandwidth i.e., $|T_D(j\omega)| << 1$ (0 dB), or $|L_D(j\omega)| >> 1$, Eqn. (5.26) can be approximated as

$$|T_D(j\omega)| \approx \frac{1}{|L_D(j\omega)|} = |l_D(j\omega)| \tag{5.28}$$

Figure 5.15 shows the translation of the disturbance rejection boundary requirement from the Bode plot to the Nichols chart for the example [99]:

$$T_D(s) = \frac{s^2 + 70s}{s^2 + 140s + 5224} \tag{5.29}$$

5.8.3 Stability Boundaries in the Nichols Chart

The desired upper limit peak amplitude M_P in system time specifications as shown in Figure 5.16, which is drawn to represent the limits in Eqn. (5.13), is translated in the Nichols chart as a magnitude circle $M_L = 20\log_{10}(M_P)$ dB. To satisfy the stability bounds, the shaped nominal system loop transmission function $L_o(j\omega)$ should never be inside the peak magnitude circle M_L or exceed it. We will assume a template $P(j\omega)$ with arbitrary chosen nominal plant $P_o(j\omega)$ as shown in Figure 5.17. If the nominal plant $P_o(j\omega)$ is chosen to be at the least magnitude point of the template, and the maximum magnitude range for this template is V, the M_L circle should be stretched down by the magnitude V to make sure that the M_L circle will never be penetrated by any element of the plant template $\mathcal{P}(j\omega)$ during loop shaping.

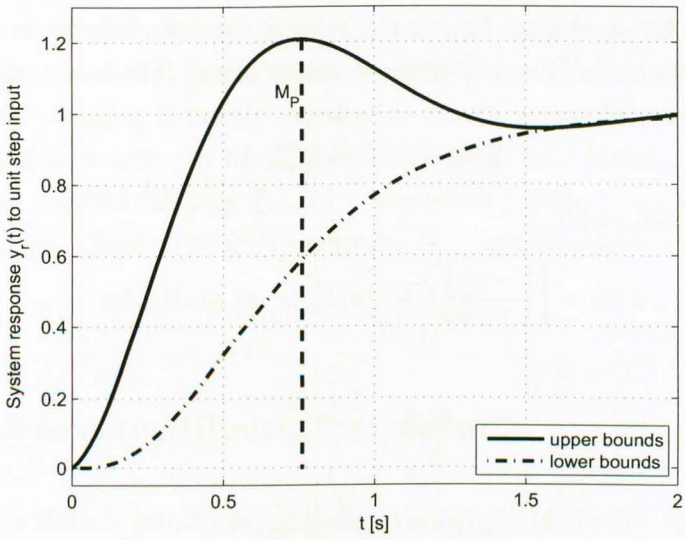

Figure 5.16: Desired peak magnitude for the closed loop system

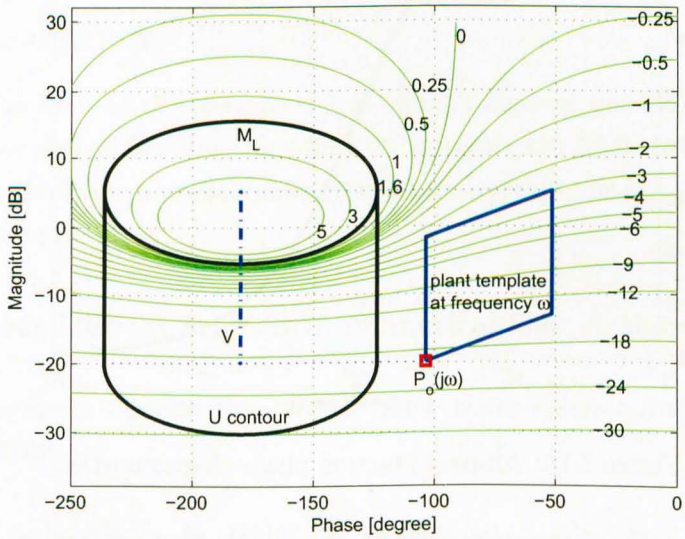

Figure 5.17: U-contour construction (stability contour)

5.9 NMP Plants

Any stable NMP plant with open loop transfer function $L(s)$ can be represented by a MP plant $L_m^{'}$ multiplied by an all-pass function $A(s)$. For example [99], let us assume a NMP plant with only one right hand zero $\frac{1}{\tau}$ in the complex plane. The loop transfer function of this plant can be expressed as

$$L(s) = (1 - \tau s)L_m^{'}(s) \tag{5.30}$$

Rearranging Eqn. (5.30) yields

$$L(s) = \left[\frac{1 - \tau s}{1 + \tau s}\right](1 + \tau s)L_m^{'}(s) = A(s)L_m(s) \tag{5.31}$$

where

$$A(s) = \frac{1 - \tau s}{1 + \tau s} \tag{5.32}$$

and

$$L_m(s) = (1 + \tau s)L_m^{'}(s) \tag{5.33}$$

It can be clearly seen through this example that $|A(j\omega)| = 1$ and $|L_m(j\omega)| = |L(j\omega)|$. Figure 5.18 shows the phase angle characteristics of the all-pass function $A(j\omega)$ for $\tau = 1$. Assuming

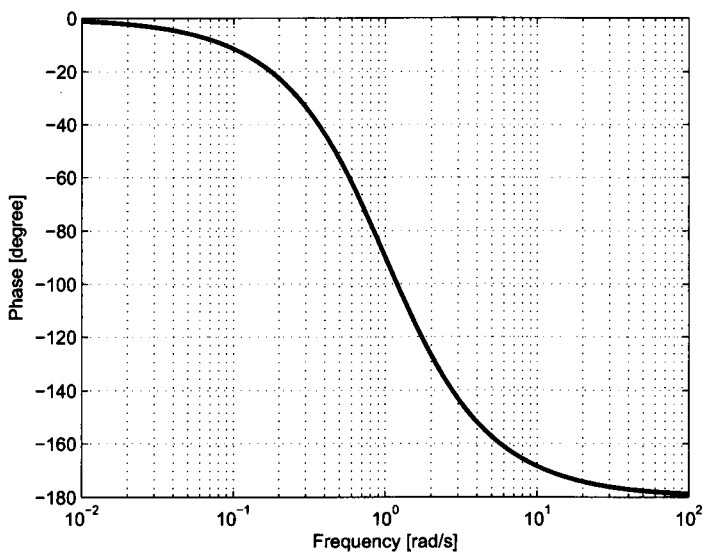

Figure 5.18: All-pass function phase characteristics

a NMP nominal plant P_o of uncertain plant $\mathcal{P}$, the nominal loop transmission function of a system which includes this plant can, by using the same principle as used in Eqn. (5.31), be expressed as

$$L_{mo}(s) = \frac{L_o(s)}{A_o(s)} \tag{5.34}$$

The phase of L_{mo} can be then calculated as

$$\angle L_{mo}(j\omega) = \angle L_o(j\omega) - \angle A_o(j\omega) \tag{5.35}$$

which means that, when a phase angle $\phi(j\omega)$ is needed for the design of $L_o(j\omega)$, a phase of $\phi(j\omega) - \angle A_o(j\omega)$ is needed for designing the equivalent MP loop transmission function $L_{mo}(j\omega)$. Because $\angle A_o(j\omega)$ is mostly negative as can be seen in Figure 5.18, a right shift of the QFT design boundaries in the Nichols chart plane by a phase $\angle A_o(j\omega)$ enables the designer to fit the nominal MP loop L_{mo} in a way which satisfies the phase requirements of the NMP plant $L_o(j\omega)$ [102]. The QFT controller $G(s)$ can be calculated as

$$G(s) = \frac{A_o(s)L_{mo}(s)}{P_o(s)} \tag{5.36}$$

5.10 The Discrete Hilbert Transform

Using the discrete Hilbert transform for shifting the phase of the NP QFT control method when a NMP plant is considered is novel in this thesis. This section presents a brief background about the Hilbert transform. In the early years of the twentieth century, the German mathematician David Hilbert proved that the Hilbert transform of the function $\cos(\omega t)$ is $\sin(\omega t)$ which is one of the properties of the Hilbert transform. The Hilbert transform $\hat{f}(t)$ of a real time function $f(t)$ is defined for a time vector t as

$$\hat{f}(t) = \frac{1}{\pi} P \int_{-\infty}^{\infty} \frac{f(\tau)}{t-\tau} d\tau \tag{5.37}$$

when the integral exists [103].

The P in the front of the integral in Eqn. (5.37) denotes the Cauchy principal value which expands the class of functions for which the integral exist [104]. It is normally not possible to calculate the Hilbert transform as an ordinary improper integral because of possible singularities at the pole $\tau = t$.

5.10.1 Discrete Hilbert Transform Numerical Calculations

Assuming that n is the discrete time vector and k is the discrete frequency vector, then defining the DFT as

$$F[k] = \sum_{n=0}^{N-1} f[n] e^{-\frac{2\pi k n j}{N}} \quad , \quad k = 0, 1, \ldots, N-1 \tag{5.38}$$

with its inverse

$$f[n] = \frac{1}{N} \sum_{k=0}^{N-1} F[k] e^{-\frac{2\pi k n j}{N}} \quad , \quad n = 0, 1, \ldots, N-1 \tag{5.39}$$

which is defines a periodic function with a period N. Eqn. (5.38) can be represented by its real and imaginary parts as

$$F[k] = F_{Re}[k] + jF_{Im}[k] \tag{5.40}$$

and from Eqn. 5.38

$$\sum_{n=0}^{N-1} f[n]e^{-\frac{2\pi knj}{N}} = \sum_{n=0}^{N-1} f[n]\cos\left(\frac{2\pi kn}{N}\right) - j\sum_{n=0}^{N-1} f[n]\sin\left(\frac{2\pi kn}{N}\right) \tag{5.41}$$

then from Eqn. (5.40) and Eqn. (5.41), the real and imaginary parts can be identified as

$$F_{Re}[k] = \sum_{n=0}^{N-1} f[n]\cos\left(\frac{2\pi kn}{N}\right) \quad , \quad F_{Im}[k] = -\sum_{n=0}^{N-1} f[n]\sin\left(\frac{2\pi kn}{N}\right) \tag{5.42}$$

Because $F_{Im}[k]$ contains sin functions, it can be concluded that $F_{Im}[k] = 0$ when $k = 0$ or $k = N/2$. The discrete Hilbert transform of the delta pulse function $\delta(t)$ gives $\frac{1}{\pi t}$ and the Fourier transform of the Hilbert transform gives the sign shift function $-j\text{sgn}(\omega)$, that is

$$\delta(t) \overset{\mathcal{H}}{\leftrightarrow} \frac{1}{\pi t} \overset{DFT}{\leftrightarrow} -j\text{sgn}(\omega) \tag{5.43}$$

where ω denotes the frequency domain representation of t. The discrete analog of the Hilbert transform for even N [103]

$$H[k] = \begin{cases} -j & , \ k = 1, 2 \\ 0 & , \ k = 0 \text{ and } k = N/2 \\ j & , \ k = N/2+1, \ldots, N-2, N-1 \end{cases} \tag{5.44}$$

so that $H[k]$ can be written in the form

$$H[k] = -j\text{sgn}\left(\frac{N}{2} - k\right)\text{sgn}(k) \tag{5.45}$$

The discrete inverse Fourier transform of the discrete Hilbert transform in Eqn. 5.45 is

$$h[n] = \frac{1}{N}\sum_{k=0}^{N-1} H[k]e^{\frac{2\pi kn}{N}} \tag{5.46}$$

$$h[n] = \frac{1}{N}\sum_{k=0}^{N-1} -j\text{sgn}\left(\frac{N}{2} - k\right)\text{sgn}(k)e^{\frac{2\pi kn}{N}} \tag{5.47}$$

$$h[n] = \frac{2}{N}\sum_{k=0}^{N-1} \sin\left(\frac{2\pi kn}{N}\right) \tag{5.48}$$

where $h[n]$ can be expressed in closed form as

$$h[n] = \frac{2}{N}\sin^2\frac{\pi n}{2}\cot \pi nN \tag{5.49}$$

The same derivation for odd N is given by

$$H[k] = \begin{cases} -j & , \ k = 1, 2, \ldots, (N-1)/2 \\ 0 & , \ k = 0 \\ j & , \ k = (N+1)/2, \ldots, N-2, N-1 \end{cases} \tag{5.50}$$

which can be written in the same closed form as in the even case but without canceling $\text{sgn}\frac{N}{2}$ so that

$$H[k] = -j\text{sgn}\left(\frac{N}{2} - k\right)\text{sgn}(k) \tag{5.51}$$

The discrete impulse response for odd N of the discrete Hilbert transform in Eqn. (5.43) is given by the discrete Hilbert transform of $H[k]$ in Eqn. (5.51) so that

$$h[n] = \frac{2}{N}\sum_{k=1}^{(N-1)/2}\sin\left(\frac{2\pi kn}{N}\right) \tag{5.52}$$

where the closed loop form of $h[n]$ can be expressed by

$$h[n] = \frac{1}{N}\left(\cot\left(\frac{\pi n}{N}\right) - \frac{\cos(\pi n)}{\sin\left(\frac{\pi n}{N}\right)}\right) \tag{5.53}$$

The discrete Hilbert transform of the sequence $\hat{f}$ is defined by the convolution on the form

$$\hat{f}[n] = \sum_{m=0}^{N-1} h[n-m]f[m] \tag{5.54}$$

When the DFT algorithm is used instead [105], the following relations can be obtained

$$f[n] \overset{DFT}{\rightarrow} F[k] \overset{\mathcal{H}}{\rightarrow} \hat{F}[k] = j\text{sgn}\left(\frac{N}{2} - k\right)\text{sgn}(k)F[k] \overset{DFT^{-1}}{\rightarrow} \hat{f}[n] \tag{5.55}$$

In practice, the Fast Fourier Transformation (FFT) [106] is generally used instead of the DFT to speed up the calculation speed in digital computers [107, 108, 109].

5.10.2 Using the Discrete Hilbert Transform for Estimating Equivalent MP Plant

This subsection presents a novel method to estimate an equivalent MP plant from a NMP plant by the discrete Hilbert transform. The phase difference between the NP plant and the estimated NMP one is essential of applying the novel NP QFT method to NMP plants as can be seen in Chapters 7 and 9. The nominal plant may be conventionally chosen as the centre of area of each frequency template as in Figure 5.19. If the nominal plant locus is found to be that of an unstable or NMP plant (ie. *unstable locus*) then the phase shift required to produce a stable MP locus must be determined. The QFT loop-shaping process then requires that the QFT boundaries are shifted by this phase to align them with the ammended stable MP nominal plant [102]. This design stage accordingly determines the required phase shift at the design grid frequencies. In case of stable MP systems, the frequency response magnitude determines a unique phase, and the phase of the frequency response determines a unique magnitude to within a scale factor [108]. Consider the FRF of a nominal plant

$$P_o(e^{j\omega}) = \left|P_o(e^{j\omega})\right| e^{j\angle P_o(j\omega)} \tag{5.56}$$

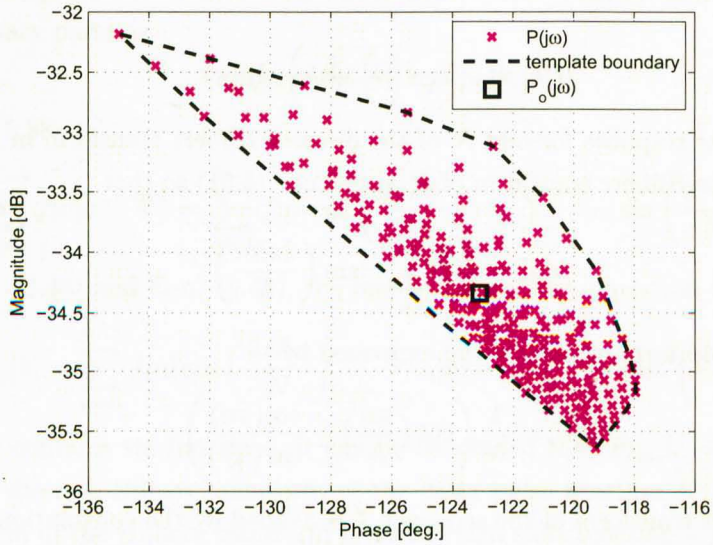

Figure 5.19: Bode plot of nominal plant of a template

for which we have the logarithmic equation

$$\log_e P_o(j\omega) = \log_e |P_o(j\omega)| + j\angle P_o(j\omega) \tag{5.57}$$

To determine the phase $\angle P_{mo}(j\omega)$ of a stable MP FRF with the same magnitude as $|P_o(j\omega)|$, the Hilbert transform is applied to the real component of $\log_e |P_o(j\omega)|$ to determine the phase as the required associated imaginary component thus

$$\angle P_{mo}(j\omega) = \mathcal{H}\left\{Re\left\{\log_e |P_o(j\omega)|\right\}\right\} \tag{5.58}$$

where $\mathcal{H}$ is the Hilbert transform. From this the required MP nominal system $P_{mo}(j\omega)$ can be formed as

$$P_{mo}(j\omega) = |P_o(j\omega)|\, e^{j\angle P_{mo}(j\omega)} \tag{5.59}$$

The required boundary phase shift form the original $P_o(j\omega)$ is thereby given in terms of the all-pass function $A(j\omega)$ by

$$\angle A(j\omega) = \angle P_o(j\omega) - \angle P_{mo}(j\omega) \quad \text{and} \quad |A(j\omega)| = 1 \tag{5.60}$$

The stable MP system nominal loop transmission locus can thus be used in the QFT design instead of the original NMP version. The shaped locus may then be converted back through multiplication by the all-pass phase shift component $A(j\omega)$ giving

$$L_o(j\omega) = A(j\omega)L_{mo}(j\omega) \tag{5.61}$$

which may then be used to obtain the QFT controller as

$$G(j\omega) = \frac{L_o(j\omega)}{P_o(j\omega)} \tag{5.62}$$

5.11 QFT Prefilter Design

When the plant templates are fitted to the design boundaries in the Nichols chart, this guarantees that the variation of the system output, when the plant magnitude changes due to the nonlinearity, is limited within the desired $\delta_R(j\omega_i)$. As can be seen in Figure 5.20, the magnitude difference between $M_{max}(j\omega_i)$ and $M_{min}(j\omega_i)$ which is $\delta_L(j\omega_i)$ is still smaller than $\delta_R(j\omega_i)$ as expected, however, the position of the chosen loop transmission needs to be shifted inside the the designed close loop boundaries $T_{R_U}(j\omega_i)$ and $T_{R_L}(j\omega_i)$. The prefilter is designed to do this shift. The first step in the design of the prefilter is to find the values of

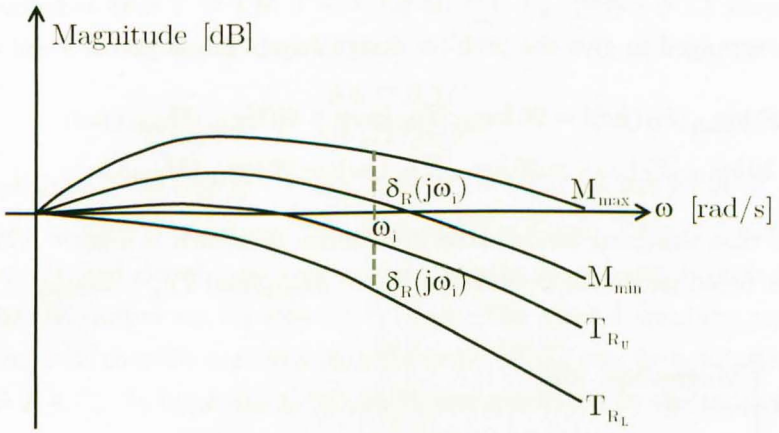

Figure 5.20: System requirements on Bode plot

M_{max} and M_{min} from the Nichols chart for each template as in Figure 5.21. The values of

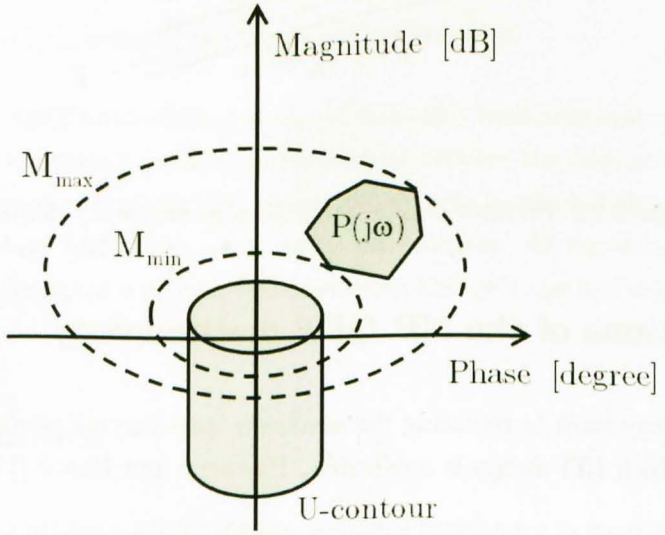

Figure 5.21: Prefilter determination in Nichols chart

M circles which represent the closed loop without the prefilter are

$$M(j\omega) = \frac{L(j\omega)}{1 + L(j\omega)} \tag{5.63}$$

however, the tracking control ratio $T_R(j\omega)$ is

$$T_R(j\omega) = \frac{F(j\omega)L(j\omega)}{1 + L(j\omega)} \tag{5.64}$$

Writing Eqn. (5.64) in units of decibels yields to

$$20\log_{10}|T_R(j\omega)| = 20\log_{10}|F(j\omega)| + 20\log_{10}|M(j\omega)| \tag{5.65}$$

which can be rearranged to give the prefilter design requirements as

$$20\log_{10}|F_U(j\omega)| = 20\log_{10}|T_{R_U}(j\omega)| - 20\log_{10}|M_{max}(j\omega)| \tag{5.66}$$

$$20\log_{10}|F_L(j\omega)| = 20\log_{10}|T_{R_L}(j\omega)| - 20\log_{10}|M_{min}(j\omega)| \tag{5.67}$$

The prefilter is then designed inside those boundaries as shown in Figure 5.22. A transfer function $F(s)$ is fitted inside the boundaries $T_{R_U} - M_{max}$ and $T_{R_L} - M_{min}$.

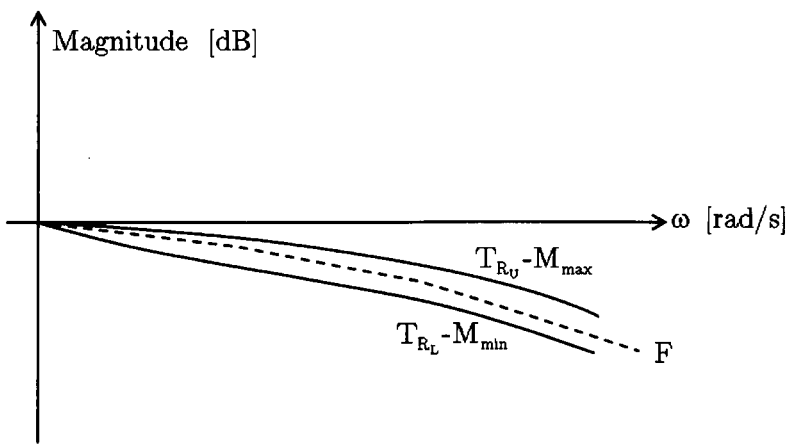

Figure 5.22: Prefilter design boundaries in frequency domain

5.12 Limitations of the NP QFT methodology

The QFT methodology built in replacing the nonlinear time-varying plant set by equivalent LTI plant set for which LTI design is applicable. Horowitz and Banos [110] justifying that by the following:

A concious mapping of a convex compact set of a Banach space into itself has a fixed point according to the Schauder fixed point theorem. If a set $\mathcal{T}$ is compact and convex then

any (R, W) pair are picked and define the mapping over $\mathcal{T}$ as

$$\phi(T) = \frac{FP(T,R)G}{1 + P(T)G} \tag{5.68}$$

where $P(T,R)$ is the mapping from $\mathcal{T} \times \mathcal{R}$ to $\mathcal{P}_e$, given by $P(T,R) = TR/U$, where U is the Laplace transform of $u = W^{-1}y$, and $Y = TR$ is the Laplace transform of y. In the mapping ϕ, since R is fixed and U is a function of T, $\phi(T)$ can be expressed as

$$\phi(T) = \frac{FGTR/U(T)}{1 + GTR/U(T)} \tag{5.69}$$

To prove that $\phi(T)$ maps $\mathcal{T}$ into itself, consider $TR/U = Y/U$, $P \in P_e$. However, F and G have been designed so that $Y = TR$, $T \in \mathcal{T}$ for all $P \in \mathcal{P}_e$. Hence $\phi(T)$ maps every T into $\mathcal{T}$, and thus ϕ has a fixed point T^*, with

$$T^* = \frac{FGT^*R/U^*}{1 + GT^*R/U^*} \tag{5.70}$$

giving the result that $U^* = G(FR - T^*R)$. Here $U^* = U(T^*)$ is the input $u^* = W^{-1}(y^*)$ in the time domain, being y^* the inverse transform of $Y^* = T * R$. Thus, Y^* is also the output of the nonlinear original closed loop system and since the fixed point T^* is in the set $\mathcal{T}$, the output is in the OK output set for this (R, W) pair. The same ϕ mapping can be made for all (R, W) pairs. It is therefor essential that the same (F, G) pair be a solution of the LTIE problem for all $P \in \mathcal{P}_e$. In brief, the LTIE set $\mathcal{P}_e$ was generated by the following steps:

1. $Y = RT$ for each $R \in \mathcal{R}$ and $T \in \mathcal{T}$;
2. For each such y which is the inverse Laplace of Y, $u(t) = W^{-1}y(t)$ is found for each $W \in \mathcal{W}$;
3. $P(s) = Y(s)/U(s)$, being U the Laplace transform of u.

In general, the QFT methodology is limited to weakly nonlinear systems in which the size of the nonlinearity template is suitable to be inserted between the relevant design boundaries. Obviously, if the template is bigger that the the design area in which it should be in a problem, the QFT methodology will fail to solve such that problem. As the driveline speed control problem is not considered as a very hard nonlinearity, the QFT method can be used effectively in this problem.

5.13 Conclusions

- One of the important reasons of using feedback techniques in control design is reducing the effect of the parameters variation of the system during operation. One of the techniques for achieving that purpose is the QFT method developed by Horowitz.

- Plant uncertainty is a description of the areas in which the identified plant parameters are found in. Uncertainty can be classified, according to the technique by which its boundary is calculated, as either structured or unstructured uncertainties

- QFT time domain requirements are chosen according to the required performance of the controlled system. These including tracking boundary and disturbance rejection boundary.

- There is no one to one translation from time domain performance to frequency domain characteristics but there are good translations which can be used effectively in the design process.

- One of the basic sequences of the QFT design methodology is to map the tracking boundaries, disturbance rejection boundaries and stability boundaries to Nichols chart. Nichols chart provide a graphical representation of gain versus phase of the systems.

- Any staple NMP plant open loop transfer function can be represented by a MP plant multiplied by an all-pass function. This fact enables the designers to apply the QFT methodology in NMP plants, however, parametric models only can be used with this conventional technique validated by Horowitz.

- Discrete Hilbert transform can provide a way of obtaining an equivalent MP plant of an original NMP plant. This technique can be used for obtaining an equivalent MP plant of an original NMP plant when NP identified models are used. Combining the discrete Hilbert transform with the QFT to control a NP model is novel.

- QFT prefilter is designed to position the chosen loop transmission locus inside the designed close loop boundaries.

Chapter 6

Parameter Space Engine Control Based on NP Modelling

6.1 Introduction

Regulating the IC engine speed about a certain set point despite the applied loads to the engine is essentially the problem of idle speed. Loads can be internal loads coming from the vehicle driver actions like switching on windshield wipers, car cassette players, or lights. The PI controller is a suitable structure for good tracking and disturbance rejection purposes, since the integral action ensures zero steady state error and the proportional action controls the speed of response.

In this chapter, the idle speed feedback control system is discussed in section 6.2. Then, the NP identification technique and the identification data are presented in section 6.3. The details of the parameter space control technique is covered in section 6.4 and the obtained controller performance is shown in section 6.5. Finally, the chapter conclusions are given in section 6.6.

6.2 The Idle Speed Feedback Control System

The vehicle engine idle speed problem is one of the active driveline problems in automotive control. An effective method of tuning the idle speed PID controllers was provided by Kokotovic and Rhode [111], Hrovat and Johnson [112] respectively.

The Linear Quadratic (LQ) based optimisation was applied to the idle speed problem by Powell and Powers [113], Powers, Powell and Lawson [114], Morris and Powell [115], Takahashi, Ueno, Yamamoto, and Sanbuichi [116], Baumgartner, Geering, Onder and Shafal [117], Abate and DiNunzio [118] and finally, Fraser, Mills and Hrovat [119].

$\mathcal{H}_\infty$ methods were also applied to the idle speed problem by William [120] and by Carnevale and Moschetti [121]. The main disadvantage in the presented methods is that, the adjustments of frequency weighting functions needs some trial and error to get the correct weighted sensitivity functions. Camevale and Moschetti [121] presented an $\mathcal{H}_\infty$ controller with a faster time response than the LQ equivalent one, but this fast response was noisier than the corresponding LQ controller response. However, the $\mathcal{H}_\infty$ controller presented by Williams and Hrovat *et al.* [120] improved the robustness compared with Hrovat and Powers's PID controller, limited model variations are allowed to maintain its stability. The μ-synthesis technique was used by Hrovat and Bodenheimer [122] to present a robust idle speed controller. They tested their controller in two sufficiently different idle speed operation points. As hard constraints on the spark advance were presented, the engine became unstable.

In addition to the parameter space method, which will be discussed in section 6.4, many other approaches have been applied to the idle speed problem such as the QFT method in Jayasuriya's paper [123]. Jayasuriya presented a frequency domain design methodology for disturbance rejection in a Multi Input Single Output (MISO) plant which has a special parallel structure. Also, the Kharitonov theorem in Olbort's paper [124] which contains the development of an analytical approach for the synthesis of a proportional PID throttle regulated idle speed control system that possesses robust stability properties in the presence of parameter variations due primarily to changing system operating point. Fuzzy logic was used in Dosio's paper [125]. The method has the advantage of not requiring the knowledge of a model of the controlled object and is also more robust and flexible than traditional approaches. Finally, neural networks technique was presented in Puskorius's paper [126] where network control achieved by 10 nodes and 100 trainable connections network. The paper describes the development of recurrent neural network controlled for an automotive engine idle speed control problem.

The presented novelty in this chapter is that new combination between NP system identification and the parameter space method. The benefits of the presented technique can be described by:

1. No limited length parametric model for the IC engine is needed for the design, so more system dynamics are presented;
2. No IC engine model structure selection is needed at all. This saves a lot of designer efforts and time.

which make the technique more suitable for industrial applications.

The IC engine idle speed control system is usually based on feedback rather than feed-forward control. The main reason for that is the relatively high cost of the sensors needed to

implement a feedforward controller. Even if a feedforward controller is used, a feedback loop must be included to allow the controlled system to respond correctly to the unpredictable behaviour of torque disturbances and the nature of the uncertainties in the engine model. Figure 6.1 displays how the conventional idle speed feedback control system works. The error signal is calculated by subtracting the actual engine speed from the demanded speed. This error signal is passed through a controller G which estimates the control variable (ABV opening). The ABV opening can vary the unloaded engine speed up to 3000 RPM to meet the demand by controlling the amount of air entering the engine as discussed in section 8.7 of the experimental setup in Chapter 8. The ABV opening is expressed in this thesis in terms of percentage duty cycle, which varies between 0.0 for fully closed and 1.0 for fully opened. Actually, spark ignition timing via the spark plugs is another control variable. The

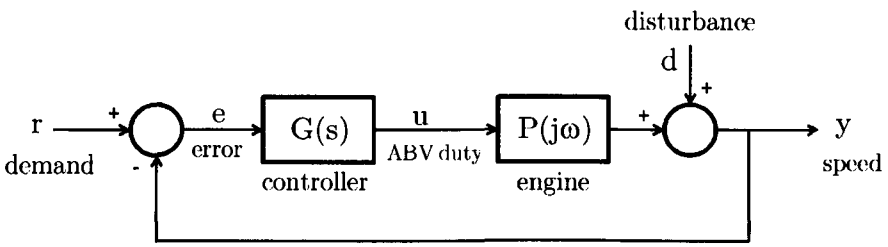

Figure 6.1: The block diagram of the idle speed control structure

spark command always has instantaneous effect of the compressed mixture inside the cylinder, but in some spark ignition engines the spark advance can be considered as a limited effect parameter in idle speed problem [127, 128]. Furthermore, if the spark is to be used, it must be set sub-optimally under normal operating conditions to provide a torque-reserve, which therefore reduces fuel economy. Fuel can be considered as a control variable in the idle speed problem [117]. However, Air-Fuel Ratio AFR regulation is essential for emissions, and therefore inefficient for use in speed regulation. In the experimental work presented in this chapter, both spark timing and AFR are ignored due to their small effect and inefficiency on the engine speed compared with the ABV duty. The spark timing in these studies is fixed at 28^o before top dead centre during both identification and control processes. Therefore, a SISO control system configuration is considered with the ABV duty as an input, and engine speed in RPM as an output and feedback signal.

6.3 NP IC engine Identification

A random walk signal has been used as an excitation signal for identifying the engine response. As discussed in subsection 2.2.3. The choice of the random walk signal is made to cover the engine nonlinear behaviour. The I/O identification data is displayed in Figure 6.2. NP

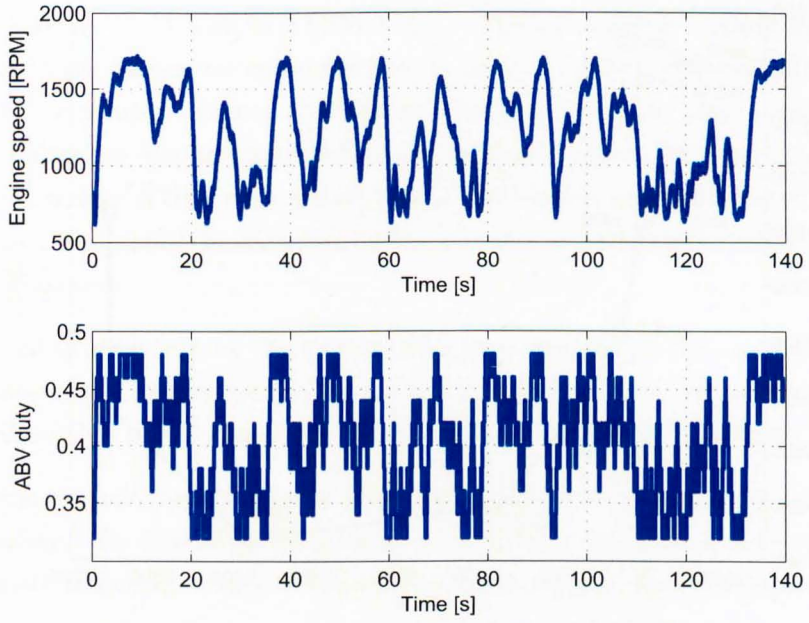

Figure 6.2: ABV duty to engine speed identification signals

identification using local frequency smoothing estimation method is used to identify a NP model of the engine. The method is described in subsection 3.5.3 of Chapter 3. A frequency set $\omega = \{0.1, 0.5, 1, 2, 3, 4, 5, 6, 7, 8, 9, 10, 12\}$ rad/s was selected to cover the system bandwidth and the obtained model is displayed in Figure 6.3.

6.4 Parameter Space Design Approach

Parameter space methods present a graphical interface for designing low order controllers. Parameter space methods extend back to Niemark [129, 130] when he used it for solving the problem of distribution of roots and polynomials and the structure of the D-partition of the space of polynomials and diagram of Vishnegradskii. Mitrovic [131], in 1959, introduced the technique as graphical analysis for controlling of feedback systems. However, early clear representations of the method were in Thaler and Brown [132] in 1960, Aizerman [132] in 1963, Siljak in [133] 1964 and Porter [134] in 1968. In 1980, Ackermann [135] presented a parameter space approach based on Kharitonov's theorem to the robustness of relative stability to transfer function parameters. Cook [136] started, in 1966, to use gain and phase margins requirements with the parameter space control design method. Cook used parametric models only to verify his technique. Chang and Han [137, 138] presented results, associated with Cook's work, for controlling systems with adjustable parameters. In Like Cook's paper [136], parametric transfer functions examples only are presented. In 1994, the parameter space

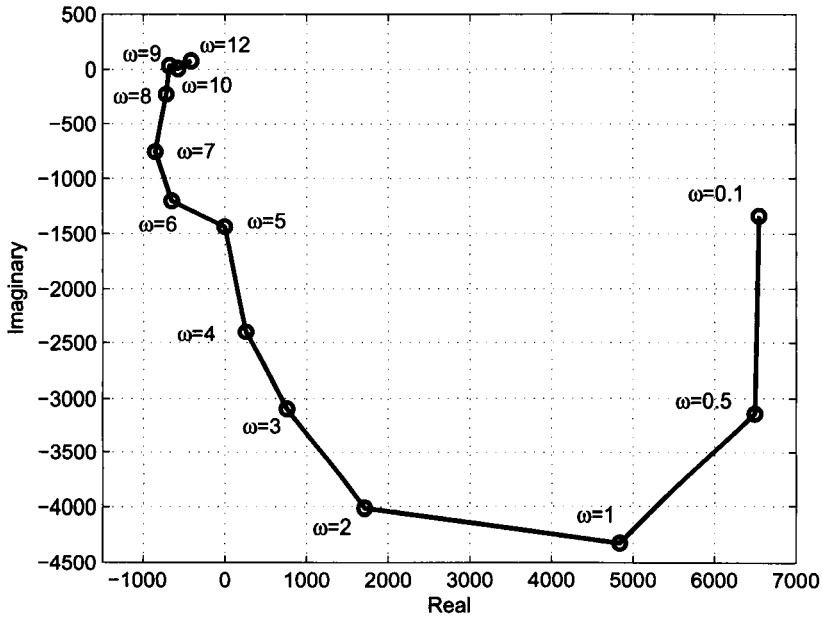

Figure 6.3: Nyquist plot of the NP IC engine model [RPM]

control design method was extended by Shafiei and Shenton to design a PID controller for relative stability in irrational systems including the full treatment of the singular conditions which were presented in Shafiei and Shenton [139] based on Shenton and Shafiei [140]. Gain and phase margin criteria and treatment of singularity conditions for parameter space PID design for simultaneous bandwidth was covered extensively in [141]. Besson and Shenton [142] developed a fixed order irrational SISO $\mathcal{H}_\infty$ parameter space method where specifications for a given weighting function are mapped into a parameter plane. In this method, many specifications can be taken in account at the same time during the design. This has been done by superimposing the design regions and set the parameters inside the common area that satisfies all design requirements. Similar results were reported by Saeki [143] in 1994 and subsequently been developed for rational PID controller [144] in 2000.

A parameter space frequency response method for irrational SISO robust performance design of fixed low order controller was first presented by Besson and Shenton [145] in 1999 and extended by them in 2000 to cover the irrational MISO problem [146]. In 1989, Siljak presented a survey paper in which, he reviewed the contributions to the parameter space methods for analysis and design of robust control systems. In 2001, Guvenc and Ackermann compared and established links between the parameter space method of the parametric approach and frequency domain methods. He concluded that it is important for the designers to be able to compare these two approaches and form links between them to combine the useful features of both them. A year later, Another survey of the parameter space control method is

presented by Ackermann [147]. Since then, using the parameter space method is continued. It has been used by Saeki [148] in a MIMO $\mathcal{H}_\infty$ frequency response method in 2006. Muhler [149] developed the parameter space method, in 2002, to obtain rational MIMO parameter space design boundaries. Besson [150] shows that the ability to map a number of single sensitivity constraints can be a good advantage because it allows the designer to graphically observe which weight is over constrained. Some graphical interface packages, such as [151], were developed to simplify the technique to the user but unfortunately these packages cannot deal with NP models.

The benefits of combining the NP identification with the parameter space technique is avoiding concentrating the system behaviour in a limited length vector. Also, the information given by a linear NP model is not constrained into a small set of parameters.

The frequency response parameter space method presents a mature tool for nonparametric control design. To determine the relative characteristic equation of the controlled system the appropriate frequency response function of the controlled system is equated as in [141] as:

$$\frac{-K_d\omega^2 + K_p j\omega + K_i}{j\omega} G(j\omega) = a + jb \tag{6.1}$$

where $a+jb$ is a specific point in the complex plane. By increasing ω from 0 to ∞ in Eqn.(6.1) a locus is traced out in parameter space for the point $a + jb$. If K_d is set to zero, K_i and K_p can be determined as follows:

$$K_i = Re\left[\frac{a+jb}{G(j\omega)} j\omega\right] \quad , \quad K_p = \frac{1}{\omega} Im\left[\frac{a+jb}{G(j\omega)} j\omega\right] \tag{6.2}$$

A parameter space boundary for a chosen gain margin GM in dB can be mapped by setting $a+jb$ to $-10^{-GM/20}$, and a chosen phase margin PM by setting $a+jb$ to $-\cos(PM) - j\sin(PM)$. Taken with the parameter space axes the boundaries determine the feasible regions to achieve the required relative stabilities [141]. K_i and K_p can be determined simultaneously to satisfy both required gain and phase margins by superimposing both the GM and PM boundaries in the parameter space. Further the boundaries are parameterised with frequency which represent the achieved phase crossover frequency and gain crossover frequency when points on the parameter space boundaries are chosen. Interrogating the frequencies of points on the boundaries accordingly gives a means of taking bandwidth considerations into account in the parameter space design method [141]

For a GM of 34 dB and a PM of 76° the parameters K_p and K_i loci can be drawn as in Figure 6.4. A PI controller which satisfies both gain and phase loci and which maximises K_i can be chosen as

$$G = K_p + \frac{K_i}{s} \quad , \quad \text{where} \quad K_p = 2.53 \times 10^{-5} \quad \text{and} \quad K_i = 6.32 \times 10^{-5} \tag{6.3}$$

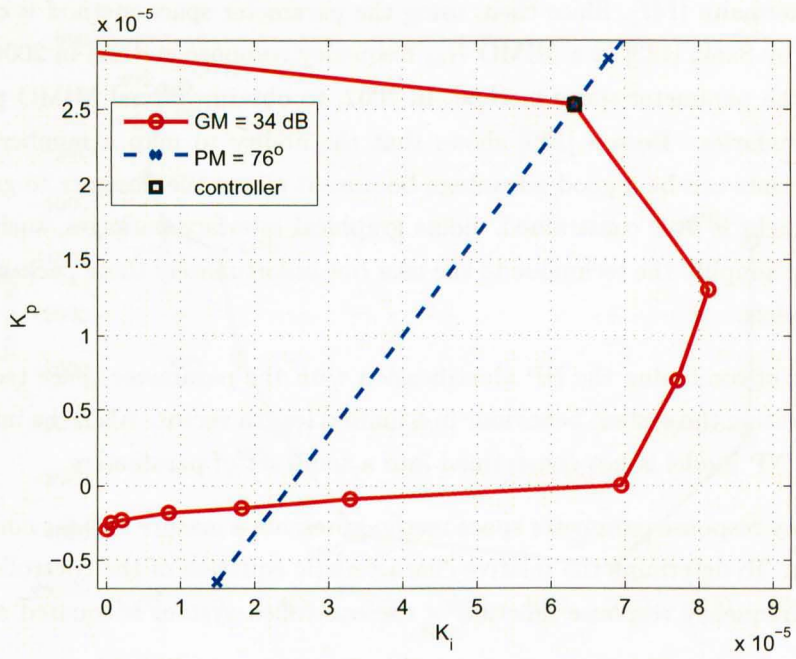

Figure 6.4: PI controller selection from parameter space

6.5 Results and Discussion

The controlled system structure can be seen in Figure 6.1, where the reference input r is the demanded engine speed and the controlled variable y is its actual response. The error signal is $e = r - y$ and the controller action u is the ABV duty which is the plant input signal. Testing the controlled system tracking for different engine speed demands as in Figure 6.5 shows a quick response but an overshoot can be noticed easily. Although, the idle speed problem is not mainly a tracking performance problem, tracking performance is checked to ensure that the controller is stable at different speeds.

The idle speed problem is mainly a disturbance rejection problem. When the vehicle driver switches on the air condition in his car, the mechanical significance of this is that additional load (torque) is suddenly added to the engine. When the device is turned off, the engine experiences a negative load. In the same sense, lights, electric windows and power steering are possible disturbances. The required controller should be effective enough at keeping the engine speed near its idle value which is required as 880 RPM to be applied in control problem in this chapter. The dynamometer in the setup allows different loads to test the controller performance against disturbances. As can be seen in Figure 6.6, the PI obtained controller is able to reject torque disturbances in an effective way.

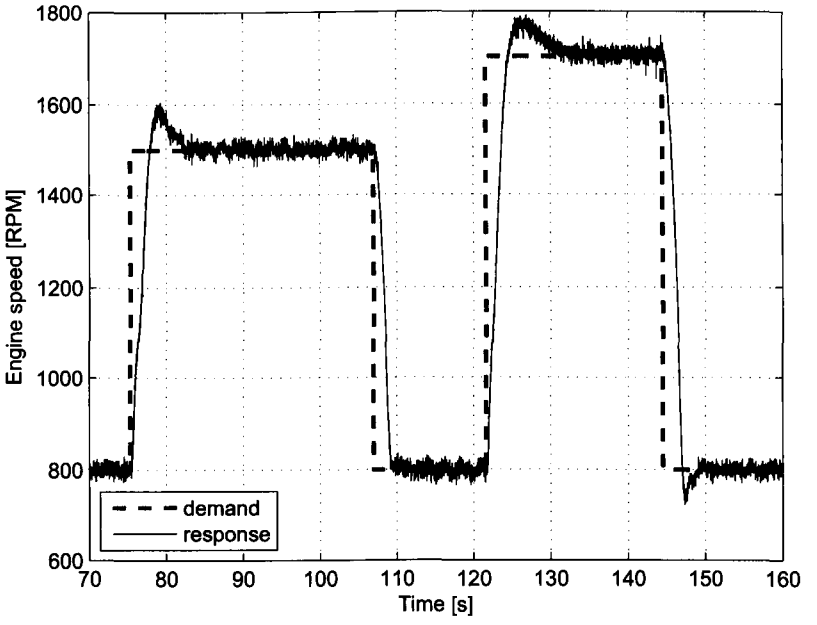

Figure 6.5: Controlled system response to speed demand

6.6 Conclusions

- A novel NP parameter space controller design method is presented for use in the IC engine idle speed control problem. NP model is obtained by local frequency smoothing estimation method. An identification frequency set is selected to cover the system bandwidth.

- The usual advantages of the parameter space technique is obtained by superimposing GM loci with PM loci. The parameter space locus based on a NP FRF model for the IC engine for a certain GM and PM is drawn, then, a PI controller which satisfies both gain and phase loci is chosen.

- An experimental implementation of the NP parameter space technique was applied to the idle speed control of the 1.6 L Ford Zetac port-fuel injection spark ignition engine of the University of Liverpool set up in the low inertia dynamometer. The experimental validation showed the advantages of using this closed loop control technique for the problem in terms of accurate tracking and efficient disturbance rejection.

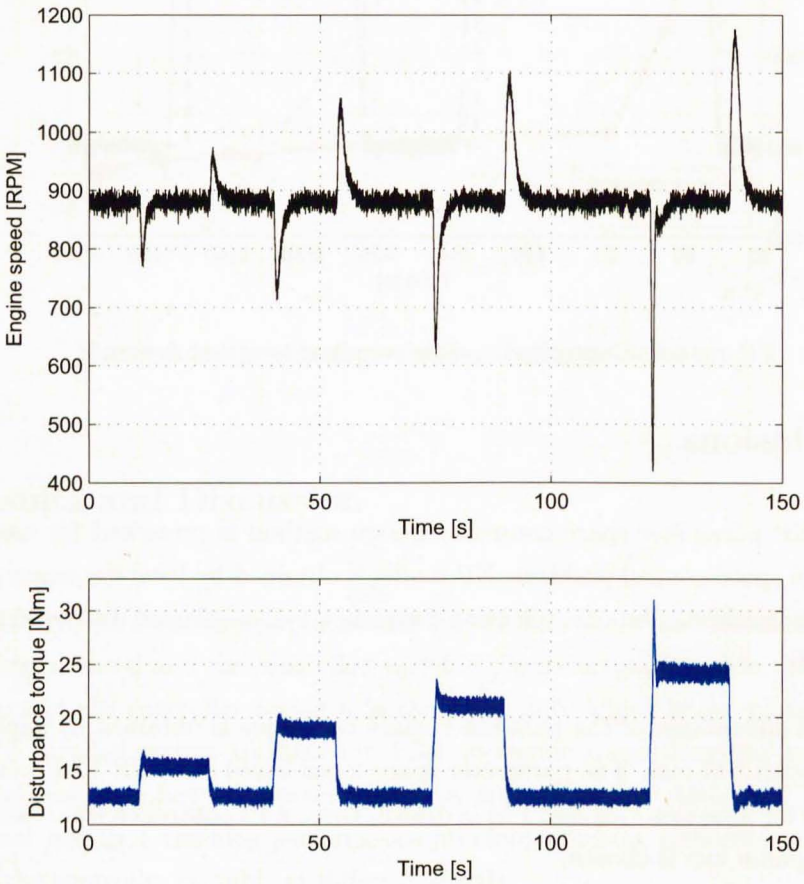

Figure 6.6: Controlled system response to disturbance torque

Chapter 7

Simulation Driveline Speed Control by NP QFT

7.1 Introduction

In the basic linear QFT technique [99] the closed loop specifications are translated into constraints ('QFT bounds') in the Nichols chart to specify the allowable range of the nominal open loop responses. The design is completed when a nominal loop transmission is shaped which achieves nominal closed loop stability and lies within the QFT bounds. In QFT it is usual to then use any remaining design freedom to minimise the gain especially at high frequency. The uncertainty in the transmission from command signal to controlled output is minimised so as to allow the design of a feedforward filter for a controller to achieve specified tracking response characteristics. Historically QFT was developed as a heuristic engineering technique, however, the work of Banos and Bailey [152] has given this a rigorous mathematical justification [153]. The important feature of linear or nonlinear QFT to tailor the design of two-degrees of freedom tracking control systems makes it a particularly suited to the driveline control problem.

The QFT technique thus allows the design of a feedback controller G and a prefilter F to satisfy desired specifications as shown in Figure 7.4. As the system investigated in this thesis is nonlinear, it is possible to associate a different FRF with each different input applied, and so when using a nonlinear QFT approach, a LTIE set $\mathcal{P}$ [100] covering all such possible FRFs is required to represent the nonlinearity.

This chapter discusses the specifications in the QFT formulation in section 7.2, then system I/O data collection in section 7.3. Section 7.4 explains the NP identification of LTIE set. Setting of QFT stability, tracking and disturbance bounds is presented in section 7.5. Section 7.6 shows the using of the discrete Hilbert transform for determining a stable MP

driveline nominal plant from the NMP driveline nominal plant. Section 7.7 presents the open loop shaping process. The controller prefilter design is presented in section 7.8. The chapter results and discussion are displayed in section 7.9. Finally, the chapter conclusions are presented in section 7.10.

7.2 Specifications in the QFT Formulation

Generally, objective of the QFT design specifications in the frequency domain is to synthesize a controller $K(s)$ such that robust stability, tracking performance, and disturbance attenuation are met these specifications. Specifications in the QFT formulation are then conveniently expressed by the following three frequency response constraints $\forall_{P(j\omega)} : P(j\omega) \in \mathcal{P}$, [154]:

1. Robust stability margin

$$\left| \frac{L(j\omega)}{1 + L(j\omega)} \right| \leq M_L \tag{7.1}$$

2. Tracking performance

$$T_L(j\omega) \leq \left| \frac{F(j\omega)L(j\omega)}{1 + L(j\omega)} \right| \leq T_U(j\omega) \tag{7.2}$$

3. Disturbance attenuation performance

$$\left| \frac{1}{1 + L(j\omega)} \right| \leq T_D(j\omega) \tag{7.3}$$

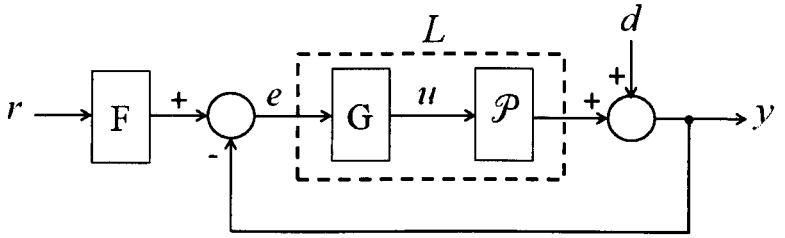

Figure 7.1: QFT structure

where $L(j\omega) = G(j\omega)P(j\omega)$, M_L is a constant positive stability bound, $T_L(j\omega)$ and $T_U(j\omega)$ are positive lower and upper tracking bounds resp. and $T_D(j\omega)$ is a positive disturbance bound.

The QFT design procedure applied on the driveline presented here can be described by the following procedural stages:

1. I/O data collection

2. NP identification of the LTIE set
3. Setting of stability, tracking and disturbance bounds
4. Determination of stable MP nominal system
5. Open loop shaping
6. Prefilter design

7.3 I/O Data Collection

A rich set of typical input signals which are sufficient to cover the full input operating range is first selected. The model parameters has been chosen to represent a typical European midrange passenger vehicle as seen in Table 7.1. Some of these parameters are taken as the parameters of Lagerberg [41]. The input signals, which in the real driveline case are the throttle (accelerator) pedal inputs of a wide range of different typical driver types, are represented for the simulation study by the output signals from a second order filter of the form $\frac{\omega_0^2}{s^2+2\zeta_0\omega_0 s+\omega_0^2}$; $\zeta_0 \in [0.5912, 1.2]$ and $\omega_0 \in [2.6667, 3.3832]$ subject to a set of initial step-up and step-down inputs ranged from 50 N/m to 150 N/m. The choice of torque range is based on of the experimental experience with a the University of Liverpool Powertrain Laboratory Ford Mondeo vehicle representing a typical European sedan, and the ranges of ω_0 and ζ_0 are selected to cover the range of possible paths of the accelerator pedal torque demand and release by different driver types. A total of 525 different input signals are thus simulated as shown in Figure 7.2.

7.4 NP Identification of LTIE Set

An estimate of the plant $P(j\omega)$ can be made as a discrete FRF, obtained from the DFT of sufficiently rich representative input $u = (u[1], \ldots, u[N])$ and output $y = (y[1], \ldots, y[N])$ data. In the present method the input and output data sequences are accordingly first transformed by the DFT into the frequency domain as $\mathcal{F}_D u = U \;;\; U = (U[1], \ldots, U[N])$ and $\mathcal{F}_D y = Y \;;\; Y = (Y[1], \ldots, Y[N])$ corresponding to the frequencies $\omega = (0, \frac{2\pi}{TN}, \ldots \frac{2\pi(N-1)}{TN})$

Since the transformed signal is necessarily a signal of limited support, N is bounded, and any obtained FRF is susceptible to leakage noise, and accordingly a local frequency smoothing technique [63] is found useful in reducing the resulting noise in the FRF estimate. From the initial unsmoothed U and Y data corresponding to the frequency vector ω as obtained directly by DFT, the local smoothing technique, described in section 3.5.3 of Chapter 3, allows the interpolation of a smoothed FRF vector for a frequency vector Ω of arbitrary frequencies

Table 7.1: Model parameters

Parameter	Value
A	3 m^2
b_e	0.05 N m s/rad
b_t	0.8 N m s/rad
b_{eq}	5.6 N m s/rad
b_{co}	0.1 N m s/rad
C_{cl}	10 N m s/rad
C_{bl}	1 N m s/rad
C_s	0 N m s/rad
C_d	0.4 Ns^2/kg m
J_e	0.3 kg m^2
J_t	0.01 kg m^2
J_{co}	0.01 kg m^2
J_v	140 kg m^2
J_w	1.2 kg m^2
K_{cl}	527.12 N m/rad
K_{cl_1}	10 N m/rad
K_{cl_2}	527.12 N m/rad
K_{cl_3}	10^10 N m/rad
K_{bl}	10^4 N m/rad
K_s	10^4 N m/rad
m_v	1200 kg
m_w	68 kg
r_w	0.304 m
t_r	13.873
α_{cl_1}	0.0087 rad
α_{cl_2}	0.0175 rad
α_{bl}	0.0646 rad
ρ	1.2 kg/m^3
τ_d	0.15 s

within the range of the unsmoothed frequency vector. Smoothing then is achieved by use of a weighting function to strengthen the spectrum of the selected frequencies and reduce the leakage errors from surrounding frequencies. This use of weighting functions in the frequency domain contrasts in particular with the Blackman-Tukey approach where the signal spectrum is smoothed by a wide window in the time domain. In the proposed design procedure in this thesis, the ability to choose the arbitrary frequencies of Ω about which the smoothing takes place, is an important requirement of the QFT loop-shaping method. The frequencies are those corresponding to those of the manipulated templates and they should cover the plant bandwidth. Guides for the choice of these frequencies are given in [99].

Thus starting with the required frequency vector of distinct increasing frequencies $\Omega =$

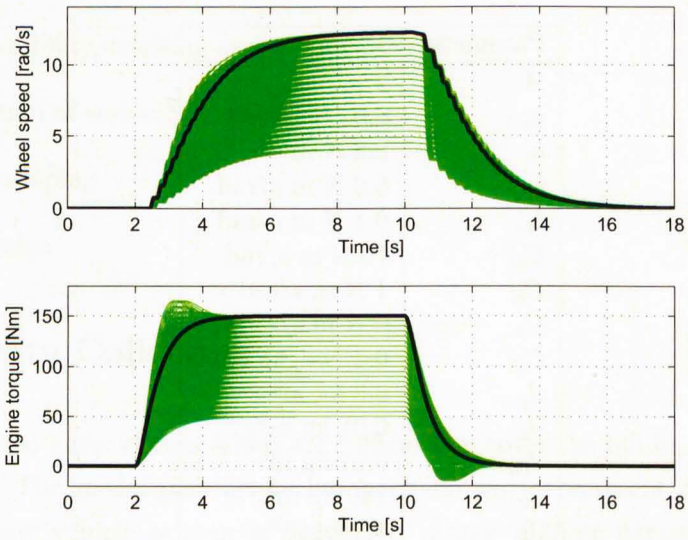

Figure 7.2: I/O data sets for typical inputs with acceptable outputs

$(\Omega[1], \Omega[1], \ldots, \Omega[M])$ [1] we obtain the resolution vector $\Delta\Omega = (\Delta\Omega[1], \ldots, \Delta\Omega[M])$ where $\Delta\Omega[1] = \Omega[2] - \Omega[1]$ and $\Delta\Omega[k] = \Omega[k] - \Omega[k-1]$; $k = 2, \ldots, M$. A weighting function W_k is constructed for each selected frequency $\Omega[k] \in \Omega$, with the form

$$\begin{aligned} W_k[i] &= 0 \; ; \; \omega[i] < \Omega[k] - \Delta\Omega[k] \\ W_k[i] &= cos\left(\frac{\Omega[k] - \omega[i]}{2\Delta\Omega[k]}\pi\right) \; ; \; \Omega[k] - \Delta\Omega[k] \leq \omega[i] \leq \Omega[k] + \Delta\Omega[k] \\ W_k[i] &= 0 \; ; \; \omega[i] > \Omega[k] + \Delta\Omega[k] \end{aligned} \tag{7.4}$$

The cross periodogram P_{yu} and auto periodograms P_{yy}, P_{uu} are calculated for each $\omega[i]$

$$P_{yu}[i] = Y[i]U[i]^* \; , \quad P_{uu}[i] = U[i]U[i]^* \; \& \quad P_{yy}[i] = Y[i]Y[i]^* \tag{7.5}$$

The weighted cross spectrum Φ_{yu} and weighted auto spectra Φ_{yy} & Φ_{uu} are obtained for each $\Omega[k]$ by multiplying the original periodograms by the relevant weighting functions $W_k[i]$ such that

$$\Phi_{yu}[k] = \Sigma_{i=1}^{N} P_{yu}[i]W_k[i] \quad ; \quad \Phi_{uu}[k] = \Sigma_{i=1}^{N} P_{uu}[i]W_k[i] \quad ; \quad \Phi_{yy}[k] = \Sigma_{i=1}^{N} P_{yy}[i]W(_k[i] \tag{7.6}$$

Then, the locally smoothed discrete frequency response estimate at the selected frequency $\Omega[k]$ is obtained from

$$P[k] = \frac{\Phi_{yu}[k]}{\Phi_{uu}[k]} \tag{7.7}$$

with a noise spectrum given by

$$\Phi_v[k] = \Phi_{yy}[k] - \Phi_{yu}[k]G[k] \tag{7.8}$$

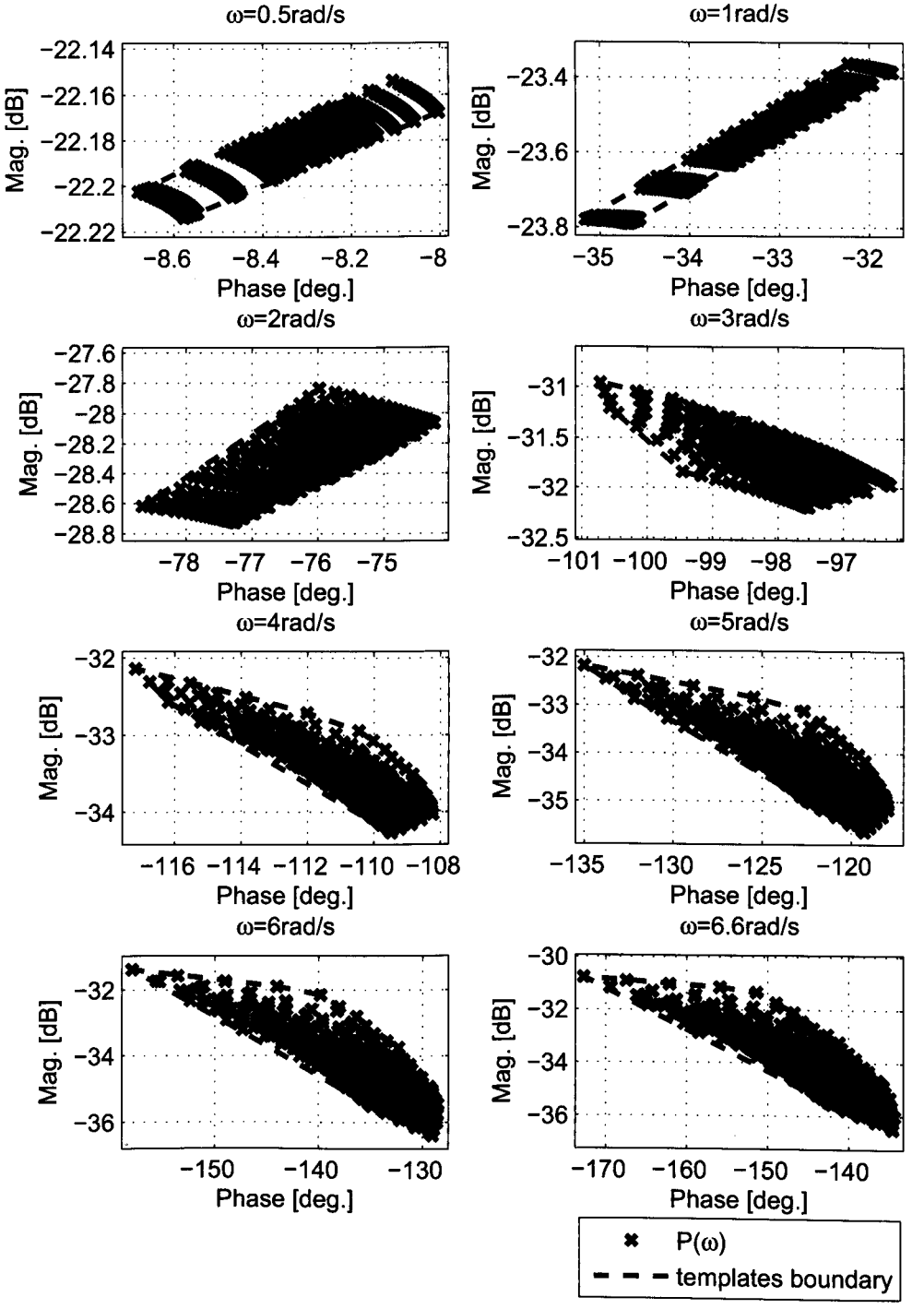

Figure 7.3: Nichols chart of the NP plant templates [rad/s/Nm]

FRFs determined for each of the I/O data sets acquired at Stage 1 are obtained with this local smoothing method. The resulting set of FRFs represents the required LTIE set to represent the plant. The set of complex responses at each frequency forms a cloud of complex points. The convex hull of these points are then taken as the plant templates for the LTIE set. The driveline input-output data from Stage 1 was transformed to the frequency domain with an $N = 2^{12}$ order FFT, to compute the DFT [155], with $T_s = 0.01$ s. The resulting boundary and complex FRF cloud of the plant templates obtained from this data at the selected frequencies $\Omega = \{0.5, 1, 2, 3, 4, 5, 6, 6.6\}$ rad/s are shown in Figure 7.3.

7.5 Setting of Stability, Tracking and Disturbance Bounds

The required system tracking performance $y_r(t)$ is dependent on the nature of the system under investigation. For example, a system with high inertia and time delay, like driveline, cannot be as fast in its response as low inertia electrical motor. Usually mechanical systems have a slow time domain response when compared with electrical systems. The same thing can be clearly seen when looking at mechanical systems bandwidth through their frequency response. The bandwidth or system operating frequency range is usually taken as the frequency corresponding to $0.707 = -3$ dB gain. To achieve designable QFT control boundaries, achievable time domain boundaries should be chosen. The approach to specifying tracking

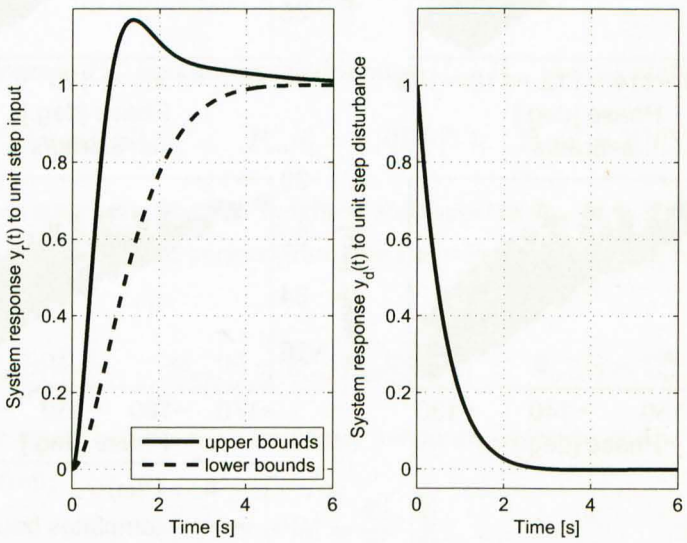

Figure 7.4: System time domain tracking performance specifications

[1] in the QFT design, usually $M << N$

performance follows the standard QFT procedure [99] of basing the requirements on an initial equivalent second order linear system of the form

$$\frac{\omega_n^2}{s^2 + 2\zeta\omega_n s + \omega_n^2} \tag{7.9}$$

for which $OS = e^{\frac{-\zeta\pi}{\sqrt{1-\zeta^2}}}$ for 2% error criterion [156] and $t_s = \frac{4}{\zeta\omega_n}$. Then these time domain requirements are converted to the frequency domain. Additional poles and zeros can be added in order to widen or tighten the range between the upper and lower boundaries in the frequency domain. In the presented driveline problem, the required system tracking performance limits for $Y(s)/R(s)$ are set by an upper bound T_U. This bound has been chosen to give a peak overshoot of 0.17 on a time of 1.36 s, and a settling time t_s of 5 s. Similarly the lower bound T_L is chosen to satisfy an overshoot of zero, a rise time of 3.21 s, by choosing a non-oscillatory second order system with $\zeta \geq 0.707$ (taken as 0.9) and an acceptable steady state error $e_{ss} = 1.4$ rad/s. We then obtain $w\omega_n = 2\zeta/e_{ss}$ (1.2857 rad/s).

An upper disturbance rejection bound $T_D(s)$ on $Y(s)/D(s)$, is chosen to make $|y_d(t)|$ decay to less than 3% of its magnitude within 4 s. Starting with the time domain representation $y(t) = e^{-at}cos(bt)$[99], which can be represented in the frequency domain as

$$Y(s) = \frac{s+a}{(s+a)^2 + b^2} \tag{7.10}$$

The parameters a and b are adjusted to achieve the required decay rate during the specified period when responding to a unit step disturbance $D(s) = \frac{1}{s}$. For the driveline problem appropriate values were found to be $a = 1.5$ and $b = 0.5$.

Accordingly in the frequency domain, the upper tracking bound was taken as

$$T_U(s) = \frac{21s + 8.399}{2.128s^3 + 9.511s^2 + 21.87s + 8.399} \tag{7.11}$$

the lower tracking bound

$$T_L(s) = \frac{1.653}{s^2 + 2.314s + 1.653} \tag{7.12}$$

and the disturbance rejection bound

$$T_D(s) = \frac{s^2 + 1.5s}{s^2 + 3s + 2.5} \tag{7.13}$$

The time domain bounds corresponding to these, T_U and T_L, are shown in Figure 7.4, and the performance boundaries in the frequency domain in Figure 7.5. The bandwidth frequency ω_b of the model for which $|T_U(j\omega_b)| = -3$ dB is 3.073 rad/s. In QFT design it is found necessary [99], to satisfy the desired performance specifications up to a higher bandwidth frequency ω_h, corresponding to $|T_U(j\omega_h)| = -12$ dB, which is 6.223 rad/s in this case. The logarithmic magnitude difference $\delta T_R(j\omega_i) = 20\log_{10} T_U(j\omega_i) - 20\log_{10} T_L(j\omega_i)$ at the design grid frequencies ω_i and the disturbance rejection boundaries $L_D = \frac{1}{T_D} - 1$ are listed in Table 7.2. These boundaries are subsequently used at Stage 5 to shape the loop transmission function in the Nichols chart.

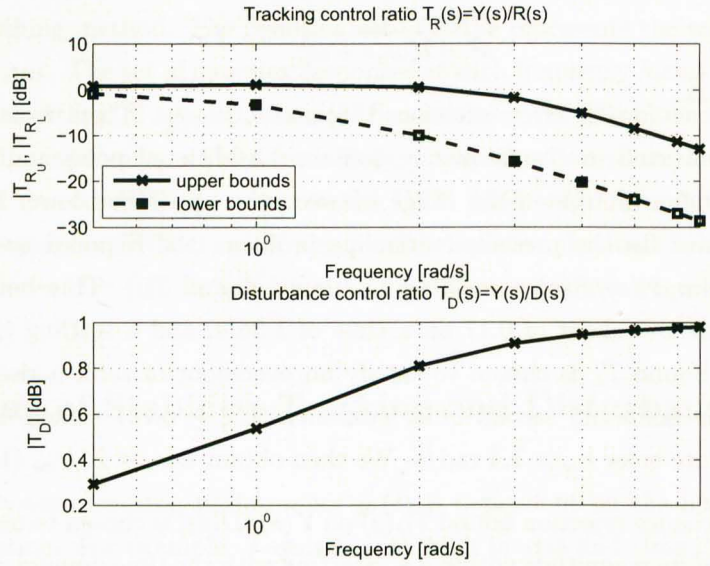

Figure 7.5: System frequency domain tracking performance specifications

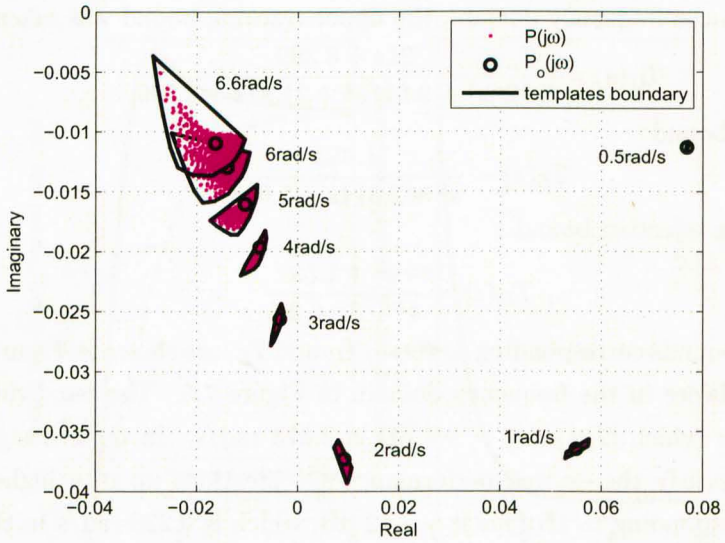

Figure 7.6: Nyquist plot of the nominal plant

Table 7.2: Frequency domain boundary data

ω_i [rad/s]	$\delta T_R(j\omega_i)$ [dB]	$L_D(j\omega_i)$ [dB]
0.5	1.6371	7.6782
1	4.4214	−1.3048
2	10.5499	−12.5075
3	13.9899	−19.7175
4	15.1838	−24.8792
5	15.5307	−28.8625
6	15.6235	−32.0981
6.6	15.6380	−33.7830

7.6 Determining of a Stable MP Nominal System

QFT loop-shaping requires that arbitrary (nominal) points are associated with each uncertainty template to form a nominal plant locus. In this design study the driveline system nominal plant is chosen as the centre of gravity of each frequency template cloud as in Figure 7.6. If the nominal plant locus is found to be that of an unstable or NMP plant (an *unstable locus*) then the phase shift required to produce a stable MP locus must be determined. The QFT loop-shaping process then requires that the plant templates are shifted by this phase to align them with the amended stable MP nominal plant [154]. This design stage accordingly determines the required phase shift at the design grid frequencies. In case of stable MP systems, the frequency response magnitude determines a unique phase, and the phase of the frequency response determines a unique magnitude to a scale factor [108]. Consider the FRF of a nominal plant

$$P_o(e^{j\omega}) = \left|P_o(e^{j\omega})\right| e^{j\angle P_o(j\omega)} \tag{7.14}$$

for which we have the logarithmic equation

$$\log_e P_o(j\omega) = \log_e |P_o(j\omega)| + j\angle P_o(j\omega) \tag{7.15}$$

To determine the phase $\angle P_o^*(j\omega)$ of a stable MP FRF with the same gain $\log_e |P_o(j\omega)|$ we apply the Hilbert transform to the real component of $\log_e P_o(j\omega)$ to determine the phase as the required associated imaginary component thus

$$\mathcal{H}Re\left\{\log_e P_o(j\omega)\right\} = \angle P_o^*(j\omega)$$

where $\mathcal{H}$ is the Hilbert transform. From this the required stable MP nominal system $P_o^*(j\omega)$ can then be formed as

$$P_o^*(j\omega) = \left|P_o(j\omega)\right| e^{j\angle P_o^*(j\omega)} \tag{7.16}$$

The required boundary phase shift for the original $P_o(j\omega)$ is thereby given in terms of the all-pass function $A(j\omega)$ by

$$\angle A(j\omega) = \angle P_o^*(j\omega) - \angle P_o(j\omega) \quad \text{where} \quad |A(j\omega)| = 1 \tag{7.17}$$

The stable MP system nominal plant can thus be obtained from the original unstable NMP

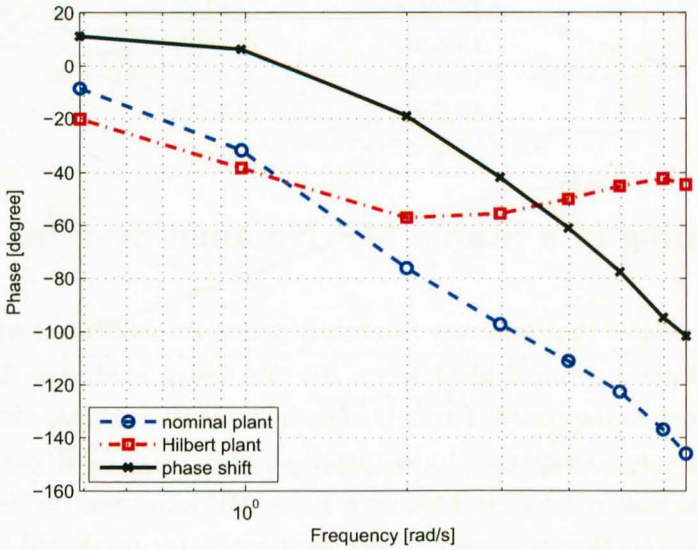

Figure 7.7: Bode plot of the phase shift determination

version from multiplication by the all-pass phase shift component $A(j\omega)$ as

$$P_o^*(j\omega) = A(j\omega)P_o(j\omega) \tag{7.18}$$

In this thesis, Hilbert transform is calculated via FFT by following Marple's technique [105]. One of the constrains to be able to use FFT for determining an equivalent MP of a NMF frequency response locus is to have the frequency response points correspond to a uniformly distributed frequency vector (i.e. of a constant sampling rate). As this is not the case in the selected frequency response points in the presented NP QFT technique, a transfer function is fitted to the original locus of the NMP plant P_o. Then, a uniform FRF locus is obtained from the fitted transfer function and used for obtaining the equivalent MP locus P_o^* by Hilbert transform. Figure 7.7 shows the NMP phase, the MP phase which obtained by Hilbert transform and the required boundary phase shift. Initial complex curve fitting technique is applied first to P_o locus, then the damped Gauss-Newton method [157, 158, 155] is used to minimise the error between P_o locus and the fitted frequency response locus shown in Figure 7.8. The minimised fitting errors are presented in Figure 7.9 and the fitted nominal transfer function is

$$P_{o_{eq}} = \frac{-0.006865s^7 - 0.005483s^6 - 0.5461s^5 + 3.529s^4 - 18.22s^3 + 116.5s^2 + 83.06s - 254.2}{s^7 + 3.276s^6 + 92.68s^5 + 122.4s^4 + 2368s^3 + 2568s^2 + 549.4s - 3046} \tag{7.19}$$

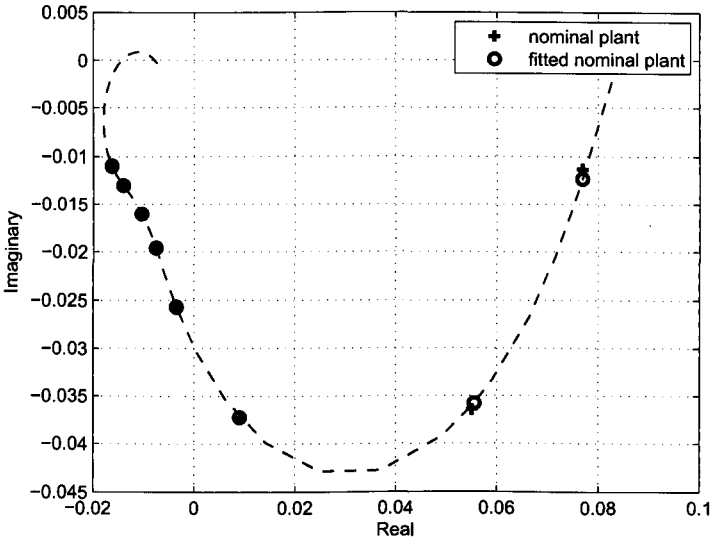

Figure 7.8: Nyquist plot of fitting a transfer function to the NMP locus [rad/s/Nm]

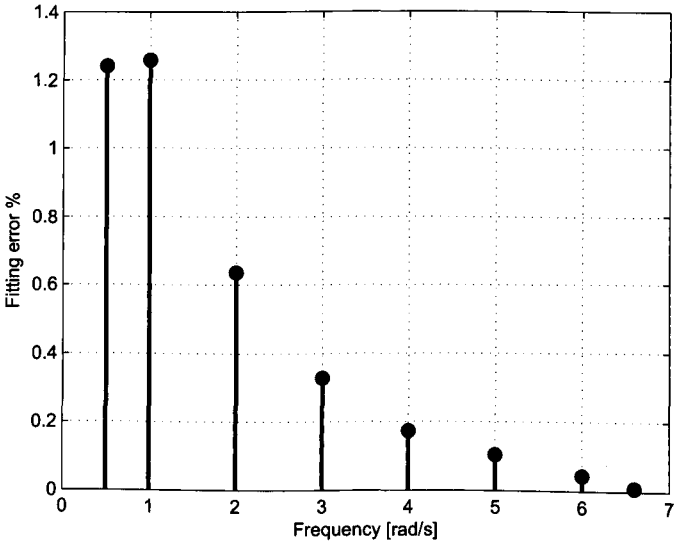

Figure 7.9: Equivalent plant fitting error

A flow chart of the sequence is displayed in Figure 7.10.

7.7 Open Loop Shaping

The nominal loop transmission function needs to be shaped to make $L_o = GP_o$ satisfy the desired requirements, a loop transmission L_{mo} is shaped. Because the driveline plant is NMP due to the time delay, the robust boundaries of the MP plant are obtained by shifting the original plant boundaries by phase shift component $A(j\omega)$ [75]. Thus the controller is obtained as

$$G(j\omega) = \frac{L_{mo}(j\omega)A(j\omega)}{P_o(j\omega)} \tag{7.20}$$

The plant templates are then mapped to the Nichols chart at the chosen design grid frequencies. The templates are then translated within the desired stability contour M_L, disturbance rejection boundaries $T_D(j\omega)$ and tracking boundaries $T_U(j\omega)$ and $T_L(j\omega)$ to obtain the shaped nominal locus, as in conventional QFT [154]. The nominal loop transmission function $L_o^*(s) = G(s)P_o^*(s)$ that satisfies all the performance bounds and the stability contours is then synthesised to minimise the overall loop gain. For the driveline example the resulting initial controller was determined as

$$G(s) = \frac{b_0 s^3 + b_1 s^2 + b_2 s + b_3}{a_0 s^4 + a_1 s^3 + a_2 s^2 + a_3 s + a_4} \tag{7.21}$$

where $a_0 = 0.1667$, $b_0 = 15.01$, $a_1 = 1.051$, $b_1 = 17.05$, $a_2 = 3.656$, $b_2 = 305.7$, $a_3 = 20.1$, $b_3 = 257.1$, and $a_4 = -0.01156$. Figure 7.11, which has been split in Figures 7.12 to 7.19, shows how the loop transmission function L_{mo} is shaped to satisfy the requirements in the Nichols chart.

7.8 Prefilter Design

In the final stage, the prefilter $F(s)$ is synthesized to position the system tracking response within the tracking specifications. When the plant templates is fitted above the design boundaries in the Nichols chart, this guarantee that the variation of the system output, when the plant magnitude is changing due to the nonlinearity, is limited within the desired $\delta_R(j\omega_i)$. As can be seen in Figure 7.20, the magnitude difference between $M_{max}(j\omega_i)$ and $M_{min}(j\omega_i)$ is less than $\delta_R(j\omega_i)$ as expected, however, the position of the chosen loop transmission needs to be shifted inside the the designed close loop boundaries $T_{R_U}(j\omega_i)$ and $T_{R_L}(j\omega_i)$ for the desired bandwidth. The prefilter is designed to do this shift, firstly by finding the values of M_{max} and M_{min} from the Nichols chart for each template. Those values of M circles are

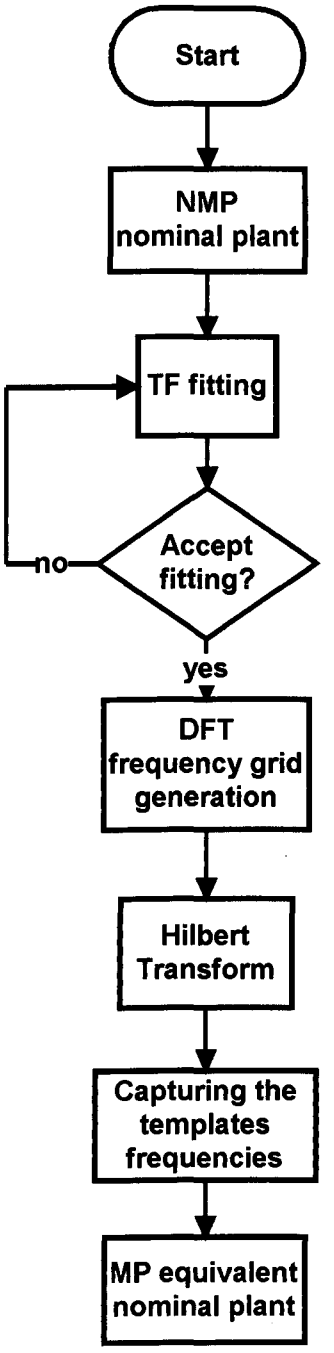

Figure 7.10: Using discrete Hilbert transform to determine a MP equivalent plant

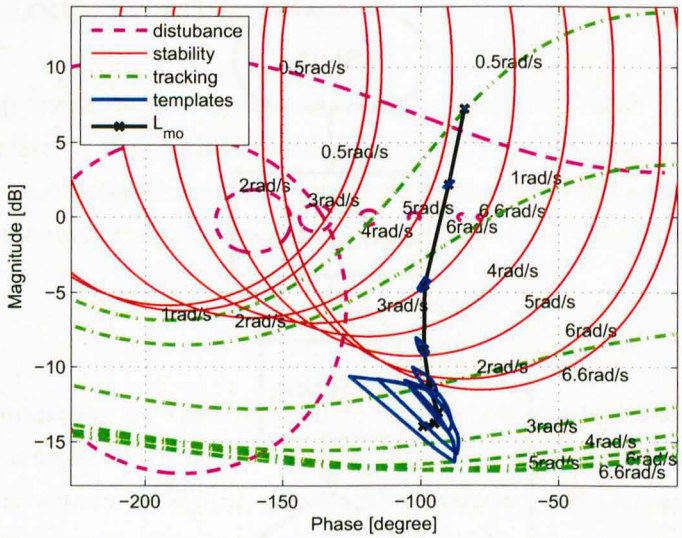

Figure 7.11: Shaping the loop transmission function in Nichols chart

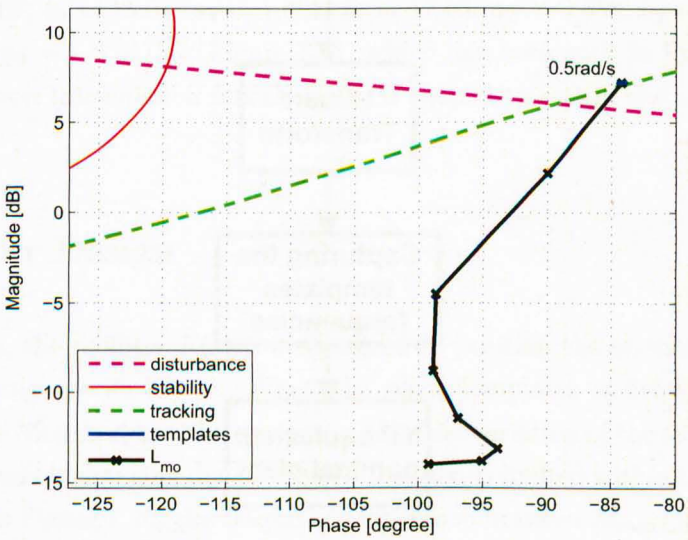

Figure 7.12: Shaping the template of $\omega = 0.5$ rad/s

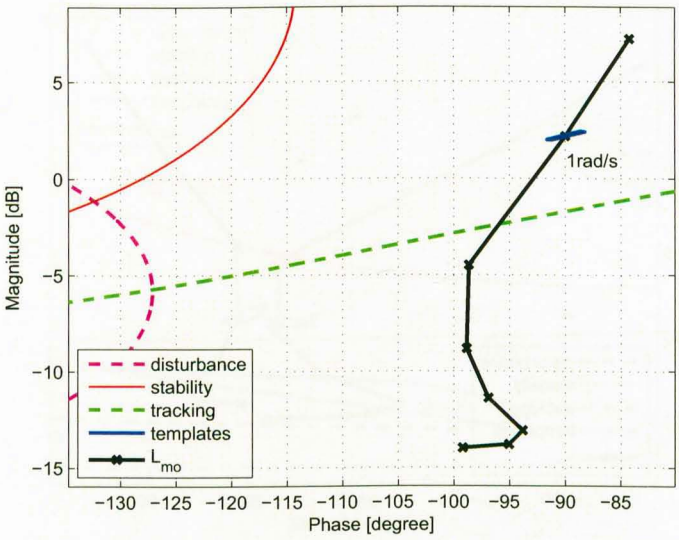

Figure 7.13: Shaping the template of $\omega = 1$ rad/s

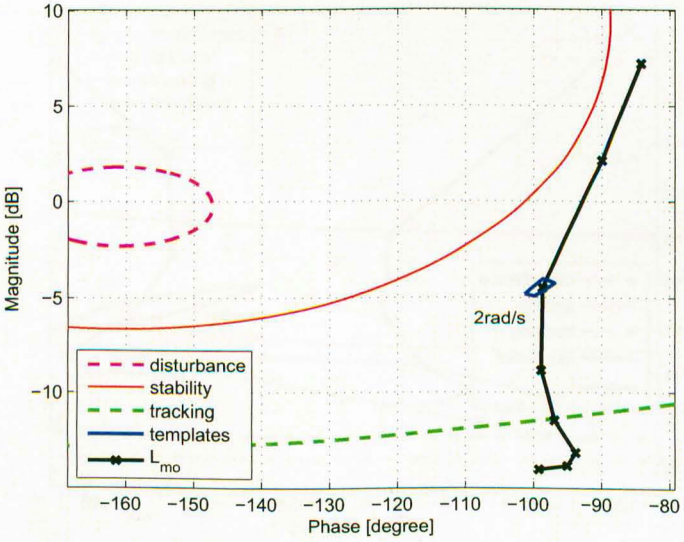

Figure 7.14: Shaping the template of $\omega = 2$ rad/s

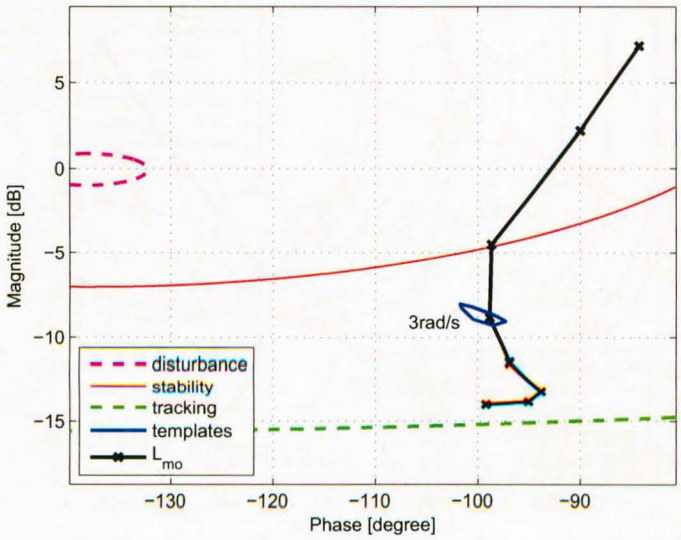

Figure 7.15: Shaping the template of $\omega = 3$ rad/s

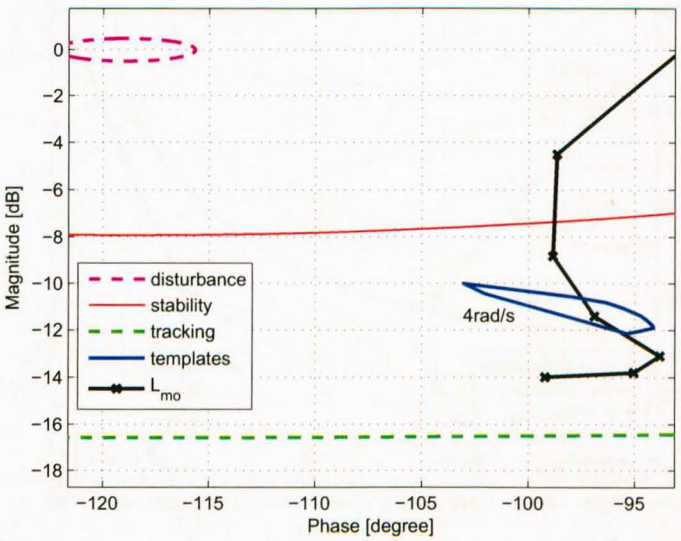

Figure 7.16: Shaping the template of $\omega = 4$ rad/s

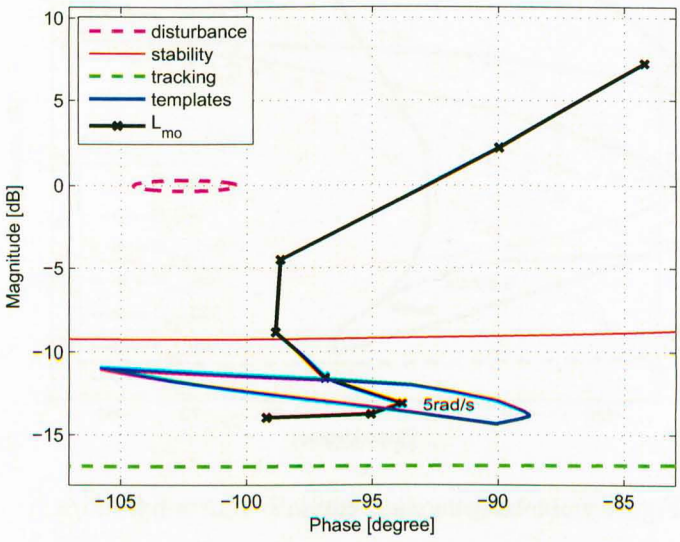

Figure 7.17: Shaping the template of $\omega = 5$ rad/s

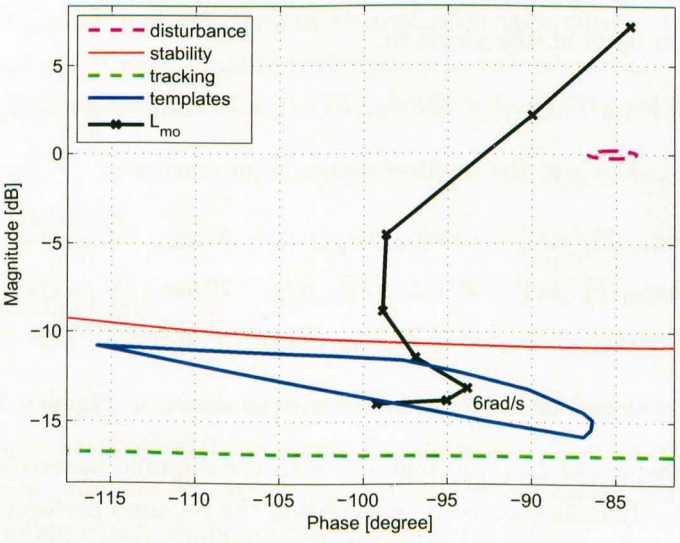

Figure 7.18: Shaping the template of $\omega = 6$ rad/s

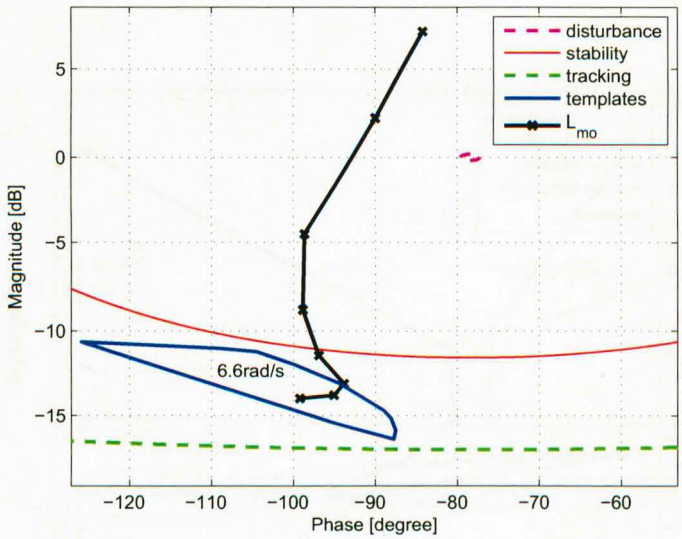

Figure 7.19: Shaping the template of $\omega = 6.6$ rad/s

representing the closed loop controlled system without the prefilter as

$$M(j\omega) = \frac{L_o(j\omega)}{1 + L_o(j\omega)} \tag{7.22}$$

however, the tracking control ratio $T_R(j\omega)$ is

$$T_R(j\omega) = \frac{F(j\omega)L_o(j\omega)}{1 + L_o(j\omega)} \tag{7.23}$$

Writing Eqn. (5.64) in units of dBs yields to

$$20\log_{10}|T_R(j\omega)| = 20\log_{10}|F(j\omega)| + 20\log_{10}|M(j\omega)| \tag{7.24}$$

which can be rearranged to give the prefilter design requirements as

$$20\log_{10}|F_U(j\omega)| = 20\log_{10}|T_{R_U}(j\omega)| - 20\log_{10}|M_{max}(j\omega)| \tag{7.25}$$

$$\text{and} \quad 20\log_{10}|F_L(j\omega)| = 20\log_{10}|T_{R_L}(j\omega)| - 20\log_{10}|M_{min}(j\omega)| \tag{7.26}$$

$$\text{where} \quad 20\log_{10}|F_U(j\omega)| \geq 20\log_{10}|F(j\omega)| \geq 20\log_{10}|F_L(j\omega)| \tag{7.27}$$

Then the prefilter is designed inside those boundaries as shown in Figure 7.20

The successful shaping of $L_{mo}(j\omega)$ together with the required uncertainty tolerance on the unfiltered tracking dynamics allows a guarantee of the required performance robustness. The prefilter for the driveline controller was accordingly determined as

$$F(s) = \frac{1}{0.2s + 1} \tag{7.28}$$

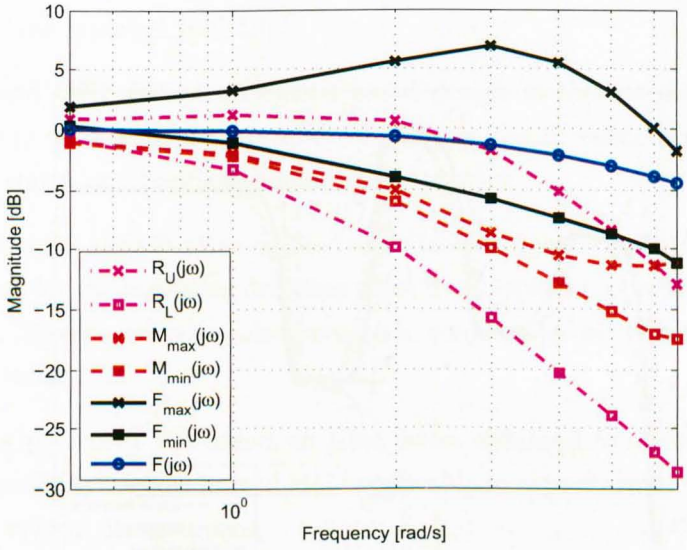

Figure 7.20: Prefiter design requirements

7.9 Results and Discussion

Figure 7.21 shows the controlled system response to input demand signal. As can be seen, the response is generally smooth and always within the desired boundaries. The controlled system response to output disturbance which is shown in Figure 7.22 shows good disturbance rejection with both positive and negative step loads. The results show that the driveline with clutch and backlash nonlinearity can be controlled very effectively using the new NP QFT approach and are at least equal in performance to the cut-and-try controllers currently employed at significant expense.

7.10 Conclusions

This chapter conclusions are:

- A fully NP approach to systematising driveline active control calibration is presented. The technique has potential for application in active driveline controller calibration without the requirement for extensive parametric identification, gain scheduling or final in-vehicle tuning which invalidates any designed robustness.
- A nonlinear model of the driveline was developed which includes the main nonlinearities of clutch and gear with coupling backlash. The backlash was embedded between inertial and compliant elements in contrast to the less realistic but analytically convenient

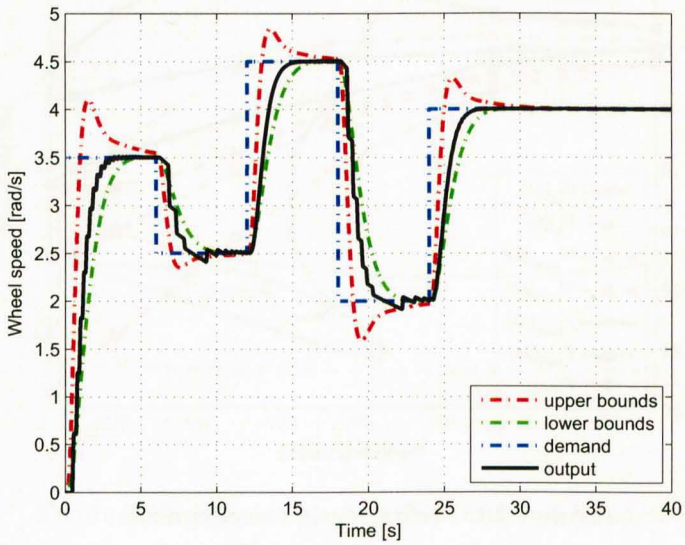

Figure 7.21: Controlled system response to input demand

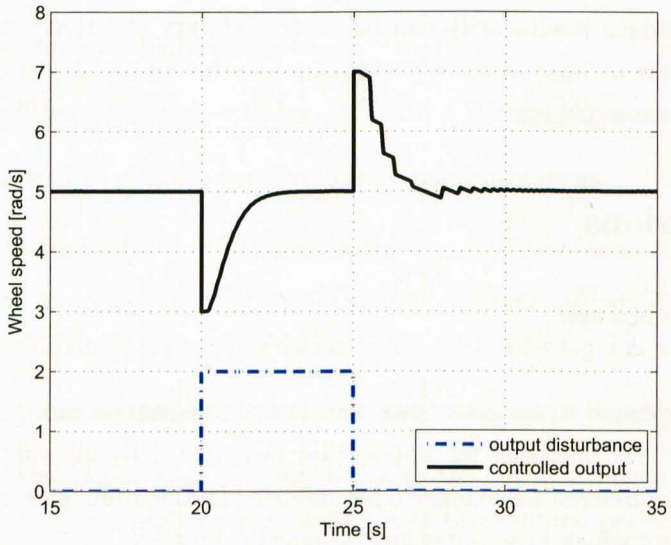

Figure 7.22: Controlled system response to output disturbance

approach of backlash connected to the end inertial element. The model gave similar results to those reported by [159].

- The proposed QFT NP identification based design method is shown in a study on the nonlinear to provide a successful solution for the driveline control problem with significant clutch and backlash nonlinearities present.
- The proposed NP identification method using local frequency domain smoothing obtains the LTIE set for the nonlinear driveline plant from typical I/O experimental data. The resulting LTIE set could then also be used in conjunction with any other robust linear control method.
- The results presented are based on time series obtained from model data, but the proposed methods are also immediately applicable to experimentally obtained driveline data using typical driver inputs.
- The driveline model is found to be NMP. An NP method for obtaining the required stable MP nominal plant for QFT loop shaping with possibly unstable NMP plants is presented and applied to the driveline model.

Chapter 8

Experimental Setup

8.1 Introduction

This chapter provides an overview of the tools and equipments which are used for achieving the experimental work for this thesis. Facilities in the IC and the chassis dynamometer laboratories at the University of Liverpool were used for measuring and controlling different signals used to investigate the presented applications. Section 8.2 explains the prototyping system used in the experimental work, and section 8.3 describes the software which has been used. Driveline specification are presented in section 8.4. The interfacing hardware is described in section 8.5, and the details of the angular encoders presented in section 8.6. Section 8.7 explains how the ABV duty is used as an input signal to the plant then, a general view of the driveline experimental setup is given in section 8.8. This includes the vehicle installation and instrumentation. Section 8.9 gives the technical details of the chassis dynamometer which is the main equipment used in the experimental set up because it provides the surface in which the vehicles wheels roll over. The chassis dynamometer configuration is detailed in subsection 8.9.1 and the torque measurement setup in subsection 8.9.2. Finally, the electronic throttle valve used in the experimental setup is finally presented in section 8.10.

8.2 Prototyping System

The experimental work has been done on three experimental setups, the IC engine, driveline, and throttle valve. A dSPACE rapid prototyping flexible development system was used for implementing the designed controllers on the physical dynamic plants. DSPACE allows the user to develop and optimise a control design for a real plant at a high level without low level manual programming. The dSPACE equipment provides the connection between the software environment and the real world plant environment. The dSPACE hardware is implemented as

Table 8.1: DSPACE board specifications

Board	Function	Specification
DS1005	processor board	power PC 750 GX running at 1 GHz in the IC engine setup and at 480 MHz in the chassis dynamometer setup
DS4001	digital I/O	timing and digital I/O
DS2003	analog to digital (A/D) board	32 channel, up to 16 bit A/D converter

boards for the dSPACE bus system. In general, dSPACE boards can be classified according to the type of their I/O signals such as digital, Digital to Analog (D/A) , and Analog to Digital (A/D) . Some boards have the capability of doing high performance processing of the data, and those cards are called processing boards. The boards with digital type plugs on them are for passing signals to/from the processor boards. The processor board is the one which runs the control loops and triggers the I/O cards. The specifications of the dSPACE boards used are shown in Table 8.1. With dSPACE's implementation software Real-Time Interface (RTI) , MATLAB/SIMULINK models can be implemented on the dSPACE hardware automatically. A graphical block library with many interface functionalities is provided for configuring inputs and outputs and connecting I/O to the model.

8.3 Software

Full control of equipments on the project was achieved through a Personal Computer (PC) by using the MATLAB, SIMULINK, Real-time Workshop and Control Desk softwares. Design calculations are done by MATLAB level language and interactive environment produced by MathWorks. SIMULINK is used in building up the control loops and testing the designed controllers. It provides a graphical interface of MATLAB in which control circuits can be represented and simulated. Control loops were always tested in SIMULINK before applying them to real world problems. Real-time Workshop software is a toolbox which the SIMULINK models into real-time code and which can then be implemented on which dSPACE. Both SIMULINK and Real-time Workshop are produced by MathWorks. Control Desk is an experiment software which provides a user interface that allows the designer to control the hardware through a PC. It takes the code generated by the Real-time Workshop toolbox and implements it in a fully controllable single working environment from the start of experimentation right through to the end. It records the data and it can convert the recorded data to MAT data files. MAT is a binary data container format readable by MATLAB software.

Table 8.2: Driveline engine specifications

Element	Specification
Cylinder bore	76.0 mm
Connecting rod length	136.2 mm
Compression ratio	10.3:1
Cubic displacement	1597 cm^3
Stroke length	88 mm
Firing order	1-3-4-2
Maximum torque	138 Nm at 3500 RPM
Maximum power	76.113 kW
Idle speed	830:880 RPM
Fuel	Unleaded RON 95 petrol
Battery	Lead-acid 500 A/75 RC

Table 8.3: Transmission gears specifications

Gear set	Gear ratio
1st	3.417:1
2nd	2.136:1
3rd	1.448:1
4th	1.028:1
5th	0.767:1
Reverse	3.46:1
Final drive	4.06:1

8.4 Driveline Specification

To apply the control theory presented in this thesis on the driveline, a 1430 kg weight five door Ford Mondeo Estate automobile has been used. The driveline has a 1.6 L, 16 valve, four-stroke, four-cylinder, in-line, double overhead cam, water cooled, multi-point fuel injected IC Zetec engine. Engine specifications are described in Table 8.2. As the nonlinear effects in the driveline control problem appear clearly during the vehicle launch, The 1st transmission gear was always engaged during testing. Table 8.3 shows the gear ratios in the used vehicle. As the first gear ratio is 3.417, and the final drive gear ratio (differential gears) is 4.06, a total speed ratio of 13.87 is expected when motion is transmitted from the engine to the front wheels through the driveline.

8.5 Interfacing Hardware

As can be seen from Figure 8.1 and the photograph in Figure 8.2, a wheel speed angular encoder is fixed on the centre of the left front wheel hub, however, an engine crankshaft angular encoder is fixed at the right end of the crankshaft. A special arrangements is made to allow fitting the encoders without affecting the vehicle performance. These arrangements contain two special bolts, one of them is fitted to the centre of the wheel hub, and the other one is fitted to the end of the crankshaft as the bolt is designed to replace the original crankshaft end bolt. These bolts end with a cylindrical turned shape to allow fitting of flexible couplings to their ends. A steel frame fitted to the front wheel suspension by an aluminum ring is designed to fit the wheel angular encoder as in Figure 8.2, however, a steel strip bolted to the engine body is used to fit the crankshaft encoder from the engine right hand side. Due to vibration during running the vehicle, alignment between both crankshaft axle and wheel axle with their encoders, flexible coupling is used.

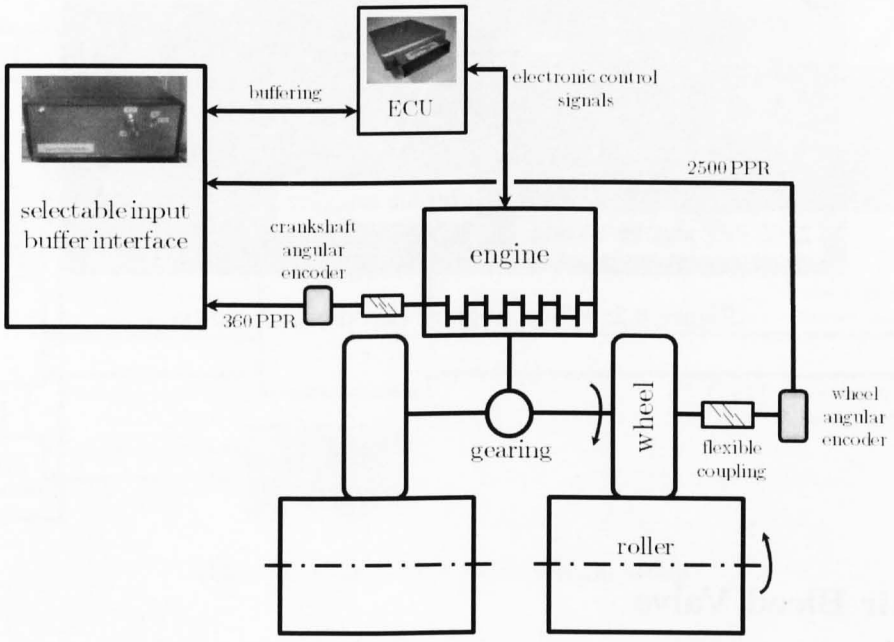

Figure 8.1: Driveline hardware setup

8.6 Angular Encoders

The driveline input demand signal is sent from a desktop PC through dSPACE to the engine management system which can be switched to work in either the standard Ford Electronic Control Unit (ECU) strategy or in the dSPACE programmed strategy. Two speeds are

measured from the driveline through angular encoders. The engine speed is captured by 360 PPR incremental angular encoder. Due to the gearing ratio reduction at the wheels, it was necessary to use a higher resolution encoder. The Anti-lock Braking System (ABS) wheel sensor, which is fitted by Ford as stander to the vehicle, is not considered suitable as its resolution is too low and therefore, for research purposes a 2500 PPR angular encoder was selected and fitted to measure the speed at the vehicle front wheel.

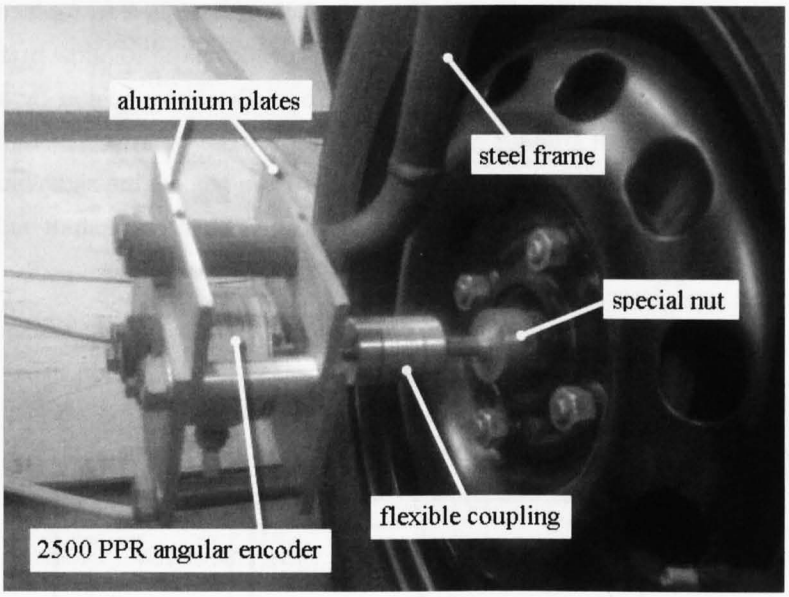

Figure 8.2: Wheel angular encoder installation

8.7 Air Bleed Valve

ABV is a solenoid valve associated with the throttle valve. As the vehicle used is fitted with a cable operated throttle, the ABV works as a throttle bypass valve delivers air when the engine is idle to achieve the designed idle speed. Like the throttle valve, ABV controls the volume of air that passes into the inlet manifold. Because of that, ABV can be used to control the engine speed through controlling the air going to the engine cylinders. Being a solenoid valve makes it fully controllable electronically by the engine management ECU or Control Desk and Real-time Workshop softwares via dSPACE and PC. The throttle valve is closed to 8^o when the engine control switched to ABV through a selectable input buffer interface.

8.8 Driveline Experimental Setup

A dSPACE expansion box is used with boards DS4001 and DS1005 in the used driveline experimental setup shown in Figure 8.3. Board DS4001 is a timing and digital I/O board. This board receives the engine speed and the wheel speed encoders signals as squared signals. The data is then exchanged with the DS1005 board, which is a digital I/O processor board. Processor boards provide the computing power for real-time system and also function as interfaces to the I/O boards and the host PC [160] through a Local Area Network (LAN) cable. DS4001 sends two signals, a Pulse Width Modulated (PWM) signal to control the ABV and 8-Bit spark-word command signal to control the spark. Those signals go through a buffer interface. The buffer interface acts to protect the dSPACE and the ECU from any erroneous signals. It has two modes of operation: normal ECU, and bypass, whereby the operator replaces the command logic signals in the ECU with their own. Both modes of operation utilise the powerstages within the ECU to drive the coil of ABV.

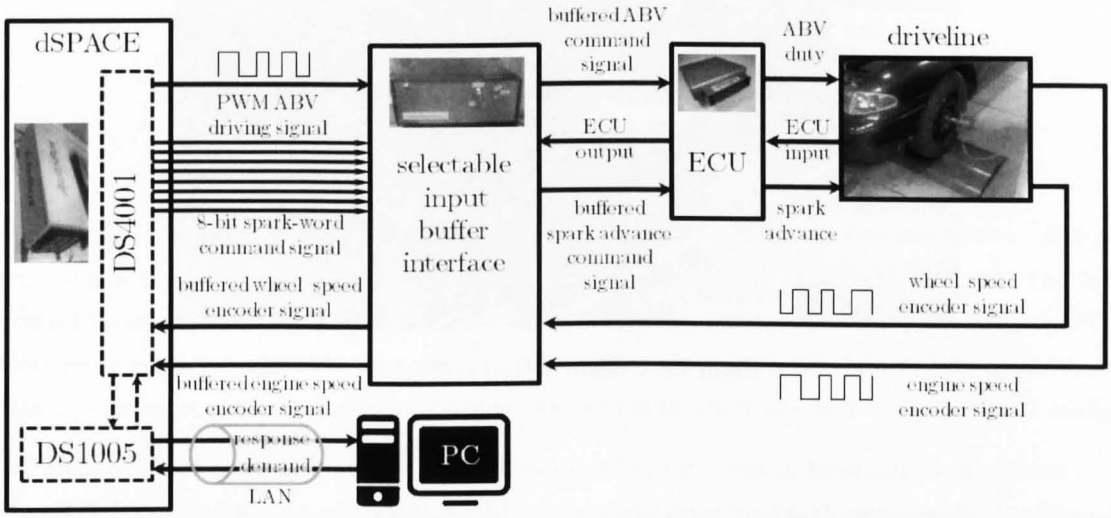

Figure 8.3: Driveline experimental setup

8.8.1 Vehicle Installation and Operation

During preparation for testing, the vehicle must be installed on the chassis dynamometer rollers. The vehicle lateral position should be set to locate front wheels as near as possible to the mid point of the rollers. Of course, achieving that physically during the test could be very difficult as the vehicle vibrates and moves about on the suspension. Axial alignment of the vehicle is made with respect to the centreline of the chassis dynamometer to provide a good reference position to ensure a stable rotation, the longitudinal position of the vehicle should

be set with the centre of the front wheels positioned 25 mm back from the roller centreline.

When the vehicle is correctly positioned on the chassis dynamometer, it should be restrained to prevent it from any longitudinal movement during the test. Three elements are used to achieve the rear wheels restraint. The vehicle handbreak is activated first. Second, the vehicle is jacked up and chocks, which are rubber pads, are placed in the front and the back of the rear wheels to prevent the vehicle from moving forward or backward in the event of handbreak failure. Thirdly, a ratchet strap is passed around each rear wheel, chocks and a steel rod bolted down to the dynamometer steel deck as in Figure 8.4.

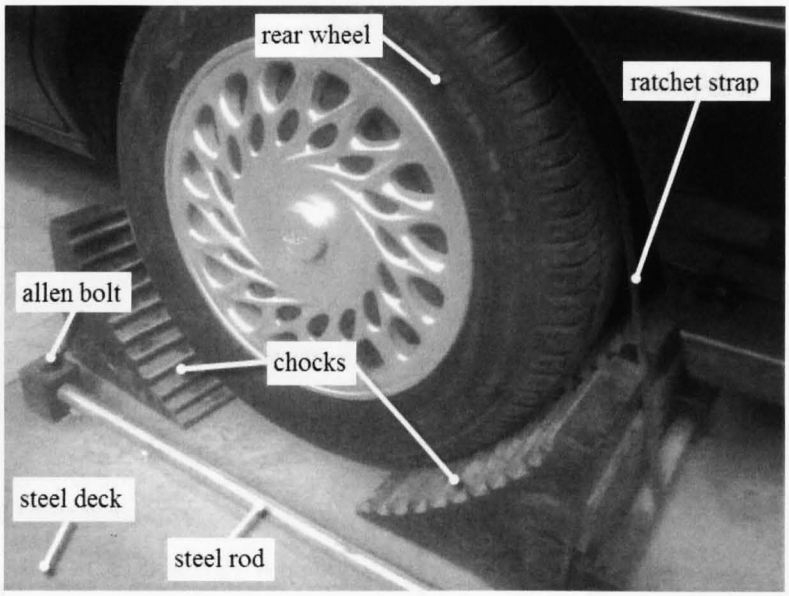

Figure 8.4: Rear wheel restraint

Vehicle front restraint is also required to maintain the lateral alignment of the vehicle on the rollers. This is important as good alignment will minimise the amount of steering input which is required during the test to keep the vehicle in the correct alignment position. Two ratchet straps are used to tie the vehicle front to both sides to prevent the vehicle front from extra lateral movement. A special anchor fixed to the concrete ground by steel stud are used from each side from which straps are fixed to the vehicle towing eye. Initially, these straps are kept slack until the vehicle is well adjusted in mid lateral position through a very slow driving speed (less than 10 km/h).

A cooling fan is used in the test to provide cooling during running the vehicle (see Figure 8.5). This fan is positioned on the front of the vehicle and fully controlled from the rolling road laboratory control room. A ten turn potentiometer is used for setting the cooling fan speed. A wind speed of 0.5 m/s is selected as an average value as it is equivalent to the vehicle speed when wheels run at 100 RPM.

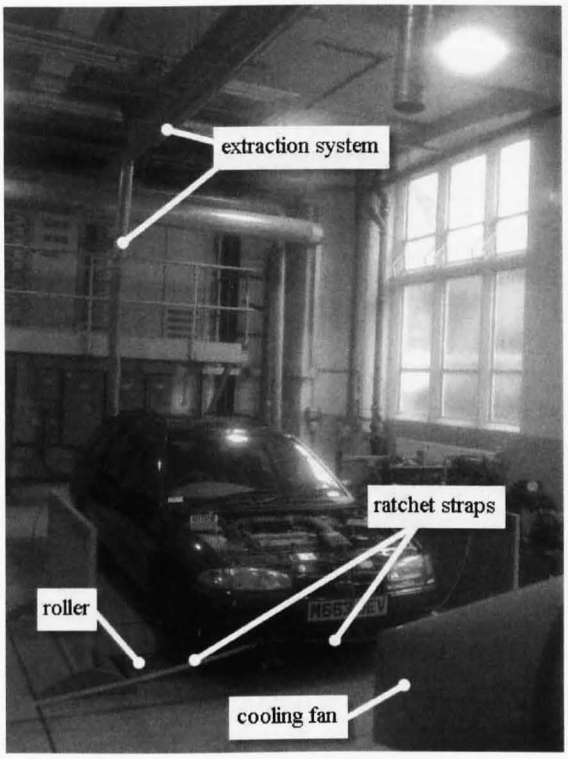

Figure 8.5: Driveline testing area

During the test, two persons should be on duty. The first one is the vehicle driver, who starts the engine and engages the first gear. The second person stays inside the lab control room, from which he can monitor and control the whole test through a desktop PC. Communication between the two persons takes place through a wireless communicator. A remote emergency stop is positioned inside the vehicle to allow the driver to operate it easily without obstruction in case of emergency.

Harmful emissions can quickly build up in the test place and causing serious health problems. Therefore, vehicle exhaust is taken out through an exhaust extraction system utilises special hoses and nozzles, which can be attached directly to the exhaust pipe of the stationary running tested vehicle. As many extraction system, the used one has an extraction fan and galvanised steel ducts linked it to each extraction point. The final connection to the vehicle is made by a suspended flexible drop. A hose is then attached to the vehicle exhaust system tailpipe via a quick release coupling at the bottom of the drop.

8.8.2 Vehicle Instrumentation

To be able to collect the testing data, the vehicle is fitted with some additional instrumentation. The purpose of this instrumentation is to provide means for monitoring and capturing

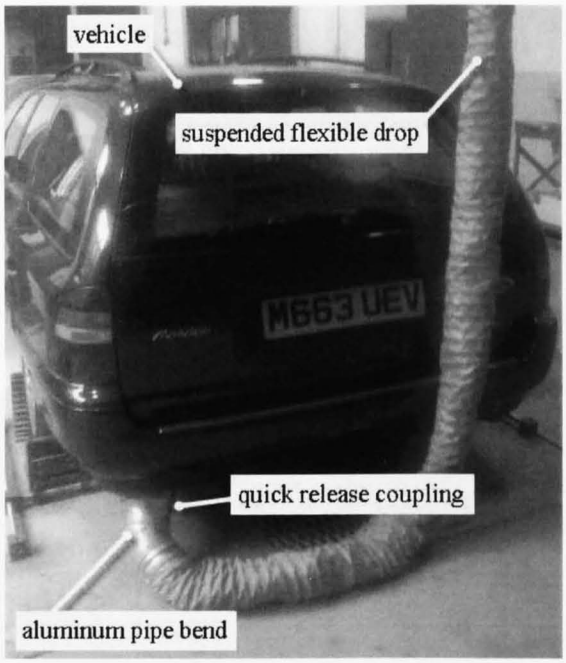

Figure 8.6: Exhaust extraction system end point

some of the important vehicle based variables which are required for control. The captured variables, and the instrumentation used to measure them are dependent upon the nature of the application. The list below describes a typical set of measurements as applied to the Ford Mondeo vehicle, along with the relevant sensors.

Driven Wheel Speed

As already discussed in subsection 8.8.1, the driveline wheel speed is measured by an angular encoder fitted to the front wheel of the vehicle. A high resolution sensor is used to ensure that the measured signal is suitable for identification and control.

Throttle Position

A voltage signal proportional to the angular position of the throttle valve can be intercepted from the ECU, the signal is captured from the ECU, and sent to the dSPACE which is connected to a PC. Then, the signal is displayed in the PC monitor.

Engine Speed

Although, engine speed can be intercepted from the variable reluctance sensor on the flywheel and intercepted from the ECU, an angular sensor is nevertheless fitted to the vehicle engine

in the setup. The reason for using this additional sensor instead of using the flywheel signal is one of obtaining a much better resolution. The engine flywheel contains 35 teeth distributed around its circumference representing one tooth per every ten degrees with a missing tooth at 360^o used for synchronising the engine events timing. This built in speed sensor is a nonadjustable sensor attached to the flywheel plate housing with special shoulder bolts. This sensor provides Top Dead Center (TDC) and engine speed information to the ECU by counting the flywheel teeth as they pass during engine operation. The flywheel has 35 trigger teeth and notches located at the known number of teeth before each TDC position. When a tooth and notch pass the magnetic core of the sensor, the concentration and collapse of the magnetic field created induces a voltage spike into the sensor pick-up coil windings. These voltage spikes give the ECU information for calculating engine speed. When the missing tooth (double size notch) pass the magnetic core of the sensor, the concentration and collapse of the magnetic field created induces no voltage spike into the sensor pick-up coil windings. This higher voltage spike indicates to the ECU that a piston will soon be at TDC. The ECU uses the speed sensor information for advancing or retarding ignition timing and other controls, dependent upon input from other sensors and switches.

During the experimental setup preparation, it was found that the quality of the signal coming from the built in engine speed sensor had a poor resolution corrupted by the missing flywheel tooth unlike the 360 PPR incremental angular encoder fitted at the end of the engine crank shaft. The binary signal collected by this sensor is amplified and sent to dSPACE which is connected to the PC displays which records the engine speed.

Spark Angle

The spark angle, which is termed also as the spark advance, is an important engine control variable and as such access to its actuation is often desirable. This angle is not be accessible in real time without special power stage hardware. A bespoke power stage designed at the University of Liverpool allows the operator to set the spark advance by bypassing the ECU signal. The work in this thesis fixed the spark advance to prevent any control loops in the ECU effecting the results.

8.9 The Chassis Dynamometer

A chassis dynamometer is a machine for measuring torque or power and speed delivered to its rollers by vehicle wheels. The chassis dynamometer in the University of Liverpool rolling road laboratory is typical of the modern motor-in-the-middle horizontal trunnion mounted type which is very common in modern vehicle industrial applications such as testing and

Table 8.4: Chassis Dynamometer Specifications

Element	Specification
Output power	120 kW
Connection	Shunt
Armature voltage	380 V
Field voltage	300 V
Maximum armature current	280 A
Maximum speed	900 RPM
Maximum torque	2547 Nm at 450 RPM
Inertia	7.0 kg m^2
Air cooling	1300 CFM
Cooling medium maximum temperature	40 °C
Weight	7700 kg

calibration. Full specifications for the chassis dynamometer used can be found in Table 8.4. The biggest disadvantage of the use of the chassis dynamometer unit in automatic control applications is that the vehicle is not operating under the typical conditions that it will experience on the real road [161]. Longitudinal acceleration is one of the missing parameters which is replaced by the dynamometer roller inertia. Although, the dynamometer roller inertia is not equal to the actual test vehicle inertia, it gives an inertia effect to validate the developed control techniques.

8.9.1 Chassis Dynamometer Configuration

The chassis dynamometer consists of two main subsystems as can be seen from Figure 8.7. The Power Absorption Unit (PAU) which is a Direct Current (DC) motor and a pair of 1.218 m diameter steel rollers. These rollers are the surfaces on which the vehicle wheels are set during the test. The chassis dynamometer is also used for applying a resistance torque to the wheels through the rollers during the tests. A schematic of the chassis dynamometer is displayed in Figure 8.8.

8.9.2 Torque Measurement Setup

The torque is measured by measuring the resulting axial force on a load cell linked between the chassis dynamometer torque arm and the dynamometer base as in Figure 8.9. The torque arm is fastened to the motor casing and terminals at a distance $l_t = 534.95$ mm from the centre axis of the dynamometer main shaft. The tangential force F_{dt} (see Figure 8.10) applied to the chassis dynamometer rollers through wheels determines the rotational torque T_d. This torque is equivalent to the inertia torque of the combined physical rollers and chassis

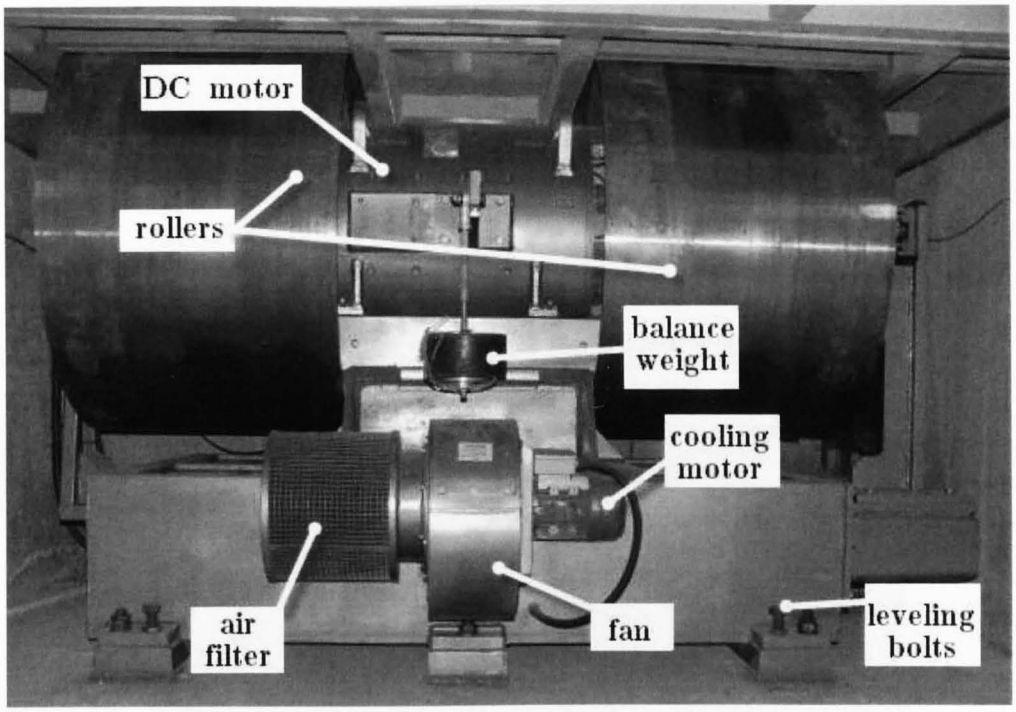

Figure 8.7: Chassis dynamometer

dynamometer main motor shaft and the PAU absorbed torque T_p.

$$T_d = T_p + J_d \dot{\omega}_d \tag{8.1}$$

The PAU torque or the reaction torque is measured indirectly as modeled in Figure 8.11 by multiplying the force detected on the load cell F_L by the torque arm length l_t

$$T_p = F_L l_t \tag{8.2}$$

The fact that the dynamometer set up is measuring the torque indirectly by measuring the force at the end of the torque arm presents some drawbacks in the measured signal. Ideally, the load cell should measure only the reaction force but significant structural dynamics are found superimposed onto the actual motor response [162].

The electronic scaled ZEMIC H3 load cell with a maximum capacity of 750 kg has been used in the chassis dynamometer torque measurement setup. The load cell was first calibrated in the University of Liverpool Structure laboratory. The load cell calibration curve is displayed in Figure 8.12. A 3rd order function is fitted to the calibration curve and then used to determine the applied force on the load cell from its output voltage. The load cell voltage is amplified to a range of ± 10 V by a special unit as in figure 8.13. This voltage is received as an analog signal by the DS2003 A/D board. This signal is then recorded through a PC computer.

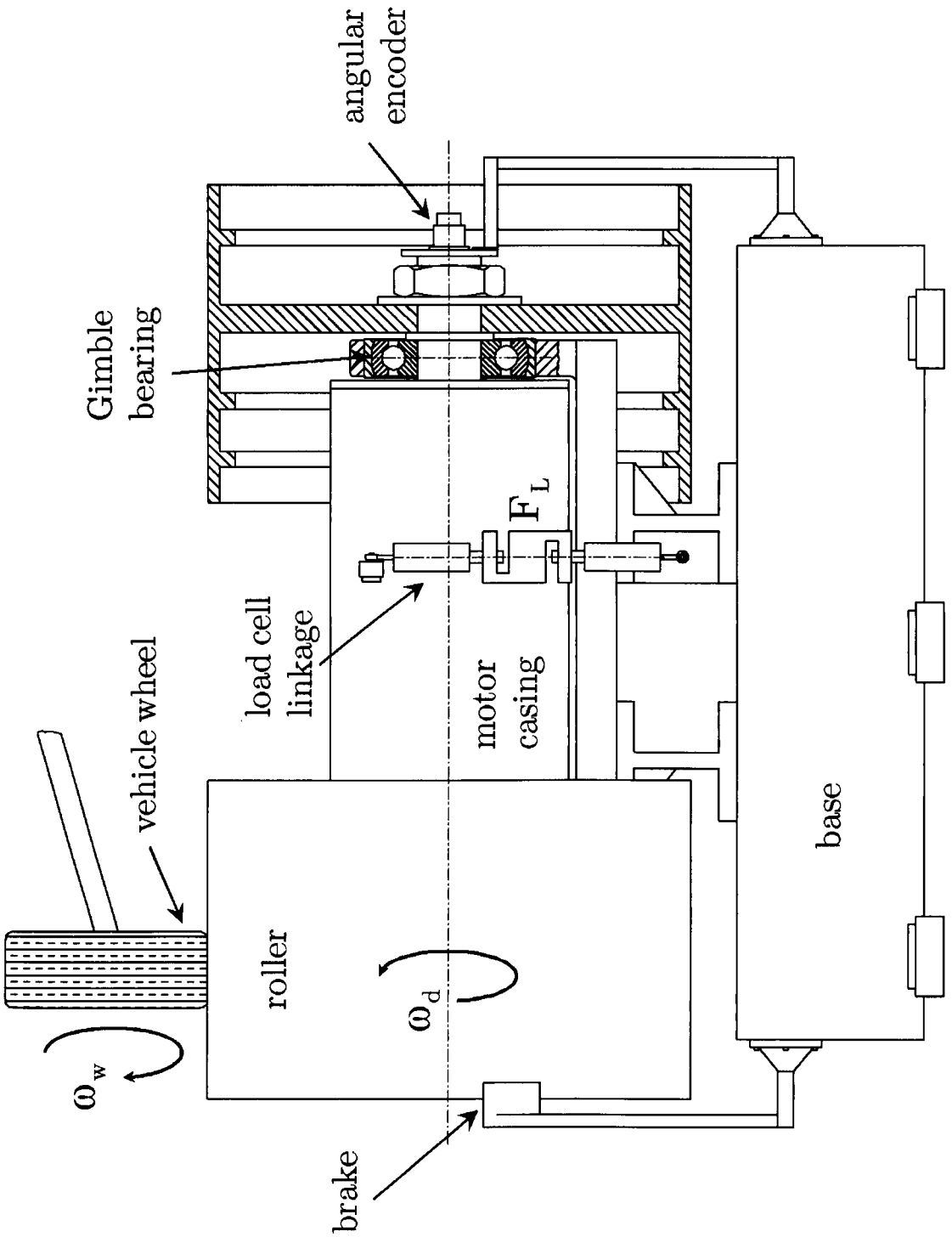

Figure 8.8: Elevation schematic view of the chassis dynamometer

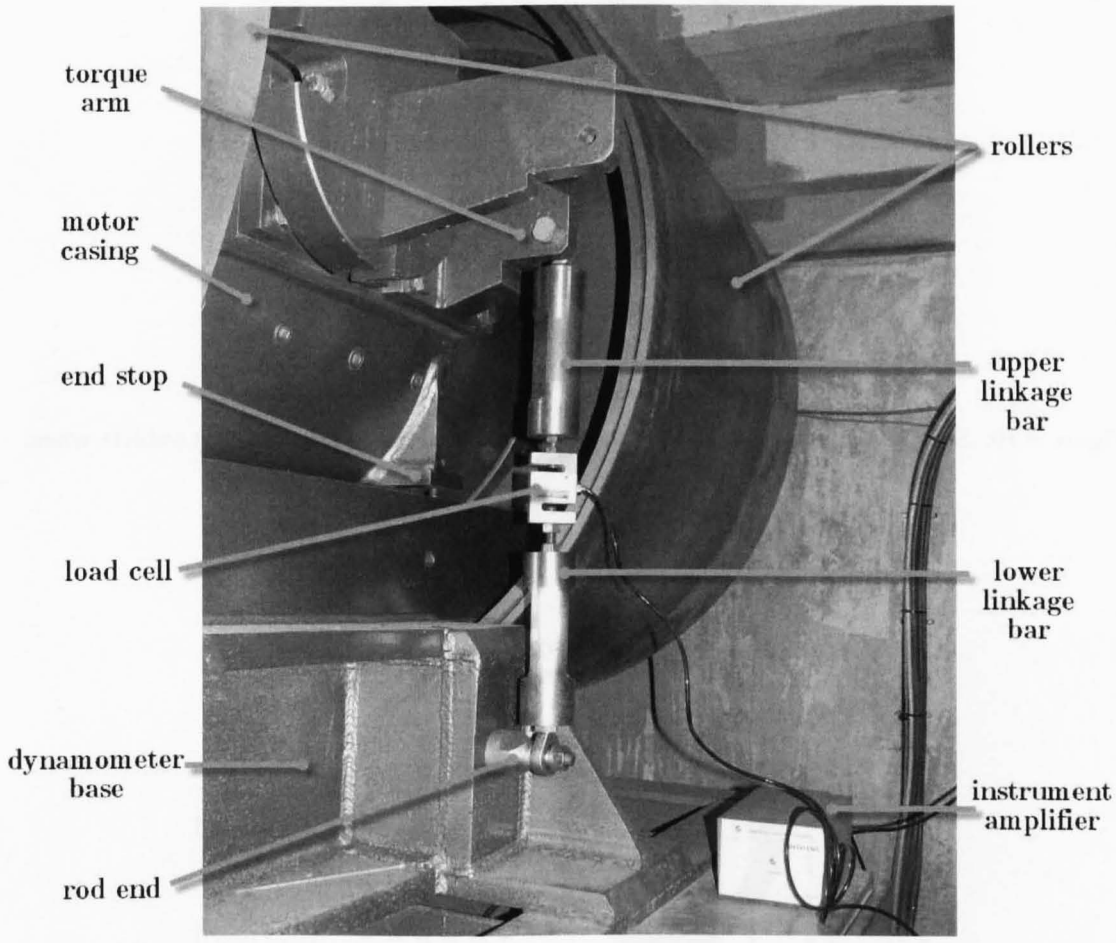

Figure 8.9: Load cell linkage

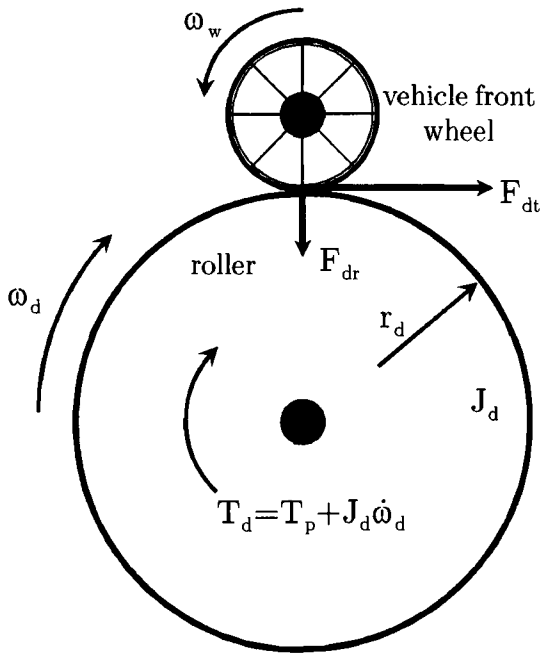

Figure 8.10: Side view schematic of the chassis dynamometer rollers and test vehicle wheel

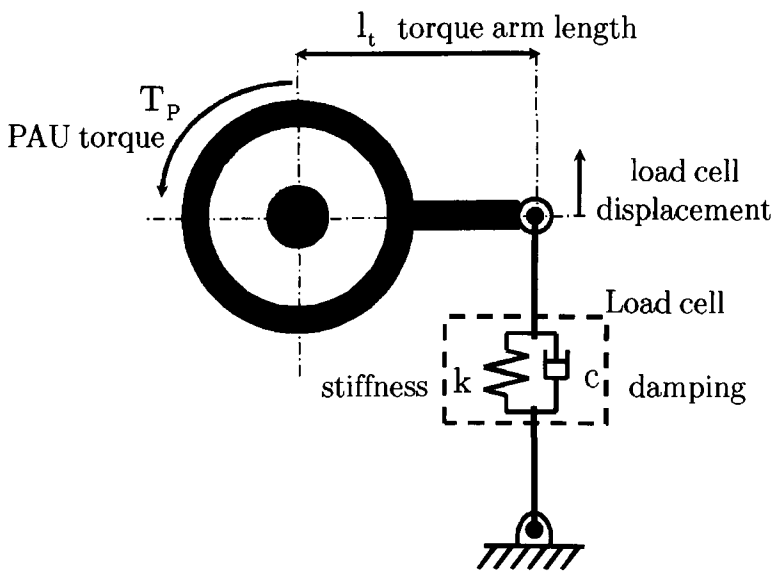

Figure 8.11: Load cell measurement system model

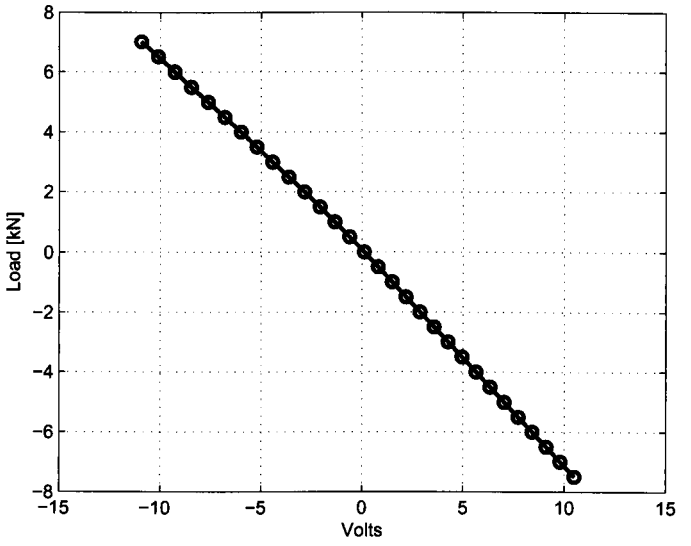

Figure 8.12: Load cell calibration curve

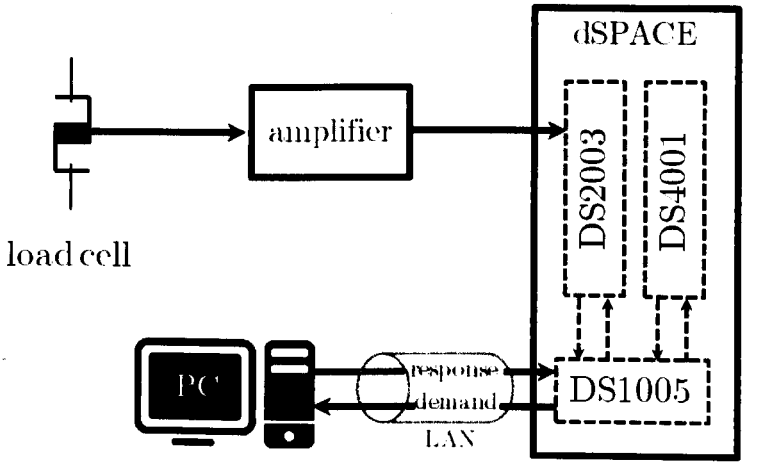

Figure 8.13: Load cell to dSPACE connection

8.10 Electronic Throttle Valve Experimental Setup

The throttle body is located between the air box and inlet manifold. The function of the throttle body is to control the intake of air into the engine. The throttle valve is present inside the throttle body. It is activated in normal vehicle operation by the accelerator pedal position sensor or by a cable in the accelerator pedal.

The electronic throttle valve controller for the experimental work was implemented by dSPACE. A schematic outlining the hardware is given in Figure 8.14 , where can be seen that a PWM signal (20 kHz) is generated using a DS4001 digital I/O board, together with a direction bit (0/1). These signals are passed to an H-bridge motor driver which amplifies these signals and passes these to the electronic throttle valve. The electronic throttle valve used here was a Bosch unit comprising geared DC motor with a 40 mm diameter throttle plate and an angular sensor in the form of a potentiometer. This 0 - 5 V signal is passed to the Analog to Digital A/D DS2003 board , where 0.5 V and 0.45 V were found to correspond to the fully closed and wide open throttle states respectively. Control algorithms where implemented on the DS1005 processor board at a rate of 0.001 s. Data acquisition and real-time inputs to the system were made through Control Desk software operating on a desktop PC.

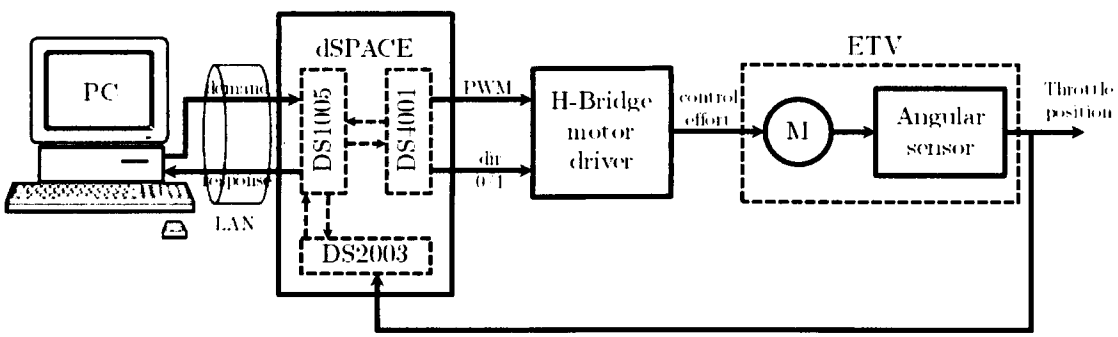

Figure 8.14: Electronic throttle valve experimental setup

8.11 Conclusions

The conclusions of this chapter are:

- The experimental work in this thesis has been carried out using three experimental systems, driveline set, throttle valve set, and IC engine set.
- Full control of equipments was carried out using a PC running the following software: MATLAB, SIMULINK, Real-time Workshop and Control Desk.

- To apply the control theory presented in this thesis on the driveline, a 1430 kg weight five doors Hatchback Ford Mondeo automobile was used.
- An optical encoder was fixed on the centre of the left front wheel hub, to measure rotational speed of the wheels. Similarly, an angular encoder was fitted to the end of the crankshaft. Special arrangements were made to allow fitting of the encoders without affecting the vehicle performance.
- The driveline input demand signal is sent from a desktop PC through dSPACE to the engine management system which can be switched to work in ECU strategy or the dSPACE programmed strategy.
- The ABV works as a throttle bypass valve delivers air when the engine is idle to regulate the engine speed. However, being a solenoid valve makes it fully controllable electronically by the engine management and that was the reason why ABV has been chosen to control the air passing to the engine.
- A dSPACE expansion box has been used with boards DS4001 and DS1005 in the used driveline experimental setup.
- The chassis dynamometer in the University of Liverpool rolling road laboratory has been used in the experimental setup. It is a typical of the modern motor-in-the-middle horizontal trunnion mounted type which is very common in modern vehicles industrial applications such as testing and calibration.
- The function of the throttle body is to control the intake of air into the engine through the throttle valve. Special experimental setup has been made to apply the investigated control techniques on the electronic throttle valve.

Chapter 9

Experimental Driveline Speed Control by NP QFT

9.1 Introduction

A novel NP QFT control design method is presented and experimentally validated in this chapter. In general, A model of a dynamic system is a mathematical representation of its characteristics [4]. This representation should be suitable for control purpose. The purpose of developing a model for the driveline in this study is to allow the design od a controller for the wheel speed in response to the driver demand actuated through the ABV duty cycle. The controlled response is required to be within the desired time domain response limits in terms of tracking and disturbance rejection. Of course, system identification techniques present many ways for constructing models of dynamic systems. The novelty of the presented NP QFT technique is the use of a NP identified model combined with the QFT control method.

In this thesis, locally smoothed NP system identification is used to develop a NP model of the driveline. The QFT method is based on the open loop shaping of the plant templates at certain frequencies distributed within the plant bandwidth in the Nichols chart. The choice of the locally smoothed NP method for identification is ideal when used with the QFT control method as it smooths locally around the specified QFT templates frequencies, whereas the other NP identification methods apply smoothing techniques over the discrete Fourier transform frequency grid which reduces the smoothing efficiency.

In this chapter, experimental validation of the NP QFT method is presented. The experimental setup used in this study is described in details in chapter 8 of this thesis. This chapter starts in section 9.2 by discussing the selection of excitation signal. The process of constructing LTIE I/O data set is explained in section 9.3 Section 9.4 discusses the setting of stability, tracking and disturbance bounds. NP identification of the LTIE set is presented

in section 9.5. Section 9.6 presents a novel method to determine the stable MP nominal equivalent system required by QFT method by the discrete Hilbert transform. System open loop shaping is presented in section 9.7. Prefilter design is presented in section 9.8, and then the experimental results of the controller testing are displayed in section 9.9 and finally, the chapter conclusions are presented in section 9.10.

9.2 Selection of Excitation Signal

The ABV opening controls the air that passes into the inlet manifold of the vehicles engine in the experimental setup used in this thesis. Actually, ABV is used mainly to achieve engine idle speed, however, the vehicle wheel speed is controlled through the throttle valve. The throttle valve opening was fixed at 8° during the tests and all identification and control actions were done by ABV duty instead. The technical reasons behind the use of ABV to control the air passed to the manifold instead of the throttle valve is discussed in section 8.7 of chapter 8, however, an experimental validation of the NP QFT method applied to control of the electronic throttle valve is presented in chapter 10. All data is collected during engagement of the vehicle transmission gearbox in first gear where the backlash and clutch nonlinear effects are usually at their maximum.

The ABV duty signal is normalised, so 1.0 represents fully opened valve opening and 0.0 represents fully closed valve opening. Because the vehicle engine stalls when the normalised ABV duty goes under 0.35, a lower limit of 0.4 is chosen to ensure stable engine running. An upper ABV limit is chosen as 0.85 because the ABV response to the driving signal becomes very nonlinear after this point. The ABV nonlinear response region is avoided to allow focusing on backlash and clutch nonlinearities in this chapter.

9.3 LTIE I/O Data Set

Input and output data is collected for a time period of over 200 s from the driveline experimental setup explained in chapter 8. All signals are sampled on-line each at 0.001 s. The input signals (ABV duty) are formed as PRBS with different amplitude ranges (0.4 to 0.8) and three Perturbation Periods (PP) (2 s, 4 s, and 6 s) for each range. Figure 9.1 shows the elements of the used input data set in which the ABV duty is changed from 0.4 to 0.8. Figure 9.2 show the relevant wheel speed responses in RPM which is the output data set. Both figures display the first 100 s of the collected data. Varying the normalised ABV duty from 0.4 to 0.8 randomly in PRBS causes wheel speed responses up to 200 RPM. The wheel speed response will be tested by demand speeds when the QFT controller and prefilter are designed at the end of this chapter.

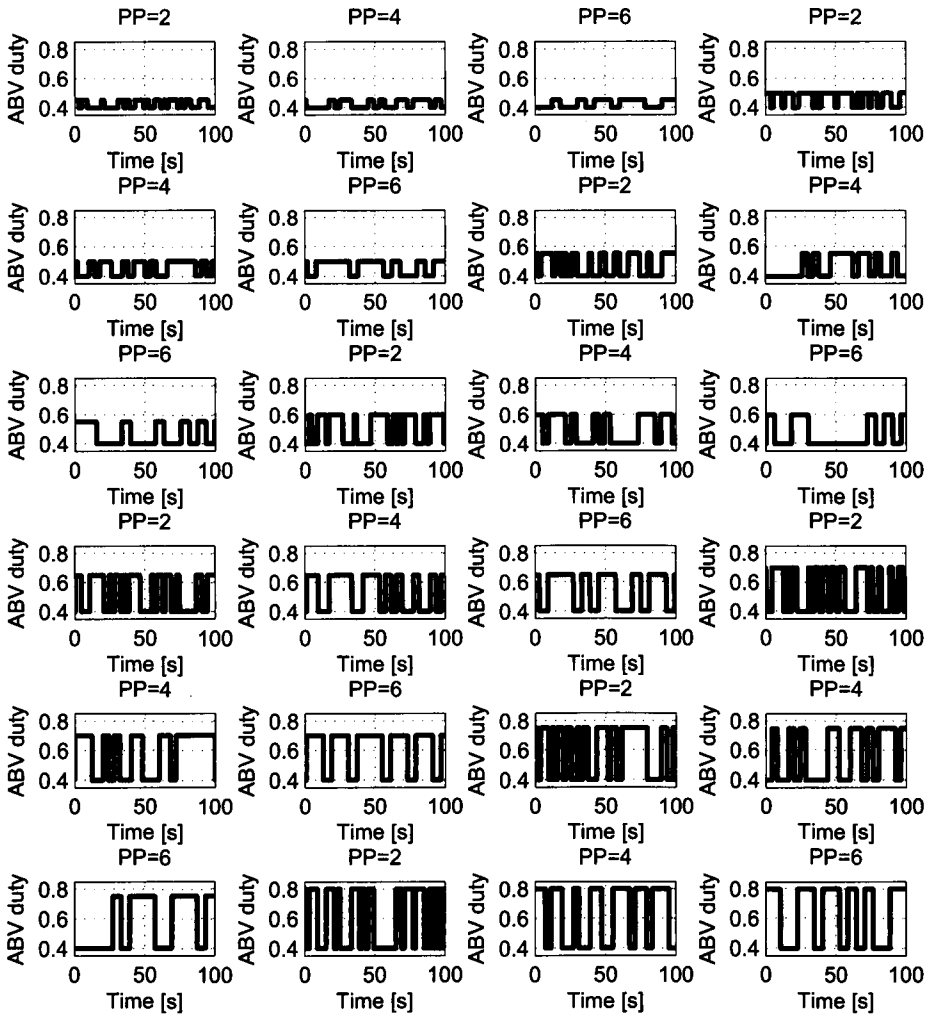

Figure 9.1: Input data set for ABV duty ranges 0.4 to 0.45 in subplots 1,2,3 & 0.4 to 0.5 in subplots 4,5,6 & 0.4 to 0.55 in subplots 7,8,9 & 0.4 to 0.6 in subplots 10,11,12 & 0.4 to 0.65 in subplots 13,14,15 & 0.4 to 0.7 in subplots 16,17,18 & 0.4 to 0.75 in subplots 19,20,21 & 0.4 to 0.8 in subplots 22,23,24

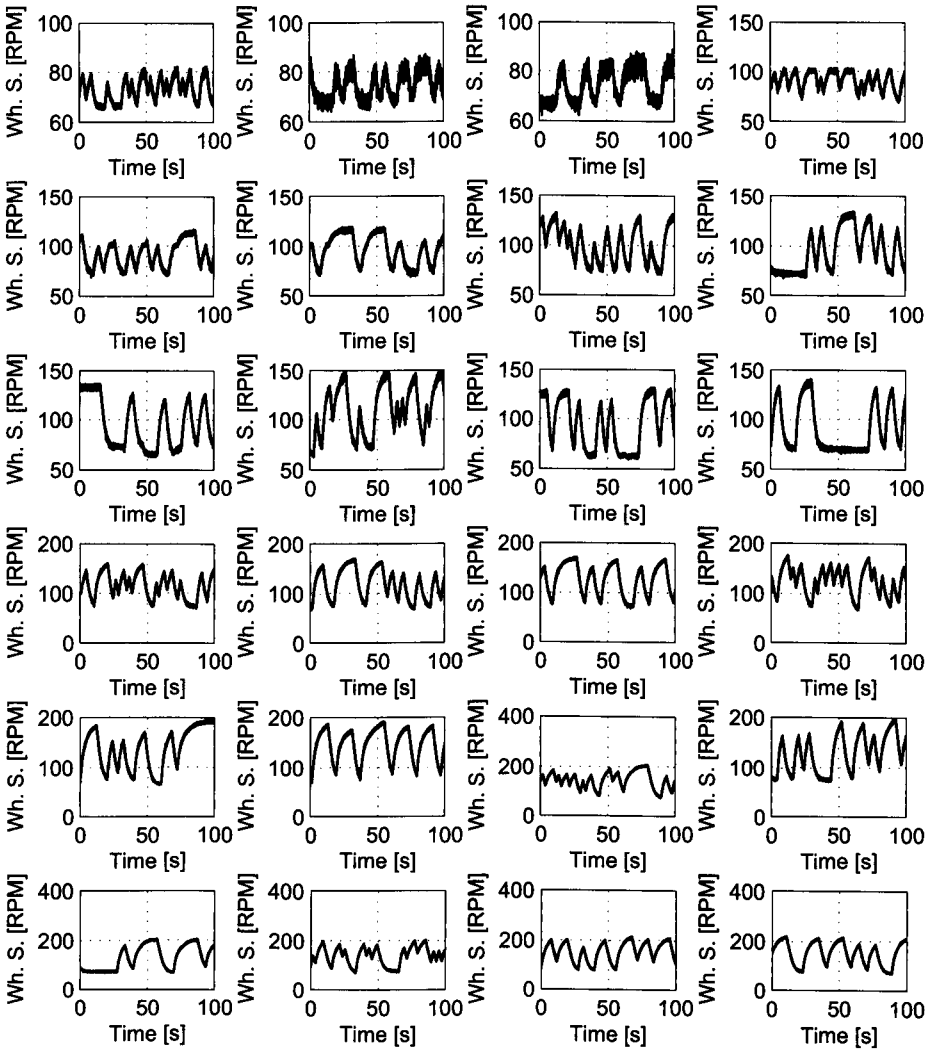

Figure 9.2: Wheel speed responses as an output data set

9.4 Setting of Stability, Tracking and Disturbance Bounds

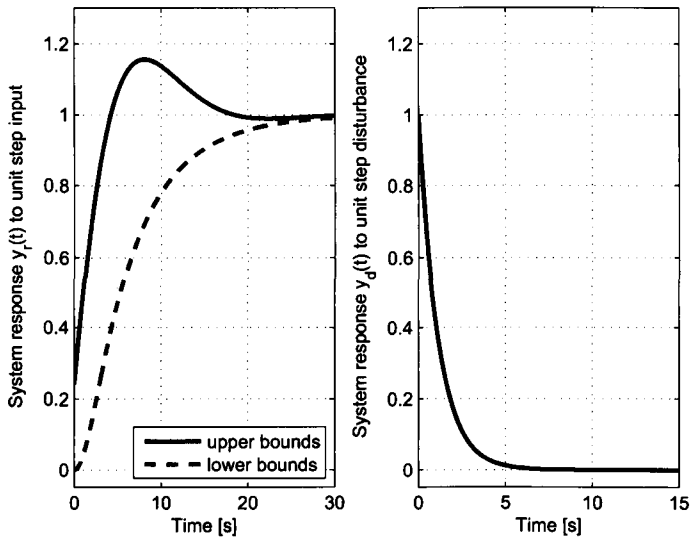

Figure 9.3: Time domain specifications

The QFT tracking boundaries are chosen according to the required time domain specification of the controlled system. In the driveline speed control problem, the upper and lower limits for tracking boundaries have been chosen to achieve a settling time of 20 s, overshoot 16%, and speed disturbance rejection within 14 s as in Figure 9.3. More details about the design of bounds is given in sections 5.5.1, 5.5.2 and 5.8.3 of chapter 5. The upper and lower tracking bounds used in the design for the experimental validations are

$$T_U(s) = \left[\frac{Y_R(s)}{R(s)}\right]_U = \frac{0.2417s^2 + 0.3601s + 0.0841}{s^2 + 0.377s + 0.0841} \tag{9.1}$$

,

$$T_L(s) = \left[\frac{Y_R(s)}{R(s)}\right]_L = \frac{0.05669s^4 + 0.53s^3 + 1.44s^2 + 0.9541s + 0.1837}{0.5051s^6 + 6.584s^5 + 17.08s^4 + 18.37s^3 + 9.47s^2 + 2.25s + 0.1837} \tag{9.2}$$

and the disturbance rejection bound

$$T_D(s) = \left[\frac{Y_D(s)}{D(s)}\right]_U = \frac{s^2 + 0.55s}{s^2 + 1.1s + 0.3025} \tag{9.3}$$

9.5 NP Identification of LTIE Set

The NP linear identification technique using local frequency smoothing estimation, which is described in section 3.5.3 in chapter 3 of this thesis, is used to obtain the driveline plant NP

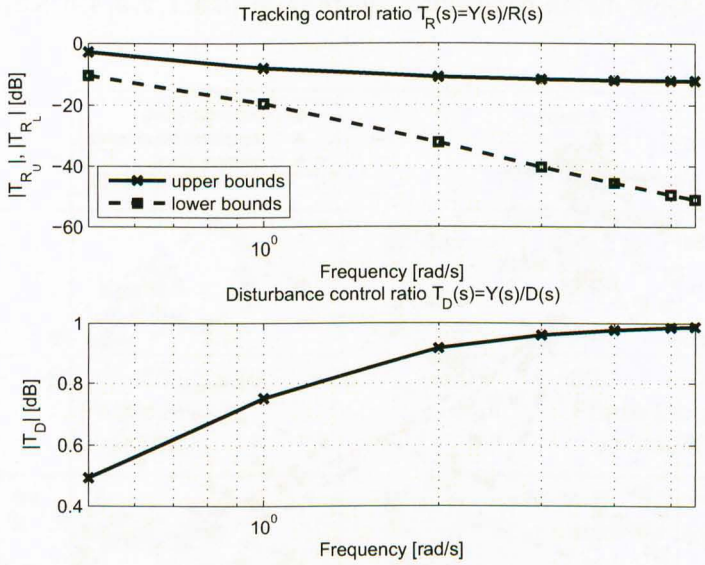

Figure 9.4: Tracking and disturbance rejection boundary widths

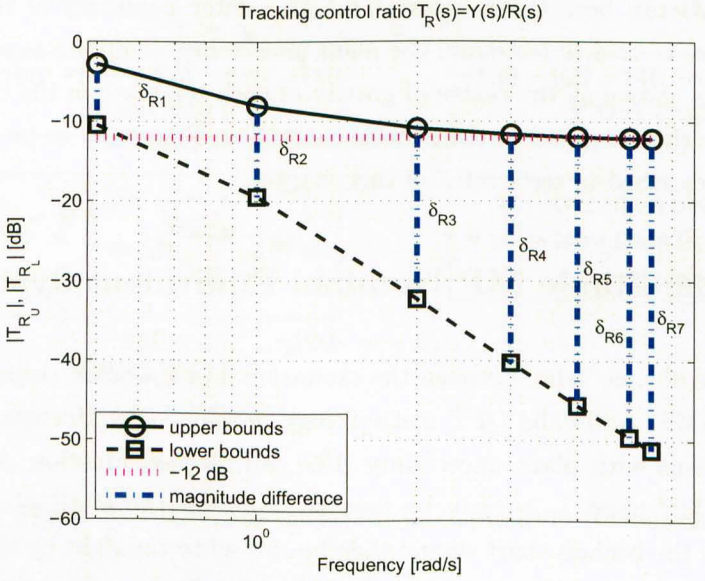

Figure 9.5: Tracking boundaries down to −12 dB

models. The frequency vector Ω_i has been chosen to cover the system bandwidth down to -12 dB according to the guidelines given in [99]. Figure 9.5 shows the selected frequencies distribution over the QFT design bandwidth, where $\Omega_i = \{0.5, 1, 2, 3, 4, 5, 5.5\}$ rad/s.

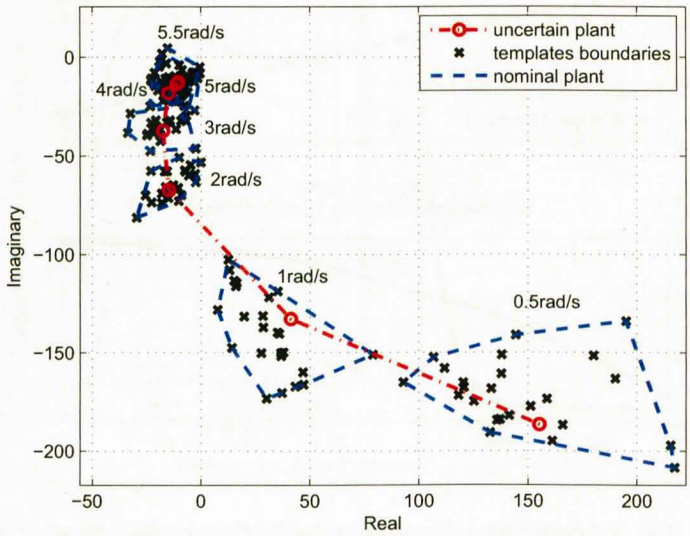

Figure 9.6: Nyquist plot of the driveline uncertainty templates [RPM]

The NP FR representation of each I/O data element of the experimental data set shown in section 9.3 of this chapter is represented by a point at each frequency element of Ω_i in the complex plane as can be seen in Figure 9.6. The outer boundary of these points at individual frequencies is used to construct the plant uncertainty template at each frequency. The nominal plant is chosen as the centre of gravity of each template in the complex plane. Those templates are then mapped to the Nichols chart as in Figure 9.7 to be ready for loop shaping as will be described in section 9.7 of this chapter.

9.6 Determine Stable MP Nominal Equivalent System

Due to the existence of time delay between the excitation and the plant response, the plant is expected to be NMP. As in the QFT methodology developed by Horowitz and Sidi for NMP feedback systems with plant uncertainty [102], an all-pass function $A(s)$ multiplied with an equivalent MP plant $L_m(s)$ can be used to represent the NMP plant. The QFT design boundaries in the Nichols chart should then be shifted to the right by the phase of the all-pass function $A(s)$ before shaping a loop locus of $L_m(s)$ (refer to section 5.9 of chapter 5). This parametric approach cannot be applied in the NP model simply because the unstable zeros are not known as a parametric value, so a different approach suitable for NP models needs to be developed.

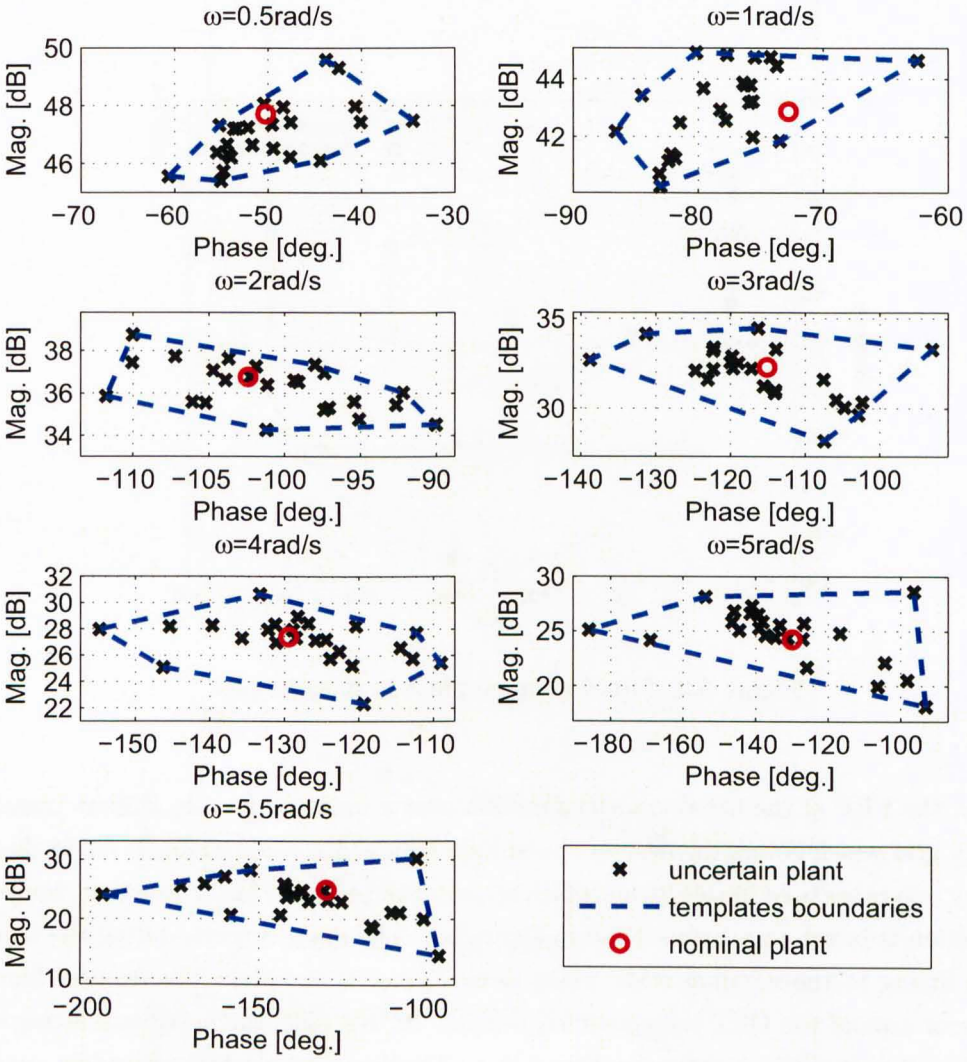

Figure 9.7: Driveline uncertainty templates in Nichols chart

In this thesis, the discrete Hilbert transform is used to determine the locus of the all-pass function locus $A(j\omega)$ by estimating an equivalent MP nominal plant locus $L_{mo}(j\omega)$ of the driveline NMP nominal plant locus $P_o(j\omega)$. Applying the discrete Hilbert transform needs a uniform frequency grid which is not the most suitable form for the set of the frequencies of the QFT templates. To deal with this problem, firstly, a transfer function is fitted to the NMP plant $P_o(j\omega)$ locus as in Figure 9.8 with a small error at the templates frequencies $\omega_i \in \Omega$.

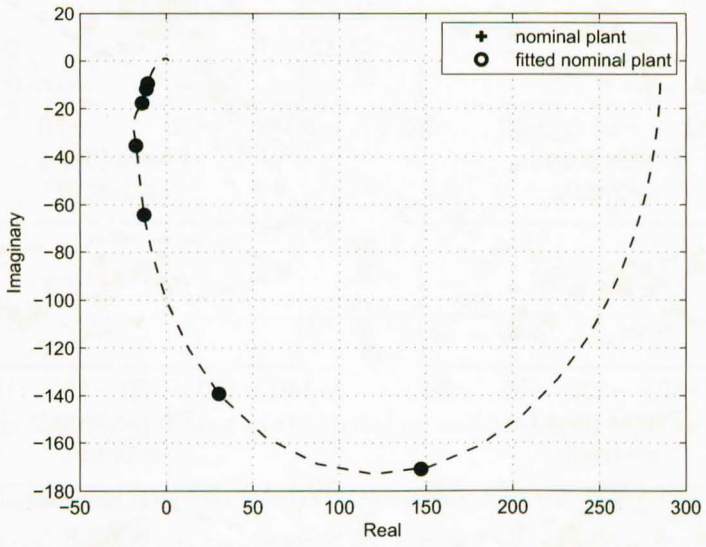

Figure 9.8: Fitted nominal plant in Nyquist plot

Secondly, the FRF of the fitted transfer function over a uniform discrete Hilbert transform frequency grid which covers the desired closed loop bandwidth is determined. 32768 discrete frequency points are used in this fitting which is carried out by the Matlab function "invfreqs". The function is based on a Gauss-Newton algorithm. The main concern during the transfer function fitting to the nominal NMP plant locus $P_o(j\omega)$ is to reduce the transfer function fitting error around the QFT templates frequencies. In this case, the maximum fitting error is less than $9 \times 10^{-10}\%$ as shown in Figure 9.9. Thirdly, a stable MP equivalent nominal plant is estimated by the discrete Hilbert transform and finally the all-pass locus $A(j\omega)$ is formed as

$$A(j\omega) = e^{\angle P_o^*(j\omega) - \angle P_o(j\omega))} \tag{9.4}$$

The equivalent MP plant is constructed as in Figure 9.10.

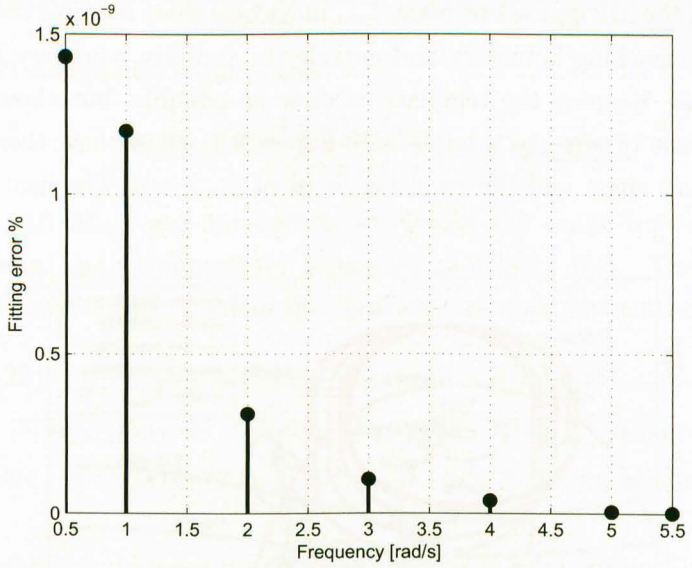

Figure 9.9: NMP NP fitting error

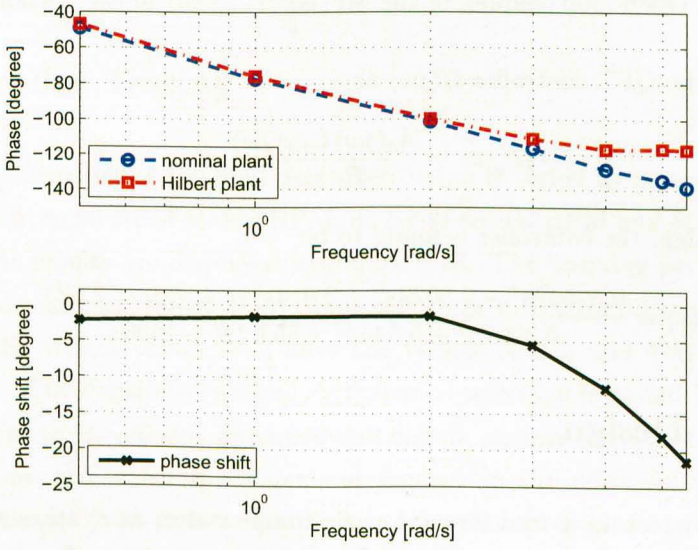

Figure 9.10: All-pass phase shift locus

9.7 Open Loop Shaping

Shaping the locus of the MP equivalent plant L_{mo} in Nichols chart requires that each template should be above the tracking boundary and outside the stability boundary and disturbance rejection boundaries. Keeping the template as close as possible, but above it, is required to keep the magnitude of $\frac{L_o}{1+L_o}$ to a minimum. Figure 9.11 shows how these templates are shaped in the Nichols chart and the resulting locus of $L_{mo}(j\omega)$. The next step is to then

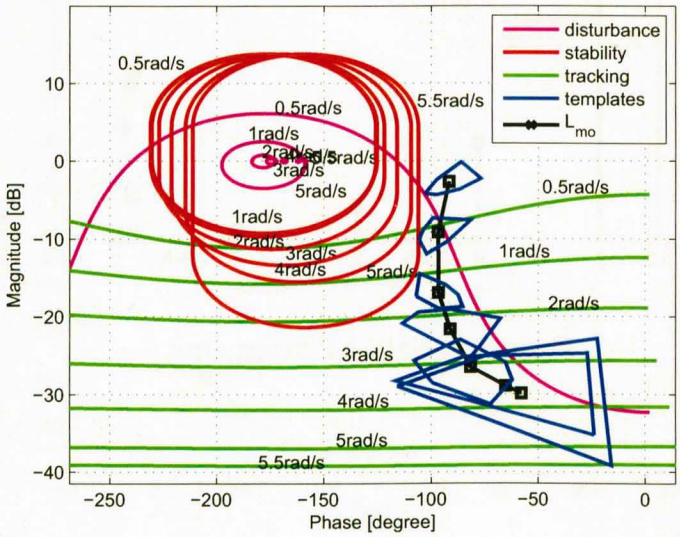

Figure 9.11: Open loop shaping of the MP NP $L_{mo}(j\omega)$ in the Nichols chart

obtain the locus of the QFT controller $G(j\omega)$ as

$$G(j\omega) = \frac{A_o(j\omega)L_{mo}(j\omega)}{P_o(j\omega)} \tag{9.5}$$

In the presented design, the controller is found to be

$$G(s) = \frac{0.02522s^4 + 0.3029s^3 + 2.014s^2 + 4.576s + 2.025}{0.3597s^4 + 5.543s^3 + 552.2s^2 + 1500s} \tag{9.6}$$

9.8 Prefilter Design

The prefilter $F(s)$, which is a feed-forward path compensator, is synthesized to position the system tracking response within the tracking specifications as in Figure 9.5. Detailed descriptions of sequence of the the prefilter design procedure are listed in section 5.11 of chapter 5. The values of the maximum and minimum magnitude M circles in the Nichols chart for each template is captured as shown in Figure 9.12. The obtained values of M_{max},

M_{min} for the closed loop loci are obtained from

$$M_{max}(j\omega) = \frac{L_{max}(j\omega)}{1 + L_{max}(j\omega)} \quad \text{and} \quad M_{min}(j\omega) = \frac{L_{min}(j\omega)}{1 + L_{min}(j\omega)} \tag{9.7}$$

However, the QFT design also requires that

$$|T_{R_L}(j\omega)| \leq \left| \frac{F(j\omega)L_o(j\omega)}{1 + L_o(j\omega)} \right| \leq |T_{R_U}(j\omega)| \tag{9.8}$$

Because M_{max} and M_{min} are not necessarily within the range between $|T_{R_U}(j\omega)|$ and $|T_{R_L}(j\omega)|$, a forward path compensator is needed to achieve this. The upper and lower limits of the prefilter frequency domain specifications are then determined as

$$20\log_{10}|F_U(j\omega)| = 20\log_{10}|T_{R_U}(j\omega)| - 20\log_{10}|M_{max}(j\omega)| \tag{9.9}$$

$$\text{and} \quad 20\log_{10}|F_L(j\omega)| = 20\log_{10}|T_{R_L}(j\omega)| - 20\log_{10}|M_{min}(j\omega)| \tag{9.10}$$

$$\text{where} \quad 20\log_{10}|F_U(j\omega)| \geq 20\log_{10}|F(j\omega)| \geq 20\log_{10}|F_L(j\omega)| \tag{9.11}$$

Then the prefilter is designed inside those boundaries as shown in Figure 9.13 The successful shaping of $L_{mo}(j\omega)$ together with the required uncertainty tolerance on the unfiltered tracking dynamics allows a guarantee of the required performance robustness. The prefilter for the driveline controller is accordingly determined as

$$F(s) = \frac{0.1818s^2 + 1.109s + 1}{0.125s^2 + 1.35s + 1} \tag{9.12}$$

9.9 Controller Testing

The tracking performance of the final controller design is tested by several step wheel speed demands. Steps from 90 RPM to 180 RPM, 80 RPM to 160 RPM and 80 RPM to 200 RPM were tested. The results are displayed in Figure 9.14. The tracking performance is always satisfying the desired boundaries. Step changes such as in Figure 9.15 in the demand could be applied by the vehicle driver soon after the vehicle launch and during the engagement of the fist gear. The controlled system disturbance rejection is tested by applying a step torque of 450 Nm to the chassis dynamometer rollers against the wheel rotation direction. During these steps the wheel speed demand was set to the reference value of 150 RPM. The disturbance signal was sent as a voltage to the chassis dynamometer DC motor. The applied torque is measured by a load cell fixed 534.95 mm away from the roller's axis. Full details of the torque measurement system in the chassis dynamometer set up are presented in subsection 8.9.2 of Chapter 8. As can be seen from Figure 9.16, the controller demonstrated significant robustness to change in load disturbance. Both loading and unloading show similar

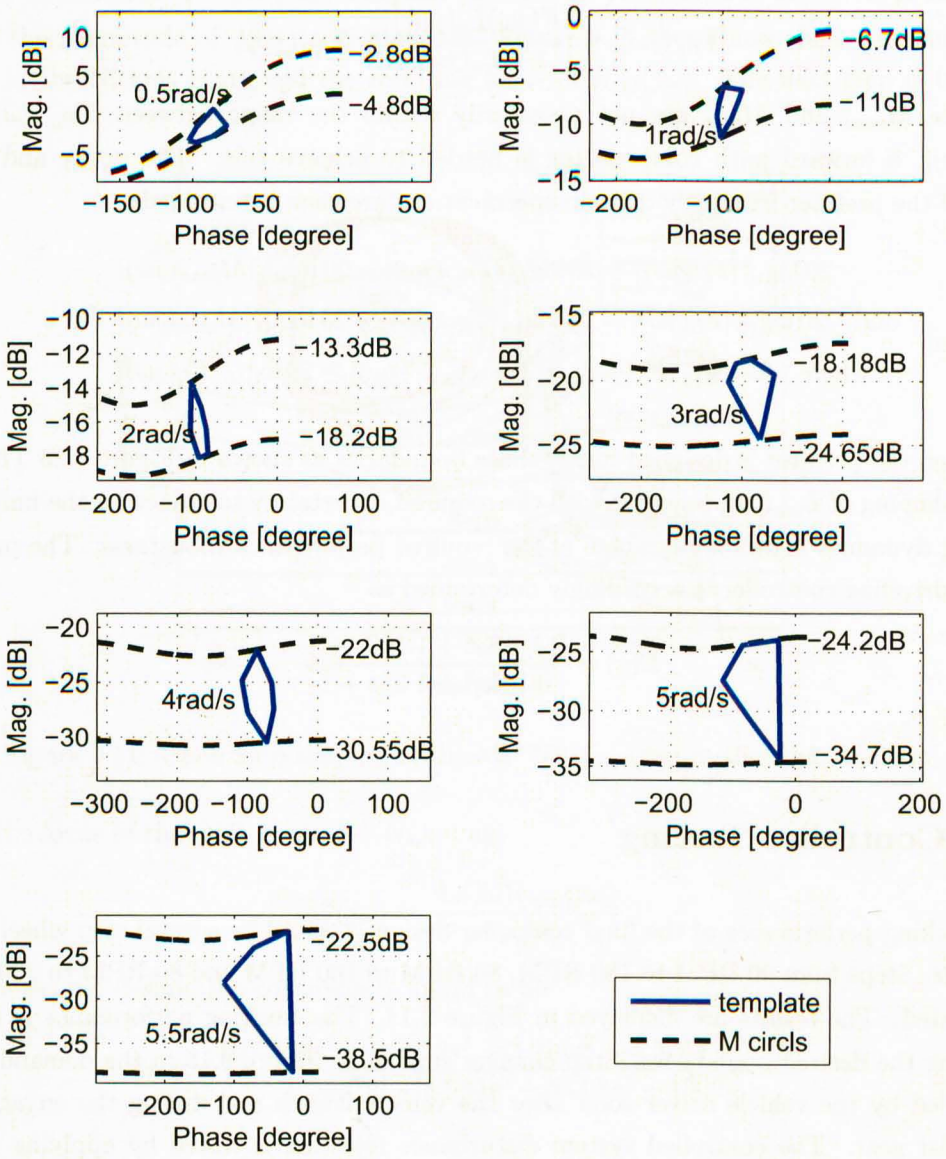

Figure 9.12: Prefilter $F(j\omega)$ design in the Nichols chart

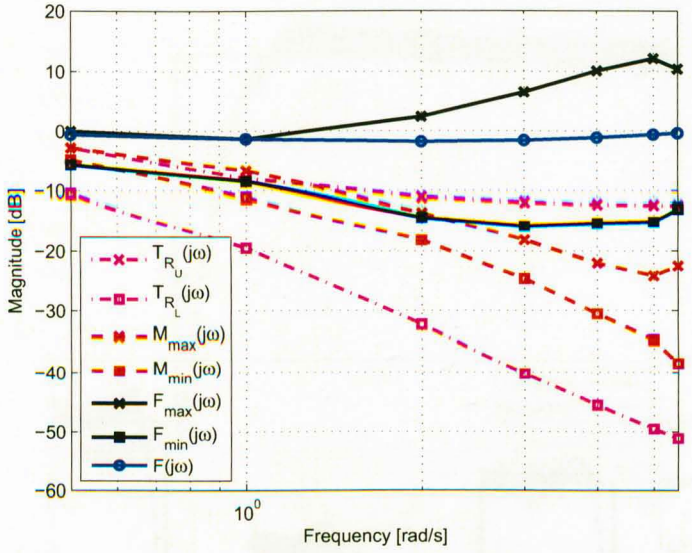

Figure 9.13: Prefilter $F(j\omega)$ design frequency domain boundaries

time response results where the wheel speed returns to ± 5 RPM of the nominal wheel speed in around 9 s. Estimation reveals that the response is always inside the pre-specified time domain closed loop response in Figure 9.3.

9.10 Conclusions

The conclusions of this chapter are:

- A novel NP QFT controller design, to control the driveline speed, has been developed and tested experimentally. NP linear model for the driveline is obtained by using the local smoothing technique and then the plant templates were calculated from it.
- ABV duty has been chosen as an excitation signal in the used experimental set up due to technical reasons. The input signal is formed as PRBS with different amplitudes and different PPs.
- Vehicle wheel speed in RPM was chosen as controlled output variable and special angular encoder was used to capture the dynamics in high resolution.
- A novel technique using the discrete Hilbert transform for determining the necessary phase shift for the QFT design when a NMP plant was applied.
- The tracking performance for the driveline with the designed controller has been tested by several step speed demands. The tracking performance was found to satisfy the

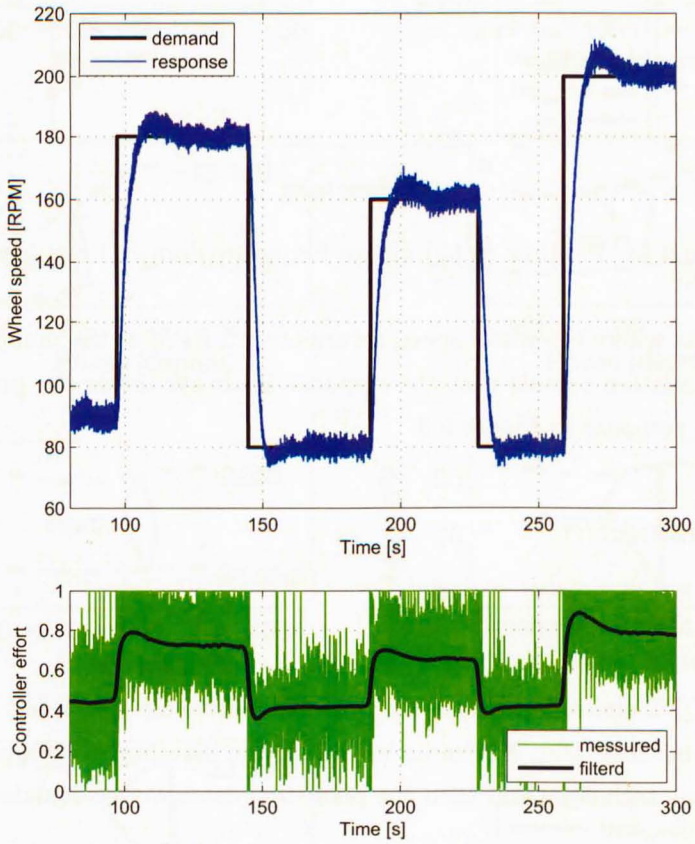

Figure 9.14: Controller tracking performance testing

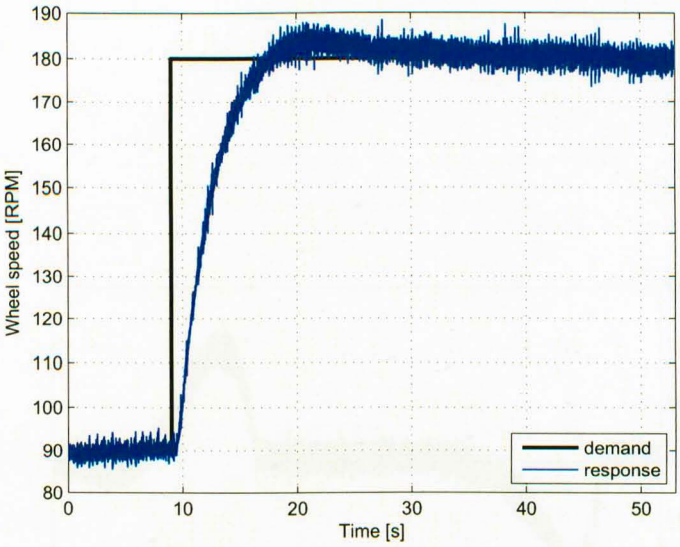

Figure 9.15: Controlled system step response

desired boundaries.

- The controlled system disturbance rejection is tested by applying a step torque to the chassis dynamometer rollers against the wheel rotation direction. The resulting speed disturbance is rejected within the desired boundary.
- The experimental validation of the presented NP QFT control design method shows the capability of designing an effective controller able to maintain the vehicle wheel speed response within the desired boundaries.

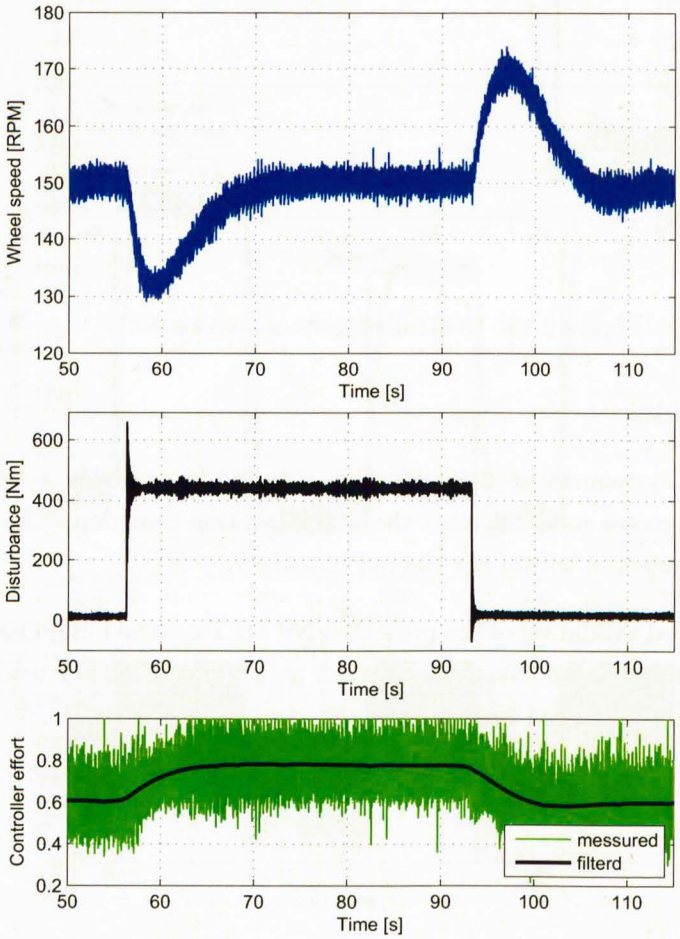

Figure 9.16: Disturbance rejection response in the controlled system

Chapter 10

Electronic Throttle Control by a NP QFT Method

10.1 Introduction

This chapter presents the application of a new systematic NP nonlinear QFT control methodology for the design of feedback controller designed for a gasoline electronic throttle valve seen in Figure 10.1. The method produces highly optimised linear feedback and linear feedforward compensators tailored to the nonlinear dynamics of the electronic throttle valve. The approach uses an entirely black-box approach in which the controllers are developed directly from experimental testing. In the experimental study presented, a NP linear identification approach is used to obtain the plant uncertainty templates directly from test data. These templates are then used to choose the nominal system loop shape by which satisfying the design requirements. The open loop function is thus obtained as a discrete FRF to which is fitted a discrete transfer function to obtain the parameterised discrete controller transfer function. Notwithstanding that nonlinear compensation could significantly enhance the outcomes of the process further, it is shown that an effective linear controller can be designed by the method without any nonlinear compensation and with an acceptable time response in a quick and systematic method from readily obtained test-data.

In this chapter, a background of the electronic throttle is presented in section 10.2. A description of the novel NP nonlinear QFT method is presented in section 10.3. This includes the choice of a set of typical inputs in subsection 10.3.1, Electronic Throttle Valve NP identification in subsection 10.3.2, electronic throttle valve performance tracking models in subsection 10.3.3, synthesis of nominal loop transmission locus in subsection 10.3.4, and electronic throttle valve controller prefilter design in subsection 10.3.5. Finally, the chapter conclusions are presented in section 10.5.

Figure 10.1: Bosch DV-E5 electronic throttle valve

10.2 Electronic Throttle

The electronic throttle is a servo-operated throttle valve which is a key component in current Engine-Management System (EMS) control of the gasoline engine. The corresponding electronic throttle valve control problem is acknowledged as an outstanding problem to the extent that it has been the subject of a recent IFAC benchmark control study [163, 164]. This electronic throttle valve control problem is that of establishing a systematic robust process for efficiently calibrating and tuning the servo control to maximize the attainment of the potential gains in fuel economy and emission reduction from the drive-by-wire technology. Typical of the recent research on this topic is that of Yang [165] who develops a Proportional Integral Derivative (PID) controller supplemented with additional term to compensate the electronic throttle valve nonlinearity. The design methodology in [165] cannot guarantee that no overshoot will exist, however the presented controller was designed to have a little or no overshoot. A further electronic throttle valve strategy including compensation of of friction and limp-home effects is presented in [166]. A dynamic friction model is developed and a PID controller with a feedback compensator is produced and verified by simulation and experiments. Another PID controller with nonlinear compensator is presented in [167] where an adaptive control strategy is applied. Yuan and Wang [168] presented an approxi-

mate model-based robust nonlinear control strategy for the electronic throttle valve. In this chapter, no nonlinear compensation is done. The idea is to find the best linear controller without any compensation at all. The linear design process is much quicker and more economical than one involving a nonlinear compensator. An economic approach would be to establish the limit of the linear compensator and only proceed to supplement this with the more involved nonlinear compensation if this proves insufficiently performance. The same linear compensator design method is then simply applied to the electronic throttle valve in tandem with the nonlinear compensation. The power of the proposed strategy is its ability to be applied on any electronic throttle valve with any size and characteristics. Nonlinear compensator design, in contrast, is generally individually designed for a particular electronic throttle valve type so the complex process of identifying the nonlinearity and providing compensation is required to be repeated with each new electronic throttle valve variant. The NP QFT approach enables the designer to quickly design a highly optimised linear controller and to systematically trade-off overshoot and settling time in the same way for any type of electronic throttle valve.

The electronic throttle valve experimental setup is described in section 8.10 of Chapter 8. The input signal is a PWM signal ($-1 : 1$ V) and the output signal is an electronic throttle valve angular sensor voltage, where 0.5 V and 0.45 V were found to correspond to the fully closed and wide open throttle states respectively.

10.3 NP Nonlinear QFT

In the QFT technique the closed loop specifications are translated into 'QFT bounds' in the Nichols chart to specify the allowable range of the nominal open loop responses [154]. The design is completed when a nominal loop transmission is shaped which achieves nominal closed loop stability and lies within the QFT bounds. In QFT it is usual to then use any remaining design freedom to minimise the gain especially at high frequency. An important feature of linear or nonlinear QFT is that it allows for the design of two-degrees of freedom systems in the presence of uncertainty. In other words, the technique allows the design of a feedback controller G and a prefilter F (see Figure 10.2) to satisfy desired specifications. In general, specifications in the QFT formulation are expressed by the following three constraints [169]:

1. Robust stability margin

$$\left|\frac{L(j\omega)}{1+L(j\omega)}\right| \leq \gamma \tag{10.1}$$

2. Tracking performance

$$T_{R_L}(j\omega) \leq \left| \frac{F(j\omega)L(j\omega)}{1+L(j\omega)} \right| \leq T_{R_U}(j\omega) \tag{10.2}$$

3. Disturbance attenuation performance

$$\left| \frac{1}{1+L(j\omega)} \right| \leq T_D(j\omega) \tag{10.3}$$

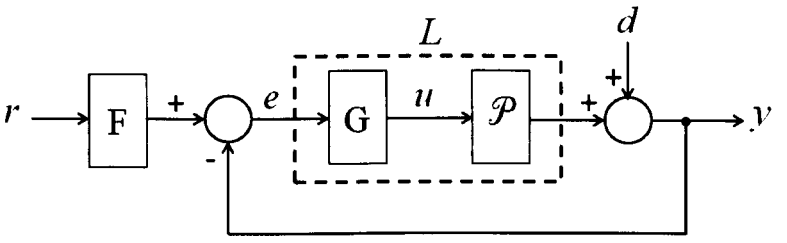

Figure 10.2: QFT structure

where $L(j\omega)$ is the open loop transfer function represented by $L(j\omega) = G(j\omega)P(j\omega)$, and $P(j\omega) \in \mathcal{P}$, where $P(j\omega)$ is a plant in the set of uncertain plants $\mathcal{P}$. Because the system investigated in this chapter is nonlinear since it is affected by friction and limp-home torque, so a different frequency responses loci are possible for each different input applied. The QFT design procedure applied on the throttle valve presented here is described by the following sequence of steps:

10.3.1 Choose a Set of Typical Inputs

A set of typical input signals which are sufficient to cover the expected input operating range is selected. Thus, a set of 14 Pseudo Random Binary Signal (PRBS) is used with amplitudes ranged from 2.5 to 4.5 V. Figure 10.3 shows the elements of the I/O data used for the application.

10.3.2 Electronic Throttle Valve NP Identification

The NP identification technique used in this chapter is described in section 7.4 of Chapter 9. The selected frequencies for the electronic throttle valve NP identification are 1, 6, 12, 18, 24, 30, 36 and 42 rad/s). These frequencies are selected to cover the electronic throttle valve bandwidth as following the guidelines in [165]. The local smoothing technique [63] is based on choosing a frequency vector which contains the selected frequencies according to the system under investigation.

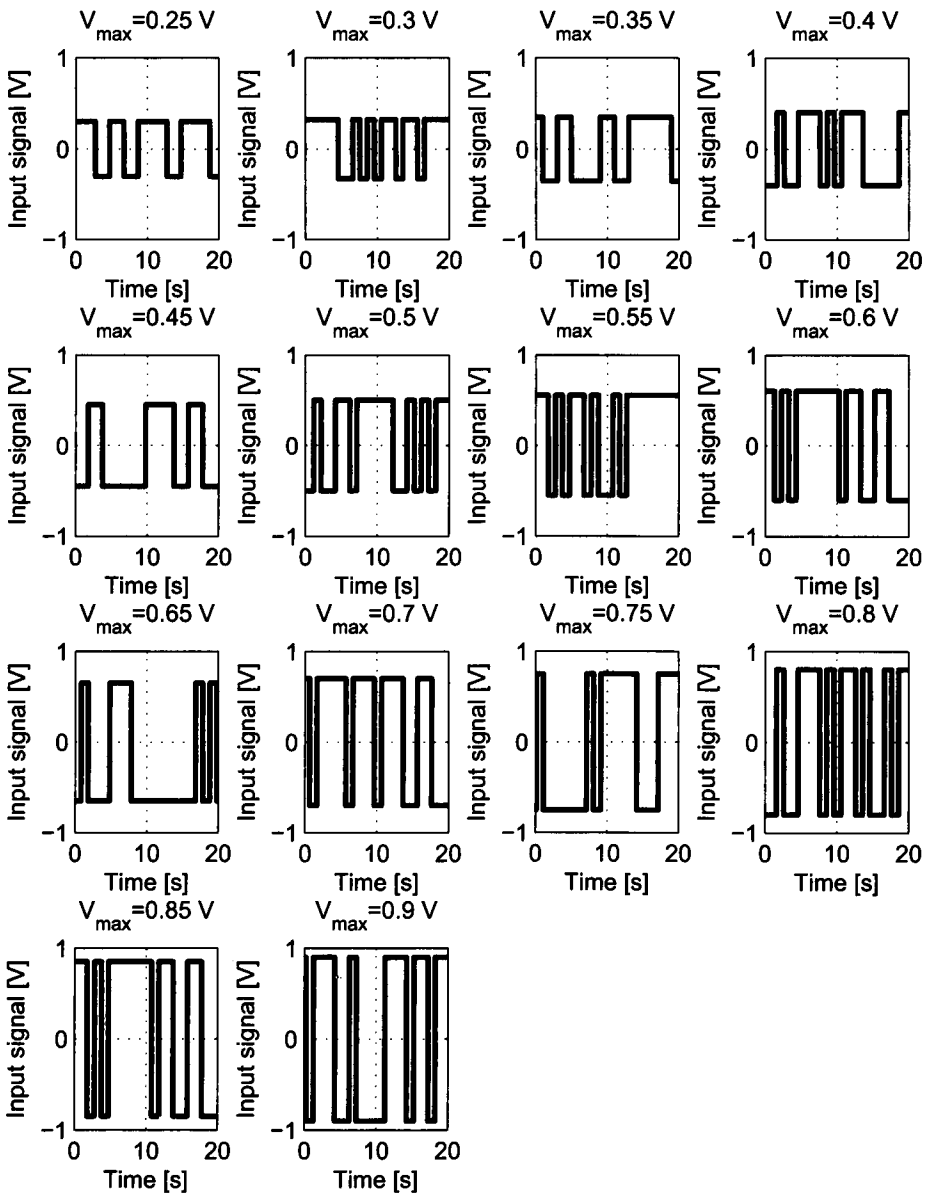

Figure 10.3: Typical elements of the input data set

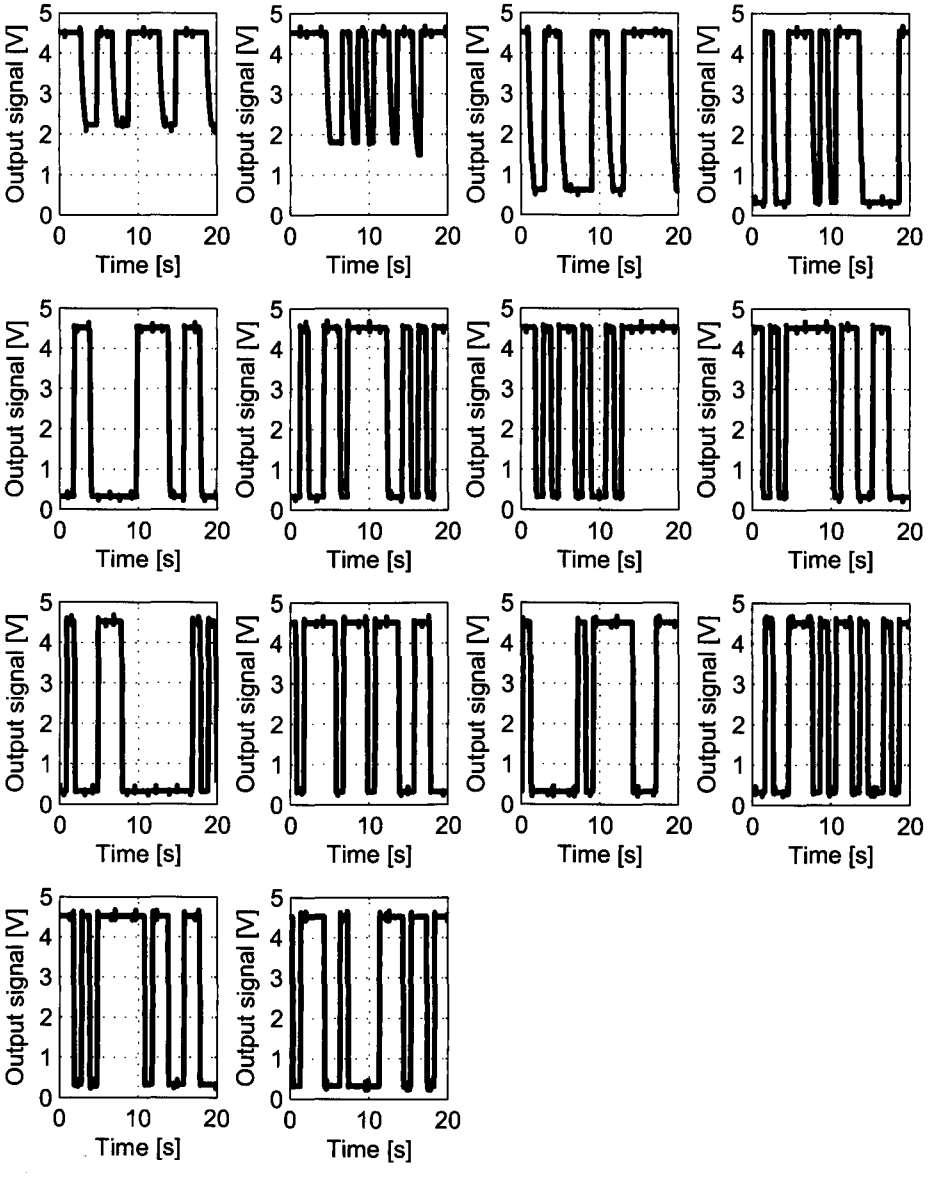

Figure 10.4: Typical elements of the output data set

As the system is nonlinear, each I/O data element gives a different point in the complex plane at any frequency within the system bandwidth. The outer boundary of those FR points form the plant uncertainty templates at each frequency. Forming the convex hull of the FR points at each frequency gives the structured uncertainty templates of Figure 10.5, which represent the stuctured uncertainty required for the non-conservative robust control design. The nominal plant is obtained by finding the centres of the minimum radius circles in the complex plane which contain all FR points at each frequency.

10.3.3 Electronic Throttle Valve Performance Tracking Models

For the electronic throttle valve control problem, the required system tracking performance limits for $Y(s)/R(s)$ are initially designed to meet a settling time of 0.2 s with no Overshoot (OS). Similarly, the disturbance rejection bound $Y(s)/D(s)$ is designed to make any disturbance signal decay within 0.2 s as well.

Since the closed loop disturbance attenuation specification requires the uncertain plant time response to be kept lower than or equal a specified value, the frequency domain disturbance specification is represented by only an upper bound. Accordingly the upper frequency domain response bound was taken as

$$T_{R_U}(s) = \left[\frac{Y_R(s)}{R(s)}\right]_U = \frac{1931}{s^2 + 80s + 1931} \quad , \tag{10.4}$$

the lower response bound as

$$T_{R_L}(s) = \left[\frac{Y_R(s)}{R(s)}\right]_L = \frac{506.3}{s^2 + 40.5s + 506.3} \quad , \tag{10.5}$$

and the disturbance rejection bound as

$$T_D(s) = \left[\frac{Y_D(s)}{D(s)}\right]_U = \frac{s^2 + 30s}{s^2 + 60s + 981} \quad . \tag{10.6}$$

The time domain bounds corresponding to these, T_{R_U}, T_{R_L}, and T_D are shown in Figure 10.6.

10.3.4 Synthesis of Nominal Loop Transmission

The plant templates are then mapped to the Nichols chart as in Figure 10.7, and shaped within the stability margin contour $20log_{10}(\gamma)$, disturbance rejection boundaries $T_D(j\omega)$ and time domain performance boundaries $T_U(j\omega)$ and $T_L(j\omega)$ as for conventional QFT [154]. The nominal loop transmission function $L_o(s) = G(s)P_o(s)$ that satisfies all the bounds and the stability contour is then synthesised to minimise the overall loop gain. For the electronic throttle valve problem the resulting controller was then found by the novel NP QFT methods

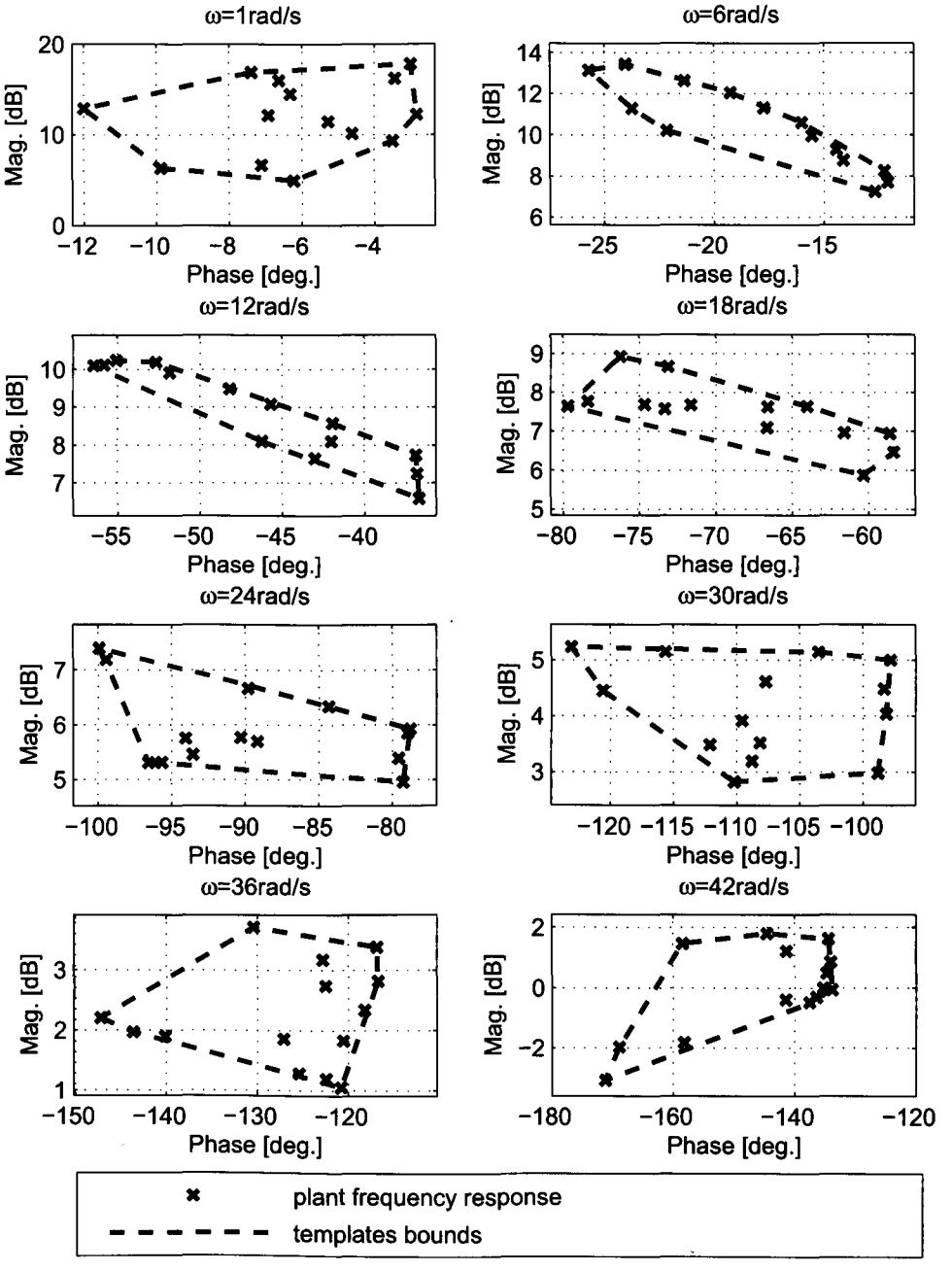

Figure 10.5: Plant templates in the Nichols chart

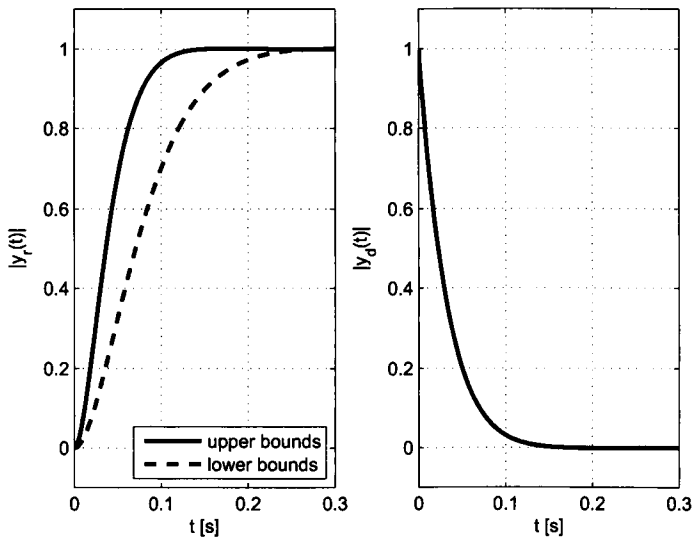

Figure 10.6: System time domain tracking performance specifications

as

$$G(z) = \frac{b_0 z^3 + b_1 z^2 + b_2 z + b_3}{a_0 z^3 + a_1 z^2 + a_2 z + a_3} \tag{10.7}$$

where

$a_0 = 1$, $a_1 = -1.719$, $a_2 = 0.6893$ and $a_3 = 0.02958$, $b_0 = 14.82$, $b_1 = -27.73$, $b_2 = 12.16$, $b_3 = 0.761$.

10.3.5 Electronic Throttle Valve Controller Prefilter Design

Following the conventional QFT procedure [99], the prefilter $F(s)$ is finally synthesized to position the system tracking response within the tracking specifications. The successful shaping of $L_o(j\omega)$ together with the required uncertainty tolerance on the unfiltered tracking dynamics allows a guarantee of the required performance robustness. The prefilter used with the desired controller was accordingly found as

$$F(z) = \frac{0.009009z + 0.009009}{z - 0.982} \tag{10.8}$$

10.4 Experimental Results and Discussion

The controller may be adjusted to eliminate any overshoot (OS) by suitable choice of M-circle value. The fully opening valve response for the corresponding zero OS controller was obtained as shown in Figure 10.8, and the fully closing valve response was as in Figure 10.9. The

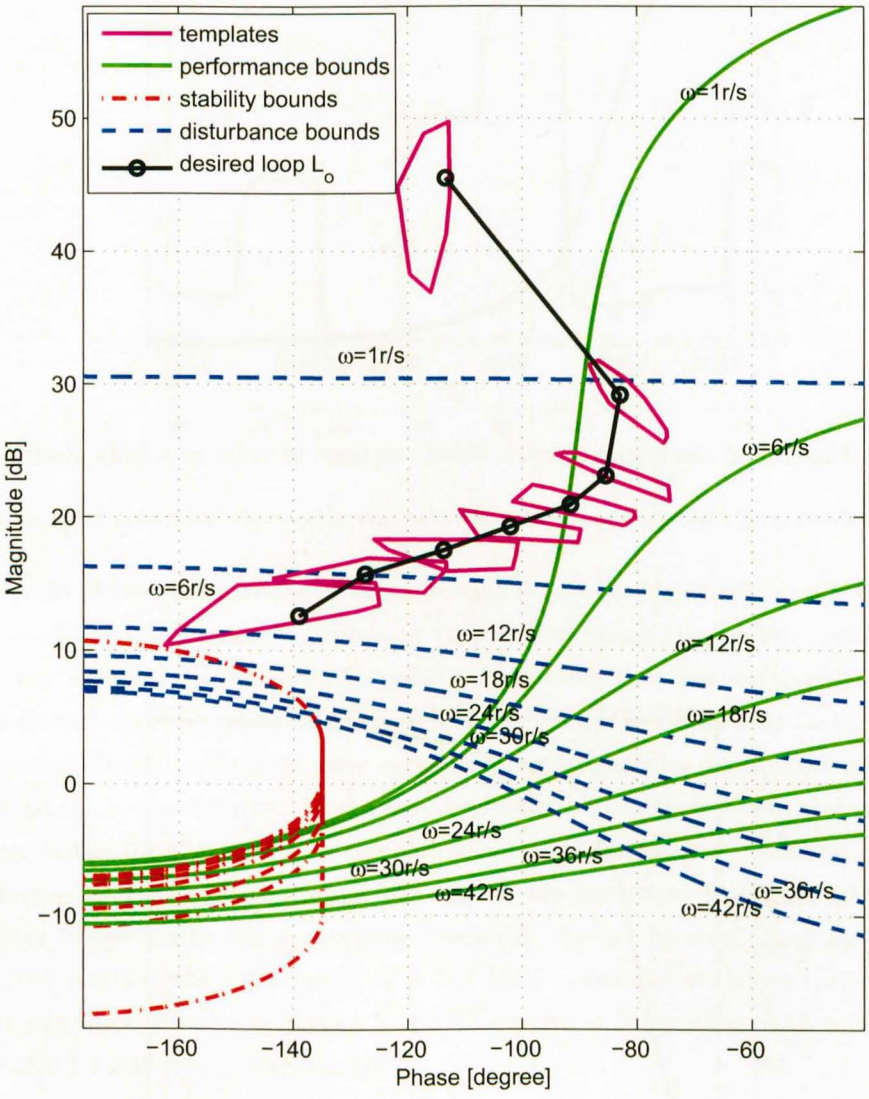

Figure 10.7: Nichols chart with QFT bounds

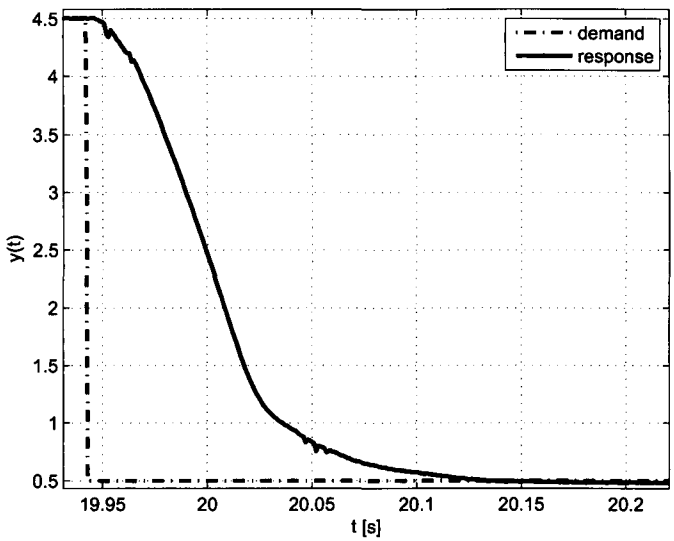

Figure 10.8: Controlled electronic throttle valve response in volts to a fully open demand

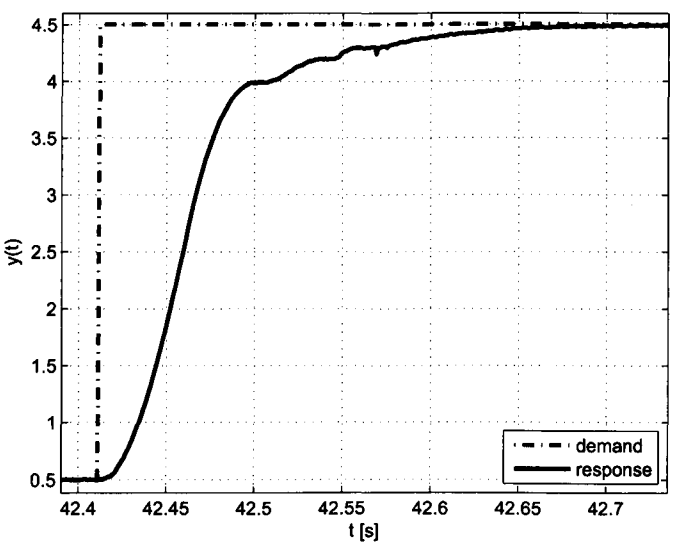

Figure 10.9: Controlled electronic throttle valve response in volts to a fully closed demand

resulting controller is very satisfactory when a random step input is applied as can be see from Figure 10.10 where it is seen to overcomes the friction and limp-home effect effectively even with a slow sinusoidal wave demand of 0.5 rad/s as in Figure 10.11 Although not very

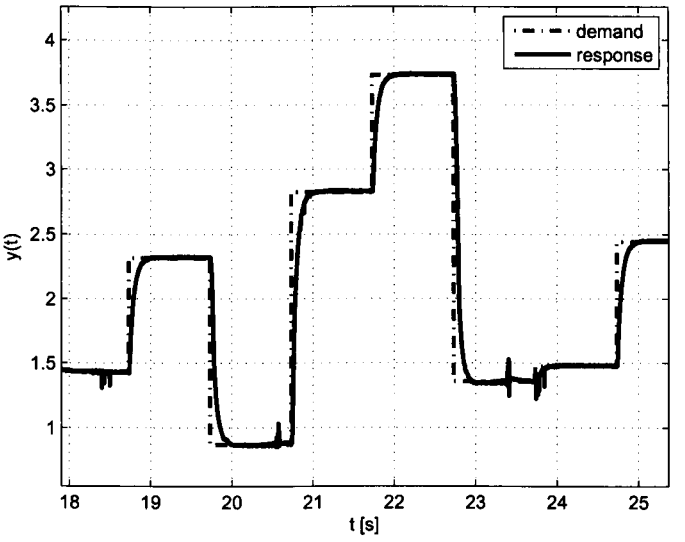

Figure 10.10: Controlled electronic throttle valve response in volts to a random demand

much external physical disturbance force or torque is expected in the electronic throttle valve working conditions, it is always important to test how much the desired controller is able to reject any external disturbance. In order to test the controlled electronic throttle valve against a disturbance signal, a sudden physical force is applied manually to the valve plate. The controlled electronic throttle valve succeeded in rejecting the disturbance as can be seen in Figure 10.12. Since different choices may be made in the OS rise-time response trade-off a guideline figure for the presented method is obtained for several iterations of the design with different M-circle specifications. The results are presented in Figure 10.13 to enable the designer to determine the appropriate trade-off. As can be seen, allowing only a small OS of 0.09% could enable the design of a NP QFT controller with rise-time 0.08 s when the electronic throttle valve is closing and 0.09 s when it is opening, with a corresponding rise-time of 0.1 s and 0.28 s respectively.

10.5 Conclusions

The conclusions from this chapter are:

- A systematic nonlinear QFT method based on NP identification is presented for the design of electronic throttle valve controllers. NP identification is carried out to obtain

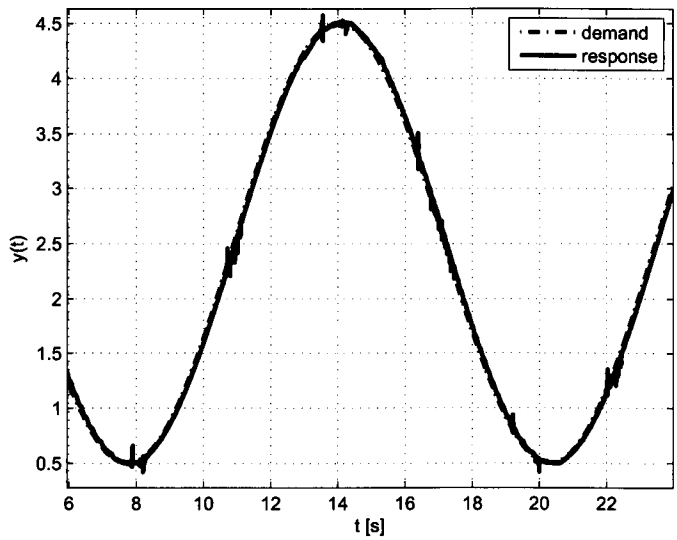

Figure 10.11: Controlled electronic throttle valve response in volts to a 0.5 rad/s sinusoidal wave demand

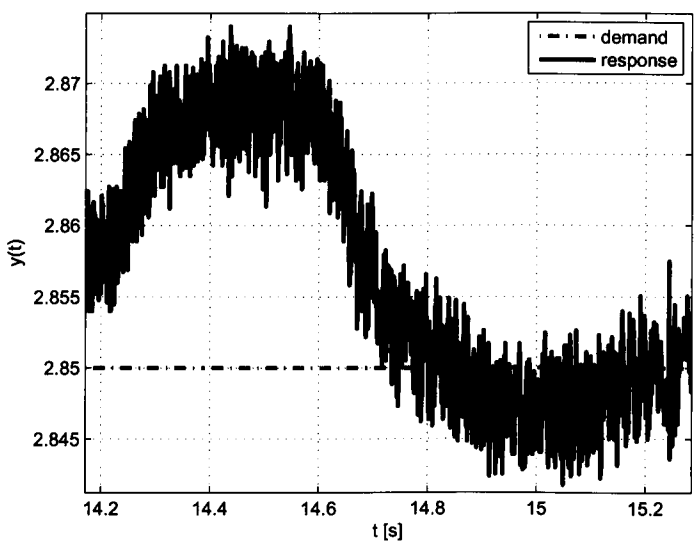

Figure 10.12: Controlled electronic throttle valve response to external disturbance

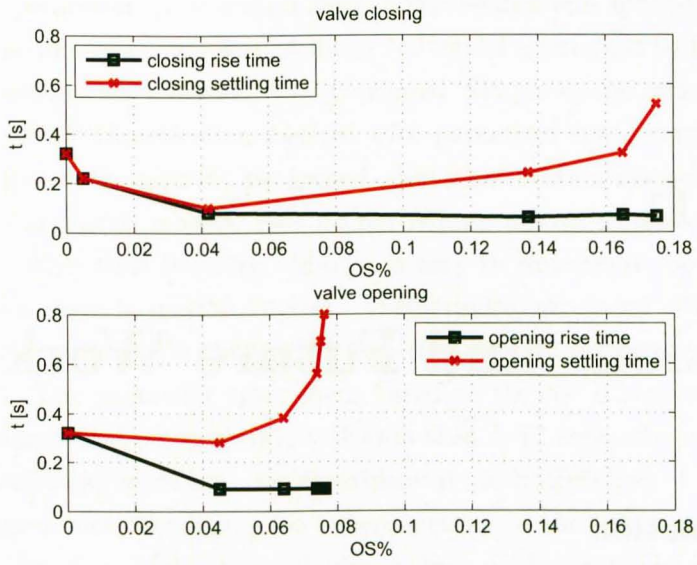

Figure 10.13: Overshoot (OS), rise time & settling time compromise

a frequency domain model of the electronic throttle valve.

- A locally smoothed frequency response of the system is obtained. This technique is suitable for the QFT frequency grid distribution.
- A NP QFT controller for the electronic throttle valve is presented. The design methodology can be applied on any electronic throttle valve regardless of its parameters and its nonlinear spring characteristics.
- No additional procedure is required for electronic throttle valves with different parameters such as valve diameter or different dynamics such as spring stiffness.
- The resulting final feedforward and feedback control compensators are linear.
- Notwithstanding that certain improvements in performance could be obtained by supplementing the controller with nonlinear compensation; an experimental application of the method showed that an acceptable settling time and rise time, may be possible without nonlinear compensator.
- A guideline figure is presented to show how the designer may use the technique to systematically trade-off the overshoot (OS) of the electronic throttle valve with the rise time and settling time.

Chapter 11

Conclusions and Future Work

11.1 Introduction

In this chapter, the conclusions from this thesis is presented in section 11.2. After that, possible future work is discussed in section 11.3. Suggested work, for the future, includes inverse modelling in subsection 11.3.1, parameter space control technique for the inverse compensated plant in subsection 11.3.2 and finally, the use of the non-uniform discrete Hilbert transform for MP equivalent nominal plant determination in subsection 11.3.3.

The principle broad conclusion is that the development of control techniques based on NP identification can be used as a tool to minimise the time and the experience needed in parametric driveline modelling approaches.

11.2 Conclusions

Based on the thesis objectives in subsection 1.1 of Chapter 1, the conclusions of this thesis are found to be satisfying the desired objectives. The final conclusions of this thesis can be sated in the following items:

- A novel mathematical model for the driveline is presented and subsequently used as one means to evaluate one of the proposed control methods. Both clutch nonlinearity and backlash nonlinearity are modelled. Backlash is more realistically sandwiched between the compliant clutch and compliant drive shafts, unlike the published driveline models. Model parameters have been chosen to represent a typical European midrange passenger vehicle. The model is used, in simulation, for applying the NP QFT control technique which is presented in this thesis. The model should be useful for further control systems development.

- A novel NP parameter space control method is presented and applied experimentally on the IC engine idle speed problem. A linear NP model is obtained by the local frequency smoothing estimation method. The presented NP parameter space control method combines the NP identification method with parameter space control and therefore, the benefits of both methods are gained. NP identification methods are easy to use and unlike parametric models, they do not require any structural assumptions about the system, other than linearity. Also, it is easy to concentrate on certain frequency ranges where there is specific interest. Furthermore, the usual advantage of the parameter space technique is obtained by superimposing the gain margin loci with phase margin loci. The parameter space locus based on the NP IC engine model for a certain gain margin and phase margin is drawn, then, a PI controller which satisfies both gain and phase loci is chosen. An experimental implementation of the NP parameter space designed controller is applied experimentally to the idle speed problem for the 1.6 L, 16-valve, four-stroke, four-cylinder, in-line, double overhead cam, water cooled, multi-point fuel injected IC Zetec engine on the University of Liverpool low inertia dynamometer. The experimental validation showed the advantages of using this closed loop control methodology for the problem in terms of rapid tracking and efficient disturbance rejection.

- This thesis integrated a NP identification approach with the QFT control methods to present a novel NP QFT method for nonlinear systems. The ability of the QFT method to reduce the effect of parameters variation of the system is one among other important reasons for using feedback techniques in controller design. This reduction of the sensitivity to the system uncertainty together with disturbance rejection is the main reasons why feedback systems are used. The QFT method developed by Isaac Horowitz is a feedback control technique for achieving that reduction in sensitivities. The method is based on obtaining a Linear Time Invariant Equivalent (LTIE) set. NP frequency response identification method is used to obtain a LTIE sets for the nonlinear system using a frequency weighted windowing approach to allow the use of obtained finite I/O data records. The method was validated in simulation first, and then it was applied experimentally to a vehicle driveline problem and to an electronic throttle valve system. The NP model is obtained by a local frequency smoothing estimation method. The aim was to design an effective QFT controller for the nonlinear systems based on NP identification which cannot otherwise be applied without nonlinear parametric models. The thesis presents a further novelty when the discrete Hilbert transform is used to estimate the NP QFT phase shift required in the QFT methodology when the identified system is found to be NMP system.

- Both the simulation and the experimental studies carried on in this thesis show the validity of the presented methods to the IC engine idle speed control and the driveline

wheel speed control problems. In the case of idle speed, the controller was able to track the reference input demand effectively. Also the disturbance rejection performance was found to be fast and effective. In the case of the wheel speed control, both tracking performance and disturbance rejection performance were found to be within the pre-designed limits which means, significantly reduced of human driving skill will be needed for achieving the required response.

- All the experimental validation approaches used a black-box modelling approach in which the controllers were developed directly from time series data acquired during testing. The experimental results showed that both the new NP parameter space and new NP QFT methods were able to achieve robust control with the required performance for both the engine idle speed and driveline wheel speed problems. The method is systematic and there is no need to change the design methodology when applied to similar systems of different size.

- Nonlinear systems such as systems with backlash may be very difficult to identify as parametric models. The presented control design methods are very useful where only experimental data is available and an efficient controller is required. No iterations are required and no trial and error calculations need to be made.

11.3 Future Work

Simplifying the design technique and obtaining for same performance could be the next target. In the next sections, some ideas are suggested to reduce the plant's nonlinearities so that, linear identification and linear controller could be used. Inverse modelling and inverse compensators are suggested so that NP QFT (see section 7.4 of Chapter 7) or NP parameter space control methods can then be used as a technique in the driveline speed control problem.

11.3.1 Inverse Modelling, Simulation and NP System Identification

One of the possible areas for future work is to explain the feasibilities of adding an inverse compensator before the identified plant in the NP QFT method. This idea is applied on parametric models only in [170] and recently in [171]. In simulation, inverse models like the one in Figure 11.3 can be used as inverse compensator with the simulation model presented in Chapter 4. Using such an inverse compensator should have a significant effect in uncertainty templates size as reported in [172]. The smaller templates particularly around the crossover frequencies gives the designer the ability to maneuvre with the templates in Nichols chart during loop-shaping process and so achieve a higher performance for the same robustness.

The proposed method here is to use NP system identification techniques to develop an inverse filter Λ fitted on the front of the original uncertain plant as in Figure 11.1. After

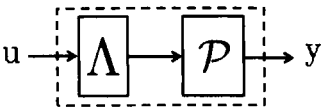

Figure 11.1: Inverse compensated plant

that, and before the control process, the compensated system may be identified by system identification techniques. NP identification can be used again to identify the compensated system. This compensated system can be controlled by the NP QFT method presented in

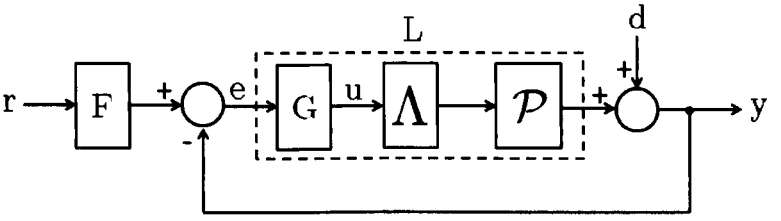

Figure 11.2: Inverse compensated plant in QFT structure

this thesis. Although, smaller templates size is expected, this cannot be assumed for the whole frequency range. The effect of an inverse compensator is expected to be benefits in the frequency range between the gain cross over frequency and phase cross over frequency by means of making the size of the uncertainty templates smaller than its original size in this range. However, the size of the templates for the compensated system may be expected to be bigger than its original size in some areas outside the mentioned frequency range. So, more care about the desired bandwidth should be taken account of when an inverse compensator technique is used.

When the output signal is used as an input signal and vice versa, the obtained model represents the inverse compensator suggested here. Shenton and Petridis [171] presented a method for determining the beneficial of any compensation on the uncertain dynamics. As seen in Figure 11.4, comparing the Vector Margin (VM) for the open loop plant locus at the same frequency before and after compensation can provide a good estimation of the benefits gained by the inverse compensation process.

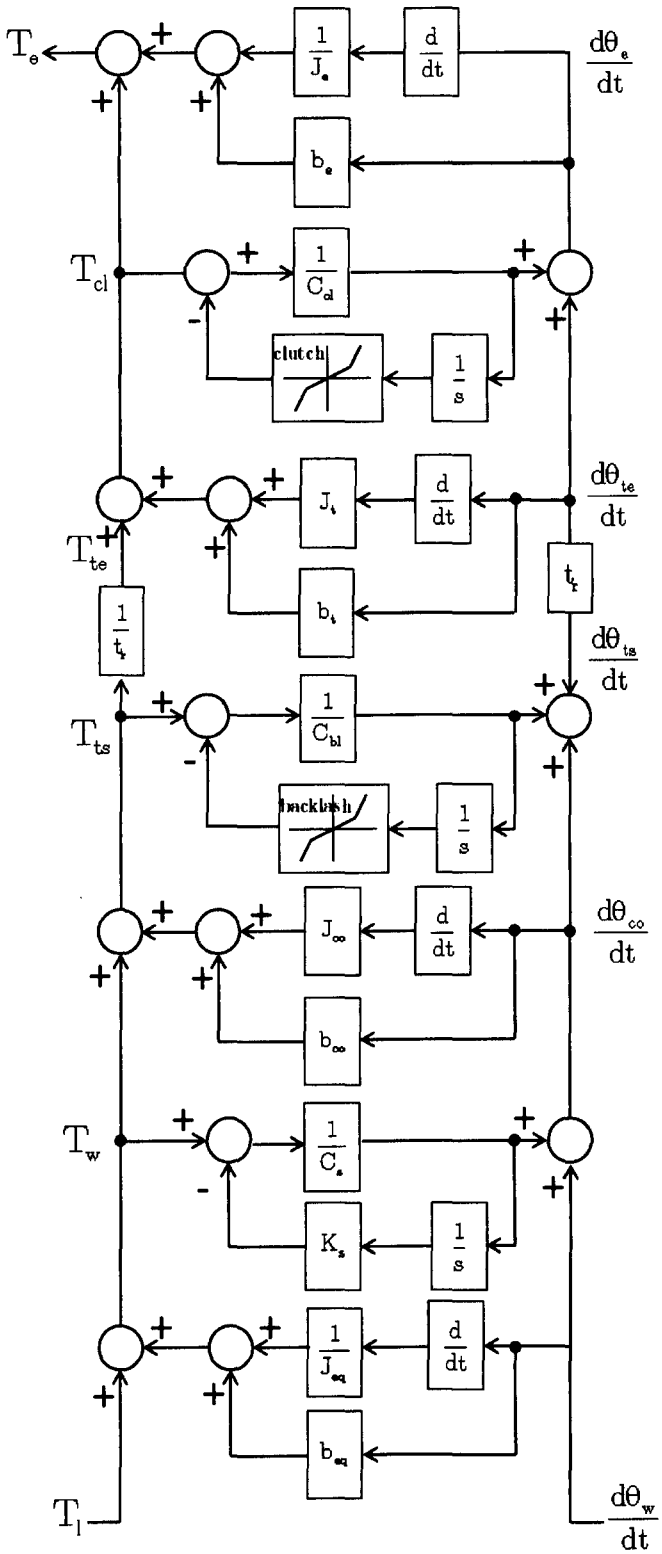

Figure 11.3: Inverse simulation block diagram

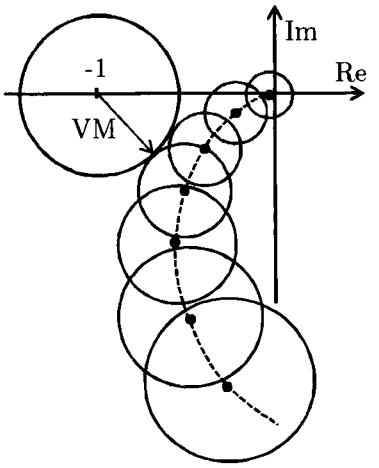

Figure 11.4: VM for the plant open loop locus

11.3.2 Parameter Space Control Technique for the Inverse Compensated Plant

Another option to is to use the parameter space control technique to control the inverse compensated system. When inverse compensator is added, the system nonlinearity is expected to decrease within a certain frequency range so PI controller is expected to satisfy the design requirements. As described in section 6.4 of Chapter 6, frequency response parameter space methods present a mature set of tools for nonparametric control design. A PI controller can be obtained by solving the equation

$$\frac{K_p j\omega + K_i}{j\omega} G(j\omega) = a + jb \tag{11.1}$$

where $a + jb$ is a point in the complex plane adjusted according to the required gain and phase margins. By increasing of ω from 0 to ∞ in Eqn.(11.1) a locus is traced out in parameter space for the point $a + jb$. Using the NP parameter space control technique combined with the inverse compensated system is believed to be a good way of designing a low order controller with high performance. Figure 11.5 shows applying parameter plane controller technique on the simulation model and Figure 11.6 displays the use of parameter plane with the experimental driveline model. Each NP model draws a locus representing the desired GM and PM. The controller parameters can be chosen inside the boundaries as it can bee seen in Figure 11.5 and Figure 11.6. No inverse compensation is done before applying the technique in these figures, so the obtained PI controllers were not giving an acceptable performance. When inverse compensation technique used, it is expected that such that method will be valid and acceptable performance is expected to be obtained.

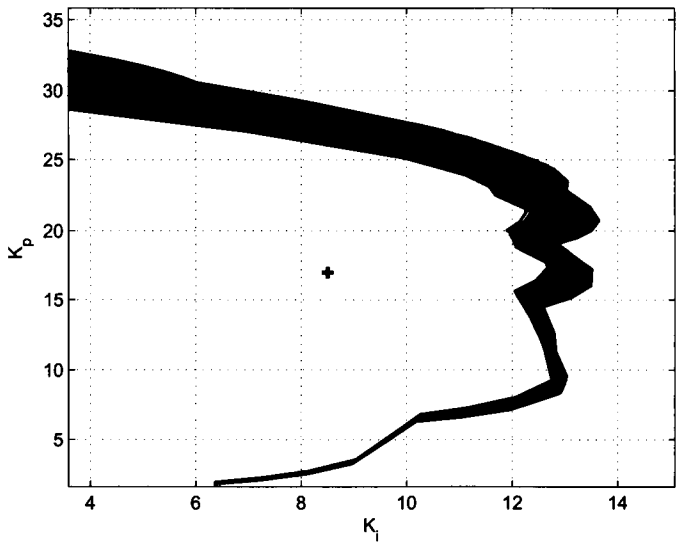

Figure 11.5: Applying parameter plane controller technique on the simulation model

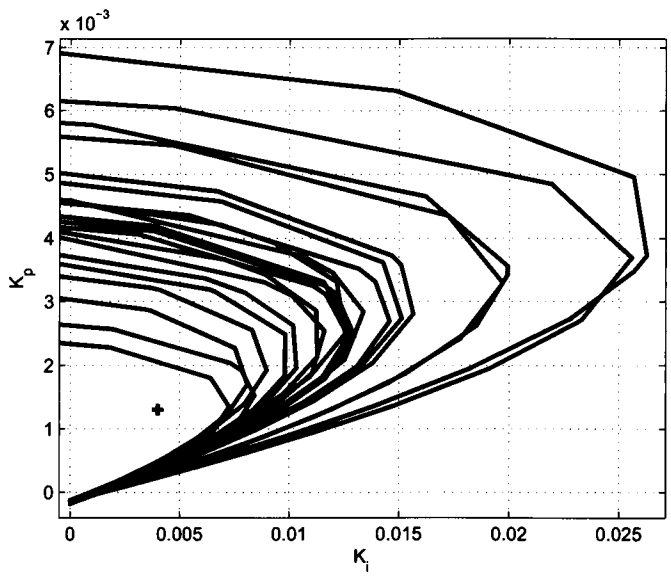

Figure 11.6: Applying parameter plane controller technique on experimental NP model

11.3.3 Non-uniform Discrete Hilbert Transform

The discrete Hilbert transform is used to obtain an equivalent MP nominal plant of the NMP system nominal plant in section 7.6 of Chapter 7. Because the templates frequencies are not uniform, and the discrete Hilbert transform is based on using a uniform frequency grid of FFT, the technique has to use a transfer function fit to overcome this problem. The unavailability of non-uniform DFT or FFT makes the methodology more complicated. Of course, if a non-uniform discrete Hilbert transform based on non-uniform DFT is developed, the flow chart of Figure 7.10 could be reused as in Figure 11.7.

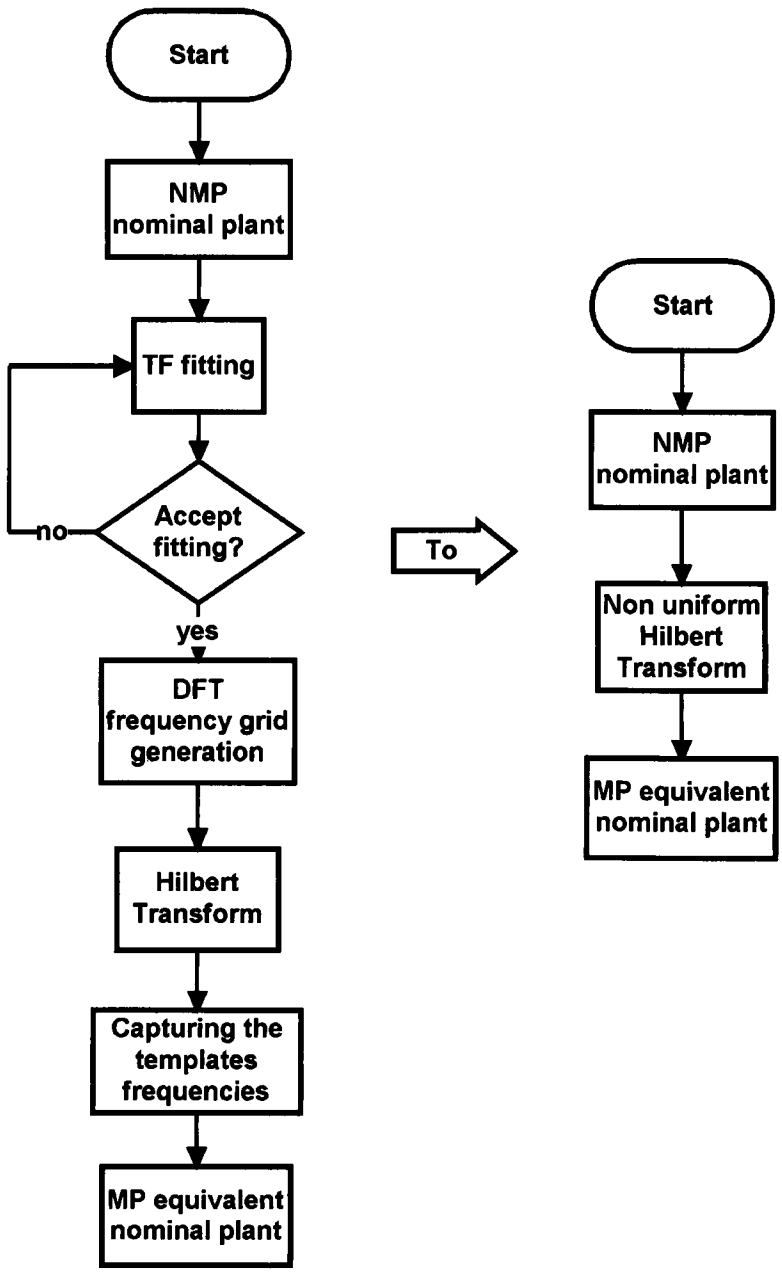

Figure 11.7: Applying nonuniform discrete Hilbert transform

References

[1] A. A. Stotsky. *Automotive Engines Control, Estimation, Statistical Detection.* Springer Dordrecht Heidelberg London New York, 2009.

[2] J. Fenton. *Advances in Vehicle Design.* Professional Engineering Publishing Limited, London, 1999.

[3] H. O. List. Objective evaluation of vehicle driveability. *SAE International*, 980204, 1998.

[4] Ljung L. *System Identification, Theory For The User.* Prentice Hall PTR, New Jersey, USA, 1999.

[5] J. Schoukens, T. Dobrowiecki, and R. Pintelon. Parametric and nonparametric identification of linear systems in the presence of nonlinear distortions - a frequency domain approach. *IEEE Transactions on Automatic Control*, 43, 2:176–190, 1998.

[6] J. M. Maciejowski. *Multivariable Feedback Design.* Addison-Wesley Publishing Company Inc., 1989.

[7] P. E. Wellstead. *Introduction to Physical System Modelling.* Academic Press, London, 1979.

[8] E. Hendricks and S. C. Sorenson. Mean value modeling of spark ignition engines. *SAE Technical Papers*, 900616, 1990.

[9] T. Soderstrom and P. Stoica. *System Identification.* Prentice-Hall, 1989.

[10] A. C. Atkinson. *Optimum Experimental Designs.* Clarendon, Oxford, 1992.

[11] E. Hendricks and S. C. Sorenson. Systematic techniques for determining modelling requirements for SISO and MIMO feedback control. *Journal of Process Control*, 5,4:213–224, 1995.

[12] G. C. Goodwin and R. L. Payne. *Dynamic System Identification: Experiment Design and Data Analysis, Mathematics in Science and Engineering*, volume 136. Academic Press Inc., 1995.

[13] M. Verhaegen and V. Verdult. *Filtering and System Identification, A Least Squares Approach.* Cambridge University Press, New York, 2007.

[14] L. Ljung. *System Identification Toolbox, Getting Started Guide.* The MathWorks, Inc., 3 Apple Hill Drive, Natick, MA 01760-2098, 2010.

[15] B. A. Shenoi. *Introduction to Digital Signal Processing and Filter Design.* John Wiley & Sons, Inc., Hoboken, New Jersey, 2006.

[16] S. A. Billing, S. Chen, and R. J. Backhouse. The identification of linear and nonlinear models of turbocharged automotive diesel engine. *Mechanical Systems and Signal Processing*, 3,2:123–142, 1989.

[17] S. A. Billing and Q. M. Zhu. A structure detection algorithm for nonlinear dynamic rational models. *International Journal of Control*, 59,6:1439–1463, 1994.

[18] G. Triantos and A. T. Shenton. NARMAX structure selection for powertrain control. *Proceedings IFAC symposium on: Advances in Automatic Control, Salerno*, pages 1–4, 2004.

[19] Ljung L. *System Identification Toolbox 7 Users Guide.* The MathWorks, Inc., 2007.

[20] R. Pintelon and J Schoukens. *System Identification, a Frequency Domain Approach.* Institute of Electrical and Electronics Engineers, Inc., New York, USA, 2001.

[21] S. R. Sanchez-Pena and M. Sznaier. *Robust Systems, Theory and Applications.* John Wiley & Sons, Inc., 1998.

[22] J.C. Doyle, B. Francis, and A. Tannenbaum. *Feedback Control Theory.* Macmillan Publishing Co., 1991.

[23] P. N. Paraskevopoulos. *Modern Control Engineering.* Marcel Dekker, Inc., 2002.

[24] R. C. Dorf and R. H. Bishop. *Modern Control Systems, Eleventh Edition.* Pearson Education, Inc., Upper Saddle River, NJ 07458, 2008.

[25] PCS Edventures Learning Network. Flyball governor, 2011. 345 Bobwhite Ct., Ste. 200, Boise.

[26] O. Mayr. *The Origins of Feedback Control.* MIT Press, Cambridge, Mass, 1970.

[27] H. Nyquist. Regeneration theory. *Bell Systems Technical Journal*, 11:126–147, 1932.

[28] H. Black. Stabilised feedback amplifiers. *Bell Systems Technical Journal*, 13:1–18, 1934.

[29] H. Bode. Relations between attenuation and phase in feedback amplifier design. *Bell Systems Technical Journal*, 19:421–454, 1940.

[30] W. Evans. Control system synthesis by root locus method. *Transactions of the American Institute of Electrical Engineers*, 69:66–69, 1950.

[31] C. Graham, Stefan F., and E. Mario. *Control System Design.* Prentice-Hall, Inc., Upper Saddle River, New Jersey, 2001.

[32] P. Dorato. *Robust Control.* IEEE Press, 1987.

[33] H. Bode. *Network Analysis and Feedback Amplifier Design.* Princeton, NJ, Van Nostrand, 1945.

[34] I. Horowitz. *Synthesis of Feedback Systems.* New York Academic Press, 1963.

[35] J. Cruz and Ed. *System Sensitivity Analysis.* Down, Hutchinson, and Ross, 1973.

[36] B. Franceis, J. Helton, and G. Zames. H^{∞} optimal feedback controller for linear multivariable systems. *IEEE Transactions*, AC-29 Technical Report:888–900, 1984.

[37] G.F. Franklin, J.D. Powell, and A. Emami-Naeini. *Feedback Control of Dynamic Systems.* Pearson Prentice Hall, New Jersey, 07458, 2006.

[38] S. Skogestad and I. Postlethwaite. *Multivariable Feedback Control, Analysis and Design.* John Wiley & Sons, 1996.

[39] A. Lagerberg. A literature survey on control of automotive powertrains with backlash. *Report R013, Department of Signal and Systems, Chalmers University of Technology, Sweden*, 2001.

[40] A. Lagerberg and B. Egardt. Evaluation of control strategies for automotive powertrains with backlash. *International Symposium on Advanced Vehicle Control*, 6:517–522, 2002.

[41] A. Lagerberg and B.S. Egadt. Estimation of backlash with application to automotive powertrains. 2003.

[42] A. Lagerberg and B. Egardt. Estimation of backlash in automotive powertrains – an experimental validation. *IFAC Symposium on Advances in Automotive Control*, a:60–65, 2004.

[43] U. Kiencke and L. Nielsen. *Automotive Control Systems for Engine, Driveline, and Vehicle.* Springer-Verlag Berlin Heidelberg, New York, 2000.

[44] H. Gerhardt J., Honinger and H. Bischof. A new approach to functional and software structure for engine management systems. *SAE Technical paper*, 49:178–190, 1989.

[45] J. Prony. Experimental and analytical test on the pea dilatability elastic fluids and cells of the expansive force of steam and water vapor alcohol which has different temperatures. *IEcola Polytechniqu*, 1, 2:24–67, 1975.

[46] Y. W. Lee. *Statistical Theory of Communication.* MIT Press, Cambridge, Mass. USA, 1966.

[47] P.E. Wellstead. Non-parametric methods of system identification. *Automatica*, 17:55–69, 1981.

[48] W. W. Peterson. *Error Correcting Codes.* MIT Press, Cambridge, Mass. USA, 1965.

[49] W. D. T. Davis. Generation and properties of maximum length sequences. *International Journal of Control*, 5, 431:302–364, 1966.

[50] K. R. Godfrey. Theory of the correlation method of dynamic analysis and its apphcations. *Measurement Control*, 65, 2, 1969.

[51] P. Guillaume. Nonparametric frequency response function estimators based on nonlinear averaging techniques. *IEEE Transaction on Instrumentation and Measurement*, 41,6:739–746, 1992.

[52] J. Schoukens, R. Pintelon, G. Vandersteen, and P. Guillaume. Frequency-domain system identification using non-parametric noise models estimated from a small number of data sets. *Automatica*, 33,6:1073–1086, 1997.

[53] R. Pintelon, J. Schoukens, and G. Vandersteen. Frequency domain system identification using arbitrary signals. *IEEE Transactions on Automatic Control*, 42,12:1717–1720, 1997.

[54] L. Ljung and K. Glover. Frequency domain versus time domain methods in system identification. *Automatica*, 17,1:71–86, 1981.

[55] M.A. Shah and M.A. Franchek. Frequency-based controller design for a class of nonlinear systems. *International Journal Robust Nonlinear Control*, 9:825–840, 1999.

[56] J.W. Glass and M.A. Franchek. Frequency based nonlinear controller design of regulating systems subjected to time domain constraints. *International Journal of Robust and Nonlinear Control*, 10:39–57, 2000.

[57] T. Inanc and M. Sznaier. Robust identification with mixed parametric/nonparametric models and time/frequency-domain experiments: Theory and an application. *IEEE Transaction on Control Systems Technology*, 9:608–617, 2001.

[58] L. Balogh and I. Kollar. Generalization of total least squares problem in frequency domain system identification. *Instrumentation and Measurement, IEEE Transactions on Instrumentation and Measurement*, 51,6:1353–1357, 2003.

[59] L. Ljung. Integrated frequency-time domain tools for system identification. *IEEE Instrumentation and Measurement Technology Conference*, pages 5594–5599, 2001.

[60] B. Miao and R. Zane. System identification of power converters with digital control through cross-correlation methods. *IEEE Transaction on Power Electronics*, 20,5:1093–1099, 2005.

[61] R.W.P. Luk and R.I. Damper. Non-parametric linear time-invariant system identification by discrete wavelet transforms. *Digital Signal Processing*, 16:303–319, 2006.

[62] L. Ljung. *Modeling of Dynamic Systems.* Prentice-Hall, Inc., A Paramount Communications Company, Englewood Cliffs, New Jersey 07632, 1994.

[63] Ljung L. Linear system identification as curve fitting. *Springer Lecture Notes on Control and Identification*, 286:203–215, 2003.

[64] D. Hrovat and W.E. Tobler. Bond graph modeling of automotive power trains. *Journal of the Franklin Institute*, 328,5/6:623–662, 1991.

[65] S. De La Salle, M. Jansz, and D. Light. Design of a feedback control system for damping of vehicle shuffle. *EAEC European Automotive Congress, Barcelona, Spain*, 1999.

[66] C.Y. Mo, A.J. Beaumount, and N.N. Powell. Active control of driveability. pages 215–221, 1996.

[67] J. Baumann, D.D. Torkzadeh, A. Ramstein, U. Kiencke, and T. Schlegl. Model-based predictive anti-jerk control. *ELSEVIER, Control Engineering Practice*, 14:259–266, 2006.

[68] G. Balfour, P. Dupraz, M. Ramsbottom, and P. Scotson. Diesel fuel injection control for optimum driveability. *SAE 2000 World Congress, Detroit, MI, USA*, 2000-01-0265, 2000.

[69] A. Gelb and W.E.V. Velde. *Multiple-Input Describing Functions and Nonlinear System Design.* McGraw-Hill book Company, New Yourk St. Louis, 1968.

[70] I. Kaya and D.P. Atherton. Parameter estimation from relay autotuning with asymmetric limit cycle data. *ELSEVIER, Journal of Process Control*, 11,4:429–439, 2001.

[71] H. Heisler. *Vehicle Engine Technology, Second Edition.* Linacre House, Jordan Hill, Oxford, 1999.

[72] U. Kiencke and L. Nielsen. *Automotive Control Systems for Engine, Driveline, and Vehicle (2nd edition).* Springer-Verlag Berlin Heidelberg, New York, 2000.

[73] I. Horowitz and M Sidi. Synthesis of feedback systems with large plant ignorance for prescribed time-domain tolerances. *International Journal of Control*, 16,2:287–309, 1972.

[74] K. Krishnan and A. Cruickshanks. Frequency-domain design of feedback systems for specified insensitivity of time-domain response to parameter variation. *International Journal of Control*, 25,4:609–620, 1977.

[75] I. Horowitz and M Sidi. Synthesis of linear time varying non-minimum-phase system with plant uncertainty. *International Journal of Control*, 27,3:351–359, 1978.

[76] I. Horowitz and M Sidi. Optimum synthesis of non-minimum-phase feedback systems with plant uncertainty. *International Journal of Control*, 27,3:361–386, 1978.

[77] I. Horowitz. Non-linear uncertain feedback systems with initial state values. *International Journal of Control*, 34,4:749–764, 1981.

[78] I. Horowitz. Improvement in quantitative non-linear feedback design by cancellation. *International Journal of Control*, 34,3:547–560, 1981.

[79] I. Horowitz. Uncertain multi-input-multi-output systems with internal variable feedback. *International Journal of Control*, 36,6:989–1009, 1982.

[80] I. Horowitz. Quantitative feedback theory. *IEE Proceedings*, 129,6:215–226, 1982.

[81] D. J. East. On the determination of plant variation bounds for optimum loop synthesis. *International Journal of Control*, 35, 5:891–908, 1982.

[82] F. Bailey and C. Hui. Loop gain-phase shaping for single-input-single-output robust controllers. *IEEE Control Systems Magazine*, 11,1:93–101, 1991.

[83] C. Houpis, R. Sating, S. Rasmuseen, and S. Sheldon. On the determination of plant variation bounds for optimum loop synthesis. *International Journal of Control*, 59,1:39–70, 1994.

[84] G. Bryant and G. Halikias. Optimal loop-shaping for system with large parameter uncertainty via linear programming. *International Journal of Control*, 62,3:557–568, 1995.

[85] I. Horowitz. Some ideas for QFT research. *International Journal of Robust and Nonlinear Control*, 13:599–605, 2003.

[86] B. C. Kuo and F. Golnaraghi. *Automatic Control Systems*. John Wiley & Sons, Inc., 2003.

[87] J. Doyle. Analysis of feedback systems with structured uncertainties. *IEEE Proceedings*, 129:242–250, 1982.

[88] C. Doyle and C. , Chu. *Robust Control of Multivariable and Large Scale Systems.* Honeywell Systems and Research Centre Minneapolis MN, 2002.

[89] D. J. East. A new approach to optimum loop synthesis. *International Journal of Control*, 34,4:731–748, 1981.

[90] F. N. Bailey, D. Panzer, and G. Gu. Two algorithms for frequency domain design of robust control systems. *International Journal of Control*, 48, 5:1787–1806, 1988.

[91] F. N. Bailey and C. H. Hui. A fast algorithm for computing parametric rational functions. *IEEE Transactions on Automatic Control*, 34, 11:1209–1212, 1989.

[92] A. C. Bartlett. Nyquist, bode and nichols plots of uncertain systems. *American Control Conference, San Diego, USA*, 1990.

[93] A. C. Bartlett. Computation of the frequency response of systems with uncertain parameters: a simplification. *International Journal of Control*, 57:1293–1309, 1993.

[94] M. Fu. Computing the frequency response of linear systems with parametric perturbation. *Systems & Control Letters*, 15:45–52, 1990.

[95] H. Chapellat and S. P. Bhattacharyya. A generalization of kharitinov's theorem: Robust stability of interval plants. *IEEE Transactions on Automatic Control*, 34:306–301, 1989.

[96] L. H. Keel and S. P. Bhattacharyya. Ieee transactions on automatic control. *Robust Parametric Classical Control Design*, 39:1524–1530, 1994.

[97] V. Pande and P. S. V. Nataraj. On the role of kharitinov segments and vertex type results in quantitative feedback theory. *Quantitative and Parametric Feedback Theory Symposium Proceedings, O. D. I. Nwokah and P. Chandler, Purdue University and Wright Laboratory*, pages 86–93, 1995.

[98] C. B. Barber, D.P. Dobkin, and H.T. Huhdanpaa. The quickhull algorithm for convex hulls. *ACM Transactions on Mathematical Software*, 22, 4:469–483, 1996.

[99] C.H. Houpis and S.J Rasmussen. *Quantitative Feedback Theory.* Marcel Dekker, Inc., New York, 10016, 1999.

[100] O. Yaniv. *Quantitative Feedback Design of Linear and Nonlinear Control Systems.* Kluwer Academic Publishers, London, 1999.

[101] J.J. D'Azzo. *Linear Control System Analysis and Design.* McGraw-Hill, Inc., USA, 1975.

[102] I. Horowitz and M. Sidi. Optimum synthesis of non-minimum phase feedback systems with plant uncertainty. *International Journal of Control*, 27,3:361–386, 1978.

[103] M. Johansson. The Hilbert transform. M. Sc. thesis, Vaxjo University, Vaxjo, Sweden, 1999.

[104] H. Peter. *Applied and Computational Complex Analysis.* John Wiley & Sons, Inc., New York, 1988.

[105] S. Lawrence Marple and Jr. Computing the discrete-time analytic signal via fft. *IEEE Transactions on Signal Processing*, 47,9:2600–2603, 1999.

[106] J. W. Cooley and J. W. Tukey. An algorithm for the machine computation of the complex fourier series. *Mathematics of Computation*, 19:297–301, 1965.

[107] P. Duhamel and M. Vetterli. Fast fourier transforms: A tutorial review and a state of the art. *Signal Processing*, 19:259–299, 1990.

[108] A. V. Oppenheim and R. W. Schafer. *Discrete Signal Processing.* Prentice Hall, Inc., New Jersey 07458, 1999.

[109] M. Frigo and S. G. Johnson. Fftw: An adaptive software architecture for the fft. *Proceedings of the International Conference on Acoustics, Speech, and Signal Processing*, 3:1381–1384, 1998.

[110] I. Horowitz and A. Banos. Fundamentals of nonlinear quantitative feedback theory. *Advances in the Control of Nonlinear Systems*, 264:63–132, 2001.

[111] K. Kokotovic and D. Rhode. Sensitivity guided design of an idle speed controller. *Report No. 1 to Ford Motor Company, PK Research, Urbana, USA*, 1986.

[112] D. Hrovat and W. Johnson. Automotive control systems: Past, present, future. *Proceeding IECON 91, Kobe, Japan*, 1991.

[113] K. Powell and W. Powers. Linear quadratic control design for nonlinear ic engine systems. *ISATA Conference, Stockholm, Sweden*, 1981.

[114] F. Powers, K. Powell, and P. Lawson. Applications of optimal control and kalman filtering to automotive systems. *International Journal of Vehicle Design Special Publication*, SP4, 1983.

[115] R.L. Morris and B.K. Powell. Modem control applications in idle speed control. *Proceeding American Control Conference*, pages 79–85, 1983.

[116] T. Takahashi, T. Ueno, A. Yamamoto, and H. Sanbuichi. A simple engine model for idle speed control. *SAE*, 850291, 1985.

[117] E. Baumgartner, H. Geering, C. Onder, and E. Shafal. Robust multivariable idle speed control. *Proc. American Control Conference, Seattle, USA*, 1986.

[118] M. Abate and V. DiNunzio. Idle speed control using optimal regulation. *SAE*, 905008, 1990.

[119] A Fraser, J. Mills, and D. Hrovat. Idle speed control based on preview information. *Ford Motor Company, Dearborn, MI, USA*, 1992.

[120] S. Williams. Idle speed control design using an $\mathcal{H}_\infty$ approach. *American Control Conference, Pittsburgh, USA*, pages 1950–1956, 1989.

[121] C. Camevale and A. Moschetti. Idle speed control with h-infinity technique. *SAE*, 930770, 1993.

[122] D. Hrovat and B. Bodenheimer. Robust automotive idle speed control design based on μ-tsynthesis. *American Control Conference, San Francisco, USA*, 1993.

[123] S. Jayasuriya and M. Franchek. A QFT type design methodology for a parallel plant structure and its application in idle speed control. *International Journal of Control*, 60, 5:653–670, 1994.

[124] A. Olbort and B. Powell. Robust design and analysis of third and fourth order time delay systems with application to automotive idle speed control. *American Control Conference, Pittsburgh*, 1989.

[125] M. Abate and N. Dosio. Use of fuzzy logic for engine idle speed control. *SAE*, 900594, 1990.

[126] G. Puskorius and L. Feldkamp. Automotive engine idle speed control with recurrent neural networks. *American Control Conference, San Francisco, CA, USA*, 0-7803-0860-3:311–316, 1993.

[127] H. Kuraoka, N. Ohka, S. Ohba, and F. Zhang. Application of $\mathcal{H}_\infty$ design to automotive fuel control. *IEEE Control Systems Magazine*, 1990.

[128] M. Takano, K. Kurotani, K. Takeda, A. Tanisaka, S. Kusumoto, and K. Yano. Application of $\mathcal{H}_\infty$ control to motor speed control systems. *IECON'91*, 1991.

[129] I. Niemark. On the problem of the distribution of roots and polynomials. *Dokl. Akad. Nauk. SSSR.*, 58:357, 1947.

[130] I. Niemark. Structure of the d-partition of the space of polynomials and diagram of vishnegradskii. *Dokl. Akad. Nauk. SSSR.*, 59:853, 1948.

[131] D. Mitrovic. Graphical analysis and synthesis of feedback control system, i - theory and analysis, ii – synthesis. *Transactions of the AIEE Applications in Industry*, 77:476–496, 1959.

[132] G. Thaler and R. G. Brown. *Analysis and Design of feedback Control Systems.* McGraw Hill, 1960.

[133] D. Siljak. Analysis and synthesis of feedback control systems PTS I, II, III. *IEEE Transaction on Automatic Control*, 34,7:449–473, 1964.

[134] B. Porter. *Stability Criteria for Linear Dynamical Systems.* Academic Press, London, 1968.

[135] J. Ackermann. Parameter space design of robust control systems. *IEEE Transactions on Automatic Control*, 25, 6:1058–1072, 1980.

[136] R. Cook. Gain and phase boundary routine for two-loop feedback systems. *IEEE Transaction on Automatic Control*, 11,3:573–576, 1966.

[137] H. Chang and W. Han. Gain margins and phase margins for control systems with adjustable parameters. *International Journal of Guidance, Control, and Dynamics*, 15, 4:404–408, 1990.

[138] H. Chang and W. Han. Gain margins and phase margins for sample-data control systems with adjustable parameters. *IEEE Proceeding*, D, 138:285–291, 1991.

[139] Shafiei Z. and A. Shenton. Tuning of PID controller for stable and unstable systems with time delay. *Automatica*, 30,10:1609–1615, 1994.

[140] Z. Shafiei and A.T. Shenton. Relative stability for control system with adjustable parameters. *International Journal of Guidance, Control, and Dynamics*, 17, 2:3342–3346, 1997.

[141] Z. Shafiei and A.T. Shenton. Frequency domain design of PID controllers for stable and unstable systems with time delay. *Automatica*, 23:2223–2232, 1994.

[142] V. Besson and A.T. S., Shenton. Interactive control system design by a mixed $\mathcal{H}_\infty$ - parameter space method. *IEEE Transactions on Automatic Control*, 1997.

[143] M. Saeki and M. Saeki. A design method of the optimal PID controller for a two disc type mixed sensitivity problem. *Transactions of the Institute of Systems Control and Information Engineering*, 7, 12:520–527, 1994.

[144] M. Saeki and K. Aimoto. PID controller optimisation of $\mathcal{H}_\infty$ control by linear programming. *International Journal of Robust and Nonlinear Control*, 10:83–99, 2000.

[145] V. Besson and A.T. S., Shenton. An interactive parameter space method for robust performance in mixed sensitivity problems. *IEEE Transactions on Automatic Control*, 1999.

[146] V. Besson and A.T. S., Shenton. Interactive parameter space method for robust performance of MISO control systems. *IEEE Transactions on Automatic Control*, 2000.

[147] J. Ackermann, P. Blue, L. Guvenc, D. Kaesbauer, M. Kordt, and D. Odenthal. Robust control: The parameter space approach. *Springer, London*, 2002.

[148] M. Saeki. Fixed structure PID controller design for standard $\mathcal{H}_\infty$ control problem. *Automatica*, 42, 1:93–100, 2006.

[149] M. Muhler. Mapping MIMO control system specifications into parameter space. *Proceeding of the 41st IEEE Conference on Decision and Control*, pages 4527–4532, 2002.

[150] V. Besson. Parameter space robust control for SI engine idle speed. *Ph.D. Thesis*, Department of Engineering, University of Liverpool, UK, 1996.

[151] P. Putz and M. Wozny. A new computer graphics approach to parameter space design of control systems. *IEEE Transactions on Automatic Control*, 32, 4:294–302, 1987.

[152] A. Banos and F. Bailey. Design and validation of linear robust controllers for nonlinear plants. *International Journal of Robust and Nonlinear Control*, 8:803–816, 1998.

[153] A. Banos. Nonlinear quantitative feedback theory. *International Journal of Robust and Nonlinear Control*, 17:181–202, 2007.

[154] I. Horowitz. *Quantitative Feedback Design Theory.* QFT Publications, Boulder, Colorado 80303, 1993.

[155] Inc. The MathWorks. Signal processing toolbox for matlab and simulink, ver 6.14. 2010.

[156] K. Ogata. *Modern Control Engineering, Fifth Edition.* Pearson Education, Inc., 2010.

[157] E.C. Levi. Complex-curve fitting. *IRE Transactions on Automatic Control*, AC-4:37–44, 1959.

[158] J. E. Jr. Dennis and R. B. Schnabel. *Numerical Methods for Unconstrained Optimization and Nonlinear Equations, Englewood Cliffs.* Prentice-Hall, New Jersey, 1983.

[159] S. DeLaSalle, M. Jansz, and D. Light. Design of a feedback control system for damping of vehicle shuffle. *Proceedings of the EAEC Conference, Barcelona*, pages 278–284, 1999.

[160] dSPACE GmbH. *Embedded Success dSPACE Catalog.* dSPACE GmbH.,33102 Paderborn, Germany, 2010.

[161] Walker D. *Engine Management, Optimising Carburettors, Fuel Injection and Ignition Systems.* Haynes Publishing, Sparkford, Yeovil, 2006.

[162] C. Matthews, Paul B. Dickinson, and A. Thomas Shenton. Chassis dynamometer torque control: A robust control methodology. *SAE International Journal of Passenger Cars*, 2:263–270, 2009.

[163] Thomasson A. and Eriksson L. Model-based throttle control using static compensator and IMC based PID-design. 2009.

[164] Vidal Y., Acho L., and F. Pozo. Robust control of an electronic throttle system via switch chattering control: Benchmark experiments. 2009.

[165] Chang Yang. Model-based analysis and tuning of electronic throttle controllers. *SAE Technical Paper Series*, 2004-01-0524, 2004.

[166] Peric N. Deur J., Pavkovic D. and M. Jansz. An electronic throttle control strategy including compensation of friction and limp-home effects. volume 1, pages 200–206, 2003.

[167] Peric N. Deur J., Pavkovic D. and M. Jansz. Adaptive control of automotive electronic throttle. *ELSEVIER*, 14:121–136, 2006.

[168] Yuan X. and Wang Y. A novel electronic-throttle-valve controller based on approximate model method. *IEEE*, 56,3:883–890, 2009.

[169] Chen W.H. and Ballance D.J. QFT design for uncertain non-minimum phase and unstable plants revisited. *International Journal of Control*, 74,9:957–965, 2001.

[170] I. Horowitz. Improvement in quantitative non-linear feedback design by cancellation. *International Journal of Control*, 34,3:547–559, 1981.

[171] A.T. Shenton and A.P. Petridis. Nonlinear MISO direct-inverse compensation for robust performance speed control of a si engine. *Springer Verlag Lecture Notes in Control and Information Science*, NCN4:335–347, 2002.

[172] A. Abass and A. T. Shenton. Automotive driveline modelling, inverse-simulation and compensation. *International Conference on Intelligent Systems, Modelling and Simulation*, 2010.